The Fermi Level in Hematite

Doping, Band Alignment, and Charge Transitions

Zur Erlangung des akademischen Grades Doktor-Ingenieur (Dr.-Ing.)
genehmigte Dissertation von Christian Lohaus aus Seeheim-Jugenheim
Tag der Einreichung: 05.10.2018, Tag der Prüfung: 07.02.2019
Darmstadt — D 17

1. Gutachten: Prof. Dr. W. Jaegermann
2. Gutachten: Ass.-Prof. Dr. O. Clemens

TECHNISCHE UNIVERSITÄT DARMSTADT

Materials Science Department
Surface Science
Surface Science Division

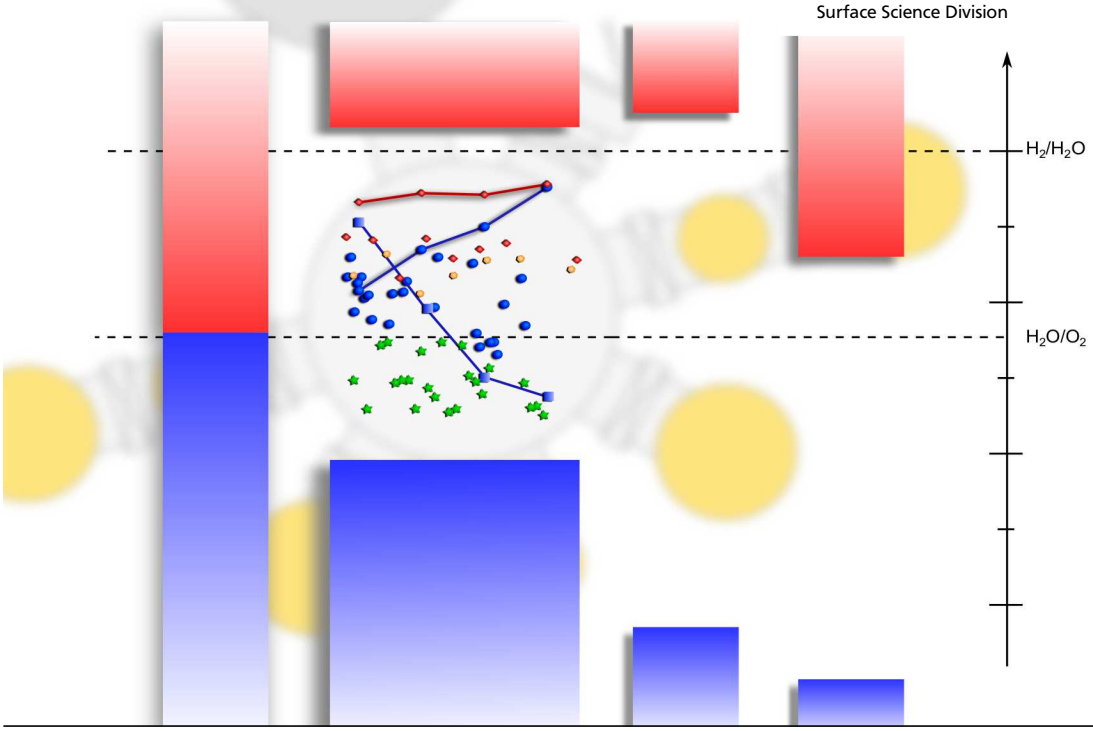

The Fermi Level in Hematite
Doping, Band Alignment, and Charge Transitions

Genehmigte Dissertation von Christian Lohaus aus Seeheim-Jugenheim

1. Gutachten: Prof. Dr. W. Jaegermann
2. Gutachten: Ass.-Prof. Dr. O. Clemens

Tag der Einreichung: 05.10.2018
Tag der Prüfung: 07.02.2019

Darmstadt — D 17

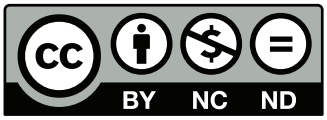

"*If in doubt, Meriadoc, always follow your nose.*"
Gandalf, Lord of the Rings

Contents

1 Motivation

Why Water Splitting?

In the wake of the 21st century mankind faces many challenges among which the closely-related growing energy demand and climate change are only two but of eminent importance. Globally the temperatures are rising and the ten warmest years since 1880 have all appeared since 1998.[1] Scientifically, it is out of question that the climate becomes warmer. The consequences on the environment, economy, global conflict potential, and migration, however, are still under debate within society and politics with different opinions on the topics.

While still denied by certain groups, the majority of scientists agree that the cause for climate change is to be found in human activities.[2] Especially the burning of fossil fuels results in the emission of greenhouse gases, such as e.g. CO_2. In addition, the pollution in cities around the world from fine particulate air, which can be associated with the burning of fossil fuels, has become an evident health concern.[3] These facts alone justify the investment and research in alternative energy solutions.

Among the different possibilities of sustainable energies the conversion of solar power into a usable energy form is of high interest. On a global scale most investments in the area of sustainable energy are in photovoltaics.[4] Even though this technique offers many advantages over the conventional burning of fossil fuels, such as oil or coal, there are also some challenges to be faced.

Of these challenges the storability of electrical power combined with the regional unavailability of power from photovoltaics due to the day-and-night-cycle are unquestionable of huge concern. One possible (and very elegant) solution is the direct conversion of solar power into chemical fuels without a further need of an external bias. On a first glance, the easiest process seems to be the production of hydrogen (and oxygen) from water with the help of sunlight. This unassisted photocatalytic process would result in a clean and sustainable product which could be directly used for the generation of electrical power in night-times, to fuel mobility, or as a reagent in further reactions to create fuels which are easier to use and store.[5–9]

The Water Splitting Process - Mechanism and Requirements

Since the early work of Fujishima and Honda it is known that the unassisted light-driven splitting of water can occur at the interface between an illuminated semiconductor and water.[10] The processes which need to take place in order to convert light and water into usable hydrogen are depicted schematically in Figure 1.1. This sketch is simplified, a more detailed description of an actual device can be found e.g. in Refs. [5] and [11].

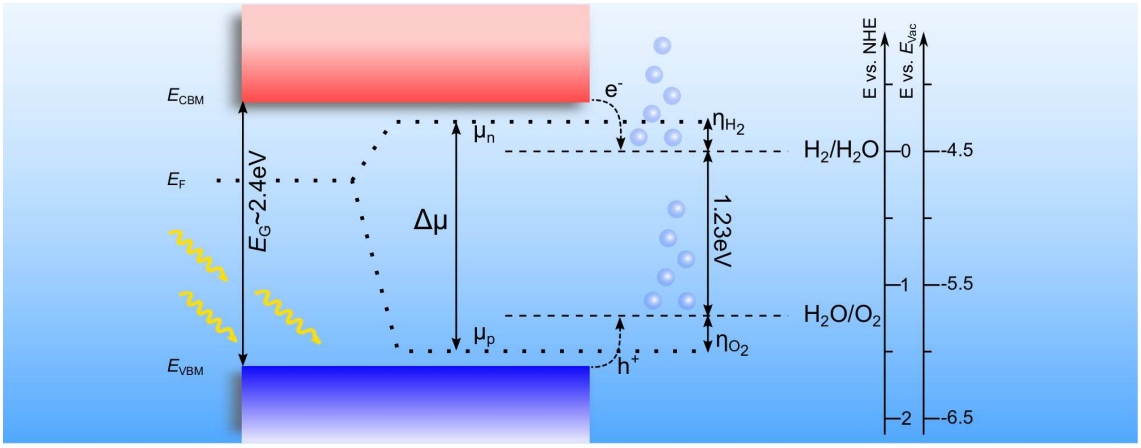

Figure 1.1: Schematic representation of the photocatalytic splitting of water at the interface of a semiconductor to an electrolyte.

The first step in order to split water is the absorption of photons by the semiconductor and the associated generation of electron-hole-pairs. These charge carriers need then to be transported to the semiconductor/electrolyte interface. During this charge transport recombination is a huge concern and needs to be prevented. At the interface a charge transfer from the semiconductor to the water molecules needs to take place. During this process it is again crucial to prevent recombination by e.g. surface states.

In an ideal situation the energy which is needed to split water into hydrogen and oxygen is given by the difference of their respective redox potentials of 1.23 eV. Due to overpotentials η the actual driving force which is required is at about 1.8 eV. This energy has to be provided by the semiconductor in form of a photovoltage of this value or larger. The photovoltage on the other hand is in a first assumption given by the splitting of the quasi-Fermi levels $\Delta\mu$, which results from the non-equilibrium situation within the semiconductor due to illumination. It is, therefore, a key requirement for the unassisted light-driven water splitting process that the splitting of the quasi-Fermi levels is larger than the required energy of 1.8 eV.

As a consequence of these considerations the band gap of the semiconductor has to be in the range of 2.4 eV as the band edges are considered to be a natural limit for the position of the quasi-Fermi level. Another limitation can be found in any energy states in the

bulk or at the surface that can prevent the movement of the Fermi level. This mechanism is referred to as Fermi level pinning and it is of major concern for any photoactive device.

In addition to a suitable band gap the positions of the band edges with respect to the redox potentials of the water splitting process have to be suitable as well. It is necessary that -under working conditions- they encompass the redox potentials as it is shown in Figure 1.1. This is crucial as for a successful charge transfer the quasi-Fermi levels have to be below (hole transfer) or above (electron transfer) the respective redox level.

Hematite as active material in a water splitting device - Challenges and Limitations

After the first proof of concept on TiO_2 many other transition metal oxides (TMOs) have been investigated in order to be utilized as the active material in a water splitting device.[5, 12] The choice for this materials class is based on their abundance, cheapness, and stability in the aqueous environment of the water splitting process. One of the most intensively investigated materials is hematite ($\alpha - Fe_2O_3$) which has been selected due to it's almost ideally sized band gap (2.2 eV).[13, 14] From theoretical considerations which are based on the size of the optical band gap a maximal theoretical efficiency of 16.7 % (solar-to-hydrogen) was proposed.

Real devices, however, are nowhere close to this value. Efficiency values of less than 2 % are reported even for the most sophisticated device architectures.[8, 13–19] In addition, the photovoltages reported for hematite are far less than what could be expected for a material with an optical band gap of 2.2 eV.[8, 18, 19] The reasons for the poor efficiencies and low photovoltages are discussed to originate from a) poor charge carrier mobilities due to small polaron hopping as charge transport mechanism, b) associated poor carrier lifetimes due to recombination (often assigned to trapping and recombination due to surface states), and c) the unsuitable position of the band edges where the conduction band edge is reported to be below the hydrogen formation potential.[6, 14, 20–24]

In order to overcome these challenges many efforts are undertaken in state-of-the-art hematite devices. These include doping, nanostructuring, surface and light-harvesting optimization and the addition of co-catalysts.[17, 23, 25–28] Many of these efforts are suggested in order to improve the charge carrier dynamics and a rising number of recent studies on this topic are available.[21, 29–31] No note-worthy advances in efficiency have been made, however. At the same time, the low photovoltages are ignored by most studies and are not further investigated.

All these challenges could suggest that hematite is just not suitable as an active material in a water splitting device and that other TMOs should be investigated. This has now

been done for decades and the advances with other materials are also not much better than for hematite[5, 8] All in all, the slow progress in water splitting devices with different materials indicates that a fundamental limitation for TMOs might exist which has not been identified, yet.

As it can be assumed that such a fundamental limitation exists also in hematite, this material can be used as a model material in order to be investigated. Considering the low photovoltages as a major, unresolved issue for transition metal oxides the reason for their limitation can be assumed to be found in their electronic structure. An experimental study on this topic may therefore be the key to identify a possible mechanism which prohibits highly efficient unassisted light-driven water splitting.

This thesis - Objectives and Structure

This thesis aims to find the assumed fundamental limitation in the use of oxides for water splitting. It uses hematite as a model material and focuses on the electronic structure and the determination of the possibility to shift the Fermi level across the band gap. These two topics are investigated in a surface science approach by means of Photoelectron Spectroscopy (PES) on RF-magnetron sputtered Fe_2O_3 thin films.

The Fermi level position is examined in dependency on deposition conditions such as temperature and oxygen partial pressure, doping with both n- and p-type dopants, and at interfaces to different molecules and solids. As the identification of a fundamental limitation can only be achieved on well defined samples a structural characterization is also essential. This is achieved by the combination of XRD measurements and Raman Spectroscopy. Additional measurements of the electronic properties are performed in order to give a measure on the performance of the thin film.

The thesis is structured as follows. First, suitable parameters for the deposition of well-defined crystalline hematite thin films are determined and discussed. Then, the influence of temperature and crystallinity on the electronic structure of the valence band and the consequences for the PE spectra are examined. In a third chapter the doping of hematite by different dopants and the consequence for the Fermi level position is explored. This chapter is followed by studies on the interface formation behavior of hematite to different molecules and solids. The observations from all these chapters are combined in a final chapter where a model will be proposed that explains many similar observations from different experiments during the thesis.

2 Fundamentals

This chapter gives an introduction to fundamental topics that this work is based upon. It is intended to give a brief overview on hematite, its properties, and the most relevant scientific models,concepts, and methods that are needed to follow the argumentation later. In order to keep the chapter reasonably short each part will discuss only the essential topics. This might require certain basic concepts. Where this applies a list of references is provided.

2.1 Hematite - an overview over basic properties and applications

Hematite ($\alpha-Fe_2O_3$) is the most stable oxide of iron. It crystallizes in the corundum structure ($\alpha-Al_2O_3$) with the space group $R\bar{3}c$. The lattice parameters of the unit cell are $a = 5.04\,\text{Å}$ and $c = 13.75\,\text{Å}$.[32] The structure can be described as a hcp anion stacking with the stacking sequence ABAB[001]. The unit cell is shown in Figure 2.1. In a) the atoms and bonds are shown, whereas in b) the polyhedra are depicted. Each unit cell contains six formular units.

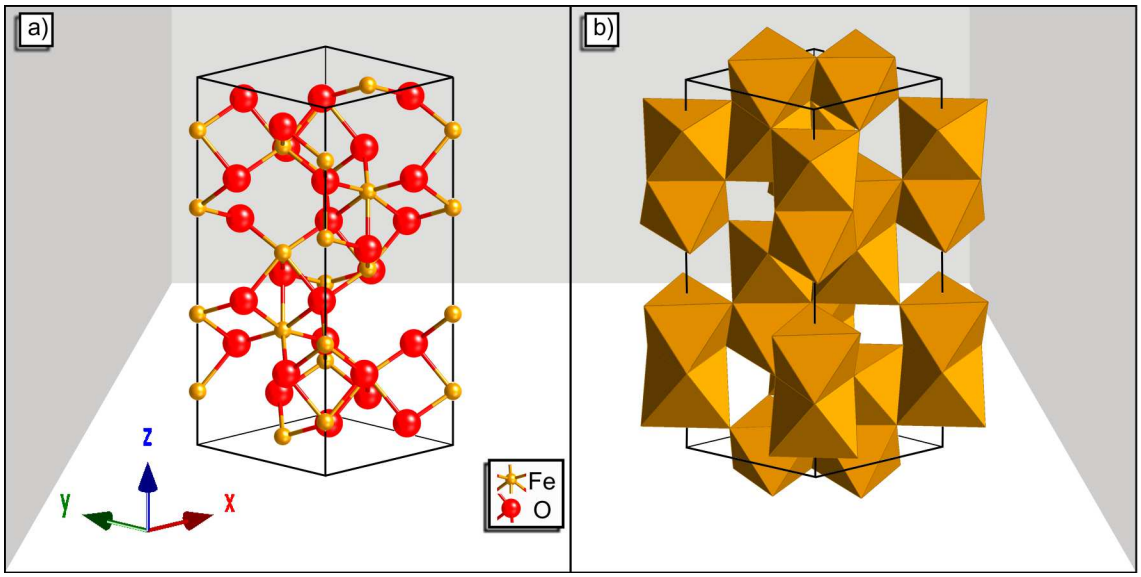

Figure 2.1: Unit cell of $\alpha-Fe_2O_3$ .a) atomic representation and b) oxygen octahedral around iron atoms. View direction is $[66\bar{1}]$ in both cases.

Every trivalent iron cation in a) is bonded to six divalent oxygen anions giving a octahedral environment as shown in b). These octahedra share edges insides the basal ((0001))

plane and faces along the [001] c-axis.[33] Due to a mismatch of ionic radii and octahedral void the octahedra are slightly distorted which lowers their symmetry from O_h to C_{3v}.[32, 34] This is manifested in two different bond lengths from iron to oxygen with Fe—O(1) = 1.945 Å and Fe—O(2) = 2.116 Å. As a consequence, three oxygen bond lengths exist with O(1) − O(1) = 3.035 Å, O(1) − O(2) = 2.669 Å and O(2) − O(2) = 2.839 Å.

Iron in hematite is always in high-spin d^5-configuration. As for all iron oxides and hydroxides the spin from the Fe3d electrons gives rise to different magnetic phases depending on the temperature. Above the Curie-temperature of $T_C = 956\,K$ hematite is paramagnetic. Below this temperature and down to the Morin temperature $T_M = 260\,K$ the material shows weak ferromagnetism[1]. This property results from a slightly non-parallel alignment of electrons spins of antiferromagnetic sublattices in the basal planes which gives rise to a magnetic moment which is slightly off-perpendicular to the c-axis in hematite.[32, 35] Below T_M the material is antiferromagnetic.

The Fe3d electrons and the occupation of the electronic density of states (DOS) are essential for the optical and electrical properties. Due to the crystal-field splitting in the ligand field of the six oxygen ions their degeneracy is lifted[2]. This is shown in Figure 2.2a) schematically.

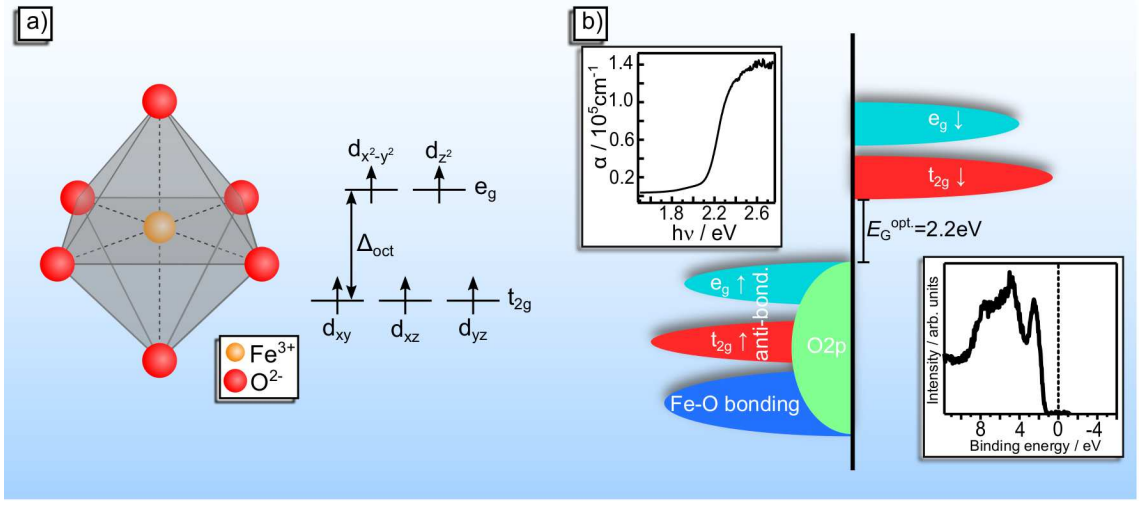

Figure 2.2: Crystal-field splitting and electronic structure of hematite. In a) the iron-oxygen octaeder is being shown which results in the splitting of the Fe3d level as shown next to it. How the Fe3d and O2p-orbitals are found in the electronic structure of hematite is schematically depicted in b) based on Ref. [34]. The insets show actual measurements of the optical absorption coefficient and the valence band region.

The electronic structure of the valence band of hematite as schematically depicted in Figure 2.2b) is derived from both, iron and oxygen states. The ordering of the states was

[1] Also referred to as ferrimagnetism

[2] Crystal-field splitting will be further discussed in part 2.2.3 of this work. The further splitting of the d-orbitals is small and can be neglected within this work.

shown by theoretical calculations using cluster interaction methods by Tossell and later Sherman.[34, 36, 37] As shown in Figure 2.2b) the Fe3de_g states form the valence band maximum. Below, the Fe3dt_{2g} states can be found. Both contain a certain amount of oxygen but show anti-bonding character. The bonding states of iron and oxygen can be found below. Here, Fe3d states as well as Fe4s and Fe4p states form bonds with O2p. In addition, non-bonding oxygen states can be found over the entire valence band.

Even though these results date back more than three decades they are in very good agreement with more recent computational studies. Of these a variety exist.[38–49] A complete discussion is seen to be unnecessary at this stage but the results of these studies will be used in later discussions.

Experimentally, the electronic structure of hematite has been accessed by different methods such as e.g. X-ray Absorption and X-ray Photoelectron Spectroscopy (XAS and XPS).[21, 50–61] A more detailed discussion on XPS measurements in literature on hematite can be found in part 2.3.2. For now, it is sufficient to state that an agreement with the electronic structure from theoretical considerations can be found. There is, however, also a striking difference in the spectra of different studies.[56, 59–61]

From XAS and XPS in combination with IPES (Inverse Photoelectron Spectroscopy) it was derived that hematite is a charge transfer semiconductor i.e. after excitation of an electron from the valence band edge (Fe3de_g) into unoccupied states above the hole does not stay at the iron site but is transferred to the oxygen ligand.[59, 62] The energy required for this excitation, which is the optical band gap, is usually given in a range of 1.9 eV to 2.2 eV.[61, 63–66] This band gap is the reason for the interest in hematite as a material for photo-driven water splitting. Reports of other optical transitions for hematite include ligand field transition, d-d spin-flip transitions, and direct O2p $\rightarrow$ Fe3d transitions.[34, 65]

Some reports also include weak transitions with an energy of about 1.5 eV which is much smaller than the reported band gap.[34, 65] These transitions are not always present and it was suggested that they originate from defect states.[67] The type of defect, however, was not specified.

From calculations of the defect properties of hematite, however, it might be argued that iron interstitials are responsible for these transitions as they should create states within the band gap at suitable energies for this transition.[68] Generally, Fe intersitials as defects have been considered to be prominent in hematite in addition to oxygen vacancies.[35, 68–71]

Besides these ionic defects, hematite, like other transition metal oxides, is known to show an electronic defect. Namely, the small (electron) polaron which is a trapped electron on an iron site. As a consequence of the additional trapped charge a displacement of the oxygen anion occurs.[30, 68]

Small polarons are regarded to be responsible for the poor mobility of electrons in $\alpha - Fe_2O_3$.[21, 30, 72] Recently, it was found that the trapping of an excited free-charge carrier appears within 2 ps.[29, 31] The formation of small polarons was suggested to be the main limitation for bulk transport and to enhance recombination in hematite. Surface states which have been regarded to act as major limitation for hematite devices before were shown to have less impact by these studies.[23, 24, 73–75]

The presence of polarons determines the charge transport properties of hematite. Like many other transition metal oxides the room temperature conductivity is rather low.[76] Usually, values of around $10^{-14}\,S\,cm^{-1}$ to $10^{-8}\,S\,cm^{-1}$ can be found in literature.[63, 77, 78] The rather larger range shows that hematite is very sensitive towards impurities and sample preparation e.g. by adding 1 % of titanium as dopant the room temperature conductivity could be enhanced by seven orders of magnitude.[63]

Temperature dependent conductivity measurements usually agree upon an activation energy of about 1.1 eV.[63, 77, 79] There are, however, also reports of much smaller or slightly larger values. The former are explained by conduction through dopants or other impurities, while the latter are taken as an indication for hopping transport.[63, 79]

Hopping transport via small polarons is by now mostly accepted as major conduction mechanisms. Is does seem, however, that not all results really agree with this. Especially by substitutional doping not only charge carriers are created but also the transport mechanisms might change which results in different mobilities due to the doping.[63, 80] This tremendously complicates the transferability of results from the given studies and might hinder the progress of understanding of the transport properties of hematite.

As an example the oxygen partial pressure sensitivity of hematite can be used. There are results which indicate that the conductivity does not depend on the oxygen partial pressure.[63, 79] On the other hand, hematite has been investigated to be used as thermoelectric oxygen sensor.[81]

This is, however, not the main application that hematite is being investigated for. Due to the optical band gap it has been considered for photoelectrochemical water splitting for decades.[6, 13, 20, 22, 82] While this is, however, only a possible application for the future the main use of hematite today is as a pigment.[32] Further technologies that

hematite has been used or considered to be a promising material for include gas sensors, batteries, and humidity sensors.[32, 61, 83, 84]

2.2 Physics of transition metal oxides - a short introduction

The transition metal oxides offer a variety of interesting properties which have have made them a promising materials class for an assortment of different applications. These range from absorber material in water splitting devices (e.g. Fe_2O_3, TiO_2), over contact materials in solar cells (MoO_3) to catalysts (CeO_3) and pigments (HgO) and beyond.

Many of the diverse properties have their origin in the number and interaction of the d-orbitals introduced from the respective transition metal. For the 3 d-transition metal oxides like hematite the valence band and conduction band states are derived from electronic states involving a high concentration of d-states. Due to their high localization the physics for the electrons are different in these orbitals compared to e.g. s-orbital.

This gives rise to e.g. semiconducting behavior where simple counting of electrons would suggest a metallic state or a break-down of the rigid-band model.
For a better understanding of the special properties of TMOs the special physics which are needed to correctly treat 3 d-electrons will be discussed in this chapter. In the beginning, however, a brief introduction into the physics of conventional semiconductors will be given. This is needed in order to see the differences that are faced once d-electrons are involved.

2.2.1 Conventional semiconductors in a nutshell

The prime examples for a conventional semiconductor are elemental Si or GaAs. These two materials exhibit physical properties that have been understood and described in the first half of the 20^{th} century. This includes the concept of a band structure, the appearance of a band gap, the relevance of doping, and the behavior at interfaces.

Today silicon is probably the most intensively investigated and best understood material at all. Without this understanding many of today's technologies would not be possible. This was achieved by the groundbreaking contributions of scientists like Hall, Thomson, Bloch, Wilson, Schottky, Mott, and many others. Until today, their collective understanding has been summarized and explained by many other different authors. A standard reference is the book by Simon M. Sze, "Physics of Semiconductor Devices".[85] This Chapter of the thesis is intended to give an overview of relevant topics and mostly is based on this book and the references within.

In Figure 2.3 important properties of semiconductors are graphically displayed. The existence of a band gap shown in a) is the fundamental property to distinguish a semiconductor from a metal. The band gap is defined as a range in energy where no electron can exists. It is usually distinguished between direct and indirect band gaps.

In the former the valence band maximum and conduction band minimum are at the same point in $\vec{k}$-space. Hence, no momentum contribution Ω is needed in order to transfer an electron from the valence to the conduction band. Direct semiconductors such as GaAs show a sharp onset of absorption at the energy of the band gap but also rather small charge carrier lifetimes due to fast recombination across the band gap.[85]

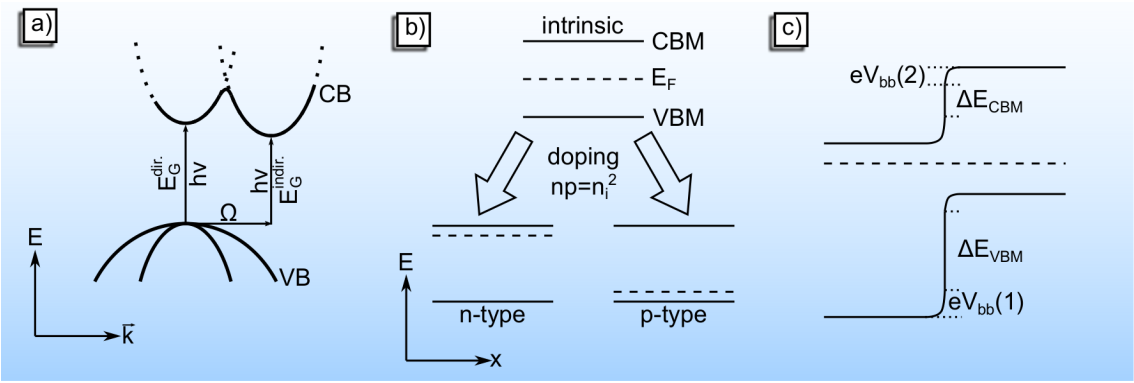

Figure 2.3: Important properties of semiconductors. The existence of a (direct or indirect) band gap (a), the dopability in order to manipulate the charge carrier concentration (b), and the potential generation at interfaces.

To transfer an electron from the valence to the conduction band in a semiconductor with an indirect band gap, on the other hand, requires an additional momentum Ω besides the energy $h\nu$ from a photon. This momentum can usually be provided by a phonon. As two particles are needed in order to fulfill energy and momentum conservation, however, the process is less likely than the transfer in a direct semiconductor. This results in a lower absorption above the indirect band gap energy. On the other hand, the lifetime of the charge carriers is higher as the recombination is suppressed as well. An example for a semiconductor with an indirect band gap is silicon.[85]

The bands in a conventional semiconductor can directly be associated with certain atomic orbitals or their hybrids. Bands can be derived as a linear combination of atomic (or molecular) orbitals. Hence, the discrete states of the atoms form a continuous band. An electron inside this band can be regarded to be delocalized over the whole solid.

The shape of the band in Figure 2.3 follows a parabola shape in a first approximation. The curvature of a band is directly related to the effective mass and thereby mobility of the charge carriers. A large curvature (broad band) gives rise to a small effective mass (high mobility) whereas the opposite is the case for a small curvature (narrow band). The

two overlapping bands at the valence band maximum in a) are referred to as degenerate as they show the same energy (at certain values of $\vec{k}$).

The size of the band gap E_G is often used in order to distinguish between semiconductor and insulator. Usually, it is argued that a semiconductor shows a value between 0.3 eV and 3 eV. This definition, however, is sort of arbitrary.

A better definition of a semiconductor is given from its dopability. That is, the control of the electrical properties by a controlled introduction of charged defects. A semiconductor should react to the presence of a charged defect by a change in the charge carrier concentration i.e. the Fermi level is shifted.

This energy level enters the description of semiconductors through the Fermi-Dirac-equation. It effectively describes whether a state is occupied (below the Fermi level) or unoccupied (above the Fermi level). The controlled manipulation of the Fermi level position in the material gives semiconductors their properties.

For an insulator it can be expected that instead of this electronic compensation the creation of other charged defects prevails. This ionic compensation limits the range in which the Fermi level can be shifted. This can go as far as to a decomposition of the material.[85]

In Figure 2.3b) the dopability is schematically shown. For an intrinsic semiconductor the Fermi level is in the middle of the band gap. This occurs if either the material is free of charged defects or any defect of a certain charge is being compensated by a defect of the opposing charge. In this case the concentrations of electrons n and holes p are the same and can be referred to as the intrinsic charge carrier concentration n_i.[85]

The intrinsic charge carrier concentration is given by

$$n_i = \sqrt{N_C N_V} \exp\left(-\frac{E_g}{2k_B T}\right)$$

The terms N_V, N_V are the effective density of states of the valence/conduction band and E_g is the energy of the band gap. The Fermi level is positioned at about equal distance from the conduction and valence band edges E_C, E_V, respectively.

With the incorporation of charged defects the Fermi level can be shifted in the direction of one of the band edges. When an upwards shift occurs the concentration of electrons is being raised. These are now referred to as majority charge carriers. At the same time the number of holes is decreased. Hence, they are now the minority charge carriers. This type of doping is referred to as n-type doping by donors.

For a p-type doping by acceptors the Fermi level is being shifted into the lower half of the band gap. The charge carrier concentration changes are vice versa to the n-type case. In all three - intrinsic, n-type, and p-type - cases, however, the relation $np = n_i^2$ holds.

The type of defect that can be used depends on the host material. For elemental semiconductors such as Si the substitution by a host atom through a heterovalent atom is being used in most cases. Atoms with higher valency act as donors whereas elements with a lower valency are acceptors. This doping mechanisms can be used in more complex systems as well. Here, however, the creation of lattice defects like oxygen vacancies $V_O^{\bullet\bullet}$ also have to be considered.[86]

The doping effect for the substitutional doping in Si can be understood on the basis of a simple hydrogen model. This will be further explained in the following on the example of a donor dopant. For acceptor doping the same applies but instead of an electron transfer into the conduction band a hole transfer into the valence band occurs.

When silicon is substituted by an element which has one valence electron more this electron is not needed in the bonding to the neighboring Si atoms. This excess electron can be regarded to encircle an atomic core which shows an effective charge of +1 in a Bohr-like atom model. This is a situation which is similar to a hydrogen atom and the binding energy of this excess electron can be calculated using the equation

$$E_B = \frac{m_e}{m_0} \times \frac{13.6\,\text{eV}}{\epsilon^2}$$

where 13.6 eV is the binding energy of the electron in hydrogen, $\frac{m_e}{m_0}$ accounts for the effective mass of the electron in the periodic lattice, and ϵ is the relative permittivity of the host material.

With this approach a binding energy of about 29.8 meV for the excess electron in Si can be derived. This is about the same energy as the thermal energy at room temperature which shows that the electron can easily be removed from the nuclei. At the same time the Bohr-radius can be calculated as well and it is found that it is about 30 Å which is much larger than for the hydrogen atom. The electron is, therefore, regarded to be dislocalized and the donor orbitals can overlap at very low donor concentrations already. Thus, they form an impurity band.

The number of free electrons depends on the temperature. At room temperature it can be assumed that every donor will be ionized and has donated it's excess electron to the lattice. As a consequence the electron charge carrier concentration n equals the number

of donors N_D: $n = N_D$. The Fermi level will be positioned close to the conduction band edge as given by

$$E_C - E_F = k_B T \ln\left(\frac{N_C}{N_D}\right)$$

In Si the usual doping concentrations are in the order of $10^{16}\,\mathrm{cm}^{-3}$ which is order of magnitudes above the intrinsic charge carrier concentration of $10^{10}\,\mathrm{cm}^{-3}$. It will later be seen that the doping concentrations used in this work greatly exceed these numbers and that certain challenges are associated with this.

For more complex systems other doping mechanisms besides the substitutional doping exist as well. Any charged defect influences the charge carrier concentrations. In some cases this might not even be beneficial e.g. if a defect introduces a compensating mechanism for the intended doping. In many oxide materials the doping is achieved by a controlled formation of oxygen vacancies.[87] In some the introduction of "dopants" does not change the charge carrier concentration by the ionization of the dopants but by a change in the chemical environment around the host metal ion due to a stronger (or weaker) bond to the "dopant".[88, 89]

Doping is not the only mechanism to manipulate the Fermi level in a semiconductor. Another possibility which can be referred to are variations of electric potentials at interfaces is depicted in Figure 2.3c). Here, a (hetero-)junction of two semiconductors with different band gaps is shown.

In order to achieve equilibrium the Fermi level throughout the whole junction needs to be a constant on the absolute energy scale. The two semiconductors, however, are n- and p-type. Hence, the Fermi level before the junction was created were at different positions. In order to compensate this difference electrons had to be transferred from the material with the higher Fermi level into the material with the lower Fermi level during the contact formation. These charges are now missing in the region in close vicinity to the interface. This region is referred to as space-charge region as here ionized dopants can be found. On the other side of the interface a space charge region with an opposing charge is being created. The potential V_{bb} from these ionized dopants results in a band bending in the space-charge region. The number of additional charges on both side (electron and holes, respectively) is the same. The width of the space-charge region and the amount of band bending behave anti-proportional to each other and depend e.g. on the doping concentration and dielectric properties of the host material.

In a heterojunction it can be expected that the bands of the two semiconductors show discontinuities. Depending whether these occur in the valence or conduction band these are labeled as $\Delta E_{VBM/CBM}$ in Figure 2.3c). These discontinuities are important parameters

for achieving good contact properties for a specific semiconductor as they can efficiently block electrons or holes.[85]

Besides the shown case of a semiconductor heterojunction also a semiconductor homojunction (same material but differently doped) or a metal semiconductor contact need to be considered. The latter is being described in a first assumption by the Schottky model, whereas the description of the semiconductor semiconductor junction are based on the Anderson model.[90, 91] Both models have in common that the charge flow from the material with the lower work function into the material with the higher work function in order to compensate for the difference in Fermi level position is related to the vacuum level as reference level.

The explanation on semiconductor junctions above assumes a very idealized situation. In reality surfaces are a very complex topic on their own and many mechanisms may occur that prevent the formation of a built-in potential as given by the idealized Schottky or Anderson model. In these situation the Fermi level cannot move as freely throughout the band gap as needed in order to compensate the given difference in the surface potentials of the two materials. This is referred to as Fermi level pinning and is a major challenge for semiconductor devices.

While also being present in the bulk due to defect formation Fermi level pinning is tremendously important at surfaces and interfaces as here many defects are created just because of the existence of the surface or interface. These defects include dangling bonds due to the missing bonding partner and less coordinated species that show different states, and metal induced gap states introduced from a metal on top of a semiconductor. As a consequence surface states exist. These might be positioned within the band gap and react to the position of the Fermi level as any other state as well. They are unoccupied when being above the Fermi level and occupied when being below.

In order to move the Fermi level freely throughout the band gap Fermi level pinning by any mechanism has to be prevented. As a consequence, for a semiconductor to be fully functional it is required that the defect concentrations are as low as possible. The vast success of Si as a semiconductor in the second half of the 20^{th} is partially due to the possibility to produce the material with very low defect concentrations.

2.2.2 Semiconducting properties in transition metal oxides

The occupation of states in a solid can be found by simply counting the electrons and band states (derived from atomic orbitals). Semiconducting (or insulating) properties can be expected if the highest occupied state is separated from the lowest unoccupied state by an energy gap. This strategy works very well for conventional semiconductors. For these

materials the one-electron approximation applies, in which the addition or removal of a single electron does not have an influence on the electronic structure of the other electrons. In other words, the electrons do not "see" each other. The bands are referred to as "rigid bands" which means that they keep their position upon addition or removal of an electron.

This is different for electrons in localized states such as e.g. 3d-states. Here, a correlation energy due to Coulombic repulsion has to be considered. This is due to the small overlap of the d-orbitals which results in very narrow bands and a strong localization of the electrons. Instead of being delocalized inside the complete solid the electrons are effectively still found at "their" atom and it matters how many electrons are to be found there. The addition and removal of an electron results in the rearrangement of the other electrons AND the electronic states. This is referred to as "non-rigid band" behavior and can be observed in many transition metal oxides.

In the understanding of the physics of semiconducting oxides many different scientists participated:

- J. Hubbard described the correlation of electrons in narrow d- (or f-) bands by a second quantization.[92–95] He introduced the Hubbard-U as a measurement of the dd Coulomb and exchange interactions. The band gap of a Mott-Hubbard-insulator is of d-d-type and includes a $d_i^n d_j^n \rightarrow d_i^{n-1} d_j^{n+1}$ transition.

- S. Hüfner (besides others and co-authors) worked on the understanding of the band gap in NiO which cannot be described by means of conventional semiconductor physics but where it was also shown that the Mott-Hubbard definition does not apply as well.[96–99] Instead the band gap is of charge-transfer type which includes the electron transfer from the oxygen ligand to the Ni3d state: $O2p^6\,Ni3d^8 \rightarrow O2p^5\,Ni3d^9$

- J. Zaanen, G.A. Sawatzky, and J.W. Allen published a number of articles in which they proposed a classification of the band gap type in transition metal oxides based on properties of the bands. This "ZSA-classification" is in use until today.[100, 101]

In the following phenomena that specifically apply to the d-orbitals in oxides will be discussed. This includes crystal-field and exchange splitting. Then, the "ZSA-classification" will be introduced which requires a short introduction into the Hubbard-model.

In crystalline transition metal oxides the metal ions are surrounded by oxygen ligands in their coordinative environments. Two of the most common ones are the four-fold tetrahedral and six-fold octahedral coordination. These are shown in Figure 2.4.

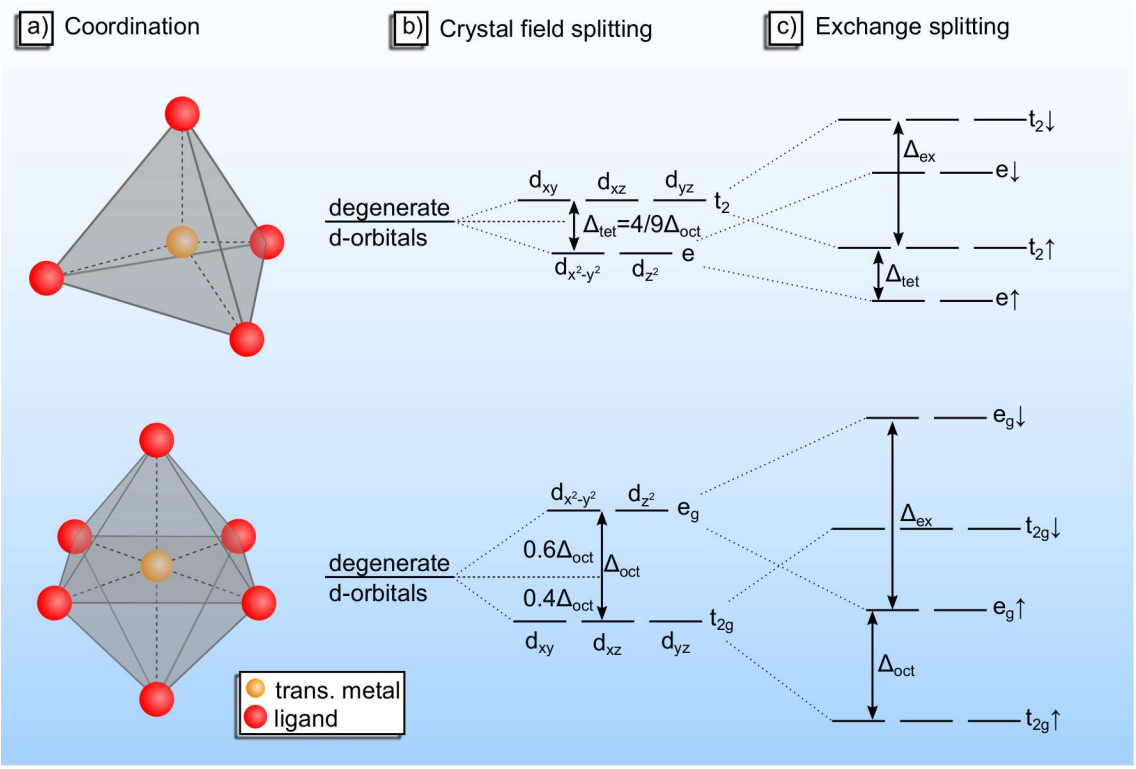

Figure 2.4: Crystal-field and exchange splitting in tetrahedral (top) and octahedral coordination (bottom).

For an electron in an orbital the negatively charged anion ligand coordination changes the electrical field. Assuming a spherical distribution of negative charge around the metal ion will result in a raise in energy compared to the free ion. In the tetra- or octahedral environment, however, the negative charge is not evenly distributed but is positioned at certain angles and distances.

Due to the highly oriented character of the d-orbital some of them are pointing towards the oxygen anions. In the octahedral environment these are the $d_{x^2-y^2}$ and d_{z^2} orbitals. Their energy is even further increased compared to the spherical field which is given as "degenerate d-orbitals" in Figure 2.4b). The orbitals d_{xy}, d_{xz}, and d_{yz} point away from the negative charges. The energy of their electrons is, therefore, lowered.[34, 36, 37, 102–104] In tetrahedral coordination the situation is vice versa. The crystal-field splitting parameter Δ_{tet} in the tetrahedral field is slightly less than half of the crystal-field splitting in an octahedral field Δ_{oct}.[102] Typical energies for the crystal-field splitting parameter are 1 eV to 3 eV.[61, 102]

Besides crystal-field splitting also the exchange splitting Δ_{ex} has to be considered in many TMOs. The splitting into spin-up (↑) and spin-down (↓) states further lifts the degeneracy as depicted in Figure 2.4c). The exchange splitting is usually larger than the crystal-field splitting with values between 2 eV to 8 eV.[102, 105] The magnitude of Δ_{ex} depends on several factors including the oxidation state of the metal, the type of ligand, and the degree of hybridization. Generally a high-spin configuration can be expected for small crystal-field splitting energies. This is usually the case for oxygen as ligand.[102]

Hubbard U versus charge transfer Δ - The ZSA-classification

The electrical properties of transition metal oxides range from metallic conductors to insulators. For some is seems to be enough to consider crystal-field and exchange splitting and fill the resulting states with electrons in order to predict the type of conductivity. The behavior of others, however, cannot be explained by this simple procedure. For some metallic behavior would be expected where semiconducting properties are measured and vice versa.

In order to solve this disagreement J. Hubbard introduced the Hubbard-U parameter that effectively represents the dd-Coulomb and exchange interactions.[92–95] The derivation of this parameter is quite complex and includes seconds quantization methods with annihilation and creation operators effectively calculating the difference in energy whether an electron is removed/added from/to a d-orbital of a certain occupancy.

To repeat the complete derivation is beyond the scope of this work and will not add for further understanding. It should be, however, noted that there are certain ways to express U.

In a first approximation U can be considered to be proportional to the Coulomb repulsion of two electrons within d-orbitals.[102] Then, equation 2.1 holds. Here, r is the distance of the electrons within the d-shell.

$$U \approx \frac{1}{4\pi\epsilon}\frac{q_1 q_2}{r^2} \tag{2.1}$$

The second expression of U is closer to the derivation from Hubbard.[92–95, 100, 101, 106] It considers the energetic difference between the excited system $d_i^{n-1}d_j^{n+1}$ to the ground state $d_i^n d_j^n$:

$$U = E(d^{n+1}) + E(d^{n-1}) - E(2d^n) \tag{2.2}$$

Equation 2.2 describes the transfer from an initially d^n-state to another d^n-state which leads to a final $d^{n-1}d^{n+1}$-state. This is graphically depicted in Figure 2.5a) as the electron transfer process on the left-hand side. The energetic situation is given in b) on the left-

hand side as well. The width of the final state is given by twice the width of the d-band states w.

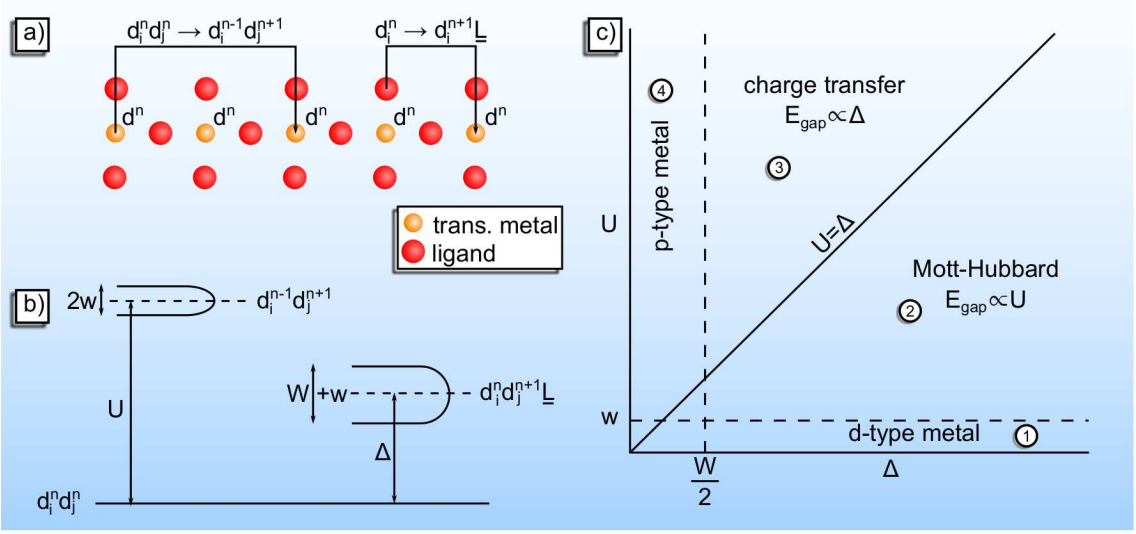

Figure 2.5: The Zaanen-Sawatzky-Allen-classification for transition metal oxides. In a) the Hubbard and charge transfer mechanisms for the transfer of an electron are schematically shown. An energetic representations of the two mechanisms is found in b). Figure c) shows the types of insulating and metallic states in transition metal oxides after the ZSA-classifications. Adapted from [106].

The second process that has to be considered is the electron transfer from the ligand into a d^n-state. Here, a d^{n+1}-state and a hole in the ligand $\underline{L}$ are created. This process is shown on the right-hand side of Figure 2.5a) with the energetics below. The width of the final state is given by the sum of the widths of the d-band state w and the ligand-band state W. The charge transfer energy Δ can be described as shown in equation 2.3:

$$\Delta = E(d^{n+1}\underline{L}) - E(d^n) \tag{2.3}$$

In the classification by Zaanen, Sawatzky, and Allen (ZSA) the four parameters U,Δ,w, and W are being used in order to describe the electrical properties of the system.[100, 101, 106] The different properties of TMOs according to their classification can be found in Figure 2.5. The four material classes ① - ④ can be described as:

① $U << \Delta$, w large
This gives an overlap of initial and final state and the system will behave like a metal with conduction in the d-states.

② $U < \Delta$, w & W small
The material shows semiconducting properties with a band gap that is proportional to U. It is referred to as Mott-Hubbard insulator.

③ $U > \Delta$, w & W small
The transfer from ligand to d-state is energetically favored. The material shows semiconducting behavior with a band gap that is proportional to Δ and is referred to as charge-transfer insulator.

④ $U >> \Delta$, W large
The material shows metallic behavior with the conduction taking place in the ligand states.

The experimental distinction between metal and semiconductor is straight forward. To determine, whether a material is Mott-Hubbard or charge transfer semiconductor, however, is more complex. Theoretical and experimental methods have to be used. Especially, a combination of resonant PES with inverse PES with the help of cluster interaction calculation of possible ground and final states can be helpful. A prime example for scientific discussion on the type of semiconductor[3] is NiO. For this material the methods stated above had to be used in order to assign it to belong to the class of charge-transfer semiconductor.[96–99] Hematite belongs to the same class which was determined by the same techniques.[56, 59, 60]

2.2.3 Fermi level pinning and charge transition points

When the doping level in a semiconductor is increased the Fermi level will follow the amount of doping at first. At a certain doping level, however, the Fermi level position stays constant and does not shift anymore despite the increasing dopant concentrations. This phenomena is referred to as "bulk" Fermi level pinning and the energy position where it occurs is regarded as pinning level. The phenomena of Fermi level pinning is both scientifically and industrially of great importance as it fundamentally determines the performance of a specific semiconducting material.

To explain its origin a perfect semiconductor without any intrinsic defects is being examined now. Two dopants are being introduced into the semiconductor of which one is a donor and the other an acceptor. In Figure 2.6a) the energy position of the dopants in the band gap are being shown. Both dopants shall be regarded to be substitutional dopants.

In the following the concept of Fermi level pinning and charge transition points shall be explained on the example of the donor. For the acceptor the same mechanisms applies. Instead of donating an electron, though, it takes one from the lattice.

In order to be an effective dopant the donor has to give one (or more, but let's keep it simple) electron to the semiconductor host material. In other words, it has to be unoccupied. This is only the case if the Fermi level is below the dopant level (at $T = 0\,\mathrm{K}$). Then,

[3] A very detailed description of the discussion and investigations that led to the classification of NiO as charge transfer semiconductor can be found in Ref. [107]

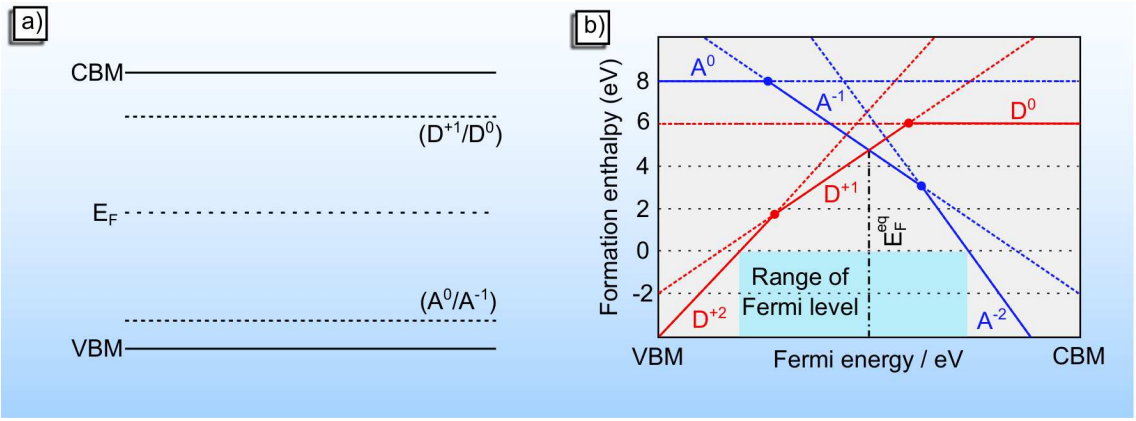

Figure 2.6: Charge transition points (CTP) in semiconductors. a) Dopant levels for a donor (D^{+1}/D^{0}) and an acceptor (A^{0}/A^{-1}) in the band gap. b) Fermi level dependency of the formation enthalpy from which the charge transition point results.

the net charge for the specific dopant site is +1 as there is one additional positive charge than compared to the occupation of the same site by a host atom.

If now the Fermi level is being raised and reaches the dopant level the donor level will be occupied. It will now have the same number of positive charges as a host atom and will, therefore, carry no net charge anymore. Due to the change in net charge the level can be regarded to be a charge transition point.

In this example the dopant level and the charge transition point are the same. This, however, is not necessarily the case. If a defect can adopt different oxidation states it can have different net charges. In comparison to a host atom at the same site this would be

- The same number of electrons: A^{0}/D^{0}
- One electron more or less: A^{-1}/D^{+1}
- Two electrons more or less: A^{-2}/D^{+2}
- And so on...

The dependency of the formation enthalpy ΔH_x of a charged defect is given by equation 2.4.[108] It results from the decrease in total energy of the crystal by exchange of the charge q with the defect. ΔH is the formation enthalpy of the uncharged defect and E_x the energy of the charge on the defect (defect level).

$$\Delta H_x = \Delta H + q(E_x - E_F) \tag{2.4}$$

It is evident from equation 2.4 that the Fermi level dependency of a defect with a higher net charge has to have a larger slope. In Figure 2.6b) the formation enthalpy of a donor and an acceptor with different charges are being plotted over the Fermi energy. Each

charge state is represented as a dotted line. Where ever two lines of one defect cross a charge transition point exists (shown as dots). The defect will always have the charge state with the lowest formation enthalpy. This is indicated by solid lines. Here, it needs to be emphasized that the defect level and the charge transition points are not the same! Once the defect exists it adopts a charge state depending on the Fermi level position.

The range of Fermi level in this material is given by the points at which the defect formation enthalpy becomes zero. If the Fermi level would go beyond this point the result would be spontaneous defect formation and an instability of the material. Outside this range a decomposition reaction occurs until the excess charges have been used up.

Also given in Figure 2.6b) is the Fermi level position in thermal equilibrium E_F^{eq}. This Fermi level position can be found, if no other mechanisms than the defect formation exist. This almost always excludes the existence of surfaces and interfaces. It can be found by considering charge neutrality from the intersection of the acceptor and donor defect of the same net charge[4]. It is valid for certain conditions e.g. oxygen partial pressures. For other conditions the defect formation enthalpy might be different and hence, E_F^{eq}.

Charge transition points of defects are important in order to gain knowledge on the electronic properties of a material at certain conditions. E.g. the Fermi level position is determined by their position. This, in the following, results in properties like the electrical conductivity that is given by defects and their net charge.

Chemists refer to charge transition points as redox-potentials. For most elements redox-potentials at which a certain reaction (e.g. $Mg^{2+} + 2e^- \rightleftharpoons Mg^0$) occurs are available as standard reduction/oxidation potentials for ions/metals in solution.[109] The redox-potentials are not entirely the same as charge transition points in solids as the environment around the ion is different. The concept, however, is similar.

2.3 Methods

2.3.1 Thin film deposition by magnetron sputtering

Sputtering is a physical thin film deposition method. In the process an atomic or ionic species is accelerated towards a target from the material that is supposed to be sputtered. By transferring it's kinetic energy and momentum the accelerated particle removes species from the target. These sputtered species are then in the gas phase and can condensate on a substrate. Often, a plasma is being used to generate positively charged ionic species and allow for the acceleration of these species by an electric field. Besides the acceleration of

[4] This is not always the case. If no such point exists E_F^{eq} can still be found. The different number of differently charged defects has to be considered, then.

the ionic species the electric field is also used to generate the plasma in first place. For this purpose, however, also dedicated plasma generators such as microwave generators can be used as well. Many gases can be used to be ionized in the plasma. Often argon is used as it is an inert gas if not ionized and has a suitable mass in order to sputter many different elements. A typical setup for plasma generation and sputter deposition is schematically shown in Figure 2.7a).

The electric field is applied between the inner ("cathode") and the outer part ("anode") of the setup. It is an requirement for a successful deposition of a thin film that the anode has a much larger area than the cathode. Due to this the latter is usually conductively connected to the chamber in order to use the entity of the chamber as an electrode.

For the electric field several possible techniques exist. These include AC, DC, or pulsed DC signals. Only the former two have been used within this work. Hence, they shall be briefly introduced in the following.

By applying a constant voltage between anode and cathode a DC-field is being generated. A simple DC-generator is necessary and this technique shows the highest rate of the different possibilities. On the other hand only good conductors can be used as target material. Otherwise, if the electrical resistance is too high, the permanent bombardment of the target by positively charged ions cannot be compensated by electrons. As a consequence the nominally negative potential at the target's surface will be diminished and the sputter process will be stopped eventually.

In order to sputter less conductive materials an AC signal can be used. The frequency is chosen at a magnitude where the impedance of the targets becomes zero. This is usually the case in the radio frequency regime and a frequency of 13.56 MHz has been established as standard. Due to the frequency regime the technique is called "radio frequency (RF) sputtering". It offers slightly lower rates than a DC signal of equal amplitude ($\approx 0.8\times$) but provides less defects and a better adhesion of the thin film.

A little attention should be paid to the details of the sputtering process with this technique. Initially, the AC signal is symmetric around zero when generated. The target acts alternating as cathode or anode. As a consequence both electrons and ions are being accelerated towards the target. The latter, however, are too heavy to follow the field. Hence, an electron excess at the target surface is created. These electrons effectively lower the potential of the target and allow for a steady acceleration of the positive ions. This mechanism is called "self-biasing".

In Figure 2.7a) a circular magnet array is positioned above the target. As is being indicated the magnetic field line form a sort of trap in which the electron density is being

raised. As a result the ionization rate in this area is drastically increased as well. As a consequence a much higher sputter rate is reached at this position which manifests itself in the formation of a characteristic "race track". Here, the target is being consumed at a much higher rate.

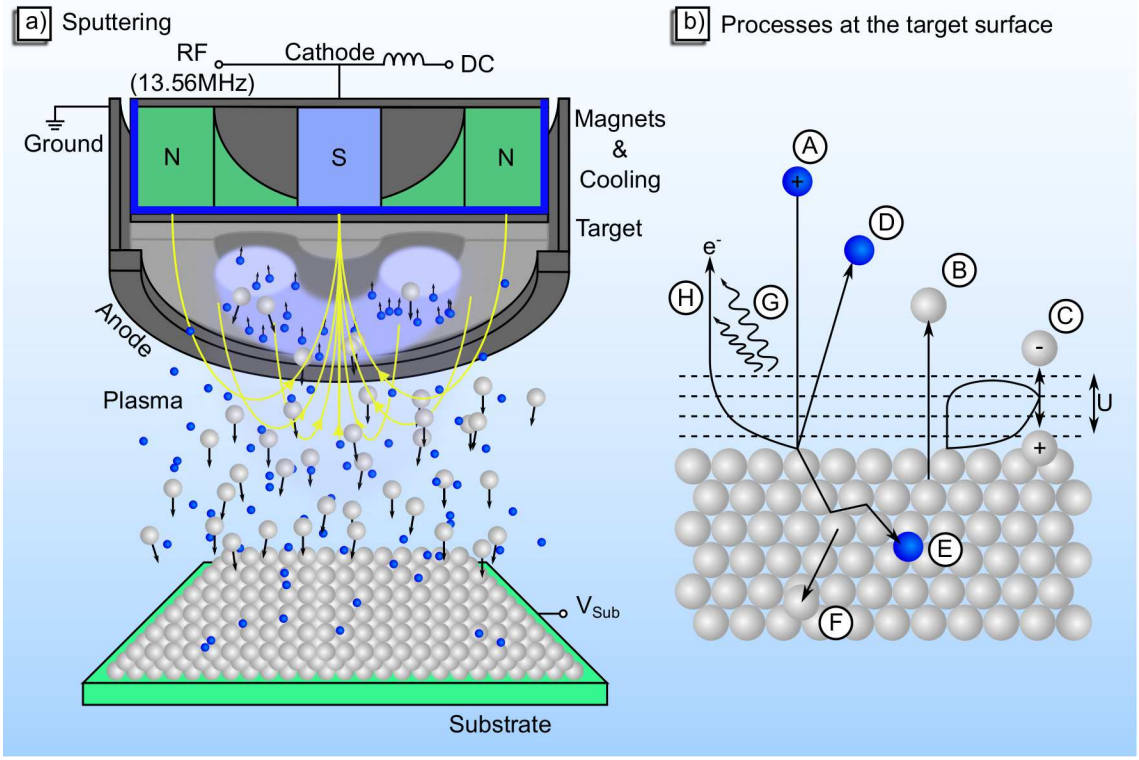

Figure 2.7: The magnetron sputtering process. a) Schematic representation of the sputter setup. b) Possible processes at the target surface. The individual processes are further described in the text.

Processes at the target surface

More or less independent of the sputter technique similar processes at the target surface (might) occur. These are shown in Figure 2.7b). The plasma species (e.g. argon) are shown in blue, whereas the target atoms or ions are being represented in light gray. The different processes are labeled from (A) - (H).

The initial state (A) is an accelerated ion in the gas phase. If it penetrates the target surface a collision cascade can occur which results in the removal of a (or several) target atom(s) from the target (B). For this to occur, the surface binding potential U of the atom has to be exceeded.

It is also possible that the target atom is being ionized (C). In this process both, negative or positive ionization might occur. The latter will be accelerated towards the target while

the former will be accelerated away from the target (acting as cathode). As it will be discussed later these ions can be detrimental for the properties of the growing film as their high kinetic energy can initiate defect formation or even lead to a sputter effect at the film.

It is not necessary always the case that the initial ion penetrates the target. Especially if the target atoms are much heavier than the gas ion the later might be reflected (D). In this process the attraction of an electron is very likely. After the reflection event the former ion would, therefore, be a neutral atom.

Besides these surface reactions after the collision cascade it is also possible that the target material is being changed in its bulk properties. Following the collision cascade it is possible for the sputter ion to be incorporated into the target (E). In this case it can either occupy an empty lattice or interstitial site as an ion or atom. In this process (and in the whole collision cascade) it is very possible that a target atom is being replaced and occupies a former unoccupied site (F). This might be a former unoccupied lattice position but can also result in the formation of interstitial atoms. The initial site of this target atom can either be reoccupied by the sputter ion or another target atom or stay unoccupied. Generally speaking, defect formation is very likely to occur in a sputter process. In addition to these atomic reactions on the collision cascade it is also possible that either secondary electrons and/or photons are being emitted.

For the schematic representation in Figure 2.7 only one target atom species was chosen. In reality many targets are either composite materials constituted by two or more elements. In these cases the defect formation can occur on any site and with any element. Due to the difference in the weight of the elements, however, it is most likely that a preferential displacement of the lighter elements occurs. This is also already the case for the sputter event and is referred to as "preferential sputtering". Even though an equilibrium situation will appear after a while of sputtering the film composition does not necessarily need be the same as the initial target composition.

For the case of oxide materials which are sputtered from an oxide target it is therefore often necessary to add some oxygen into the argon sputter gas to compensate for the slow deprivation of the target of oxygen. This would be referred to as "semi-reactive" sputtering as the additional oxygen is only added to the oxygen from the target itself. A reactive sputtering process is present if the reactant (oxygen, sulfur, nitrogen...) is being added from the gas phase only.

It should be noted that the addition of reactive gases in most cases decreases the deposition rate as scattering events with the reactive gas species deflect target atoms or the target surface can react with the gases as well. The deposition rate can be very sensitive towards the amount of reactive gas in the atmosphere of the sputter system and it might

be the case that a change of the composition by just one percent drastically changes the sputter rate. In order to at least partially evade this challenge it is possible to separate the gas inlets of sputter and reactive species. In this chamber setup the sputter gas inlet would be positioned close to the target and the reactive gas inlet close to the substrate. By carefully optimizing the sputter power (i.e. rate) and the respective gas flows it can be possible to optimize the deposition rate.

Thin film growth

The growth of thin films is a complex topic on which entire books have been written and which cannot be discussed in it entity here. Some important details with regard to sputter depositions should be discussed, however, at this point. An arbitrary beginning of such a discussion would be the classification of thin film materials into stable and meta-stable phases.

Their difference lies in the possibility to deposit these materials. For a stable phase an equilibrium deposition method is most suitable. By choosing the right deposition parameter the system will eventually seek the configuration with the lowest possible total energy. These phases are often deposited with low deposition rates ($\approx 1\,\text{Å}\,\text{min}^{-1}$) at high substrate temperatures (e.g. 1000 °C) as this will allow for good atomic diffusion. As a consequence the atoms are given the time needed to "find" the right position for the stable phase to form. Examples for such methods at high enough substrate temperatuers are e.g. electron beam evaporation or atomic layer deposition (ALD).

Meta-stable materials on the other hand can be expected to be deposited with a high probability if the substrate temperature is rather low (400 °C can be counted as low in this regard for some materials) and the deposition rate is high. Following the argumentation above these parameters will not allow for a lot of atomic movement and the atoms cannot arrange themselves as to be expected in thermodynamic equilibrium. Especially for the deposition of compound materials this might be necessary.[110]

Sputtering as it is performed in the DAISY-MAT lab at TU Darmstadt does rather belong to the non-equilibrium deposition methods. Substrate temperatures are in a range of room temperature to 600 °C and the deposition rates are about $0.5\,\text{nm}\,\text{min}^{-1}$ to $10\,\text{nm}\,\text{min}^{-1}$. It does, however, depend on the materials that are supposed to be sputtered whether an equilibrium or non-equilibrium situation appears. Bismuth-compounds for example could only be sputtered in a single phase at room temperature as phase segregation appeared at elevated temperatures.[110] Oxides in the perovskite structure on the other hand were sputtered at the highest temperatures possible with very low deposition rates.[111]

Besides a dependency of the composition and phase on the sputter parameters also the crystallographic properties are known to rely on deposition conditions such as temperature and pressure. The well established Thornton model distinguishes between different zones in which the grain structure of the sputtered thin film shows a different appearance.[112] A schematic representation of the Thornton model, adapted from Ref. [112] is shown in Figure 2.8. The temperature at which certain grain structures form is expected to depend on the melting point T_M of the sputtered compound. The higher the melting point the higher the substrate temperature T_S has to be in order to achieve a similar grain structure.

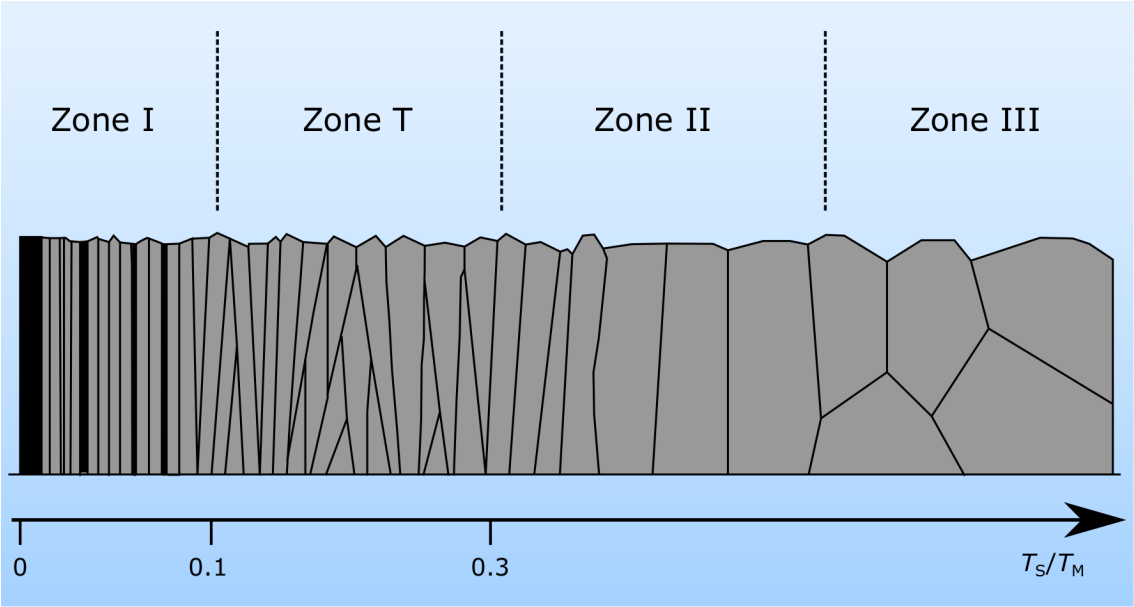

Figure 2.8: A schematic represenation of the grain structure of sputtered thin films according to the Thornton model.[112]

At the usual sputter pressure around 0.5 Pa and at low temperatures a grain structure of tapered crystallites can be expected. These are usually separated by voids. Due to these voids charge transfer from grain to grain might be diminished. From a functional point of view this grain structure is, therefore, most likely to be unfavorable.

Increasing the deposition temperature will lead to a columnar grain structure with the grains growing perpendicular to the substrate surface. Increasing the temperature should result in a flattened surface of the thin film and grains with a larger diameter. These grains, however, can be expected to show sizes of about 50 nm in a sputter process.[61, 76, 88] The length of the grains can be as large as the film thickness for quite high temperatures. For intermediate temperatures such as 400 °C it can be expected, however, that the thin film growth starts with very small grains on which then the columnar grain growth sets in.

At very high temperatures the grain size increases and the grains are not strictly oriented anymore. In order to reach this growth mode the substrate temperature has to come quite close to the melting point. Such deposition conditions are often hard to reach for oxide materials where melting points often exceed 1500 °C.[109]

On the atomic level the sputter process can give rise to some interesting mechanisms. Similar to the effects that take place at the target a bombardment of high-energy particles (atoms, ions, clusters, radicals) can occur at the growing of the film as well. Especially at high oxygen partial pressures possible sputter effects by oxygen have to be taken into account.

The effects on the thin film include (preferential) sputtering, incorporation of the sputter species, and defect formation. Especially defect formation has to be considered in the sputtering of functional thin films. The formation of charged defects such as vacancies or interstitials can have a heavy influence on the charge carriers and determine the properties of the material or device.[113, 114]

High deposition temperature or post-deposition annealing are sometimes necessary to allow for a "healing" of these lattice defects. Such treatments, on the other hand, are not always applicable when meta-stable materials are being sputtered as heating might result in phase separation.

An interesting effect on the properties of the thin film can be expected to originate from the substrate. Sputtering is capable to give epitaxial thin films if the crystallographic properties of the thin film and the substrate show a good match.[115] Here, also the deposition conditions have to be optimized in order to achieve an as ideal growth as possible.

As an example the sputter deposition of platinum thin films can be used. By depositing Pt at 0.5 Pa in pure argon and at 650 °C on quartz a non-epitaxial poly-crystalline thin film is formed. The same deposition conditions on Al_2O_3(0001) or MgO(110) will result in Pt(111) or Pt(110) oriented films, respectively. Pt(100) can be deposited on MgO(100) but only if the pressure is increased to 4 Pa and some oxygen is added. This shows how important the careful selection of the deposition parameters including the substrate can be for the properties of the thin film.

An interesting aspect of epitaxial growth is the possibility to stabilize different phases by selection of the proper substrate. A meta-stable phase can be stabilized if the deposition conditions and substrate are right. This might allow for the possibility to deposit phases which are not achievable with methods which are closer to the thermodynamic equilibrium than sputtering.

2.3.2 Photoelectron Spectroscopy on transition metal oxides

Transition metal oxides (TMOs) are a challenging materials class for investigation by Photoelectron Spectroscopy (PES). Due to their complex electronic structure resulting from the (partially filled) metal d-orbitals hybridized with oxygen states the interpretation of the measured spectra is more delicate than for other materials. In addition, in most cases the transition metals can exhibit different oxidation states which are not necessarily very well separated in the XP spectrum. This only adds to the complexity of analysis.

On the other hand, the TMOs offer with their spectra an unique insight into their electronic structure. Due to final state effects from the interaction of the valence band DOS with the photohole in the core-level there is a variety of information that can be gathered from the measurement.
This part is intended to discuss the basics of PES measurement and spectra interpretation for TMOs. Only a very brief introduction into the fundamentals of PES will be given as it is the authors opinion that this topic has been covered in literature extensively. A very comprehensive book on this topic is "*Photoelectron Spectroscopy: Principles and Applications*" by S. Hüfner.[107] Shorter reviews are given e.g. in Ref. [116] and Ref. [117] and the references within.

Photoelectron spectroscopy is based on the photoelectric effect. By using photons of a sufficient energy $h\nu$ (photo-)electrons are being extracted from the sample and their number ("Intensity") and kinetic energy E_{kin} is being measured. From the kinetic energy of the electron it is possible to determine the binding energy E_{B} which is a property of the electron within the sample as given by equation 2.5.

$$E_{\mathrm{B}} = h\nu - E_{\mathrm{kin}} - \phi_{\mathrm{A}} \tag{2.5}$$

Here, ϕ_{A} is the work function of the analyzer. This reference level can be determined by a sample with a known binding energy of a certain state. A possible calibration material is, for example, silver. For this material the $Ag3d_{5/2}$ core-level is expected to be found at a binding energy of 368.26 eV. In addition, the Fermi edge of silver can easily be interpreted. By definition the Fermi energy in any PE spectrum which does not show charging effects is at a binding energy of 0 eV.

Electrons in solids have a mean free path λ that depends on their kinetic energy and ranges from about 5 Å to about 50 Å for electron energies that are available in the lab. The information depth in PES is usually considered to be about 3λ. It is, hence, limited from only a few atomic layers to about 10 nm.

In equation 2.5 it appears as if the binding energy would depend on the photon energy. This is not the case. In reality it is the kinetic energy which increases with the photon energy for a given binding energy.

First, after a minimum at a kinetic energy at 50 eV the mean free path of electrons increases. Hence, the photon energy of excitation has an influence on the information depth.

In addition, the information that can be collected changes. For low photon energies of ≤ 100 eV only the electrons from valence band states and shallow core-levels can be excited. Using higher photon energies of about 1000 eV it is possible to measure also the signal from deeper core-levels.

These two dependencies are the reason for the distinction into X-Ray Photoelectron Spectroscopy (XPS) and Ultraviolet Photoelectron Spectroscopy (UPS) as laboratory based techniques:

In the former case X-rays (e.g. AlK_α, $h\nu = 1486.6$ eV) are being used to extract electrons. Core-levels and valence band states can be measured and the information depth can be considered to be up to 10 nm.

In UPS ultraviolet radiation is used (e.g. He I, $h\nu = 21.22$ eV). Due to the lower photon energy the measurement is restricted to the valence band states a much higher surface sensitivity results with an information depth of only a few atomic layers.
Equation 2.5 is only valid for primary electrons i.e. electrons that have been excited from their orbital but did not interact inelastically on their way into the detector. This, however, is not the case for all electrons.

Inelastically scattered electrons, the so called secondary electrons form the background in any PE spectrum. This background can be subtracted by using suitable methods. Usually a background subtraction based on the work of Shirley or Tougaard is being employed.[118, 119]

There is, however, also information that can be found in the signal of the secondary electrons. Some of these have a kinetic energy of 0 eV when they leave the sample. These electrons are found at the binding energy of the secondary electron cut-off E_{SEC}.

Accelerating these electrons by applying a bias ϕ_{bias} to the sample it is possible to detect these electrons. As their kinetic energy is known to be equivalent to the bias the work function of the sample can be determined. This is usually performed in UPS measurements.

As a consequence, equation 2.6 gives the work function ϕ_S of a sample measured with He I radiation at a photon energy of $h\nu = 21.22\,\text{eV}$ under an applied negative bias of ϕ_{bias}.

$$\phi_S = 21.22 - E_{\text{SEC}} - \phi_{\text{bias}} \tag{2.6}$$

Changes in the spectrum - initial and final state effects

Until now the binding energy was treated to be a real property of the electron in the solid. This, however, is strictly not the case. In order to understand the real meaning of the binding energy that is measured the photoexcitation process has to be discussed in more detail.

Before the excitation the N-electron system is in its initial or ground state. Due to the excitation a photohole is created and the system is now in an (N-1) final state. By using the Hartree-Fock approximation the energies of initial and final state $E_{\text{i}}(N)$ and $E_{\text{f}}(N-1)$ can be calculated. Please note that this approximation does not reflect real physical meaning. It assumes a static background of all other electrons to calculate the energy of a single electron by adding kinetic energy to the Coulomb and exchange interaction. This is then performed for all electrons of the system to achieve the energies given above.

In a next step it is assumed that the electrons that are not removed during the photoexcitation do not change their wave function. Then, the difference of the initial and final state energies equals the energy eigenvalue ϵ_{i} of the initial state. This assumption is known as the Koopmans theorem and is a fundamental explanation for the meaning of the binding energy measured with PES.[120]

Including correction terms for the correlation interaction ΔE_{c} and electron relaxation E_{R} which must be considered for a complete consideration of the electron excitation the measured binding energy is given by equation 2.7. As the two corrections show most often the same magnitude they can be canceled out.

$$\begin{aligned} E_{\text{B}} &= E_{\text{f}}(N-1) - E_{\text{i}}(N) + \Delta E_{\text{c}} \\ &= -\epsilon_{\text{i}} + \Delta E_{\text{c}} - E_{\text{R}} \\ &\approx -\epsilon_{\text{i}} \end{aligned} \tag{2.7}$$

The result from these considerations is that the binding energy that is measured in PES does not represent the initial energy of the excited photoelectrons but instead the energy difference between initial and final state.[114, 121]

If the emission line of choice for different samples shows a change of binding energy it can be assumed that either the initial and/or the final state must have been changed. In the following it will be discussed how the two states of the sample can be changed and how this might affect the binding energy.

Initial state effects

From equation 2.7 it is obvious that the binding energy will change if the energy eigenvalue $-\epsilon_i$ is changed. This energy includes the background potential of all electrons on the electron from the orbital of which the emission is observed. If this background potential is changed the energy eigenvalue of this emission is changed as well. Hence, any change in the density of states of the initial state will change the binding energy.[121] Examples for this so-called chemical shift are the change of oxidation state (e.g. Fe^{2+} instead of Fe^{3+}) or the change in chemical environment inducing charge redistributions (i.e. a change in the ligand or a surface adsorbate).

Final state effects

Final state effects occur in equation 2.7 in the two corrections terms. While the change in the correlation interaction is often neglected as a good assumption the changes in the relaxation correction can be separated into two contributions. Namely, either intra-atomic and extra-atomic screening can be considered.[121]

Screening refers to the reaction of the remaining electrons to the creation of the photohole which manifests itself in an electrostatic potential.[107]. Intra-atomic screening is hereby the reaction of the electrons of the same atoms. In constrast to this, the extra-atomic screening refers to the reaction of the delocalized valence electrons of the lattice.[107, 114]

The intra-atomic screening is in most cases believed to be independent of the chemical environment. It does, therefore, not contribute to a binding energy shift unless the valence configuration is changed (e.g. $3\,d_4^6s^2$ for elemental iron vs $3\,d_4^5s^0$ for iron in hematite).[121] For the extra-atomic screening this does not apply. Here, changes in the binding energy are to be expected if the screening is affected by the change in chemical environment.[121] The competition of different screening channels leads to different final states that are separated by the change in relaxation ΔE_R.

In the model by Kotani and Toyozawa a core hole can either be compensated by an initially unoccupied d-state on the metal or by an initially occupied sp-band on the ligand.[122] The first case is considered to be "fully-screened". In the second situation the d-state is being drawn below the Fermi energy but stays unoccupied. Hereby, a

two-hole situation is created which allows for only a "poorly-screened" situation which is given by increasing the charge density in the sp-band around the ionization site. The "fully-screened" final state shows a lower binding energy than the "poorly-screened" final state.[107, 114, 122]

The two screening possibilities occur instantaneous with the photoionization. Such final state effects are referred to as intrinsic. After the first step of photoionization, however, the electron has to travel to the surface and, in a third step, escape through the surface to reach the detector. At any time during step two and three of this so-called three-step model by Berglund and Spicer further interactions can occur that lead to a change in the kinetic energy of the electron[5].[123] Such interactions are regarded to be extrinsic.

In table 2.1 a short overview on possible processes that can occur during the photoemission is given. A more detailed description has been given by M. Weidner in Ref. [114].

Table 2.1: Possible **processes** that can occur during the photoemission with a short description. Each process is marked whether it is regarded to be *intrinsically, i*, occuring in step one of the photoemission, or *extrinsically, e*, occuring in step two or three.

Photohole screening	*i*	Availability of different screening channels as discussed in the text.
Spin-orbit coupling	*i*	Coupling of the spin of an unpaired core-electron left behind by the photoexcitation with the angular momentum of the orbital.
Spin-spin coupling	*i*	Coupling of the spin of an unpaired core-electron to the total spin of the valence shell. Also referred to as "**multiplet splitting**". Important mechanism for the M2p levels in TMOs where the unpaired core-electron can couple to the spin of the d-electrons in the valence shell.
Plasmon excitation	*i,e*	Excitation of plasmons by screening of the photohole through conduction electrons (*i*) or by interaction between the electron gas and the travelling photoelectron (*e*).
Electron shake-up	*i,e*	Energy transfer from the photoelectron to a second electron that is excited into a higher bound state.
Electron shake-off	*i,e*	Energy transfer from the photoelectron to a second electron that is thereby ejected from the sample
Phonon interactions	*i,e*	Interaction of photoelectron and phonon through inelastic scattering.

[5] Which manifests itself as a change in binding energy

Valence band spectroscopy on hematite

The valence band of hematite has been intensively studied already decades ago. Especially two works are worth to be noticed:

First Fujimori et al. have investigated the valence band and core-level on hematite single crystals and explained the spectral characteristics with the help of cluster interaction (CI) calculations.[59] Then, Lad & Henrich used a similar approach to also show the spectral differences of Fe_2O_3 hematite compared to Fe_3O_4 magnetite and Fe_xO.[60] The spectra of these two studies and corresponding CI calculations are shown in Figure 2.9.

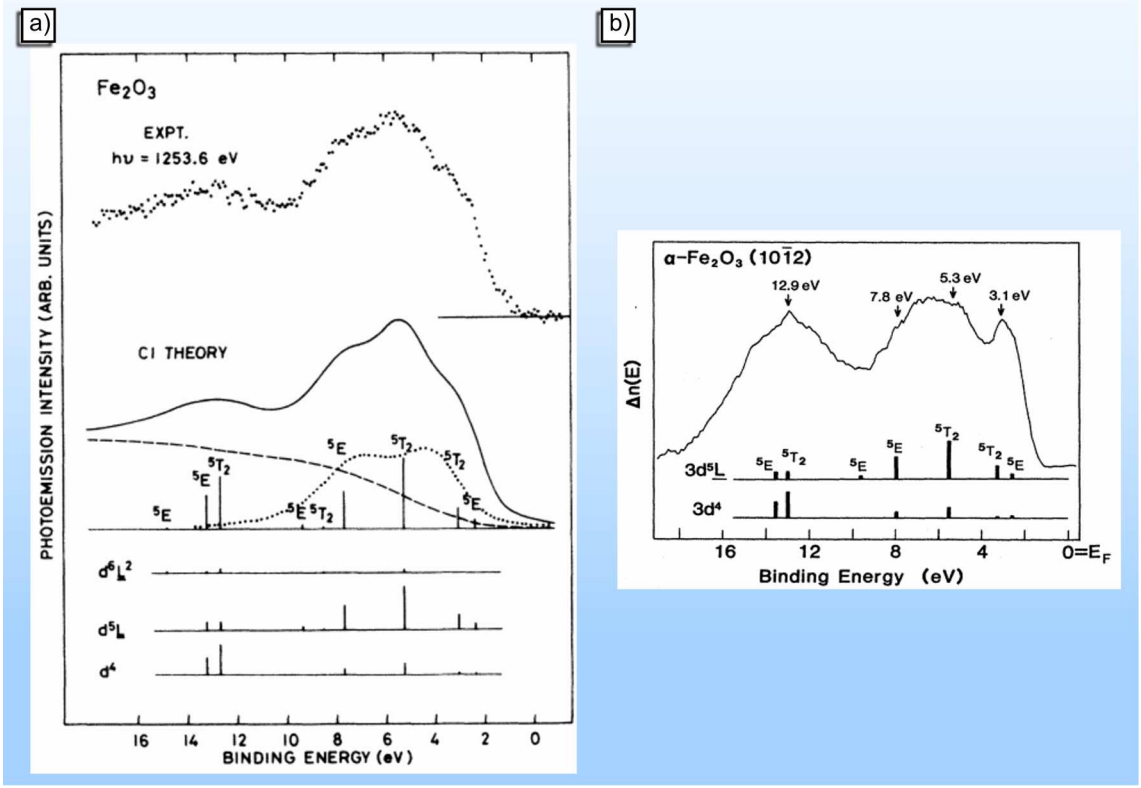

Figure 2.9: Valence band measurements and cluster interaction calculations of hematite from a) Fujimori et al. and b) Lad & Henrich.[59, 60]
a) Reprinted figure with permission from A. Fujimori, M. Saeki, N. Kimizuka, M. Taniguchi, S. Suga, Phys. Rev. B, 34, 7318, 1986. Copyright 1986 by the American Physical Society.
b) Reprinted figure with permission from R. J. Lad, V. E. Henrich, Phys. Rev. B, 39, 13478, 1989. Copyright 1989 by the American Physical Society.

Due to the photoexcitation process a hole is created. For materials that have a valence band which is derived from *s* or *p* states it is a good assumption that this hole stays in the band where it has been created. The electrons in the iron d-orbitals as prototype of localized d-electrons, however, give rise to a different behavior.

After the photoemission the high-spin d^5-configuration of hematite in the ground state can be found in different final states. Namely, the hole could still be in the d-states which would now show a d^4-configuration. It is, however, also possible that an electron from the oxygen ligands is transferred into the d-state. Then the hole resides in the ligand states which gives a $d^5\underline{L}$-configuration. In addition, it was considered that more than one electron is transferred i.e. a $d^6\underline{L}^2$-configuration is created. Here, however, a very low probability was calculated and this possibility can be neglected.

The work of Fujimori et al.[6] in Figure 2.9a) showed that the main intensity actually results from the $d^5\underline{L}$-configuration as final state.[59] The different states are named according to their term symbol. This was confirmed by the work of Lad & Henrich[7] shown in Figure 2.9b).[60]

These results have proven that hematite is a charge transfer semiconductor. It should be noted, however, that there is no energetic difference in the position of the emissions from the $d^5\underline{L}$- and d^4-configuration. This allows for the assignment of the features in the valence band to the real density of states consisting of a d^5-configuration.

One aspect for the spectra in Figure 2.9 has to mentioned. Despite the similarity of their interpretation the spectral appearance is different for the two studies. Different shapes of the valence band of hematite can be frequently observed in literature. The topic will be discussed in more detail in Chapter 5 of this work and a possible reason will be given there.

Core-level spectroscopy on hematite

For hematite the most important core-levels in PES are the Fe2p and O1s levels. Both have been extensively measured.[55, 61, 74, 124–126] The complexity of interpretation of the two different spectra, however, is drastically different.

The interpretation of the O1s level is rather straight forward. In most experiments it is mainly focused on the observation of shoulders in order to identify different oxygen species e.g. from adsorbates on the surface.[127, 128] In addition, the binding energy of the emission is usually extracted and compared to available data from literature.

As can directly be observed from Figure 2.10 the structure of the Fe2p peak in a) is much more complicated than the single O1s emission in b). Consequently, the interpretation is more complex as well. Included in the inset of a) are multiplet calculations for Fe^{3+}

[6] Reprinted figure with permission from A. Fujimori, M. Saeki, N. Kimizuka, M. Taniguchi, S. Suga, Phys. Rev. B, 34, 7318, 1986. Copyright 1986 by the American Physical Society.

[7] Reprinted figure with permission from R. J. Lad, V. E. Henrich, Phys. Rev. B, 39, 13478, 1989. Copyright 1989 by the American Physical Society.

compounds adapted from the work of Gupta & Sen in comparison to an Fe2p-spectrum from hematite.[129, 130]

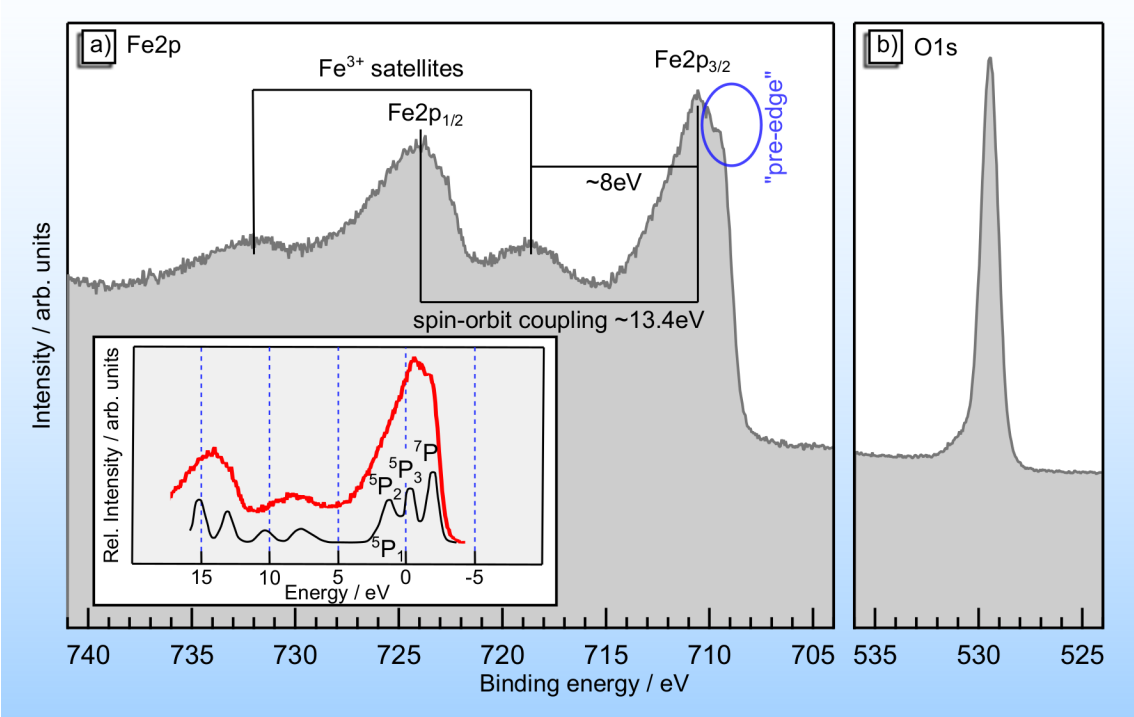

Figure 2.10: Example spectra of the Fe2p and O1s core-levels in hematite measured as part of this work. The inset shows the multiplet splitting expected for an Fe^{3+}-compound which was adapted from the work of Gupta & Sen.[129, 130] The assignment of the multiplet splitted peaks was compared to Ref. [131].

The Fe2p spectrum consists of the $Fe2p_{3/2}$ and $Fe2p_{1/2}$ main lines which result from spin-orbit splitting. Their separation is about 13.4 eV.[61, 125, 126] In addition there are two satellites which can be found at higher binding energies about 8 eV seperated from the respective main line. These satellites result from a shake-up process where an electron is excited into a higher energy state.[129, 132]

The separation of the satellite from the main line of 8 eV is larger than the ionization potential of hematite[8]. It might, therefore, be possible that it results from an shake-off process. Usually, however, it is considered to be of shake-up type.[132]

Considering the $Fe2p_{3/2}$ main-line it is obvious that it includes contributions from different effects that give it a rather asymmetric appearance. Fundamental work on this topic was done by Gupta & Sen, who calculated the multiplet splitting resulting from spin-spin coupling for a variety of transition metal ions.

[8] Please see Figure 6.13.

The inset in Figure 2.10a) shows their result in comparison to a Fe2p spectrum of hematite. This spectrum was measured as part of this thesis. The assigned term symbols indicate the final state from which these multiplets result.

There is a very good agreement between measured and calculated spectra. This shows that the Fe2p$_{3/2}$ main line already consists of four different final-states. These originate from the removing of a p electron out of the $2p^6 3d^5$ ground-state configuration which results in a $2p^5 3d^5$ configuration. The ground term of a Fe^{3+} ion is ^6S which has to be coupled with the p^5 shell. As a consequence ^7P and ^5P terms are obtained. The former can only be created with one subshell coupling ($p^5(^2P)$ with $d^5(^6S)$(ground state)) whereas the ^5P term can be formed from three d shell couplings: $p^5(^2P)3d^5(^6S)$, $p^5(^2P)3d^5(^4P)$, and $p^5(^2P)3d^5(^4D)$.[129, 131, 133]. The satellite has been calculated as well and was explained by a shake-up process.

In addition to the multiplets, however, there are sample specific contributions. At lower binding energies of the top-most part of the Fe2p$_{3/2}$ emission a "pre-edge" can be observed. It is not included in the theoretical prediction and will be further explained in part 5 of this work.

Also, it should be mentioned that the theoretical predicted multiplet splitting does not consider surface effects. At the surface the bonding situation is different as in the bulk. Usually a "surface peak" has to be added when multiplet fits of actual spectra are performed.[61, 125, 132] As the "pre-edge"', however, it is not a final but an initial state effect. Without a detailed knowledge of the bonding rearrangement on the surface it is nearly impossible to assign these "surface states".

Interface experiments

In an interface experiment the electrical contact formation with two materials is being analyzed. It is based on the fundamental work by Kraut, Waldrop et al.[134, 135] They showed that the interface potential in a semiconductor in contact to a metal or different semiconductor can be determined by means of XPS. The procedure that they established is being used vastly in the Surface Science Division at TU Darmstadt.[136, 137]

The experimental procedure during an interface experiment is rather straight forward. Initially, the substrate material is being measured by XPS/UPS. From this measurement the position of the relevant core-levels and the valence band maximum are being extracted. In addition, it is proven that no contact has been formed so far by measuring the regions of the relevant core-levels of the contact material the film of choice. From the UPS measurement a work function and ionization potential of the substrate can be extracted.

In a next step a very small amount of contact material is being deposited as a thin film on top of the substrate. The amount is usually assumed to be even less than a full monolayer in this deposition. Then, the sample is being transferred back into the XPS chamber and is being measured again. In this measurement the relevant core-levels of both the substrate and the film material have to be measured. In most cases, however, it is possible to omit the valence band region from being measured as a superposition of the valence bands from the two materials can be expected.

This procedure of film deposition and XPS measurement is being repeated with increasing deposition times until no substrate signal can be acquired anymore by XPS. The repeatedly transfer from XPS into deposition chamber and back requires an integrated system which allows for a transfer in UHV conditions for best results. It would also be possible to remove the sample from the vacuum between measurement and deposition but then surface contaminations by hydrocarbons and water have to be expected.

A schematic representation of the experimental procedure of an interface experiment can be found in Figure 2.11a) as a flow diagram. In b) and c) the protocol of interpretation is being shown which will be explained in the following. The interpretation of the acquired spectra of an interface experiment requires certain assumptions and precautions.

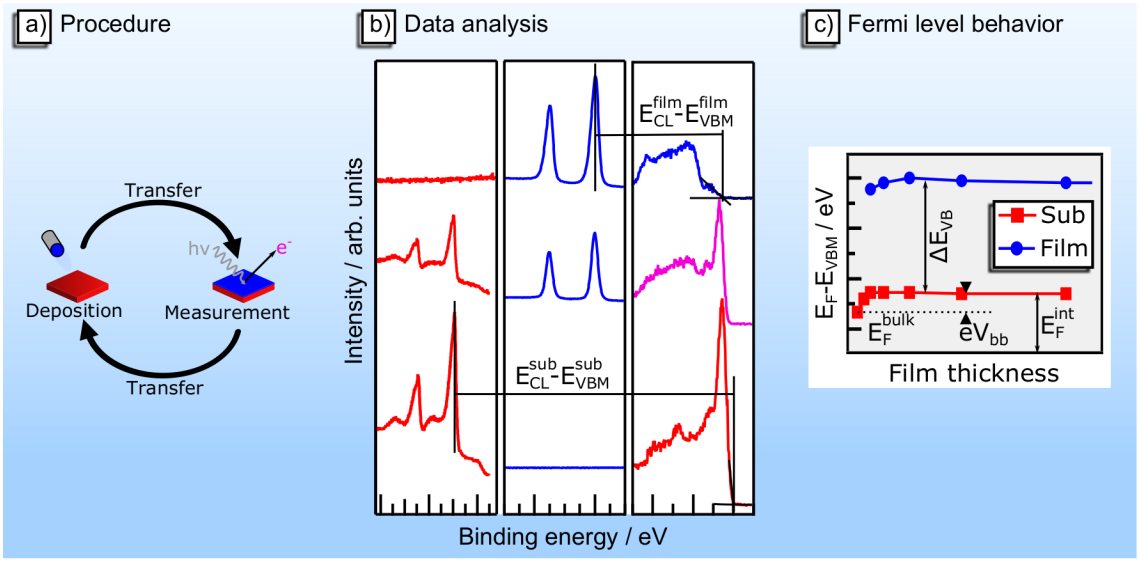

Figure 2.11: Procedure of an interface experiment. In a) the deposition/measurement cycles are schematically depicted. These cycles are repeated until no emission from the substrate can be measured anymore. In b) and c) the acquired data of an interface experiment is shown in short form. As the valence band is a superposition of the signal of substrate and film the core-levels need to be used to follow the Fermi level. The dependency of these levels on the thickness of the film is shown in c) with the extractable parameters from an interface experiment.

The first and most important assumption is the constant distance between a certain core-level and the valence band maximum E_{CL}−E_{VBM} in a given material. With this assumption any shift in Fermi level position $E_F - E_{VBM}$ can directly be seen in a shift in the core-level's binding energy. In reality this assumption holds as long as the substrate material is not being changed due to the deposition of the film material. A structural change or a reaction with the film material, however, lift the assumption and raise the complexity of interpretation.

Secondly, the material should ideally be chosen to have well separated core-levels if possible. In Figure 2.11b) the core-levels of the substrate in red and of the film in blue are not interfered by the other material. The valence band in the middle, on the other hand, shows emission from both materials and is thereby not easily analyzed. This is indicated by the purple color. In reality it is sometimes not possible to chose the materials according to this restriction. Then, other core-levels than the most intense ones can be used or it is necessary to develop a "deconvolution/subtraction" procedure.

A third precaution is related to the complexity of the experiment itself. In model experiments the film material should be chosen to show reliable results. Complex systems which require high-temperature growth and are prone to phase separation are obviously possible to be used but make the experiment more complicated. For a good comparison to other experiments it is good practice to use the same film material for all experiments.

The analysis of the spectra include the following steps. First, the binding energies of all relevant core-levels are determined. In addition, the valence band maximum of substrate and film and possibly also the work function are being extracted from the first and last measurement, respectively. These have been performed on the bare materials and a assumed to show the "bulk" Fermi level position. In order to extract the Fermi level position at the interface it is necessary to determine E_{CL}−E_{VBM} of the relevant core-levels for both, the substrate and the film. For the former this is done with the first measurement and for the latter from the last. By subtracting these constant from the binding energies after each deposition step it is now possible to determine Fermi level positions in the two materials after each deposition step. These can now be plotted in dependency of the deposition step, deposition time, or film thickness as is being shown in Figure 2.11c).

Other aspects that should be considered from the core-levels are possible changes in appearance due to e.g. a change in oxidation state or occupation of the conduction band. It is also possible to extract the composition of the materials during the experiment if all core-levels are free of interference from the other material. If the substrate and contact materials react during interface formation a change in composition will appear.

The Fermi level behavior during the interface experiment as shown in Figure 2.11c) allows for the extraction of certain parameters that are essential in order to fully understand the band alignment of two materials. For the substrate it is possible to extract the Fermi level position in the bulk E_F^{bulk} and at the interface E_F^{bulk} as indicated from the first and the last few positions. Their difference can be regarded to give the band bending eV_{bb}.

The same applies for the film with the difference, that the Fermi level position in the substrate also affects the Fermi level position in the ultra-thin substrate. A band bending can therefore only be extracted if the band bending in the substrate is being considered as well. As a first assumption it can be subtracted from the result of the film but in general a new, reverse experiment is necessary to fully extract the Fermi level behavior in the film material if in contact with the substrate material.

If the two materials show a parallel behavior of the Fermi level it is possible to extract the valence band offset ΔE_{VBM}. This value is of high importance as it allows for the determination of contact properties. An ohmic contact for example requires quite similar valence band positions. In addition, this value can be used to compare the substrate material to other materials that have been measured with the same film material in a similar experiment. From their respective valence band offset to the same film material it is possible to suggest a valence band offset to each other without measuring it in first place. This assumed transitivity gives a more profund decision criteria to chose suitable contact materials.[138]

2.3.3 Raman Spectroscopy on iron oxides

Raman spectroscopy is a powerful technique for molecules and solids. It is often used as a fingerprint technique to identify certain molecululars structures. It can, however, also give information on crystallinity, crystal orientation, composition, stress, doping, and relaxation. Within this work Raman spectroscopy has been mainly used as a fingerprint method to distinguish between amorphous and crystalline Fe_2O_3 in corundum structure.

This introduction is meant to provide basic information on the Raman process as well as give an in-sight into the expected spectra for possible structures of iron oxides. The discussion on the measured spectra in the following parts of the work will provide more detail where it is necessary. This part is based on the two book "Modern Raman Spectroscopy - A practial Approach" by E. Smith and G. Dent and "Introductory Raman Spectroscopy" by J. Ferraro, K. Nakamoto, and C. Brown.[139, 140]

Raman spectroscopy is based on the scattering of light. By using a single photon energy the sample is being lifted into an excited virtual states. This virtual state can be described as a distortion (polarization) of the electron cloud around the nuclei. From there it can

fall down again. If it falls into the initial state the scattering event is elastic. No change in energy is observed. This process is referred to as Rayleigh scattering.

Information on the sample, however, requires an observable change in the energy of the photon after the scattering event. These changes in energy can be translated into changes in the wavelength and are referred to as Raman shifts. Here, two mechanisms are possible: Stokes and anti-Stokes scattering.

In the former the sample is being excited from the **Ground states** into the **Virtual state** and falls then down into an excited **Vibrational state**. Hence, the energy of the outgoing photon is reduced by the energetic difference between vibrational excited and ground state (the wavelength will be increased - positive Raman shift). In the latter, the sample is already in a vibrational state before being lifted into the virtual state. It then falls back into the ground state which increases the energy of the photon by the difference between vibrational excited and ground state(the wavelength will be decreased - negative Raman shift).

While the Raman shift of Stokes and anti-Stokes are the same the probability of the two processes is different. An anti-Stokes shift requires a certain population of the excited vibrational state which lowers its probability compared to the Stokes shift. Hence, usually in Raman spectroscopy the latter is being measured for a higher intensity. Comparing the intensity of both at different temperatures, however, can give information on the change in population of the vibrational states.

In order for a molecule to show Raman modes it has to exhibit easily displacable electrons i.e. it needs to be easily polarizable. This is in contrast to IR-spectroscopy where a strong dipole change in the mode increases the activity. Due to symmetry considerations no vibration can be both Raman and IR active if point-symmetry exists. This makes these techniques complimentary with the full spectrum of vibrational modes only accessible with a combination of both techniques.

Each Raman active vibrational mode in a solid can be described by the type of vibration and the participating species. This, however, is tedious work which involves detailed measurements and sophisticated calculations. Luckily, however, for common structures of solids the vibrations have already been identified and it is possible to use the measured spectra as a fingerprint for certain structures.

In Figure 2.12a) and b) the calculated position of the Raman modes for Fe_2O_3 in corundum structure and Co_3O_4 in spinel structure are shown as blue bars. Measured spectra show very good agreement.

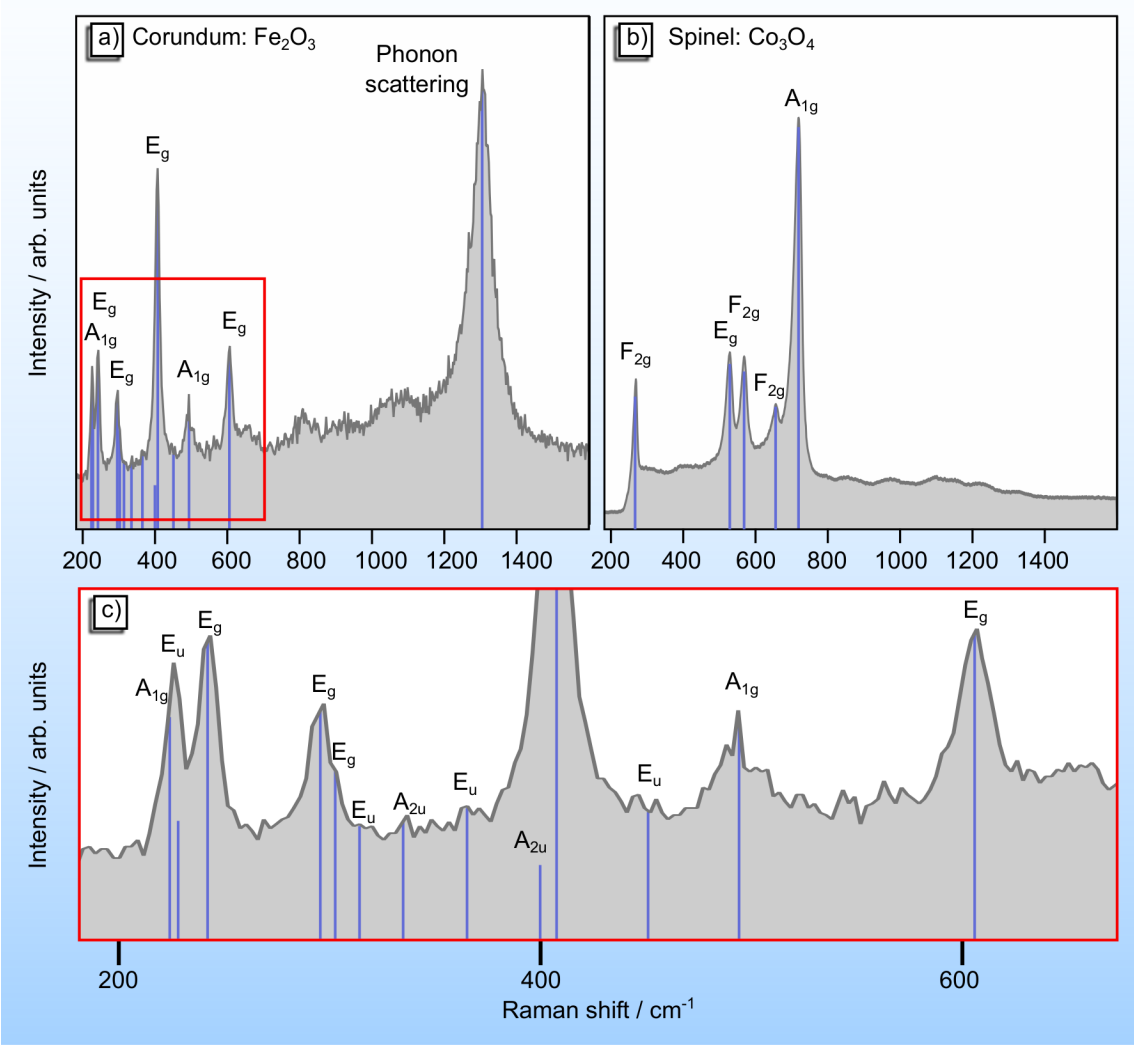

Figure 2.12: Raman spectra of different oxides. Calculated positions of the Raman modes are indicated as blue lines.[141, 142] The grey spectra show measurements on a) a Fe_2O_3 sample in corundum structure and b) a Co_3O_4 sample in spinel structure. In c) the indicated excerpt from a) is shown in more detail.

The exact position differs from compound to compound due to e.g. changed bond lengths and ion mass. Hence, Fe_3O_4 in the spinel structure will show a similar spectrum to Co_3O_4 but with different positions. An excerpt from a) with a more detailed view is being given in Figure 2.12. Due to the unique set of modes for each structure it is possible to use Raman spectroscopy as a fingerprint method. That is, if the phases that the material can exhibit are already known and in the best case have been measured already. For the iron oxides, luckily this is the case and the distinction of the different phases is possible with this technique.[143, 144]

2.3.4 Brief introduction to X-ray diffraction

The determination of structural properties such as crystal phase and orientation, grain size, texture, and internal stresses is essential for a good knowledge of the samples properties in many cases. By correlating these properties to the results from other measurements it is often possible to find descriptors in the structural properties that can be used to predict the properties of a material or even of a material class. The most widely used technique to gather information on the structural characteristics is X-ray diffraction (XRD).

XRD may be used in may different special arrangements that all have in common that they are based on the diffraction of X-rays. The range of complexity of these special cases range from the determination of a crystal phase, over the extraction of the grain size, to the creation of a full orientation matrix which gives the structural connection of a thin film to a substrate. In this work most XRD measurement were on the low complexity side and were only used to identify the crystallographic structure of the thin films by comparison to measurements on powdered samples with a known structure. The proof of epitaxial growth of hematite on certain substrate, however, also required more sophisticated measurements. This part is intended to give an overview of XRD with an introduction of the most important parameters that had to be manipulated in order to perform the measurements for this work. A much more detailed handbook (in german) is written by L. Spieß et al. in "Moderne Röntgenbeugung".[145]

In XRD the sample is being illuminated by monochromatic X-rays under a certain angle. If the sample is crystalline diffraction occurs. Then, due to constructive and destructive interference a detector will find high and low intensities in dependence on the orientation angle. A graph of intensity versus the angle 2θ from a 2θ-scan is referred to as diffraction pattern. High signals are found at diffraction angles and are referred to as reflections. They can be assigned to certain crystal planes within the sample. The appearance of reflections is based on Bragg-law (equation 2.8) which connects the wavelength of the X-rays λ to the angle of diffraction θ and the lattice spacing d_{hkl}.[145]

$$2d_{\mathrm{hkl}}\sin(\theta) = n\lambda \tag{2.8}$$

The lattice spacing depends on the crystal plane (hkl) that fulfills the diffraction conditions at the given angle. The lower the symmetry of the crystal structure the more complicated is the dependency of d in equation 2.8 on the hkl values. For the cubic system with only one lattice parameter a it is quite easy and is given by

$$d_{\mathrm{hkl}} = \frac{a}{\sqrt{h^2 + k^2 + l^2}} \tag{2.9}$$

Due to this complexity in reality a comparison to already existing measurements is often applied. Here, data from powdered samples are the standard reference. These are given in so-called "powder diffraction files" (pdf-cards). Their advantage towards ceramic or thin film samples is the absence of an orientation dependency. Hence, all reflections scan be expected to occur with their intensity ratio being characteristic for a non-oriented sample.

The comparison of the diffraction pattern of the sample to be analyzed then starts with an educated guess. Pdf-cards from possible structures (which include all or some of the elements of the sample) are used. If the measured diffraction pattern shows reflections at the same angles the phase is being determined. Some complexity is added as in thin films usually not all reflections occur due to orientated growth. This comparison, however, also gives information on the orientation as the ratio between different reflections is changed.

An extreme case of high orientation is the epitaxial growth. Here, the film matches the crystal phase of the single crystalline substrate to a high degree and grows in the same orientation. In order to identify epitaxial growth not only 2θ scans are necessary but also other angles have to be used to fully identify the epitaxial dependency. Namely, these angles are ϕ, Ω and χ. These can be found in Figure 2.13 together with 2θ.

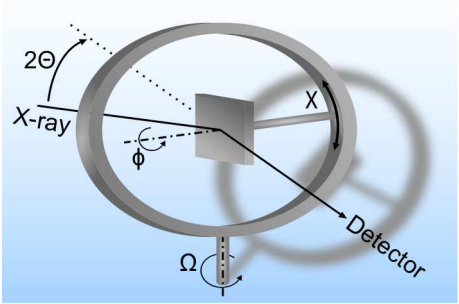

Figure 2.13: Important angles in XRD.

In this work 2θ and ϕ-scans have been used to identify the epitaxial growth. For this purpose, first diffraction pattern in dependency of 2θ have been recorded. For epitaxial samples only at very few angles a reflection exists. These are assigned to a certain lattice plane and multiples thereof. These 2θ scans alone only proves the high oriented growth but sometimes it can be hard to distinguish the signals of the thin film from the reflections of the substrate which occur at quite similar angles[9].

To prove epitaxial growth of the thin film a ϕ-scan is performed. For this purpose a 2θ value is used at which the pdf-card of the film material predicts a reflection but there is none of the substrate to be expected. Then, ϕ is changed (sample rotation) in order to fulfill the diffraction conditions at certain angles ϕ. If reflections occur the epitaxial growth can be regarded to be proven. For a full orientation matrix, though, more measurements have to be performed which also include the manipulation of the other angles χ and Ω.

[9] Not the same angles as d_{hkl} in the substrate is slightly different from the one in the film

With the angle Ω the incident angle of the X-rays is chosen. For non-oriented thin films very small angles of Ω often give higher intensities. If a high orientated or even epitaxial growth occurred, however, no reflections can be measured. Measurements at these very low angles are referred to as "Grazing Incidence X-ray Diffraction" (GIXD).

2.3.5 Conductivity measurements

The electrical properties of transition metal oxides are of high interest as their application always involves charge carrier transport phenomena. Hence, very early studies have already investigated the conductivity of hematite samples.[77] In this work the thin film samples were measured in a home-built setup which allows for the conductivity measurement at elevated temperatures and in an controlled atmosphere of two samples on a ceramic sample holder in a quartz tube oven at the same time. The setup had already been installed at the beginning of this work and a detailed (german) descriptions can be found in Refs. [146] and [113]. In the following a brief introduction into the setup and into the chosen sample geometry is given. Physical concepts on the conductivity and how it is influenced by e.g. the atmosphere is given in the discussion on the results.

The measurements are performed in a geometry proposed by L.J. van der Pauw.[147] Here, a thin film can be measured regardless of its exact shape. It is, however, necessary for the film to have a homogeneous thickness without holes.

In addition, the contacts should be as small as possible and be positioned on the edge of the film to be measured. Figure 2.14 shows a schematic sample with substrate, film and contacts. The latter have to cover also parts of the edges of the substrate in order to be contacted.

In the present example a current is being applied between the contacts A and B. In order to measure a current-less voltage drop the potential between C and D is being measured. This allows for a measurement of the conductivity which is independent on the contact resistance. For better statistics each possible contact pair is being used in both directions (forward/backward mode) with the respective potential measurement. This gives eight measurements of which the mean value is used. The specific resistance and thereby the conductivity of a single measurement is given by a geometry factor, the resistance that is being measured and the thickness of the film d:

$$\rho = \frac{1}{\sigma} = \frac{\pi}{\ln 2} \cdot d \cdot \frac{U_{\mathrm{DC}}}{I_{\mathrm{AB}}} = \frac{\pi}{\ln 2} \cdot d \cdot R_{\mathrm{AB,CD}} \tag{2.10}$$

The current should be chosen as high as possible with two boundary conditions. First of all, it must be able to inject all carriers into the sample. If it is not possible to apply the

current the sample is "in compliance" and the measurement cannot be used. Secondly, the potential measured in forward mode has to be the same as in backward mode. Hence, their ratio times 100 needs to be at 100. If deviations from this value are observed the current has to be potentially lowered. This, however, requires also the delay time between two measurements to be increased. For high resistive samples such as hematite often the measurement is only possible with very low currents at higher temperatures.

The temperature can be controlled by a Eurotherm controller and is being applied according to a calibration measurement which has been performed before. There is no direct measurement of the temperature within the oven. By noting the times at which the temperature is being changed, however, an almost correct temperature program can be created.

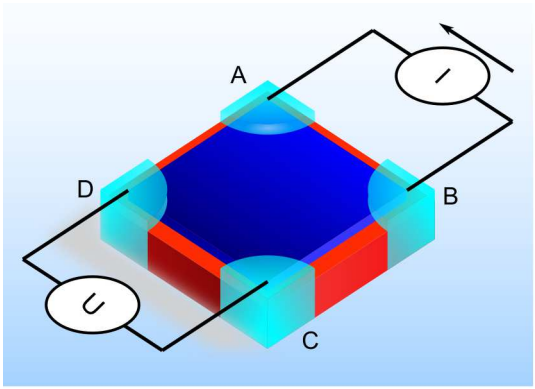

Figure 2.14: Sample with contacts for measuerments in van der Pauw geometry.

For the control of the atmosphere different gases are available. On the oven that has been used in this work these are pure argon and pure oxygen. By controlling the flow of the respective gases a range between 100 % argon to 100 % oxygen is possible. The oven also features a vacuum pumping system to lower the oxygen partial pressure even further. This feature, however, has not been used.

3 Experimental Procedure

3.1 The lab

All samples of this work were prepared in the DAISY-MAT system at TU Darmstadt. In this integrated system the XPS and UPS analysis of the samples could be performed as well. As an integrated system it allows for the sample transfer from the preparation chambers into the XPS chamber without leaving the ulta-high vacuum (UHV) conditions. This ensures clean sample surfaces without the contamination of carbon hydrates or water from the atmosphere.

In addition to the sputter chambers a few other possibilities to treat samples are available. These are an ALD chamber in which the sample can be exposed to water or its surface can be modified by an alumina layer and a plasma source in which oxidizing or reducing plasmas can be ignited. A schematic representation of the lab can be found on the left hand side of Figure 3.1. Further descriptions of the lab can be found e.g. in Refs. [148] and [149].

Photoelectron spectroscopy measurements on non-contaminated samples are essential to study the intrinsic electronic surface properties of the material. Any adsorbate on the surface might influence the electronic properties by a charge transfer and result in a shift of the Fermi Level. In addition, the oxygen emission that can give information on the chemical state of oxygen in oxide materials is being altered if oxygen-containing species are adsorbed.

Many PES measurements from literature are performed on samples, which have been prepared elsewhere and are introduced into the PES chamber in order to be measured. Cleaning by heating or ion etching are effective sample treatments that will change the properties. Such measurements are referred to as ex-situ in order to identify them as being performed on potentially contaminated samples.

The measurements on samples, which have never left the vacuum conditions, on the other hand, are referred to as in-situ[1]. This shall distinguish these measurements as being performed on clean, non-contaminated samples.

[1] Strictly speaking an "in-situ" measurement would be performed during the sample preparation/treatment. This has NOT been done. The forgiveness of the reader for this small flaw is appreciated.

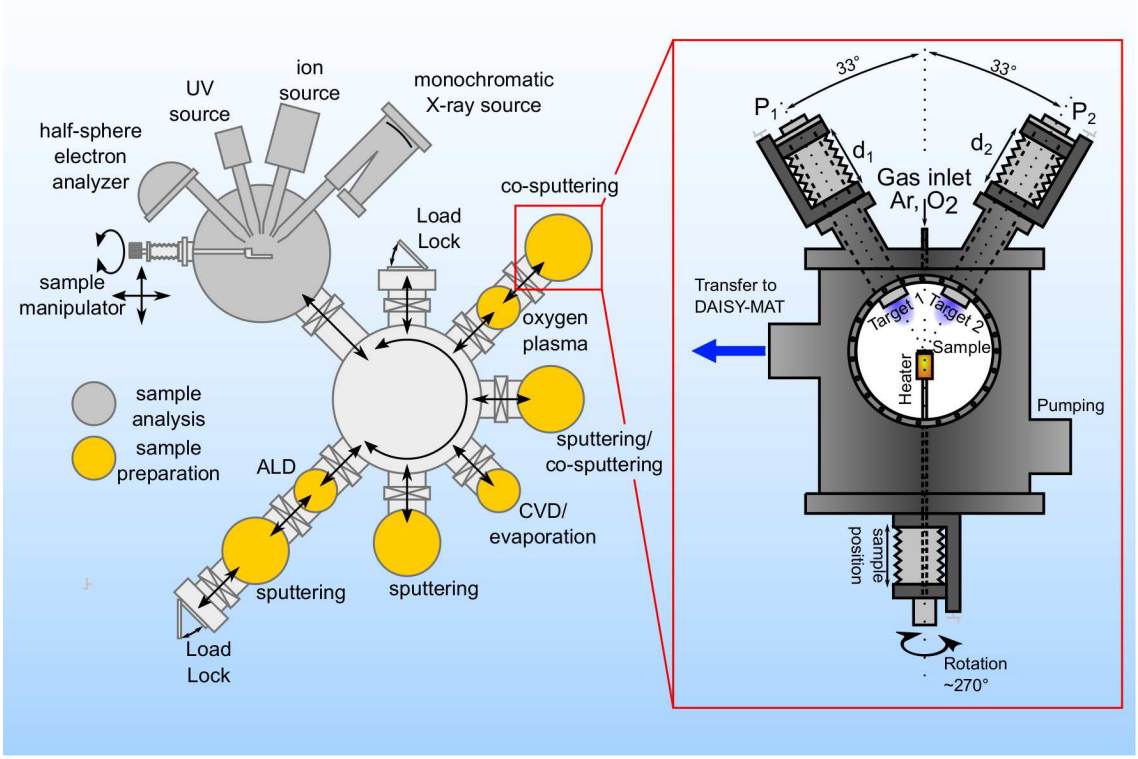

Figure 3.1: The DAISY-MAT system from the Surface Science Division at TU Darmstadt. On the left hand side a schematic drawing of the system with the central distribution chamber around which the preparation chambers are located is shown. The integration of a Physical Electronics PHI5700 multitechnique surface analysis system allows for the characterization of the samples by XPS/UPS without breaking the UHV conditions. The right hand side shows a schematic drawing of the chamber (Ox0) in which most samples of this work have been prepared. The chamber had to be rebuilt into a co-sputtering chamber with rotating heater prior to the first sample depositions. Schematic drawing of DAISY-MAT adapted from Ref. [148].

On the right hand side of Figure 3.1 a sketch of the co-sputtering chamber in which the iron oxide samples have been prepared is shown. Prior to the first deposition the chambers top flanche had to be designed in order to allow for the co-sputtering of the doped samples. During the deposition the sample is positioned at the point where the normals of the two targets cross (focus point). This point is being reached by manipulation of the height of the sample. Each target has an angle of 33° to the normal of the top flanche. To compensate for this angle a sample rotation was being established. As wiring makes it complex to achieve a 360° rotation it was decided to settle for a 270° back-and-forth rotation.

Each target can be manipulated in the distance d to the focus point and power P. With these values the sample composition can be changed. In addition, the use of RF and DC signals for plasma generation is possible.

Heating of the sample is achieved by a halogene light bulb below the sample. The temperature of the sample cannot be measured directly. Instead two thermo-couples are being installed on the heater itself. By using a calibration sample it is possible to correlate the heating current to a certain sample temperature, which can be controlled by the temperature at the two thermo-couples.

In this context one important aspect has to be mentioned. For years it was the standard procedure to use a silicon calibration sample for the temperature calibration. At one point, however, this sample was lost and was replaced with a quartz substrate. It was noticed that the temperature at the same current was much lower on a quartz substrate than compared to the silicon substrate. From this point on , calibrations were being done by using quartz and/or sapphire as calibration samples. The difference between the latter two can be up to 150 °C at the maximal heating current of 10 A. The best calibration can always be expected with the same substrate as calibration sample that is to be used during the deposition. For the chamber Ox0 which was used during this thesis temperature calibrations were performed for quartz and sapphire substrates.

3.2 Sample preparation

3.2.1 Sputter deposition and doping

Samples were prepared by means of RF-magnetron sputtering. For doping of hematite both targets of the co-sputter chamber described above were used. The range of parameters that have been used to deposit doped and undoped films can be found in Table 3.1. In the following chapters the relevant parameters for the discussion will always be highlighted. It should be mentioned that the minimal oxygen content in the sputter gas in order to achieve Fe_2O_3 thin films was found to be 6 %.

The substrates which were used will also be stated if necessary. Generally, two different substrates were used in every deposition. First, a blank substrate that was either sapphire(0001) or quartz was chosen. On the thin films on these substrate optical and electrical measurements could be performed as well as structural characterization.

In addition, an additional piece of the respective substrate was coated with platinum at 600 °C in order to achieve a conductive film for PES studies. In addition, structural characterization by Raman spectroscopy could be performed on these substrates as well. From previous experiments it was known that at the same conditions platinum grows as polycrystalline thin film on quartz while it shows epitaxial growth in a Pt(111) orientation on sapphire(0001).

Table 3.1: Deposition conditions for undoped and doped hematite thin films.

	Fe_2O_3	$Mg:Fe_2O_3$	$Si:Fe_2O_3$	$Zr:Fe_2O_3$
Target	Fe	Fe/Mg	Fe/Si	Fe/Zr
Power / W	60	60/15	60/15-30	60/15-45
Target distance / cm	8	8/7-14	8/8-12	8/10
Temperature / °C	RT-600	RT-400	400	
Oxygen content / %	1-20	8		
Pressure / Pa	0.5			
Substrate	Pt(111), pc-Pt, Sapphire, Quartz ($10 \times 10 mm^2$)			

For a few number of studies other substrates such as ITO-coated floating glass or sapphire in different orientation were used. It is indicated in the following chapters where this applies.

3.2.2 Sample treatments

Besides measurements on freshly deposited samples also studies on samples that were treated in different ways were conducted. A treatment in this sense is defined as a process that potentially alters the properties of the sample. For most of the treatments that are being introduced here, measurements before and after the treatment were compared.

In-situ & ex-situ Heating

Heating experiments were performed in-situ and ex-situ. The difference between these two sets lies in the place of heating. For the in-situ heating treatments the samples were heated within the DAISY-MAT without being removed from the vacuum. The ex-situ heated samples on the other hand were removed from the system and heated in a Carbolite quartz tube furnace. Figure 3.2 shows the procedure of the heating experiments as a flow diagram. The respective experiments are being discussed in Chapter 4.2.2 and Chapter 4.2.3.

The aims of these experiments were to gather information on the behavior of hematite in reducing or oxidizing conditions (reduction/oxidation - most left flow-diagram) and of the structural changes and respective properties upon heating of room temperature deposited films. This second set of experiment was conducted in-situ and ex-situ.

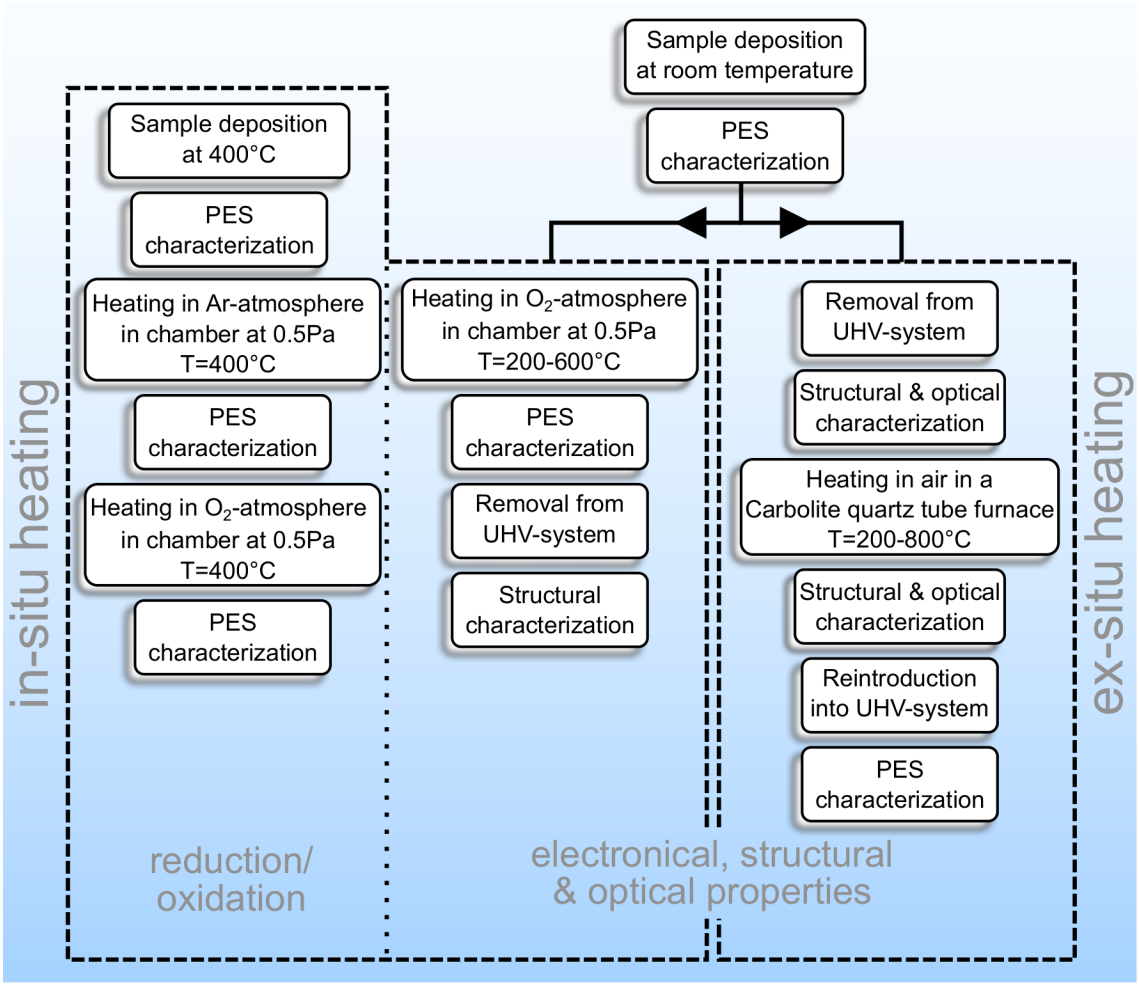

Figure 3.2: Flow diagramm of heating experiments. The in-situ heat treatments were performed within the DAISY-MAT system without removing the sample from the vacuum. This treatment is divided into two groups. First, reduction and oxidation experiments and second in-situ heating with the purpose to study structural changes. The ex-situ heat treated samples were removed from the UHV-system to be annealed in air in a Carbolite quartz tube furnace.

Oxygen Plasma

Sample treatment in oxygen plasma were performed with an Atom/Ion Hybrid Plasma source GenII by tectra which was attached to chamber Ox0 at DAISY-MAT. The functionality and design of the plasma source has been described elsewhere.[150] It offers the choice between an atom and ion mode. In the former an aperture plate inhibits ion bombardment of the sample from the plasma. The latter, on the other hand, allows for an acceleration of the charged ions in the plasma to ion energies of up to 1 keV.

In this work only the atom mode has been used. The atom flux in this mode is given in the manual of the plasma source[2] to exceed 2×10^{16} atoms $\mathrm{cm}^{-2}\,\mathrm{s}^{-1}$ at the working

[2] Can be found at `www.tectra.de`

distance of 100 mm. The experiments were performed with a pure oxygen flow of about 2 sccm resulting in a working pressure of about 1×10^{-4} mbar. The plasma current was kept at a constant 40 mA during the treatment time of 15 min. The plasma is generated with microwaves at a power of about 180 W. Even though a sample heater was installed during the duration of this work each experiment was performed at room temperature. The results from the experiments described by this procedure can be found in Chapter 7.1.

Surface modification by ALD

Attached to chamber Ox3 a chamber for an Atomic Layer Deposition (ALD) can be found at DAISY-MAT. This chamber was originally designed by T. Bayer and has been described before in different works.[108, 114, 151] A detailed explanation for the mechanism of the Al_2O_3 deposition can be found in Refs. [108, 114, 151]. In a nutshell, it includes several cycles of Trimethylaluminium (TMA, $Al(CH_3)_3$) exposure and a first pumping step followed by the addition of water and a second pumping step.

The exposure to TMA and water is controlled by opening and closing of the two ALD-valves v_1 and v_2 for the respective times T_1 and T_3. The pumping times T_2 and T_4 can be chosen independently as well. The exact times can be found on the left-hand side of Table 3.2. The deposition is being performed at a temperature of 250 °C.

By the number of cycles the thickness of the alumina layer can be modified. For most experiments five cycles were being employed. It was shown before that this results in an alumina film of about 1 nm.[151]

Table 3.2: Parameters for one cycle of Al_2O_3-deposition (left) and H_2O-exposure (right) in the ALD-chamber. The actual experiments were performed with five and 15 cycles for the former and latter, respectively. An opened/closed valve v_1, v_2 is indicated by ✓/⊗, respectively.

Al_2O_3-deposition			Step	H_2O-exposure		
duration / ms	v_1	v_2		v_1	v_2	duration / ms
80	✓	⊗	① TMA-exposure	⊗	⊗	10
300000	⊗	⊗	② Pumping 1	⊗	⊗	10
150	⊗	✓	③ H_2O-exposure	⊗	✓	500
300000	⊗	⊗	④ Pumping 2	⊗	⊗	60000

Water Exposure

Water exposure experiment were performed in the ALD-chamber as well. For these experiments v_1 was constantly kept closed. Due to this the sample was only exposed to water and no reaction with TMA or with alumina occurred. The times were slightly being modified and can be found on the right-hand side of Table 3.2. This cycle was repeated 15 times. Then, the sample was transferred into the XPS chamber as soon as the pressure in the ALD dropped into the 10^{-7} mbar range, where a transfer into the distribution chamber was possible.

3.3 Sample Characterization

3.3.1 Photoelectron Spectroscopy

The characterization of the samples' electronic surface properties by X-ray Photoelectron Spectroscopy was performed in a Physical Electronic PHI 5700 multi-technique surface analysis system which is integrated into the DAISY-MAT lab shown in Figure 3.1. In this section first the measurement setting will be explained, followed by an overview on the procedures how to subtract the background and determine binding energies from core-level, valence band, and UP spectra. Then, the procedure of an interface experiment will be introduced.

Measurement settings

The XPS measurements were performed with monochromatized Al K_α-radiation which has a photon energy of $h\nu = 1486.6\,\text{eV}$. The energy resolution has been determined from the Gaussian broadening of a sputter cleaned Ag sample to be $\approx 400\,\text{meV}$. This procedure was regularly performed whenever an alignment of the X-ray gun had to be done.

In this spectrometer the incident angle of the X-rays onto the sample is 45°. X-ray gun and detector have an angle of 90°. The geometry is an important information e.g. for the use of atomic sensitivity factors for quantitative analysis of the surface composition.

The analysis system offers different measurement modes. These will shortly be explained in the following:

- **Survey mode**
  In the survey mode a fast scan over a broad range of binding energies can be performed. It allows for a qualitative overview of the elemental composition and can exclude unwanted contaminations. In Figure 3.3 an example survey spectrum of

hematite with all core-level assigned is shown. The region around 280 eV is shown in the inset. Here, carbon would be found. The absence of any emissions shows that the sample is free of carbon containing contaminations. Usually, a survey spectrum is measured with the following settings:

  - Range: −1 eV to 1400 eV
  - Pass energy: 187.75 eV
  - eV/step: 0.800 eV
  - time/step: 100 ms

- **High-resolution (HRES)**
  This mode is the working horse of XPS. It offers a detailed scan with a high-resolution of any region wanted. The results can be used to determine binding energies. In addition, the area below the emissions from one measurement can be used for a quantitative determination of the surface composition. Usually, it is measured with the following settings:

  - Range: variable, depends on extend of measured region
  - Pass energy: 5.85 eV
  - eV/step: 0.050 eV
  - time/step: 100 ms

- **Utility mode (UTIL)**
  The UTIL mode offers a fast scan over dedicated regions with a higher sensitivity of trace elements than the HRES mode due to a higher pass energy. On the other hand, it does not have such a good energy resolution. This mode has not been used within this work.

  - Range: variable, depends on extend of measured region
  - Pass energy: 57.70 eV
  - eV/step: 0.250 eV
  - time/step: 50 ms

For the determination of absolute binding energies it is important to calibrate the measurement. This calibration corrects for small deviations (e.g. different voltage drops) in the set-up and allows for a comparison of binding energies from different measurements.

In order to perform a calibration a metal sample is being sputter cleaned for at least ten minutes with an Ar-ion gun. The ion have a kinetic energy of about 1 keV and the sample current is around 0.9 μA. The ion gun is usually set to scan the sample in a $4 \times 4\text{mm}^2$ square. After the sputter cleaning a survey scan is performed to proof the absence of any carbon hydrates or water on the surface.

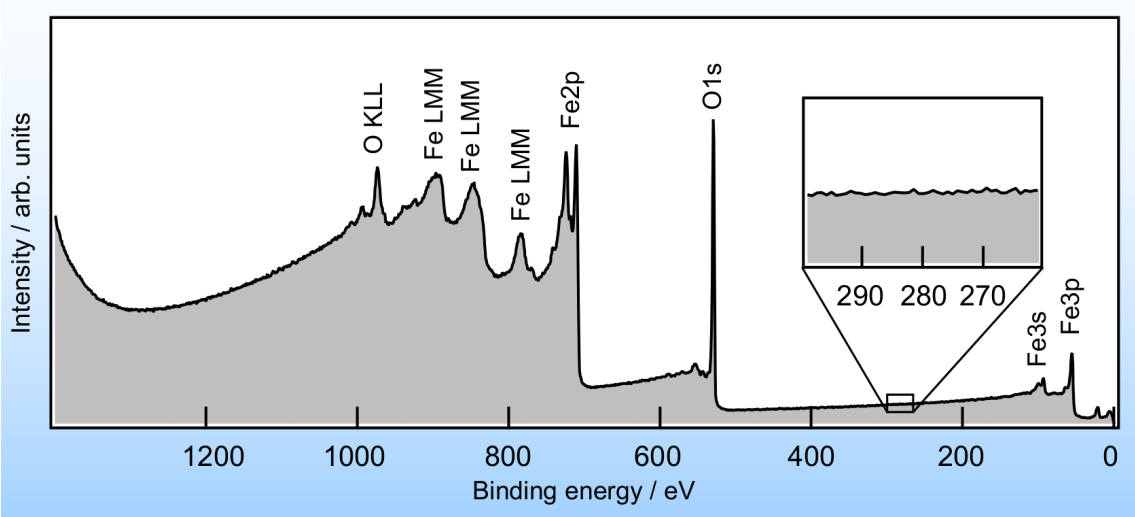

Figure 3.3: Example for a survey spectrum of hematite with all observable core-level emissions labeled.

As metal samples gold, silver, and copper are available. These offer core-levels at very different binding energy positions ($Au4f_{7/2} = 83.98\,eV$, $Ag3d_{5/2} = 368.26\,eV$, and $Cu2p_{3/2} = 932.67\,eV$). In addition, the Fermi edge of silver can easily be analyzed and a Fermi level can be extracted. With these four different regions a large portion of the spectrum can be calibrated in order to remove binding energy shifts.

In reality, also a stretching of spectra i.e. different shifts depending on the binding energy can occur. This is the reason why not only one metal is used for calibration. It was shown, however, that this does usually not occur in DAISY-MAT and a measurement of all three metals is unnecessary to be performed every day. The usual procedure, therefore, included the core-level and Fermi edge of silver to be measured every day with a measurement of the other metals from time to time.

Measurement of the valence band region with Ultraviolet Photoelectron Spectroscopy (UPS) were performed in the same chamber with the same detector. For this measurement, however, a bias of $-4\,V$ was applied to the sample. This bias accelerates low kinetic energy electrons (as low as $E_{kin} = 0\,eV$ at the surface) into the detector. In addition, the sample is tilted in order to have an angle of 90° towards the detector. This is done in order to homogenize the electrical field distribution.

The measurement is usually performed with HeI-radiation ($h\nu$ =21.22 eV) from a helium-discharge lamp. HeII-radiation at a higher photon energy ($h\nu$ =40.8 eV) would be available as well. It can offer a different insight into the electronic structure of oxide materials due to different cross-sections of the elements. However, it has not been used extensively within this work.

The detector settings for an UPS measurements are the following:

- Mode: modified HRES or Survey
- Range: variable, usually −2 eV to 21 eV (bias subtracted here)
- Pass energy: 2.95 eV
- eV/step: 0.025 eV
- time/step: 100 ms

Data evaluation - background subtraction and determination of composition, binding energy, and Fermi level position

The evaluation of the data includes different aspects. First, a visual inspection of the general peak shape. Differences in shape between two spectra such as e.g. shoulders contain information on the chemical state and/or adsorbates. Next, the binding energy is of importance. As can be seen in Figure 3.4b) and d) it can be determined by a manual procedure with a line towards the maximum of intensity. Even though semi-automatic methods are available this method has proven to be a good choice. Especially with complicated peak structures as it is the case for the Fe2p core-level it is often hard to impossible to receive reliable data from anything but the manual method. Hence, the binding energies in this work were extracted with this procedure.

A third important information from XPS is the composition. The ratio of two elements $x_{A/B}$ in a binary sample can be calculated with Equation 3.1 from the intensity I_i^{CL} of a certain core-level for the respective element and the atomic sensitivity factor ASF_i^{CL} of the respective core-level.

$$x_{A/B} = \frac{I_A^{CL}/ASF_A^{CL}}{I_B^{CL}/ASF_B^{CL}} \tag{3.1}$$

This equation, however, only hold for the intensity that originates from the core-level itself. Inelastically scattered electrons which have the same kinetic energy cannot be tolerated. It is, therefore, necessary to remove these from the spectra. For this purpose a variety of possibilities are available. Polynoms with any order can be used but are not physically correct. More physically correct approaches have been suggested by Shirley in 1972 and Tougaard and Jansson in 1992.[118, 119]

In this work both have been used. In Figure 3.4 a) and b) the effect of a background subtraction by the above methods on the Fe2p emission from hematite can be seen. Aronniemi et al. compared the two methods with the results from electron energy loss measurements and concluded that the Tougaard-method renders more suitable results.[152] It was, therefore, decided to employ this method for all Fe2p core-level in this work. As

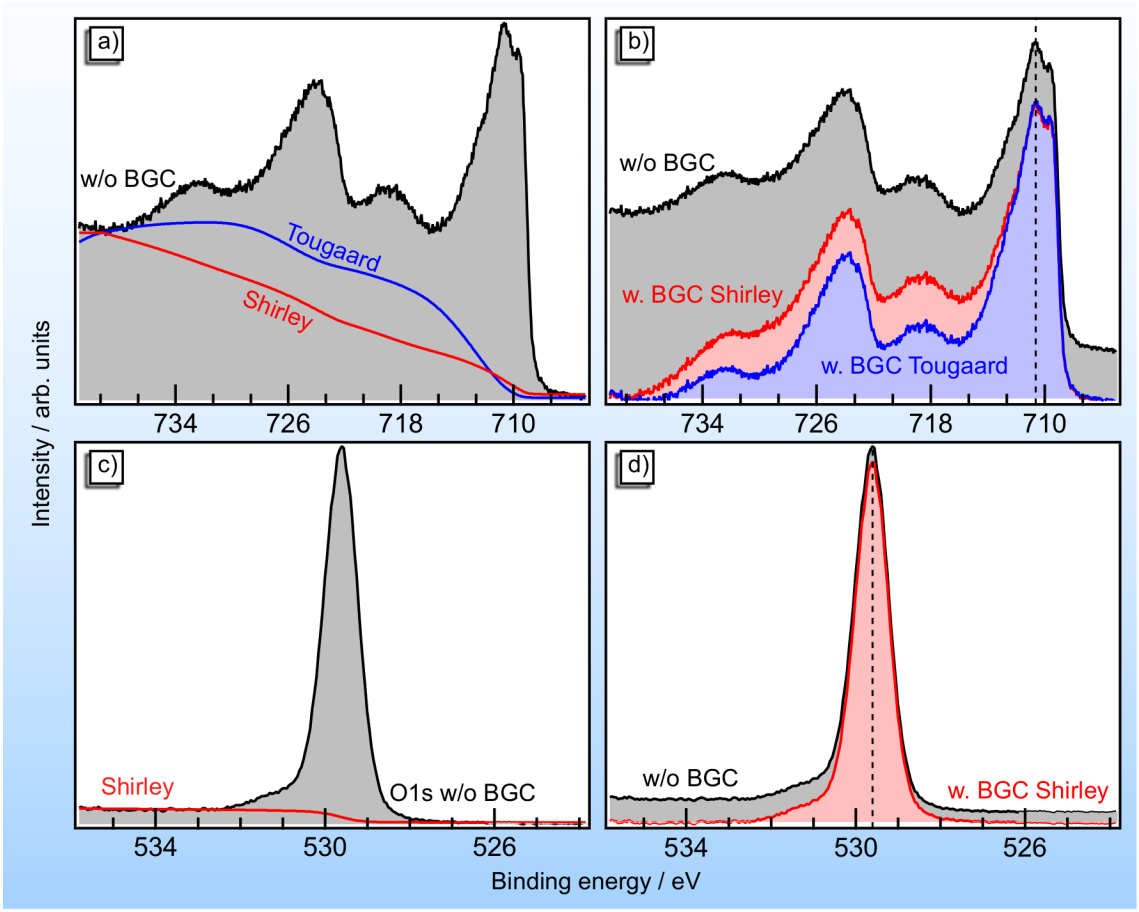

Figure 3.4: Determination of the binding energy by a manual method (dotted line) and the removal of the inelastic background with different methods.

can be seen in Figure 3.4b) the difference is only to be found in the peak area. The binding energy of the peak is not affected by the choice of background subtraction method and is the same for the uncorrected peak as well.

For less complex peaks such as the O1s emission or any peak from the dopant Mg, Si, or Zr the difference between Shirely- and Tougaard-method is neglectable. It was, therefore, decided to use the former as it is easier to conduct. Here, it can be seen from Figure 3.4d) that no difference in binding energy of the O1s core-level can be found between the corrected and uncorrected peak as well.

The valence band can be measured with both, XPS and UPS. In order to extract the Fermi level position $E_F - E_{VBM}$ (which is the same value as the valence band maximum E_{VBM} as the Fermi level is defined to be at 0 eV) a linear extrapolation to the lower part of the low binding energy side of the valence band can be used.

This is shown for the valence band measured by UPS and XPS in Figure 3.5b) & c). Fermi level positions from valence band measurements within this work have been extracted by this method.

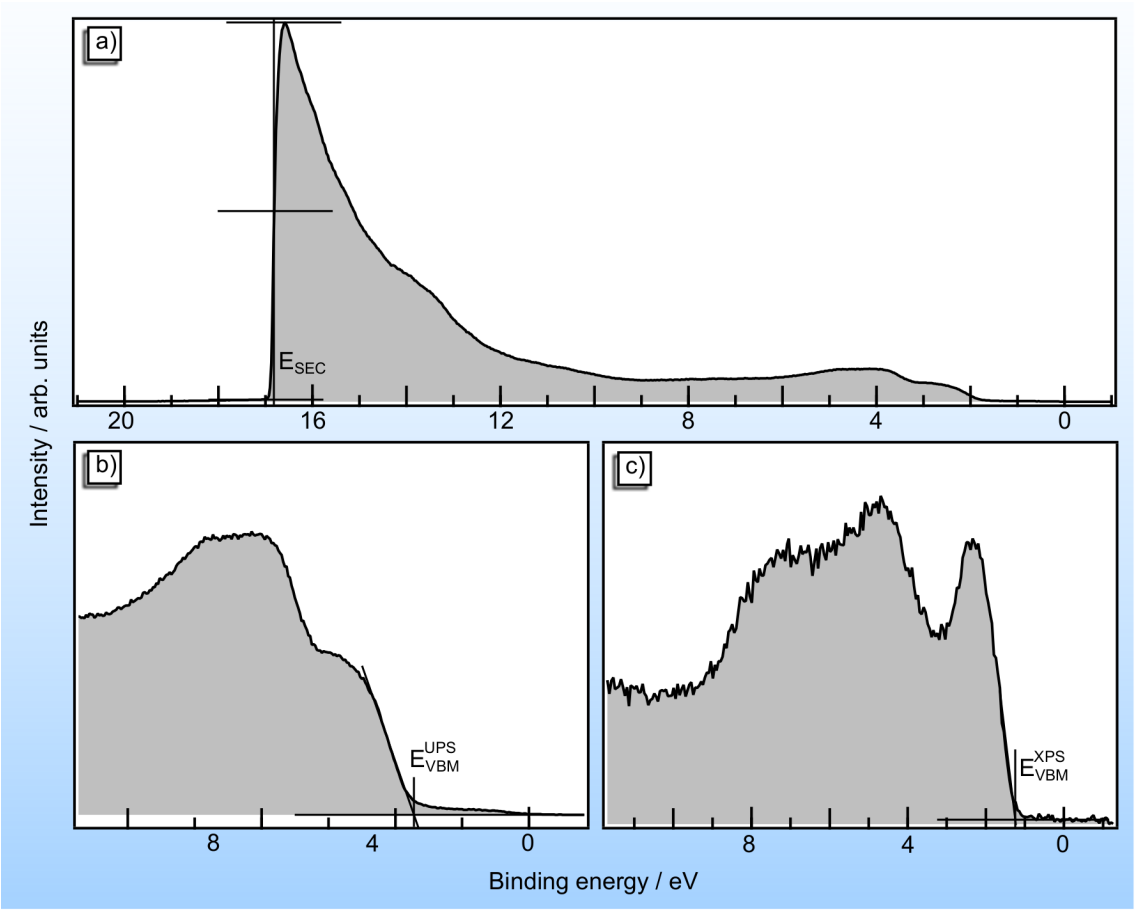

Figure 3.5: The valence band region of hematite measured by UPS and XPS.

In Figure 3.5a) a complete UP spectra is shown after bias correction. The most prominent feature on the left hand side is the secondary electron cut-off. It's energy E_{SEC} is defined to be the position on the x-axis of the center of the sharp onset.

This point can be found by determination of the highest and lowest point of the edge and calculation of the middle position. From this value the work function can be calculated. As these electron are scattered so many times that they are barely able to leave the sample their kinetic energy is zero. Without bias they would not be able to reach the detector. The knowledge of their energy allows for the use of Equation 2.6 in order to calculate the work function.

3.3.2 Interface experiments

An interface experiment is a combination of sample preparation/modification and characterization by PES. The general procedure has been introduced in Chapter 2.3.2. At this point, only the deposition parameters for the different contact materials will be shown.

In general, the binding energies have been extracted using the procedures introduced in the previous part. For the interface experiments to ITO and NiO a slightly different procedure was necessary. A clarification is included in the discussions in Chapter 7.3.3 and Chapter 7.3.2.

For most interface experiments the contact films were sputtered onto hematite on a platinum coated substrate. For these substrates the deposition parameters can be found in Table 3.3. Only in the case of the interface to $SrTiO_3$ this was not the case. Here, hematite was grown onto the substrate. This is clarified in Chapter 7.3.4.

For the other interface experiments the deposition conditions of the contact films can be found in Table 3.4. These are standard parameters within the DAISY-MAT lab at TU Darmstadt and have been used previously for interface experiments with other materials. This allows for a better comparison of one experiment to the other.

Table 3.3: Deposition conditions for the hematite substrates in interface experiments

Parameter	undoped Fe_2O_3			Zr-doped Fe_2O_3		
	RuO_2	NiO	ITO	RuO_2	NiO	ITO
Power Fe/ W	(RF) 60					
Fe Target distance / cm	8					
Power Zr/ W	-			30		
Dopant Target distance / cm	-			10		
Substrate	QP	ITO-glass		QP		
Oxygen content / %	30		7	8		
Deposition time / min	20	30				
Temperature / °C	400					
Pressure / Pa	0.5					
Further oxygen annealing	no	yes		no		
Annealing Temperature / °C	-	400		-		
Annealing time / min	-	100	250	-		

Table 3.4: Deposition conditions for the contact materials in interface experiments

	ITO	RuO_2	NiO	Fe_2O_3
Target	ITO (10 %Sn)	Ru	Ni	Fe
Power / W	25 (RF)	5 (DC)	40 (DC)	60 (RF)
Taret distance / cm	10	9.4		8
Temperature / °C	RT			400
Oxygen content / %	0	7.5	20	8
Pressure / Pa	0.5			

3.3.3 Raman Spectroscopy

Raman measurements were initially performed on a Horiba LabRam HR Raman/FT-IR spectroscope HR800. This spectroscope is operated and maintained by Prof. Dr. Riedel's working group "Dispersive Solids" of the Materials Science Department at TU Darmstadt. The opportunity to use the machine is gratefully acknowledged. It exhibits an Argon multiline laser with available wavelengths of 488 nm, 514.5 nm and 633 nm. The 514.5 nm emission was chosen to be used within this work.

A defect within the laser system made the spectroscope unavailable for some time. Luckily, it was possible to use another spectroscope (Witec Alpha300 R confocal Raman microscope) which is operated by Prof. Dr. Stark's working group "Physics of Surfaces" of the Materials Science Department at TU Darmstadt on short notice. This opportunity is gratefully acknowledged as well. Here, a ND:YAG laser with a wavelength of 532 nm was used.

3.3.4 X-Ray Diffraction

XRD measurements on amorphous and polycrystalline samples were carried out in $\theta-2\theta$ geometry in a Seifert XRD 30003 PTS-3 using Cu K_α radiation. In addition to conventional $\theta-2\theta$-measurement Grazing Incidence X-Ray Diffraction measurement were performed as well in order to optimize the low intensity of the thin films. These measurements were carried out under an angle $\Omega = 5°$. For epitaxial samples ϕ-scans were performed on a STOE 4 circle diffractometer. Here, Cu K_α radiation was used as well.

All measurements have been performed by Dr. Joachim Brötz from Prof. Dr. Donner's working group "Structure Research" of the Materials Science Department at TU Darmstadt. His efforts in the acquisition and interpretation of the data is gratefully acknowledged.

3.3.5 Thickness Determination

The thickness of the thin films was determined from measurements with a Dektak XT Advanced System Profilometer. By moving the needle from the thin film onto the substrate the height of the edge can be measured. In order to receive better statistics several measurements per edge were being conducted. It was taken care that the measurement did not take place too close to the corners or in regions were the microscopic picture during the measurement showed poor film quality.

With three measurements per edge it was possible to obtain up to twelve measurements per sample. The mean value of these measurements was then used as film thickness. The margin of error of this method can be assumed to be at least 10 % of the mean value. In some cases the standard deviation of the mean value exceeded the 10 % mark. In these cases the higher value was taken as error of the film thickness.

The profilometer is being operated and maintained by the group of Prof. Dr. Ensinger "Materials Analysis" of the Materials Science Department at TU Darmstadt. The opportunity to use this machine is gratefully acknowledged.

3.3.6 Optical Spectroscopy

The optical properties of the thin films were measured with an Agilent Cary 7000 Universal Measurement Spectrophotometer.

This spectrophotometer features a deuterium lamp for the UV and a quartz-iodine (halogene) lamp for the Vis/NIR regime. Depending on the photon energy the detection of transmitted or reflected light is achieved by either a Si or an InGaAs detector. By using bare quartz or sapphire as substrate it was possible to measure both, transmission and reflection spectra. The typical measurement range was 250 nm to 2500 nm with a step width of 1 nm.

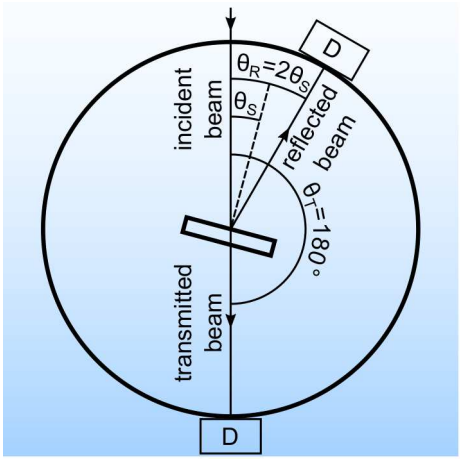

Figure 3.6: Geometry of measurements in the Agilent Cary 7000.

As shown in Figure 3.6 the machine allows for the rotation of the sample by a certain angle θ_S. This sample angle is being measured between the incident beam and the sample normal. For the reflection measurement the detector is positioned at an angle $\theta_R = 2\theta_S$. The transmission measurement is always performed at an angle of $\theta_T = 180°$.

The reflection measurement is being performed at an angle which correlates to the spectral reflection. Besides, diffuse reflection can also appear. The detector was used with an aperture which showed an opening of 6°. It was shown that for the sputtered hematite thin films no diffuse reflected or scattered light can be found at other positions than $\theta_R = 2\theta_S$ and $\theta_T = 180°$. The reflection measurement is, therefore, a measurement of the total reflection.

Hence, it is possible to assume that the sum of the reflected light R, the transmitted light T, and the absorbed light A equals unity: $R + T + A = 1$. From this the absorption coefficient α was calculated using the film thickness d with equation 3.2. The cosine considers the longer way of the transmitted beam through the sample due to the rotation.

$$\alpha = -ln\left(\frac{1-R}{T}\right) \times \frac{1}{d \times cos(\theta_S)} \tag{3.2}$$

3.3.7 Conductivity measurements

Conductivity measurements were performed in a home-built setup as described in Chapter 2.3.5. For the measurements it was necessary to contact the samples with platinum contacts. These contacts had to cover the edges of the samples as well. In order to sputter deposit the contact onto the sample in a Quorum Q300T D sputter coater shadow masks on sample holders in a 45° angle were being employed.

The sputter coater is being operated and maintained by the group of Prof. Dr. Ensinger "Materials Analysis" of the Materials Science Department at TU Darmstadt. The opportunity to use this machine is gratefully acknowledged.

The conductivity measurements itself were being performed at elevated temperatures and in different atmospheres. These parameters are part of the discussion of the results of the measurements. Hence, they can be found there.

4 Setting the baseline - Phase verification

The determination of any property of a material depends strongly on the quality of the samples that are available. A good knowledge about properties such as e.g. composition and structure is crucial in order to extract usable information from any sample. In order to prepare samples with the right structure and composition, the work was started with a study on the dependency of the iron oxide phase on deposition parameters such as oxygen partial pressure and temperature. The results can be seen as the fundament of any further characterization and modification. It is, hence, straight forward to start with thi part of the work.

Important aspects of this chapter

- ... more than 6 % oxygen in the sputter gas gives Fe_2O_3
- ... for sample temperatures of 300 °C and higher the samples crystallize
- ... epitaxial growth is possible on sapphire with different orientations
- ... shape of spectra depends strongly on the crystallinity
- ... the optical band gap is about 2.2 eV
- ... the Fermi level is within 0.8 eV to 1.6 eV above the valence band
- ... the work function is between 5.2 eV and 5.8 eV and the ionization potential $\sim$ 6.6 eV
- ... the distance of the valence band to the $Fe2p_{3/2}$ core level is 709.5 eV
- ... the distance of the valence band to the O1s core level is 528.4 eV

4.1 Oxygen partial pressure dependencies

The phase of an oxide material deposited by means of reactive sputtering depends among other parameters strongly on the oxygen partial pressure in the sputter gas. The two possible choices for a target were either metallic iron or iron oxide of different composition. For the latter case the oxygen partial pressure in the chamber depends on the sputter rate as well as on the composition of the added gas. This complicates the precise adjustment of this crucial parameter. Using a metallic target, however, solves this issue as oxygen has to be added as gas in any case. Hence, the control of the oxygen content is facilitated.

It was, therefore, decided to only use metallic targets over the course of this work. Please note, that the oxygen needed for fully oxidized samples is depending on the sputter rate and, therefore, on the power that is applied to the target. It was decided to use the same power of 60 W at the iron target for all depositions within this work.

In order to find an oxygen partial pressure, where hematite would be formed, samples were deposited with different gas composition. All samples were deposited at 400 °C. The results of the structural characterization by means of XRD and Raman Spectroscopy are shown in Figure 4.1.

For a very low oxygen content of 1 % the X-ray diffraction pattern in Figure 4.1a) shows reflections from both, cubic iron and magnetite Fe_3O_4. The former has been identified with the help of the pdf-card 6-696 while for the identification of the latter the pdf-card 1-1111 has been used. The intensity of the most intense reflection, originating from the iron phase and marked with an asterisk has been manually cut in order to make the other reflections visible on this scale. The corresponding Raman spectrum in Figure 4.1b) shows peaks that are characteristic for magnetite while for the cubic iron no first order Raman modes exists as all atoms sit on inversion centers.[143, 144, 153, 154]

Increasing the oxygen content to 5 % eliminates the metallic iron in both XRD pattern and Raman spectrum. Now, both techniques show a composition of magnetite and hematite. Please note that for the Raman spectrum only the peak at 660 cm^{-1} is related to magnetite.

Later, it will be argued that this peak origins from a initially Raman forbidden phonon scattering process that becomes Raman active due to symmetry disorder [1]. Here, however, the XRD pattern clearly shows magnetite which allows for the assignment of this mode to originate from this phase. For the identification of magnetite the same pdf-card as for the 1 % sample was used, while the hematite phase was identified with the pdf-card 84-307.

[1] Please see in 4.2.3 Figure 4.9 and in 6.1 Figure 6.1

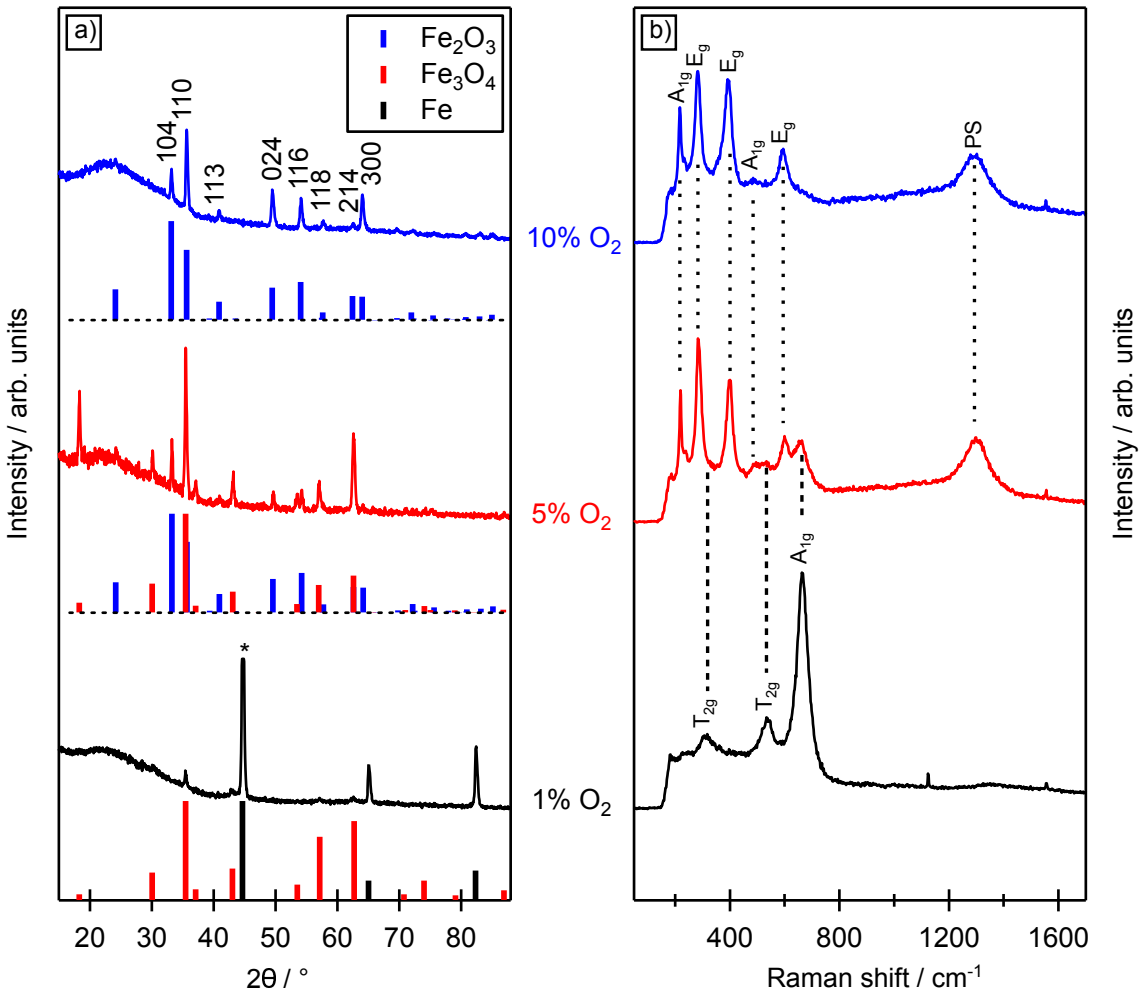

Figure 4.1: Structural characterization of iron oxides deposited with different oxygen partial pressures in the sputter gas by a) GIXRD and b) Raman Spectroscopy. XRD reflections were identified with the help of the pdf-cards 6-696 (Fe), 1-1111 (Fe_3O_4), and 84-307 (Fe_2O_3).

For 10 % oxygen in the gas phase pure hematite samples are deposited. Both, XRD and Raman spectroscopy show only signals which correspond to $\alpha - Fe_2O_3$. The XRD pattern shows an enhancement of the (110) reflection with respect to the (104) reflection which is most prominent in the powder file of the pdf-card. This indicates that a preferred (110)-orientation is associated with the sputtered hematite thin film.

With the knowledge of the structural characteristics of the samples the development of the electronic structure with increasing oxygen content in the sputter gas can be observed by XPS. For this purpose Figure 4.2 shows core-level and valence band spectra measured by XPS and UPS.

The Fe2p spectra clearly show the change from the metallic iron containing sample to the phase pure hematite. In the spectra of the 1 % sample there are three features observable, which can be attributed to the three different oxidation states of iron in this sample.

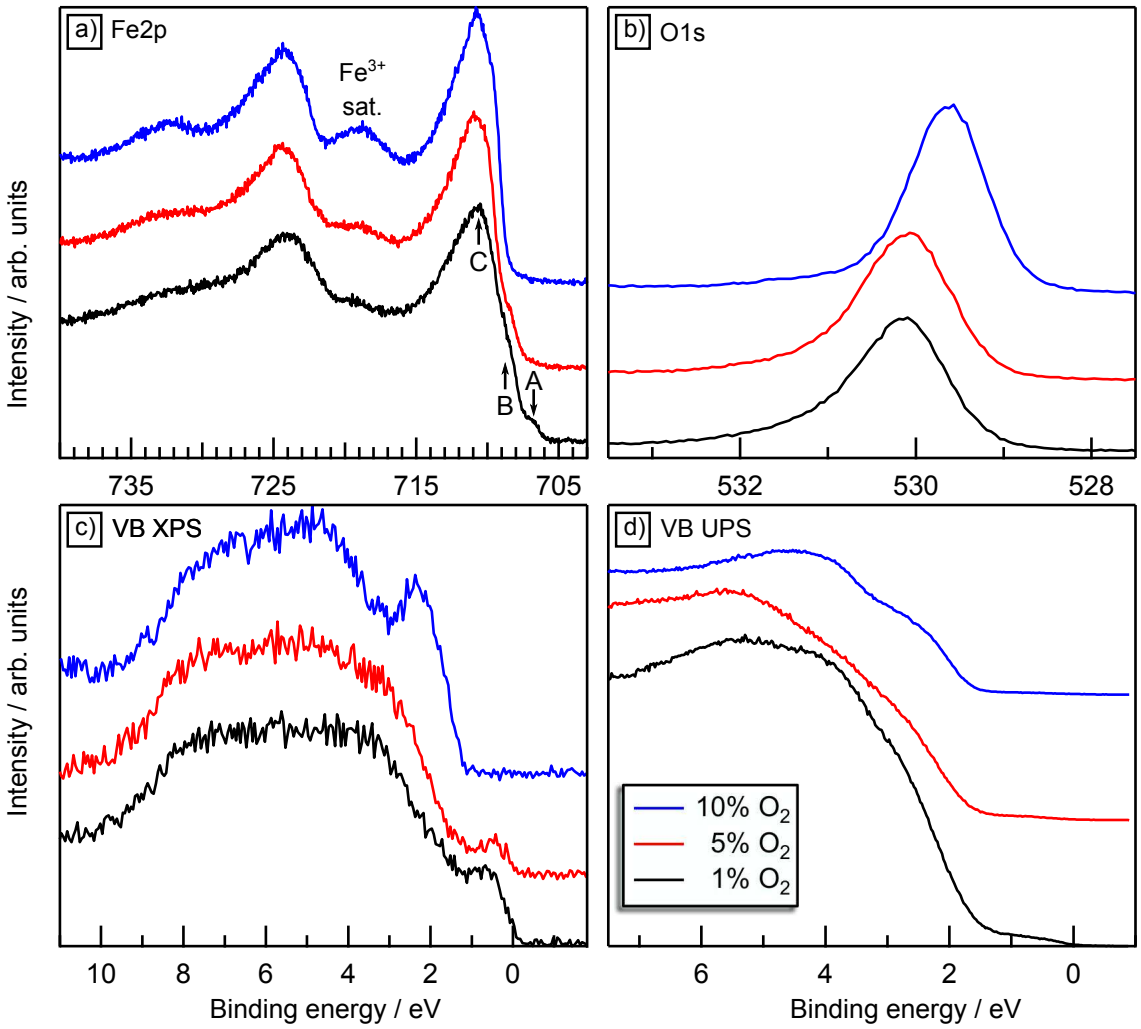

Figure 4.2: Characterization of the composition in dependence of the oxygen partial pressure. a) Fe2p-, b) O1s-, and c) valence band spectra measured by XPS and d) the valence band measured by UPS.

Namely, on the low binding energy side of the $Fe2p_{3/2}$ emission a shoulder is visible, which is labeled as A. This signal originates from the metallic iron in the sample.[125, 126] Besides the metallic iron there are two further emissions. Another shoulder at slightly higher binding energies labeled with B can be attributed to originate from Fe^{2+} cations and the main emission C arises from Fe^{3+} cations.[125, 126]

The existence of three different oxidation states in this sample can be explained by the two verified phases. Within one phase this situation would not be very likely as the Fermi level would need to be in the vicinity of two charge transition points[2]. In two phases, however, more oxidation states can occur.

As can be expected from the structural analysis the addition of more oxygen into the sputter gas results in the disappearance of the signal from metallic iron. In the 5 % sample

[2] See section 2.2.3

only the signals B and C are present. This observation can be expected from a mixture of Fe_2O_3 and Fe_3O_4 .

By adding 10 % oxygen into the sputter gas the signal B from Fe^{2+} cations vanishes as well. Now, the signal does only originate from Fe^{3+} cations. The strong satellite at about 718.5 eV is characteristic for Fe^{3+}.[129, 130, 155]

The O1s-peaks in Figure 4.2b) show a broadening of the signal of the mixed-phase samples compared to the phase pure Fe_2O_3 sample. The higher binding energies of these two emissions is expected for Fe_3O_4 containing samples compared to Fe_2O_3 as has been reported in e.g. Refs. [125, 126, 155] before.

The valence bands of the mixed-phase sample in Figure 4.2c) and d) both show a signal at the Fermi energy. This is expected for metallic iron and the low band gap material magnetite. The valence band of the 10 % sample shows the features for hematite e.g. the valence band maximum indicates a band gap. The electronic structure of the valence band of hematite will be discussed in Chapter 5.

As the desired material of this work was hematite, no efforts were undertaken to isolate the phases of magnetite Fe_3O_4 or wurtzite FeO. It should be possible to deposit these by choosing the right oxygen partial pressures. For Fe_3O_4 this would be less than 5 % as here there is already some Fe_2O_3 included in the films. For FeO the oxygen content should be even lower. Besides the control of the oxygen content, also the temperature at which the phase should be deposited has to be chosen accordingly.

The oxygen partial pressure, however, at which hematite is being formed was of interest for this thesis. The sputter rate of any deposition is drastically decreased by the addition of oxygen. It was, therefore, attempted to chose an oxygen partial pressure which results in a reasonable rate and phase pure samples.

Figure 4.3 shows $Fe2p_{3/2}$ and O1s core-level binding energies and Fermi level positions in dependence of the oxygen partial pressure. The colors indicate the present phases in the respective samples. A black dot represents a mixture of Fe and Fe_3O_4 , a red dot of Fe_3O_4 and Fe_2O_3 , and a blue dot of pure Fe_2O_3 . The phase composition of the sample represented by the green dot is unknown. As it is found at low oxygen contents it might be possible that FeO is included in this sample but this was not further investigated. Until 5 % the Fermi level is at zero binding energy which indicates that the samples contain metallic iron, wurtzite or magnetite.

With 6 % or more oxygen in the sputter gas hematite is being formed as a single phase. This was confirmed by Raman measurement on these samples. Additional XP and Raman spectra of samples deposited with higher oxygen contents in the sputter gas can be found

in Figures A1 and A2. Only for the highest oxygen concentrations the Raman measurement did not correspond to crystalline hematite. However, the satellite structure of the Fe2p emission indicated pure Fe_2O_3 . It will be shown in part 4.2.3 that the crystallinity of the samples has a great influence on the Raman spectrum.

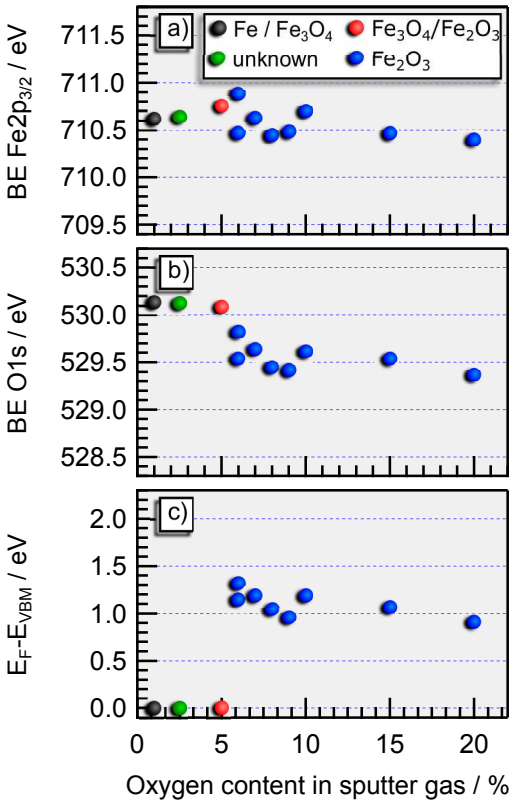

Figure 4.3: The dependency of the Fermi level position on the oxygen partial pressure.

The development of the phase is directly observed from the different behavior of the binding energies of the three samples that were deposited with less than 6 % oxygen. Increasing the oxygen partial pressures lead to changes of the binding energy of $Fe2p_{3/2}$ and O1s spectra. These are different from each other for the two core-levels.

As a consequence the core-levels show a different distance to the valence band maximum than samples which have been deposited with higher amounts of oxygen. This is expected, if a phase change occurs. In the present case, where there is even a phase mixture present, no constant distant of the core-levels to the valence band maximum can be expected.[134, 135]

At 6 % oxygen, however, the situation changes. Now, the binding energy values measured for $Fe2p_{3/2}$, O1s, and valence band maximum shift parallel and their relative position indicates that, both, $Fe2p_{3/2}$ and O1s have a constant distance to the valence band maximum of 709.5 eV and 528.4 eV, respectively.

After hematite is being formed the position of the Fermi level is almost independent on the oxygen content of the sputter gas. All values are between 0.9 eV to 1.2 eV. Considering the optical band gap of hematite to be 2.2 eV this indicates an intrinsic Fermi level position at mid-gap.[61, 64] This is somewhat surprising as undoped hematite in literature is described to be an n-type semiconductor. The reason for this misconception can be found in Chapter 8 and will be further discussed there.

The results from the structural and electronic characterization show that by a combined study of the three techniques the phase of the sample identified. Raman spectroscopy and XRD are both structural characterization techniques and it was shown that their results

show a very good agreement to each other. It was, therefore, decided that for most samples within this study a phase characterization by one of the techniques was adequate. For the sake of time and simplicity Raman spectroscopy was chosen to give a structural reference.

4.2 The influence of the temperature

Besides the oxygen partial pressure, which has been discussed in the previous section of this work, the temperature is an essential parameter for the development of the desired phase. In order to deduce the influence of heating on the structural and electronical properties of the samples several different approaches were chosen:

- Heated depositions at different temperatures
  In this straight-forward approach samples were deposited at temperatures between room temperature and 600 °C.

- In-situ (in vacuo) heating
  In these experiments the effect of annealing of room temperature deposited samples and heating at different oxygen partial pressures was tested, inside the vacuum chamber.

- Ex-situ heating of samples deposited at room temperature
  This work was based on the results of the in-situ heating process to assure high oxygen partial pressures while heating. It allows the structural characterization before and after the heating steps.

4.2.1 Deposition at heated substrates

In order to investigate the influence of temperature on the growth process samples were deposited at substrate temperatures ranging from room temperature (RT) to 600 °C. The oxygen content in the sputter gas was chosen to be within 8 % to 10 % to assure the formation of Fe_2O_3. The phase formed was confirmed by Raman measurements. The respective spectra are presented in figure A3 in the appendix. Figure 4.4 shows XP core-level and valence band spectra for these samples.

All samples show the same satellite structure which is characteristic for Fe_2O_3 and prove that iron has an oxidation state of +III.[125, 126] There are, however, some changes in the appearance of the Fe2p core-level spectra. These changes can be traced back to different substrate temperatures during deposition.

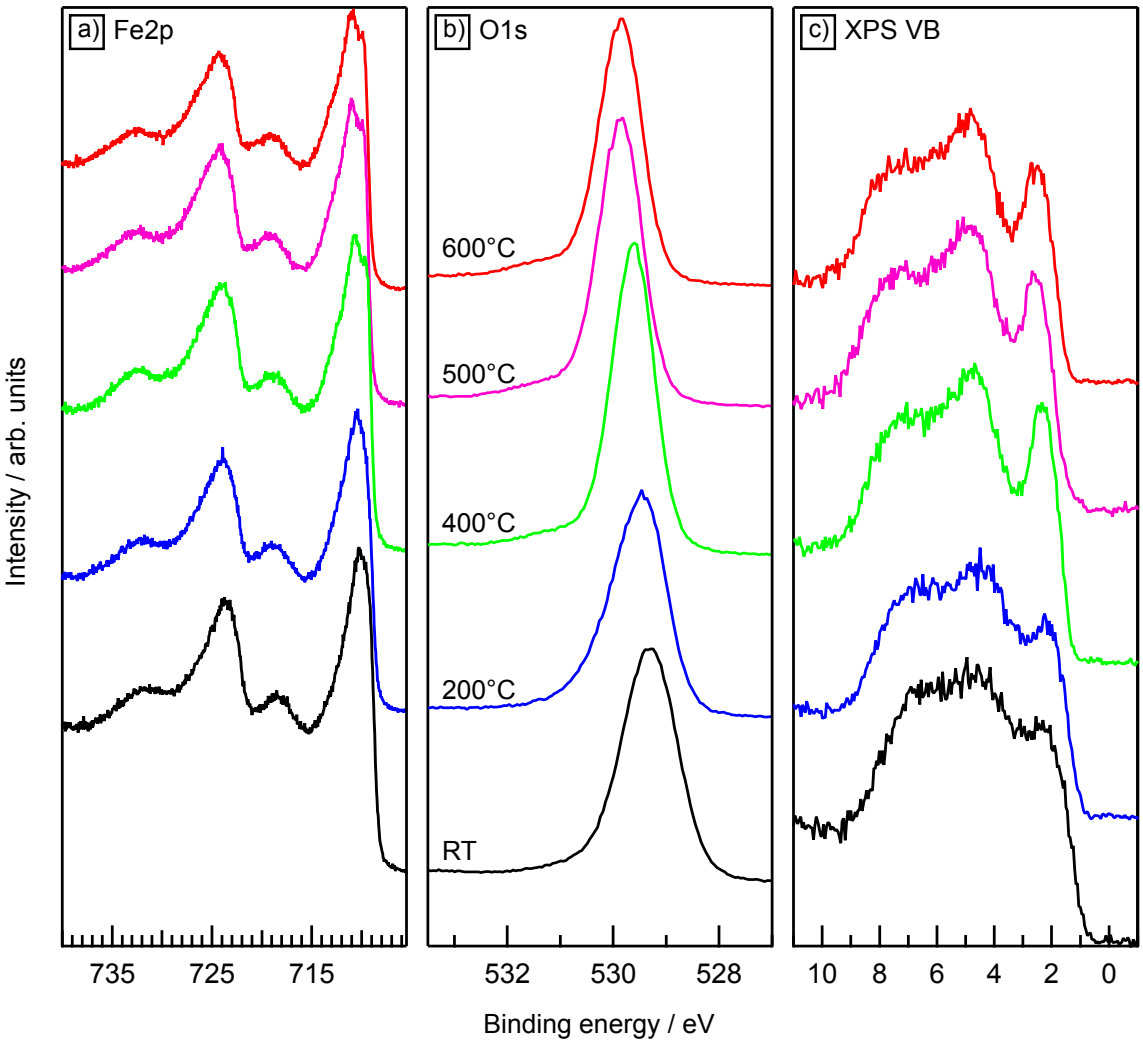

Figure 4.4: XP spectra of Fe_2O_3 samples in dependency of the temperature. a) Fe2p-, b) O1s-core-level, and c) valence band spectra.

For depositions at room temperature and 200 °C the top most part of the $Fe2p_{3/2}$-main line has a quite symmetric shape. At temperature of 400 °C and higher a shoulder to low-binding energies develops. This "pre-edge" has been discussed in literature to be only present in the bulk of hematite and originate from the ligand-field symmetry. In the top-most layer or once the symmetry and strength of crystal field splitting of the sample is overall lowered the "pre-edge" vanishes.[61, 156]

Its appearance can also be connected to the shape of the valence band. For the low temperature samples the valence band shows a plateau at about 2.5 eV. Deposition at higher temperatures results in the transition of the plateau into a peak. In addition, another peak appears at a binding energy of about 4.5 eV for higher temperatures . A detailed discussion on the electronic structure of the valence band and its connection to the shape of the $Fe2p_{3/2}$ main line can be found in Chapter 5.

The shape of the O1s core-level does not change with temperature. There is, however, a shift towards higher binding energies with higher temperatures. A similar shift can be found in the other spectra as well as is shown by the binding energies of the Fe2p$_{3/2}$- and O1s-core-levels and the valence band maximum in dependency of the deposition temperature in Figure 4.5.

It is evident that there is a trend to higher binding energies. This trend can be regarded to arise entirely from a shift of the Fermi level within the band gap as the positions of the core-levels and the valence band maximum are shifted parallel. Usually, such an observation indicates that the phase is not changed. Here, however, a change from amorphous (RT and 200 °C) to crystalline (above 400 °C) is present.

The parallel behavior of the three binding energies indicates that this structural change does not entirely change the bonding situation. Even though, there are some spectral changes as will be discussed in more detail in Chapter 5, the bonding situation between oxygen and iron cannot be changed completely upon crystallization.

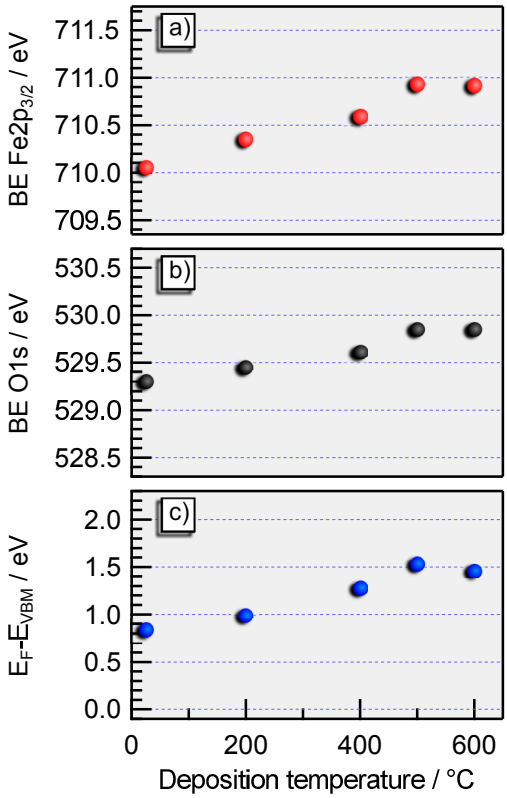

Figure 4.5: Temperature dependency of the binding energies of core-level and the Fermi level position.

The parallel movement of the binding energies allows for an extraction of a core-level to valence band maximum distance $E_{\text{CL-VBM}}$ for, both, Fe2p$_{3/2}$ and O1s. The values are determined to be 709.5 eV and 528.4 eV, respectively. They are identical to the values that have been extracted from Figure 4.3. As a consequence, they can be regarded to be a material property of hematite and can be used for the interpretation of the following interface experiments with undoped hematite samples.

The Fermi level positions are found within 0.85 eV to 1.5 eV versus the valence band edge. This covers about one third of the optical band gap of hematite of 2.2 eV. The values are, however, all centered around the mid-gap position at 1.1 eV of this optical band gap. This would result in intrinsic behavior of the material in disagreement with literature where hematite is generally being discussed to be an n-type semiconductor.[71, 157] The same was observed in Chapter 4.1 and will be discussed in more detail in Chapter 8.

4.2.2 In-situ heating

This part of the work explores the changes in the electronic structure upon heating samples inside the integrated system in pure oxygen. These experiments were performed by Céline Steinert as part of her Advanced Research Lab.

In difference to the previous parts of this chapter, no structural data will be discussed. Raman measurements revealed that after annealing the samples remain to be crystalline hematite. These spectra can be found in Figure A4 in the appendix.

However, it also became clear that one hour of heating in oxygen was not enough time to fully crystallize the samples. Besides, as the samples were deposited and annealed without leaving the vacuum the initial state after the deposition for each sample was not characterized by Raman spectroscopy.
It was, therefore, decided to plan an experimental series to verify the conclusions that were achieved from the in-situ experiments by characterizing the samples completely before and after annealing. This experimental series is presented in Chapter 4.2.3. The conclusion drawn there can be applied to this Chapter as well.

Figure 4.6 exhibits XP spectra from two sets of samples. Namely, the first were deposited on platinum coated quartz (spectra a)-c)) and the second on Pt(111) on sapphire(0001) (spectra d)-f)). All samples were initially deposited at room temperature with 10 % oxygen in the sputter gas. After the characterization by PES the samples were annealed at temperatures from 200 °C to 600 °C in 0.5 Pa oxygen for 1 h. Following the annealing step the samples were characterized by PES, again.

The observation, which could be made on this experimental series, agrees well with what was already found in Chapter 4.2.1. Upon heating the Fe2p$_{3/2}$develops a "pre-edge" towards lower binding energies which increases in intensity if the annealing temperature is higher. At the same time the valence band changes from a plateau-like structure at low temperatures to a two-peak structure. Both observations could be made on both substrates. It was, therefore, concluded that the annealing has to be the reason for these changes. Similar observations and more profound conclusions will be discussed in more detail in Chapter 4.2.3.

The high binding energy emission for the sample on quartz, which was heated at 200 °C, can be attributed to a carbon contamination on the sample after the heating step. The exact origin of this contamination is, however, unclear. Adsorbates on the surface of the sample might also be the reason for the clear shift of the O1s-spectrum of this particular sample.

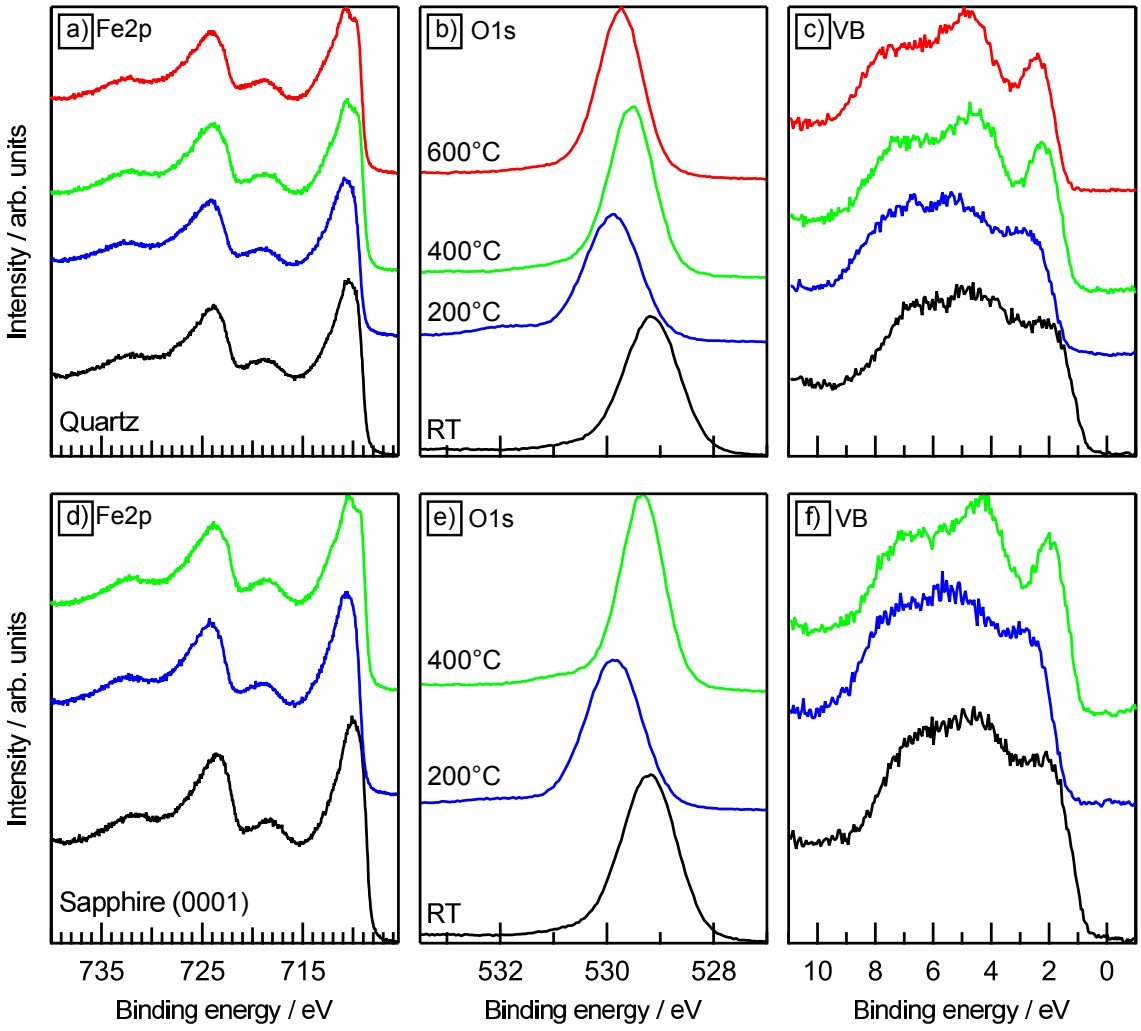

Figure 4.6: XP spectra of samples, which were deposited at room temperature and afterwards annealed in-situ. Spectra a)-c) are from samples on platinum coated quartz and spectra d)-e) from samples on Pt(111) coated sapphire (0001).

Besides the in-situ annealing in pure oxygen it was also tested how samples react to heating in reducing/oxidizing conditions. For this purpose, a sample was deposited at 400 °C (nominally, see below) with 9 % oxygen in the sputter gas. Then, this sample was heated at 400 °C for 16 h in an argon atmosphere. Afterwards, the same sample was heated again at 400 °C in pure oxygen for 16 h. After each step PES measurements were performed. For this purpose ITO coated glass was used as a conductive substrate. The resulting XP spectra are presented in Figure 4.7.

After the deposition the satellite structure of the $Fe2p_{3/2}$ emission clearly shows the expected position for Fe^{3+}.[125, 126] This changes upon heating in argon atmosphere. Now, the satellite's intensity is dramatically reduced. Additionally, a new shoulder appeared on the low binding energy side of the $Fe2p_{3/2}$ main line (marked with an arrow). The reduction of the satellite's intensity and the presence of this shoulder can both be explained by the formation of Fe^{2+} within the sample.[58, 125, 126]

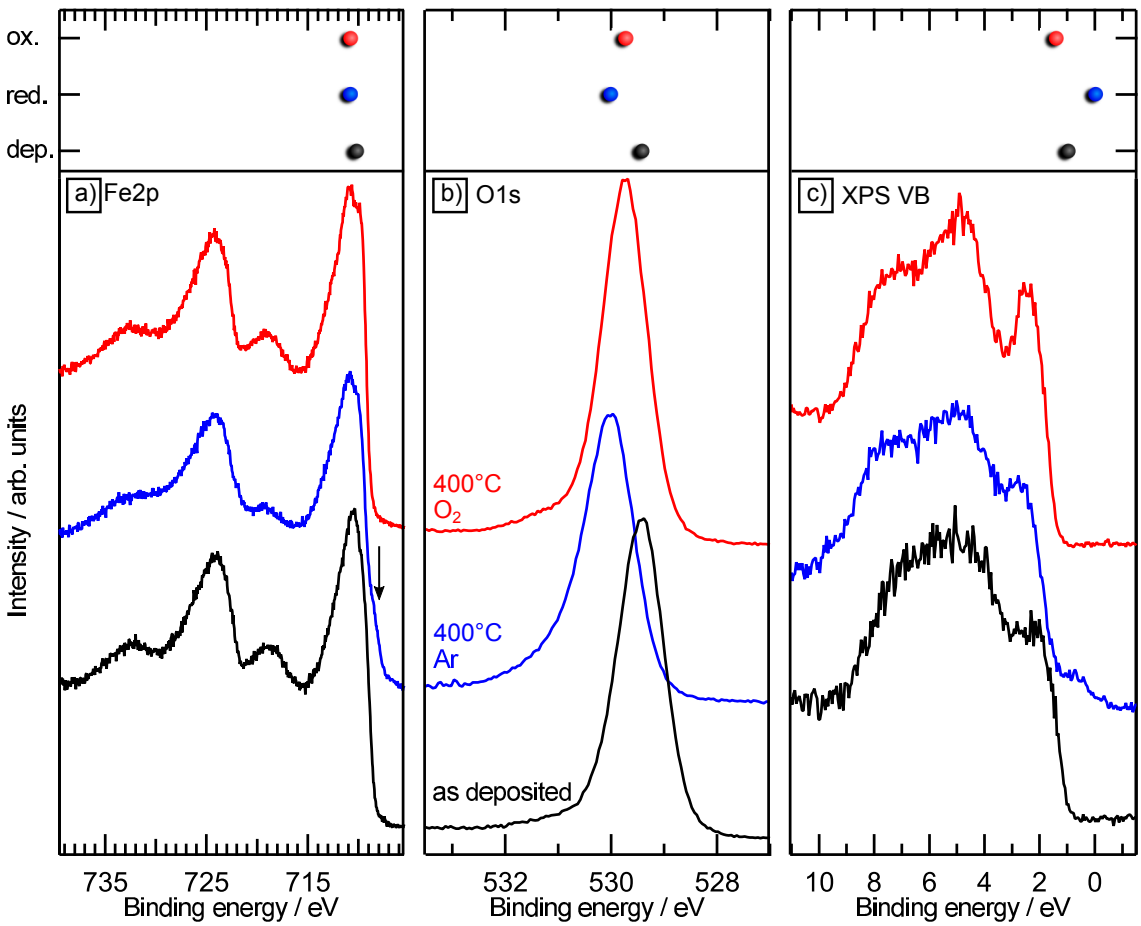

Figure 4.7: XP spectra of a sample after deposition [400 °C, 9 % oxygen] (bottom), after heating under reducing conditions [400 °C, Ar, 16 h] (middle), and after heating in oxidizing conditions [400 °C, O_2, 16 h] (top). In addition to the spectra the respective binding energies are shown above.

Heating in oxygen removes the low binding energy shoulder again and restores the satellite structure. In addition, the sample develops the characteristic "pre-edge" that can be assigned to the formation of crystalline hematite.[61, 156]

It has to be noted that in the previous and following parts of this thesis the "pre-edge" always appeared for depositions at 400 °C. The reason for the absence in this case can be found in the substrate. In difference to the quartz or sapphire substrate, which have been used for the vast majority of the other parts of this thesis, here, ITO-coated glass was used.

The substrate, however, can have an influence on the real temperature of the deposition. In our lab, a halogene light bulb below the sample is being used for heating. Temperature calibration is done by using a calibration sample with a thermocouple to measure the temperature on this particular substrate at a certain current.

There are huge difference between substrates. Namely, material, crystallinity, and thickness are sources of major influence for the real temperature on the substrate. In general,

thin substrates like quartz and sapphire (0.5 mm) show higher temperatures than thick substrates like ITO-coated glass (1.1 mm). For substrates with similar thickness the structural properties are essential. Single crystals usually show higher temperatures than amorphous substrates.

The current for this particular deposition on ITO-covered glass was 6.3 A which is about the same current that is usually used to achieve 400 °C on a quartz substrate. It can, therefore, be assumed that the real temperature during the deposition was lower than 400 °C which explains the absence of the "pre-edge".

The heating treatments, however, were done in a different chamber with a more recent calibration. Hence, the 400 °C in these cases are expected to be exact and explain why after excessive heating the sample crystallized. As here the heating time was also much longer than for the samples presented in Figure 4.6 it also becomes clear that for these samples the heating time was just not enough to fully crystallize the samples.

The heating in argon is accompanied by a shift of the O1s-spectrum in comparison to the as deposited case. At the same time, the valence band smears out to the Fermi level at 0 eV. Heating in oxygen removes the smeared-out part of the valence band and shifts the oxygen peak back to lower binding energies. The different appearance of the valence band compared to the spectrum after the deposition has the same origin as the "pre-edge" in the $Fe2p_{3/2}$-spectrum.[61]

While the smeared-out part of the valence band can be explained by the presence of Fe^{2+}-states the shift of the oxygen emission is more complex. A shifting of a peak to higher binding energies can have several reasons. In this case, two different reason have to be considered:

- Shift of the Fermi level to higher positions
- Formation of a new phase at the surface

In the following it will be shown, that both reasons contribute to the shift of the O1s-emission and are connected to the presence of the Fe^{2+}-emission as well. For this purpose difference spectra of the spectra in Figure 4.7 will be used. These are presented in Figure 4.8. The spectra in a)-c) compare the spectra of the reduced sample to the as deposited sample, while the spectra in d)-f) compare the oxidized sample to the as deposited sample.

In order to create these difference spectra the following procedure was used. First, the O1s emission was considered. Here, the intensity and position of the spectrum from the sample after deposition was adjusted in order to get a good agreement with the low-binding energy onset of the other O1s-spectrum.

The shift which was extracted from the O1s-core-level was then used for the Fe2p- and valence band difference spectra as well. In order to achieve a good agreement with the reduced sample the spectrum from the as deposited sample had to be shifted towards higher binding energies by 0.55 eV. In case of the oxidized sample a shift of 0.31 eV in the same direction was necessary.

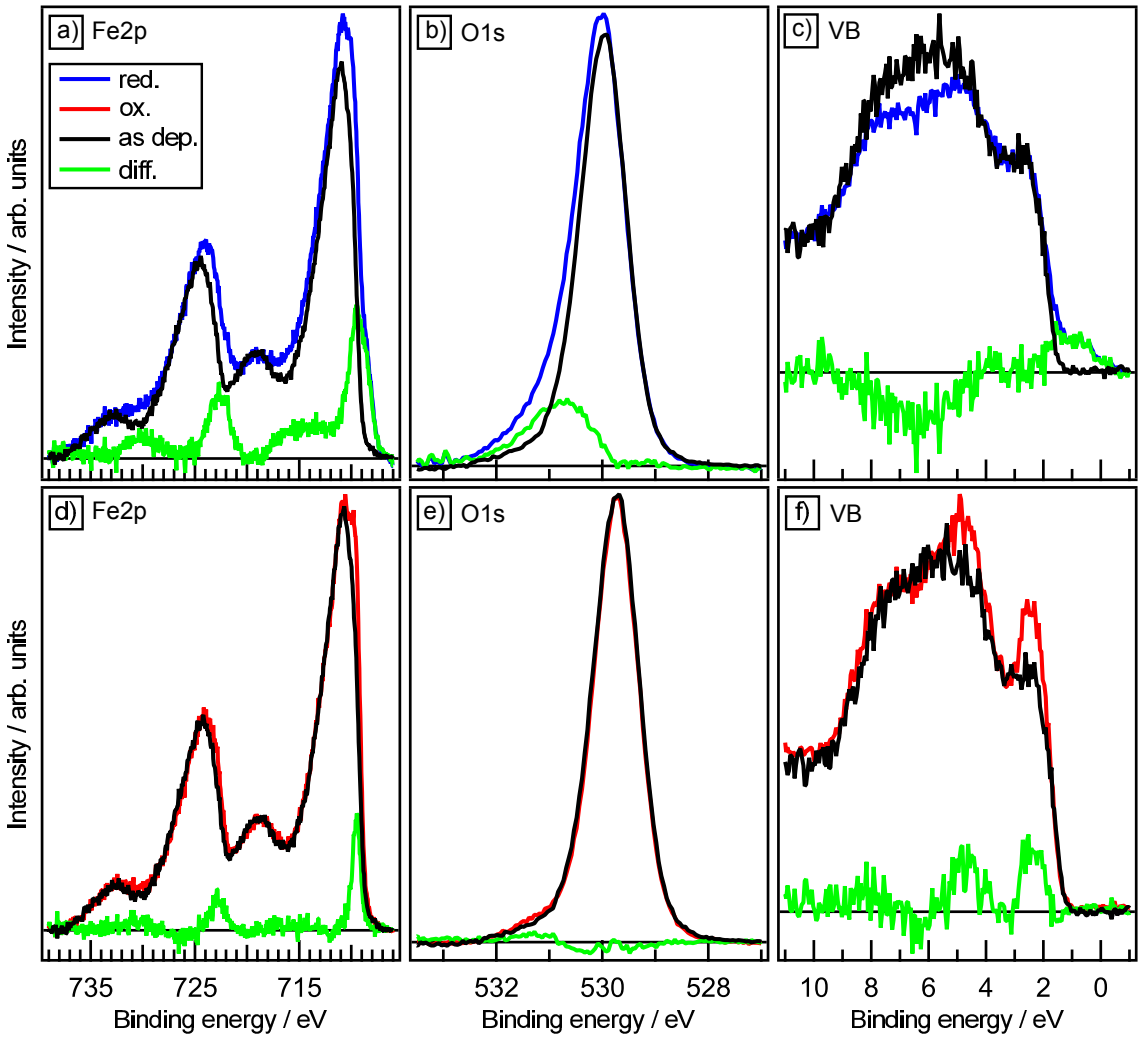

Figure 4.8: Difference spectra comparing the spectra from Figure 4.7. The spectra after heating under reducing/oxidizing conditions are compared to the spectra after deposition.

The Fe2p difference spectrum was extracted by adjusting the intensity to match the intensity at the position of the Fe^{3+}-satellite. This procedure was chosen in order to extract the difference in the oxidation state of iron upon the heat treatments.
Finally, the valence band difference spectra were created by adjusting the intensity. Here, it was tried to find a good match on the left hand side at about 8 eV to 11 eV and for the upper part of the onset of the valence band around 2 eV.

The difference between the Fe2p-spectra of the reduced and as deposited samples clearly resembles the spectrum that would be expected from a Fe^{2+}-compound.[126, 129, 130, 158–160] In the O1s-spectrum after reduction a second oxygen emission appears. Finally, the valence band shows a smaller intensity between 4 eV to 8 eV in addition to the smeared out part at the Fermi level.

All these findings indicates that several changes appeared while the sample was heated. First, the additional oxygen emission can be explained by the presence of another phase. This reduced phase does most likely contain the Fe^{2+}-cations and is responsible for the smeared-out part of the valence band as well.[60, 161] As the intensity of the changes is still small it can be assumed that this phase has mainly formed at the surface.

Besides the formation of the second phase the spectra of the as deposited sample had to be shifted by 0.55 eV towards higher binding energies. This parallel movement shows that the Fermi level has indeed been shifted. The reason can be a crystallization of the sample due to heating[3] and/or the change in defect concentration due to the reducing environment in which the sample was heated. Following this argumentation it can be stated that after heating in reducing conditions the sample consists of a bulk hematite phase with a Fermi level position of about 1.5 eV and a reduced phase at the surface which is responsible for the smeared out emission at the valence band maximum.

Heating in oxygen removes any changes, which appeared in the oxygen spectrum due to the reducing conditions. Also, the difference between the Fe2p-emission is changed as well. Now, the only difference is the additional "pre-edge" that was already discussed above. There are no traces of Fe^{2+} to be found anymore. It is, therefore, concluded that the reduced surface phase has been completely removed by heating in oxygen. The difference in the valence bands lies purely in the two peaks that evolve. For these peaks it will be shown in chapter 5 that their presence is connected to the existence of the "pre-edge" and is characteristic for well-defined crystalline hematite.

In Chapter 8 the formation of Fe^{2+} will be connected to the position of the Fermi level. It will be concluded that for Fermi level positions above 0.75 eV a reduction of Fe^{3+} to Fe^{2+} occurs. This Fermi level position corresponds to the charge transition energy of this particular reaction. The Fermi level position of 1.5 eV in the bulk hematite after reductive heating, however, does not agree with the formation of Fe^{2+} if the same argumentation that will be used in Chapter 8 applies.

In thermodynamic equilibrium there should no formation of Fe^{2+} without the Fermi level having reached the Fe^{3+}/Fe^{2+} charge transition energy. However, the studies[4] on

[3] Please see Figure 4.5
[4] Please see Chapters 7.1.2, 7.2, and 7.3.3

which the conclusion in Chapter 8 is based have been performed at room temperature while here, the sample was heated. Also, as the Fe^{2+} species are considered to be within a different surface phase their presence might be possible even with a lower Fermi level.

Different scenarios are imaginable. First, it might be possible that during heating oxygen vacancies at the surface are created which are then compensated by the formation of Fe^{2+}. This defect mechanism would not be expected in the studies presented in Chapter 8 but could be possible at elevated temperatures. While cooling no oxygen would be present to replace the oxygen vacancies a reduced phase at the surface would be created.

Also, it could be possible that during the heating process the Fermi level at the surface actually reached a charge transition level[5] and, therefore, Fe^{2+} was created. At the higher temperatures, however, a reorganization of the lattice involving oxygen ion transport due to the presence of Fe^{2+} might be possible which would again result in the reduced phase. The question which of these two possibilities really occurred or whether even another mechanism was involved was not further studied and cannot conclusively being answered.

4.2.3 Ex-situ heating

After the observation of changes in the electronic structure upon heating for in-situ conditions the stability and formation conditions of well defined Fe_2O_3 samples were further investigated. For this purpose samples were deposited at room temperature with 8 % oxygen in the sputter gas. Following the deposition, the samples were characterized by PES, Raman, XRD, and NIR-UV/Vis Transmission/Reflectance Spectroscopy. Then, the sample were annealed in a tube furnace in air at different temperatures for 5 h and characterized by the same techniques again.

The work allowed for a valid interpretation of the valence band electronic structure.[61] Here, only the results from the characterization techniques are presented. The interpretation of the electronic structure of the valence band can be found in Chapter 5.

Raman measurements were performed before and after heating the thin films in air. The spectra could be used to identify the iron oxide phase and structural properties of the thin films. They are shown in Figure 4.9.

The left hand part of Figure 4.9 shows spectra from samples that have just been deposited without further annealing and after annealing at 200 °C. Both spectra are rather similar. They do, however, strongly differ from the spectra that are presented in the right hand part of Figure 4.9.

[5] Please see Chapter 8 for further insight.

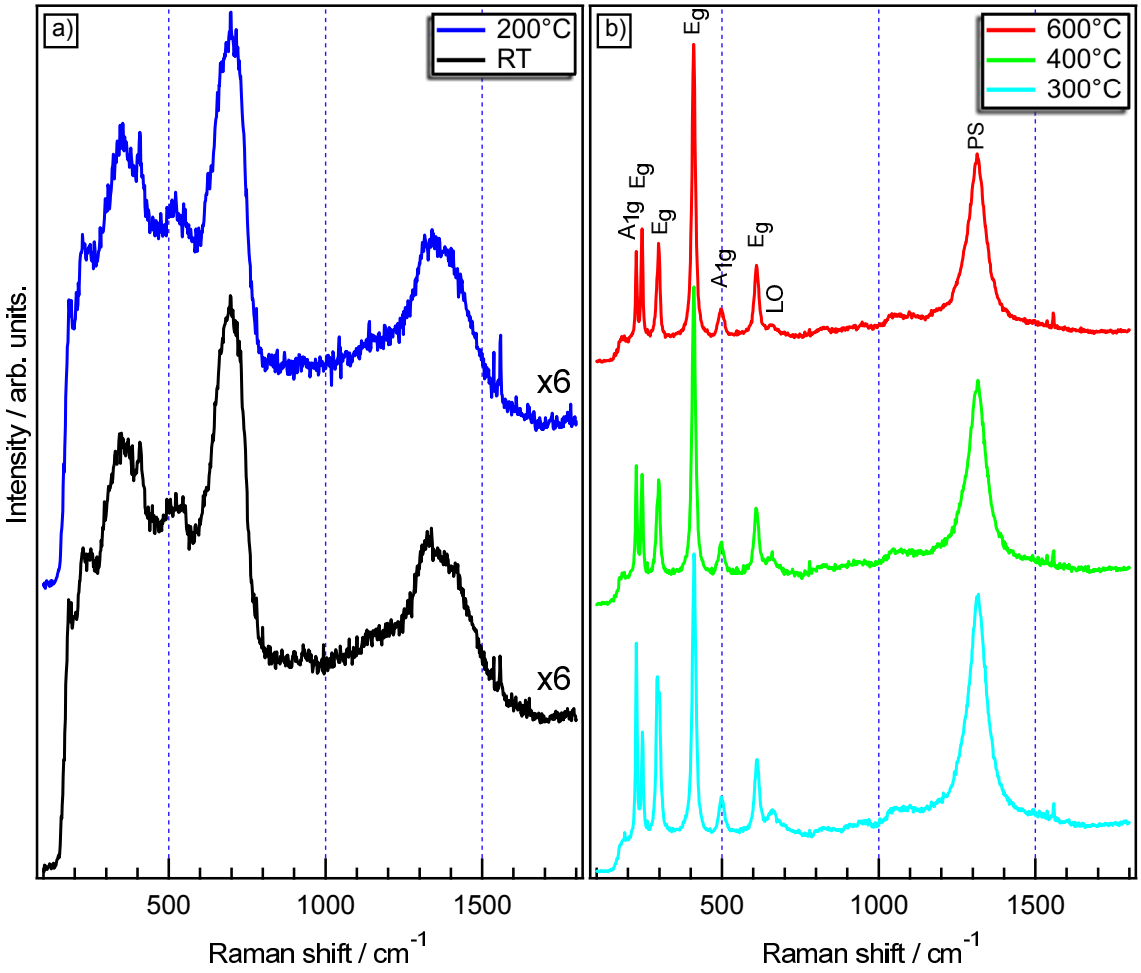

Figure 4.9: Raman spectra of samples that were a) deposited at room temperature and annealed in air at 200 °C and b) annealed at higher temperature in air.

In the former, broad peaks can be found at 335 cm^{-1}, 505 cm^{-1}, 720 cm^{-1} and 1365 cm^{-1}. The intensities of these spectral features are rather low and were multiplied with a factor of six in order to be of the same intensity as the spectra in Figure 4.9b).

Similar spectra have been observed for amorphous iron(III) oxides before.[162] The emission at 720 cm^{-1} has been assigned to be characteristic for the maghemite phase $\gamma-Fe_2O_3$.[141, 144, 163] The peak at 411 cm^{-1} stems most likely from trace amounts of hematite.

After annealing at 300 °C or higher the samples show completely different spectra. Now, sharp emissions are observed at 225 cm^{-1} (A_{1g}), 245 cm^{-1} (E_g), 298 cm^{-1} (E_g), 411 cm^{-1} (E_g), 499 cm^{-1} (A_{1g}), and 612 cm^{-1} (E_g). These lines are characteristic for hematite.[141, 143, 144] In addition, a broader peak at 1310 cm^{-1} appears which can be explained by phonon scattering and which is characteristic for hematite, as well.[164, 165]

A quite small signal can be observed at 660 cm^{-1} which is labeled with LO. It appears to be decreasing with increasing annealing temperature. This band is controversially discussed in literature.

It was often assigned to origin from trace amounts of foreign iron oxide phases. This assignment is based on the fact that both, magnetite and maghemite exhibit Raman modes in the close vicinity of 660 cm^{-1}.[166] Most often, magnetite is being argued to be present in literature.

On the other hand, it was also discussed by various authors to originate from phonon scattering as well. The corresponding mode would be Raman forbidden but IR-active in a perfect crystal. Due to disorder, however, the mode becomes observable in Raman as well. The argumentation by these authors seems valid as they were unable to detect traces of other phases by other methods such as Mößbauer-Spectroscopy, XRD, and XPS.[144, 164, 166–172]

Following this argumentation the small signal is being attributed to the longitudinal optical (LO) E_u phonons, which is usually only IR-active. The change to lower intensity can be seen as an indication for increasing the symmetry within the sample. This seems to be reasonable regarding the fact, that both, XRD and XPS data, shown in Figure 4.10 and Figure 4.11, do not show any evidence for an additional phase.

One detail to notice is the changing intensity ratio of the two leading peaks with increasing annealing temperature:

After heating at 300 °C the first peak (A_{1g}) is more intense than the second (E_g) whereas due to the annealing at 600 °C the opposite is the case. For the sample heated at 400 °C both peaks show the same intensity. The changes in intensity ratio can be explained by changes in the texture of the thin film with increased orientation films for higher annealing temperatures.[165, 173, 174]

X-Ray diffraction patterns from $\theta - 2\theta$-scans are shown in Figure 4.10. Again, the left hand side a) of the figure shows the diffraction pattern of a non-heated and 200 °C annealed sample. In b) the diffraction pattern for samples which were annealed at higher temperatures are presented. Additionally, reflection angles for hematite and platinum from pdf-cards are represented as bar graphs on both side of the figure.

Both samples in Figure 4.10a) show mainly reflections originating from the platinum substrate. These reflections are labeled with asterisks for all diffraction patterns. However, in addition one small (110) reflection from the hematite phase at 35.7° can be observed. This agrees well with the presence of a characteristic peak from the hematite

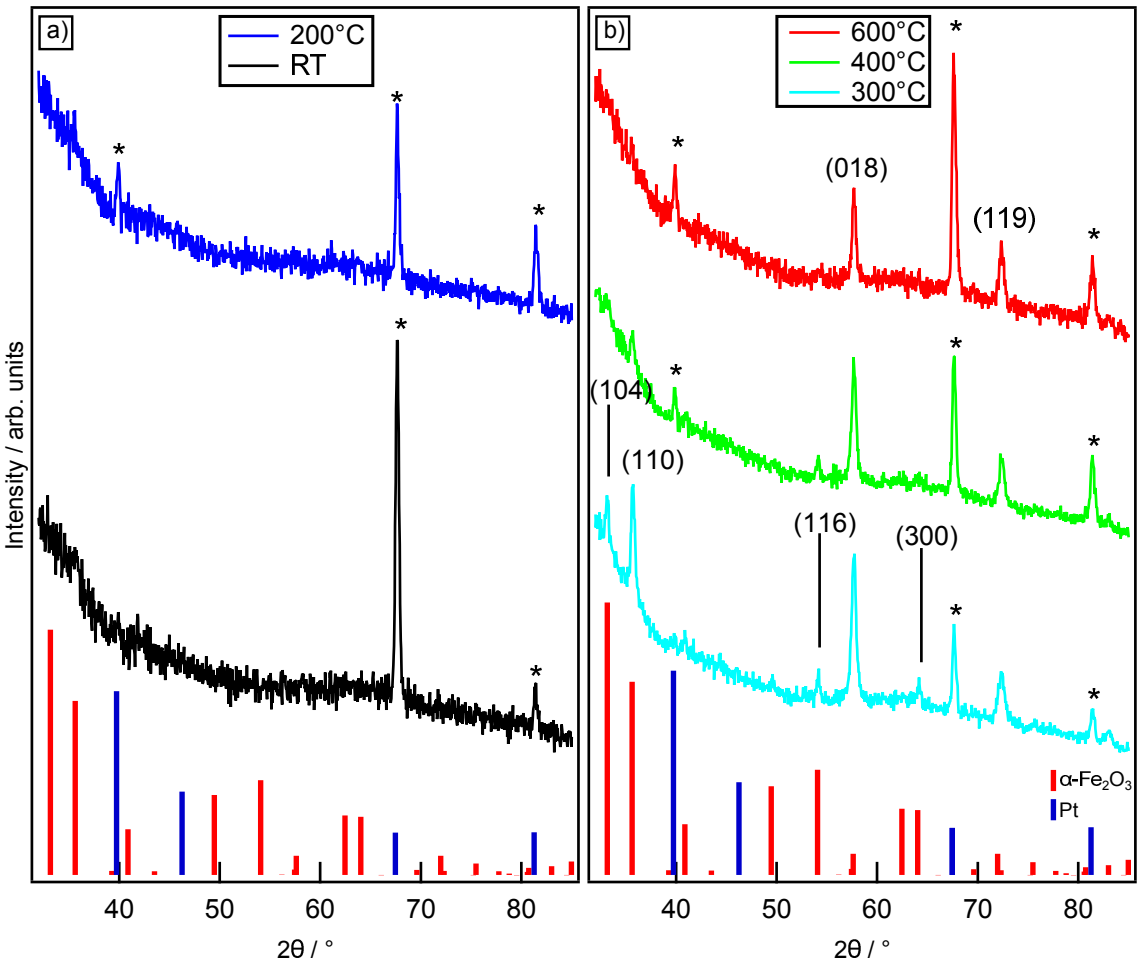

Figure 4.10: XRD pattern of samples that were a) deposited at room temperature and annealed in air at 200 °C and b) annealed at higher temperatures. Reflections from powder Pt (blue, PDF-card 70-2057) and hematite (red, PDF-card 79-1741) are shown as bar graphs. The asterisks show the Pt-reflections from the substrates whereas hematite reflections are labeled in brackets.

phase in the Raman spectra for these two samples. It indicates that the deposition at room temperature leads to the formation of mainly amorphous films with some traces of hematite.

After heating at higher temperatures the diffraction pattern change and show reflections which can be attributed to hematite. For an annealing temperature of 300 °C a variety of reflections are observed. Some of these are decreased when the annealing temperature is increased. After annealing at 600 °C only the (018) and (019) reflections remain. This indicates well oriented films which has been seen in the Raman spectra as well.

The width of the remaining reflections decreases slightly with increasing annealing temperature. The grain size calculated using the Scherrer-equation slightly increases from around 30nm to 50nm.[175] According to the Thornton-model such a grain size can be expected for sputtered films.[112] Also, the orientation of the films can be ex-

plained from this model. Heated, sputtered films can be expected to have a certain orientation. While this might not be the case for the room temperature deposited iron oxide films in this study, the platinum films below were deposited at 600 °C by sputtering. Their X-ray diffraction pattern show an orientation already. Upon heating, hematite is formed. As hematite can grow epitaxially on certain platinum surfaces[6] it can be assumed that upon heating the hematite phase adapts to the orientation of the platinum film below.

In Figure 4.11 XP spectra of the Fe2p and O1s-core-levels and the valence band are presented. Please note that the core-level spectra have been processed in order to remove the background [7]. In addition to the spectra of the samples whose structure has been discussed above the spectra of a sample measured directly after deposition without exposure to air (in-situ) is included for comparison.

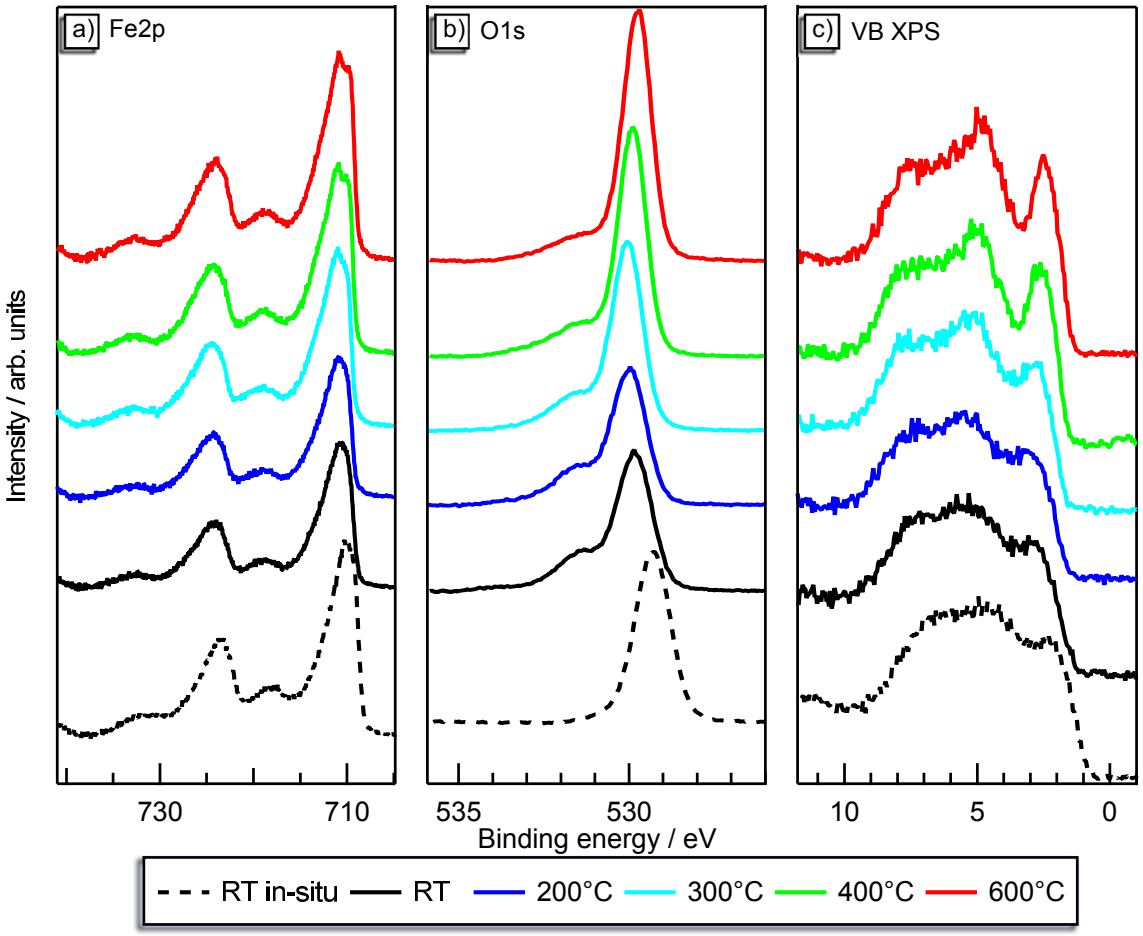

Figure 4.11: XP spectra of the a) Fe2p, b) O1s, and c) valence band region of samples in dependence of the ex-situ heat treatment. The solid line represents ex-situ samples whereas the dashed line show spectra from an RT-deposited in-situ sample. For the core-level spectra the background was subtracted as described in Chapter 3.3.2.

6 Please see Chapter 4.3 and Ref. [115]
7 Please see Chapter 3.3.2 for details on the background removal procedure

For the low temperature samples the $Fe2p_{3/2}$ core-level spectra exhibit a single maximum and a quasi symmetric top part. This applies for both the in-situ as well as the air exposed sample. The valence band spectra of the unheated samples show a flat plateau between 2 eV to 3 eV and a broad emission at 5 eV.

Upon heating the $Fe2p_{3/2}$ peak changes to a more asymmetric appearance of the topmost part and a shoulder towards lower binding energies develops. This change appears to increase with increasing annealing temperature. The low binding energy shoulder ("pre-edge") of the $Fe2p_{3/2}$ emission shows the highest intensity after the highest annealing temperature.

This shoulder has been assigned to be characteristic for crystalline bulk $\alpha - Fe_2O_3$. It stems from the symmetry within the hematite structure and vanishes if this symmetry is broken e.g. at surfaces or for amorphous samples.[61, 156] The presence (and intensity) of this "pre-edge" is, therefore, a clear indication of highly crystalline samples.

The valence band spectra also change with increasing annealing temperature. The plateau at 2 eV to 3 eV vanishes and a peak at around 2.5 eV appears. Furthermore, the peak at 5 eV sharpens and its intensity is increased.

Comparing the 600 °C annealed and RT-deposited sample the following is observed. Except for the "pre-edge" in the Fe2p spectra, the spectra of the two samples are alike. The specific satellite structure of the Fe2p emission indicates that the oxidation state of iron is 3+ in all cases.[55, 155, 176]

The O1s- spectra of all ex-situ samples are quite similar with a symmetric main emission and an additional emission at higher binding energies. This signal slightly decreases with increasing annealing temperature. In general a decrease of the peak width (FWHM) is observed with higher annealing temperature.

No high-binding energy emission is observed for the room temperature sample which was recorded in-situ. As a consequence, the high-binding energy emission of the O1s peak can, therefore, be attributed to oxygen-containing surface adsorbents.[177]

Possible charge transfer from these adsorbents is most likely a reason for the present upward shifting of all spectra with respect to the in-situ sample. The shapes of the valence band and the Fe2p emission are apparently not affected by this shift as there is no difference between the spectra of the in-situ and ex-situ sample which have both been deposited at room temperature.

Besides the shift due to adsorbents which is present in all ex-situ samples also an upward shift in dependence of the annealing temperature can be observed. This shift is present in the core-levels as well as the valence band. It, therefore, indicates a shift of the Fermi level in reaction to the heat treatment and/or changes in the amount of surface adsorbents.

There are no significant changes in the sample composition depending on the heat treatment. All samples show a slightly higher iron content than the nominal hematite stoichiometry. This issue is known in literature and attributed to the presence of iron interstitials.[71] An effect on the valence band DOS is, however, neglected as structural changes that are clearly present outweigh the small changes in sample composition that do not follow a trend.

Both shapes of the Fe2p core-level and of the valence bands observed here can be found in literature.[55, 56, 59, 60, 155, 156, 178] There is, however, no discussion available about the different appearance of the spectra and where they originate from. For now, it can be stated that the valence band exhibits a two-peak structure if the Fe2p$_{3/2}$core-level emission shows the "pre-edge". The connection of these two features was also not available in literature. A more detailed discussion on the electronic structure of the valence band (and how this affects the core-level emission) can be found in Ref.[61] and chapter 5 of this work.

The optical properties of the thin films are explored in Figure 4.12. The transmission spectra in Figure 4.12a) show almost identical interference patterns, which indicate smooth sample surfaces and similar film thickness. All samples show a drop in transmission at wavelengths around 550 nm. Here, a dependency of the optical properties on the annealing temperature is revealed. While all sample heated at 400 °C or higher show a sharp edge in their transmission spectra, the unheated and the 200 °C annealed samples show a less sharp edge with a higher transmission at lower wavelengths and a lower transmission for wavelengths above 550 nm. The transmission spectrum of the sample heated at 300 °C seems to have the same steep edge as the spectra of the samples heated at higher temperatures but it still shows higher transmission at lower wavelengths. The spectra for the sample which have been heated to 400 °C and higher resemble spectra of hematite from literature.[63]

The differences are also evident in the calculated absorption coefficients α in Figure 4.12b). The low temperature samples show a shallower dependence on photon energy compared to the high temperature samples with the 300 °C sample as an intermediate. The order of magnitude of α of all samples is in the range of $10^5\,\mathrm{cm}^{-1}$, which is similar to findings in literature.[63]

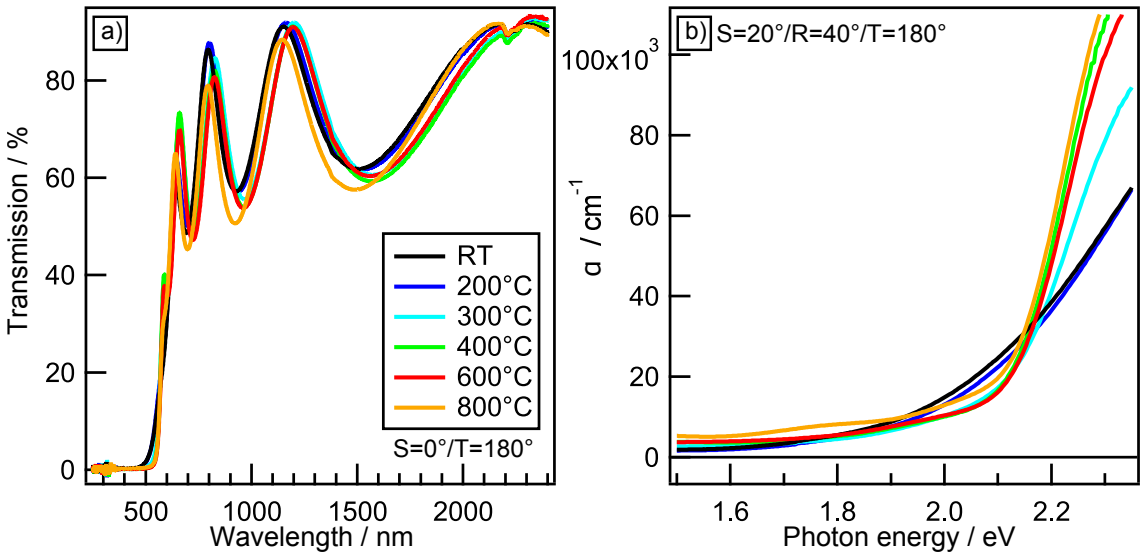

Figure 4.12: Optical properties of Fe_2O_3 samples before and after being annealed at various temperatures in air. The transmission in a) was measured under a sample angle (S) of 0° and a detector angle (T) of 180° while the absorption coefficient in b) were calculated from transmission (T) and reflection (R) measurements with a sample angle (S) 20° and detector angles of 180° (T) and 40° (R)

The determination of the optical band gap of a material is not as straight forward as it is sometimes implied in literature. Data processing using Tauc-plots requires a good knowledge of a possible band gap, its character, and is, therefore, quite delicate.[179] On thin films the interference fringes that are present in the transmission measurement make a determination of the zero signal of the absorption coefficient often impossible.[180] Using transmission and corresponding reflection measurement can reduce this problem. This was done here. It is, however, still questionable where to set the exact position of the band gap. One possible statement concerning the crystalline samples is that between 2.1 eV and 2.2 eV there is a sharp increase of the absorption coefficient. The optical band gap of the material is therefore within this range. This is in very good agreement with literature where the band gap range is often even spread from 1.9 eV to 2.2 eV, thereby revealing the challenges to determine a correct band gap value.[63, 64, 82, 181]

4.3 Epitaxial hematite thin films

A polycrystalline material like sputtered hematite shows a variety of grains with differently oriented surfaces. Measurements of surface properties e.g. the surface potentials will, therefore, show a superposition of the possible different properties of these differently oriented surfaces. Epitaxial thin films offer the chance to study more defined surfaces.

It was shown that for hematite nanoparticles the properties as a photocatalyst strongly depend on the orientation of the facets. Low index planes like {0001} show lower pho-

toactivity compared to high index planes like {10$\bar{1}$4}.[182, 183] On the other hand the conductivity along a {0001} facet was shown to be larger than along the [110] direction by up to four orders of magnitude.[72, 183]. The reasons for these differences are found in the different alteration of iron and oxygen layers and the density of unsaturated ions which are active e.g. in water oxidation.

Besides the different properties of the surfaces, epitaxial thin films can be regarded to be more well defined than their polycrystalline counter part. As PES studies on hematite single crystals always suffer from charging effects, it was seen as a good alternative to study epitaxial thin films.

For this purpose, thin films were grown at elevated temperatures on differently oriented sapphire substrates. XRD studies were performed to confirm the epitaxial growth. Conductivity measurements at elevated temperatures in different gas atmospheres of differently oriented hematite films were used to test whether the orientation influences the electrical properties. Unfortunately, it was only possible to study (0001) oriented hematite thin films on Pt(111) by means of PES as for other orientations the conductive substrate was not available. Hematite (0001) films on Pt(111) are probably the most studied films with a defined orientation.[184–194]

The preparation and characterization of the epitaxial hematite thin films were part of a master thesis conducted by Céline Steinert[8]. As the PES results did not show vast differences compared to polycrystalline films these will not be discussed here. This part is intentionally restricted to the XRD measurements and parts of the conductivity measurements. Additional conductivity measurements and a corresponding discussion to the ones that will be discussed here can be found in chapter 6.

Epitaxial thin films were sputter deposited onto sapphire substrates with the orientations ((0001)), ((10$\bar{1}$0)), ((11$\bar{2}$0)), and ((1$\bar{1}$02)). All films were deposited at 400 °C with 8 % oxygen in the sputter gas. The respective X-ray diffractograms from $\theta - 2\theta$ scans are shown in semi-logarithmic display in Figure 4.13.

All samples show well defined reflections which can be attributed to either hematite or sapphire. Namely, the sample grown on (0001)-oriented sapphire in Figure 4.13a) shows two reflections at 41.67° and 39.27°. Both are (006) reflections from the substrate and hematite thin film, respectively.[187, 190]

For the sample on (10$\bar{1}$0)-oriented sapphire only one reflection could be measured. It is positioned at 64.2° and can be attributed to the hematite (300) lattice plane.[187, 190] The corresponding (300) reflection from the sapphire substrate would be expected

[8] Please see Ref. [115]

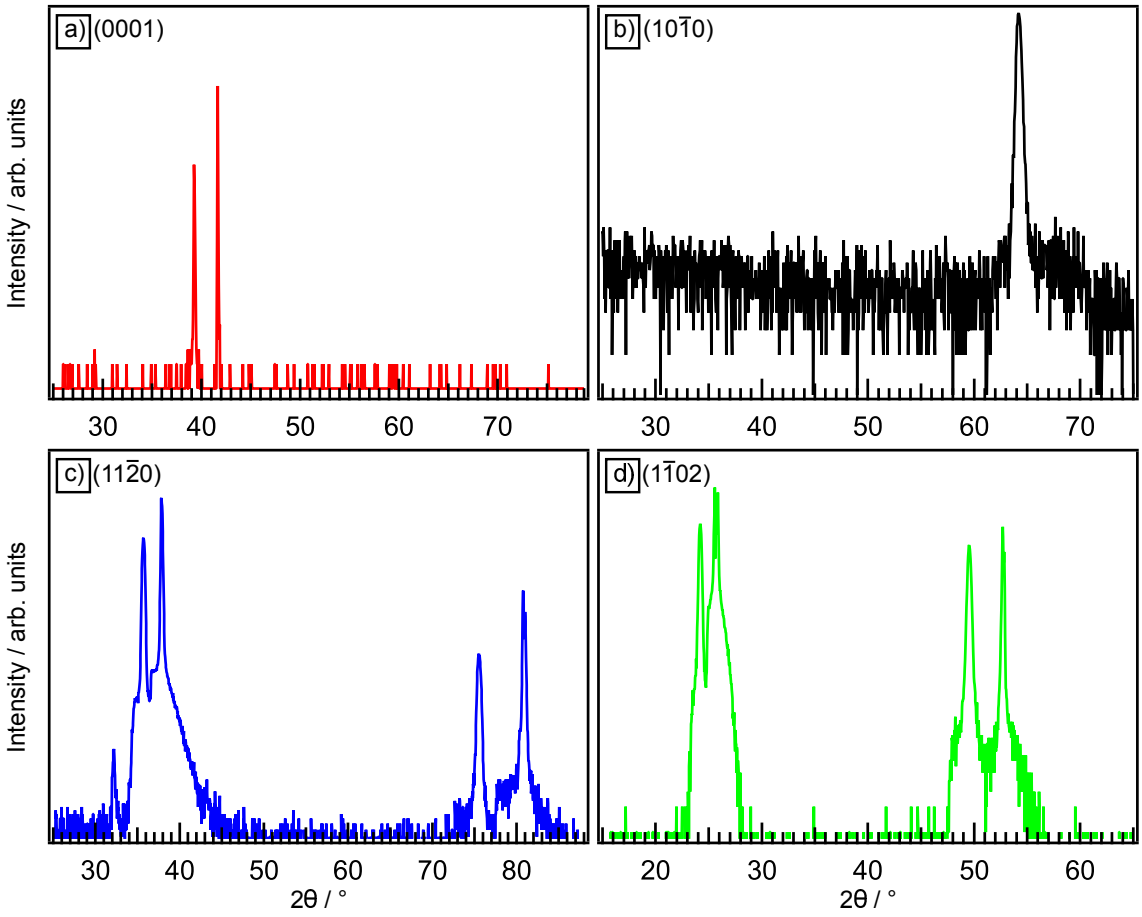

Figure 4.13: X-Ray diffractograms from $\theta-2\theta$ scans in semi-logarithmic display of epitaxial hematite thin films. The samples were deposited at 400 °C on sapphire substrates with the orientations a) ((0001)), b) ((10$\bar{1}$0)), c) ((11$\bar{2}$0)), and d) ((1$\bar{1}$02)).

at 68.18°. The reason for its absence is not clear. There is, however, a somewhat increased background noise at this angle, which might correspond to the signal of this lattice plane.

The diffraction pattern in Figure 4.13c) originates from the sample on (11$\bar{2}$0)-oriented sapphire. It shows four intense reflections. These are located at 35.71°, 37.84°, 75.54° and 80.77°. While the former two arise from the (110) plane of hematite and sapphire, respectively, the latter two stem from the (220) lattice plane.[187, 190] In addition, a less intense reflection at about 32° is visible in the semi-logarithmic display. This reflection cannot be attributed to either hematite or sapphire. As its intensity is far below the intensity of the other reflections its existence can be ignored in further interpretations.

Four reflections are also shown in the diffraction pattern of the sample deposited on (1$\bar{1}$02)-oriented sapphire in Figure 4.13d). Here, the reflections are located at 24.2°, 25.75°, 49.49° and 52.64° and can be attributed to the (012) and (024) lattice plane of hematite and sapphire, respectively.[187, 190] The reflections at 24.2° and 49.49° correspond to the hematite thin film.

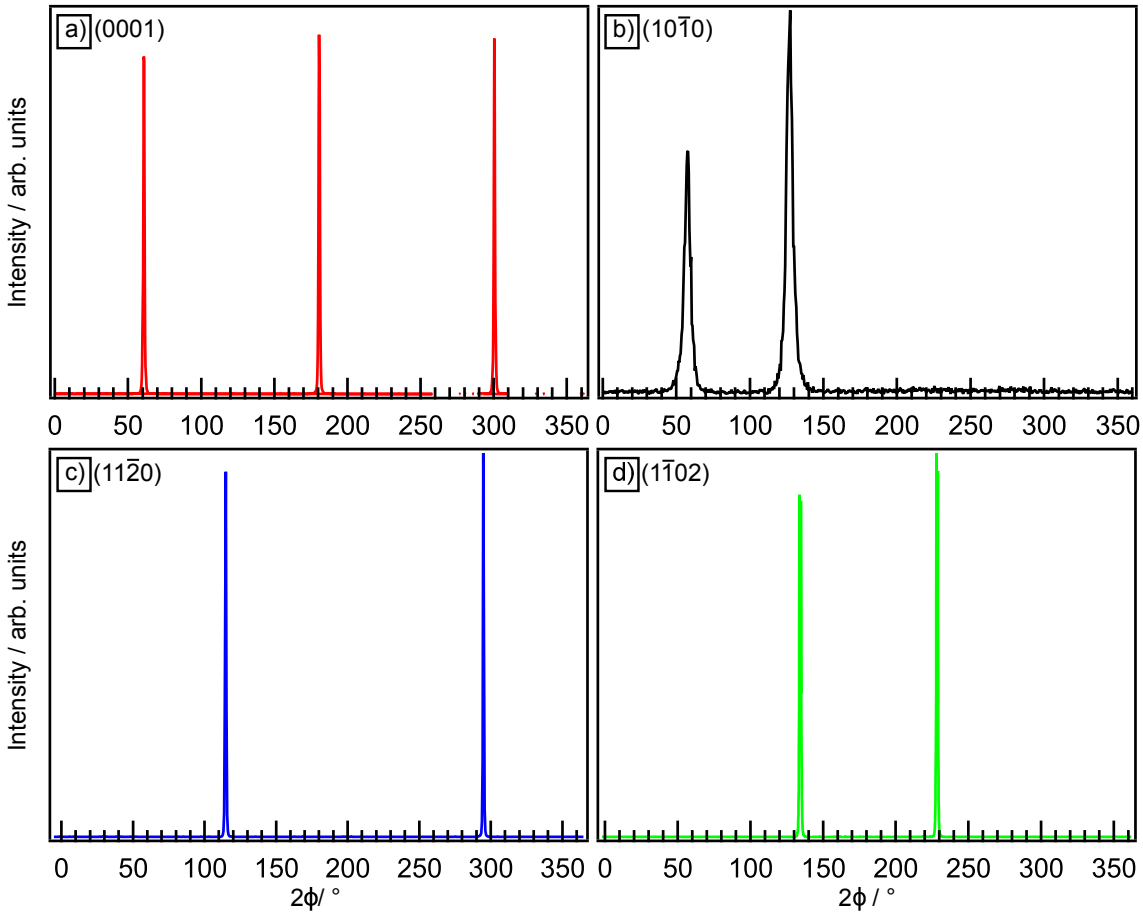

Figure 4.14: X-Ray diffractograms from ϕ scans on epitaxial hematite thin films. The samples were deposited at 400 °C on sapphire substrates with the orientations a) (0001), b) (10$\bar{1}$0), c) (11$\bar{2}$0), and d) (1$\bar{1}$02).

Ignoring the absence of the substrate reflection in Figure 4.13b) all samples show the hematite reflections corresponding to the same lattice plane as the given orientation of the substrate. This strongly indicates highly oriented or even epitaxial growth. To verify the epitaxial growth of hematite ϕ-scans were performed. These are displayed in Figure 4.14.

For all ϕ-scans the 2θ value was set to match the Bragg conditions for the (104) reflection of the hematite phase. Then, different Chi-values were set for each sample in order to optimize the resulting diffractogram. The Chi-values were 37°, 68.7°, 55.2° and 46.9° for the (0001)-, (10$\bar{1}$0)-, (11$\bar{2}$0)-, and (1$\bar{1}$02)-orientation, respectively.

All samples show reflections in their ϕ-scans. In addition, the 2θ measurements only showed reflections from the hematite phase that corresponded to the reflections of the orientation of the sapphire substrate. These two findings are proof enough for the conclusion that hematite grows epitaxially on the different sapphire surfaces.[187]

After the confirmation of epitaxial growth, the electrical properties of the differently oriented hematite thin films were examined by conductivity measurements at elevated

temperatures. The atmosphere during the experiment was an argon/oxygen mix with 10 % oxygen. The conductivity over times is plotted in Figure 4.15.

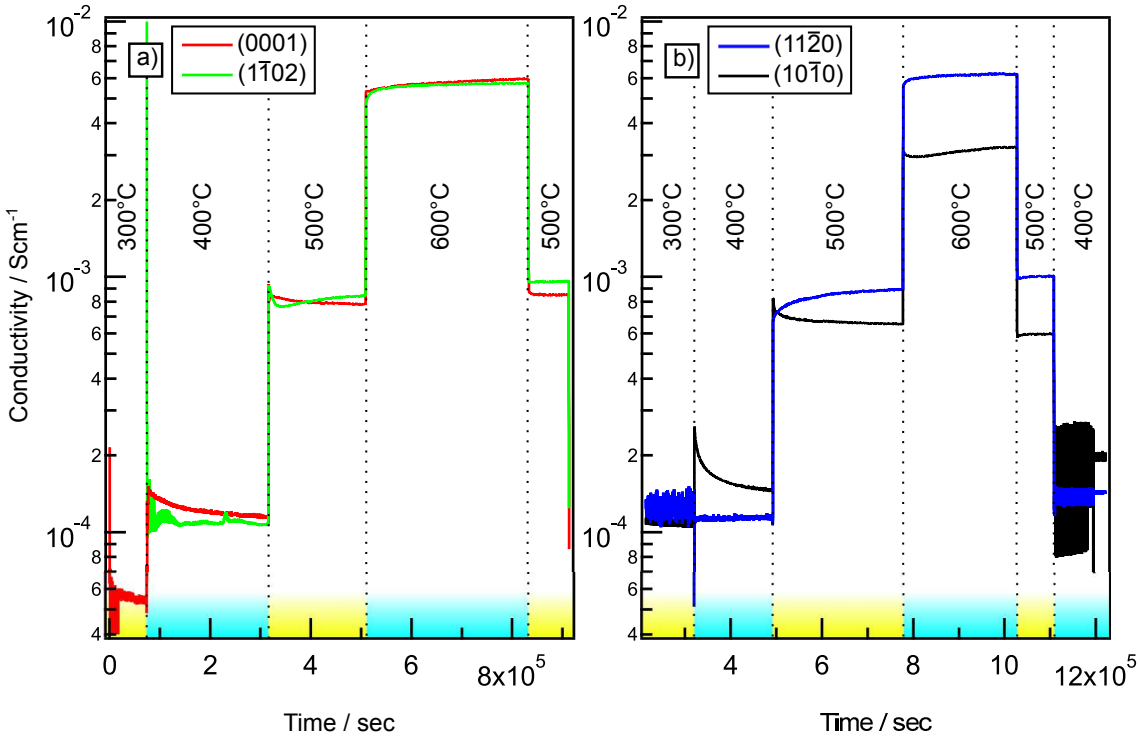

Figure 4.15: Conductivity over time and in dependence of the temperature of epitaxial hematite thin films. The samples with (0001)- (597 nm) and (1$\bar{1}$02)-orientation (632 nm) were measured together, as were the samples with (11$\bar{2}$0)- (650 nm) and (10$\bar{1}$0)-orientation (527 nm).

The comparison of the four measurements results in the conclusion that the electrical properties of the thin films in (0001)-, (1$\bar{1}$02)-, and (10$\bar{1}$0)-orientation are alike. At each temperature these sample show similar conductivities to each other. Only in the immediate behavior after changing the temperature there is some deviation. It is, however, not possible to conclude on any reason for this from these measurements alone. While e.g. at 500 °C the (10$\bar{1}$0)-oriented thin film shows a small but steady increase in conductivity over time the conductivity of the (0001)-oriented sample decreases. The (1$\bar{1}$02)-oriented thin film shows an initial decrease followed by a steady increase. The conductivities at the respective temperatures show a good agreement with undoped samples from literature for these three samples.[63, 77, 195, 196]

The possible reasons for such a behavior are manifold and cannot be concluded solely from one measurement. Among the possible explanation are e.g. grain growth, recrystallization, decomposition, oxygen exchange and oxidation or reduction of the surface.[194] Especially, grain growth is very likely for all samples above 400 °C as then the temperature was above the deposition temperature for the first time.[163, 197] In Chapter 6 conduc-

tivity measurements in different atmospheres of samples presented here will be discussed to explore the influence of the oxygen partial pressure on the electrical properties of hematite. From these measurements it will be seen that the measurement atmosphere has a different influence on the conductivity depending on the Fermi level position of the sample. This might be assigned to a difference in the oxygen exchange depending on the Fermi level position.

In contrast to the samples above, the thin film in $(10\bar{1}0)$-orientation shows different conductivities. While at 400 °C it is slightly more conductive than the other samples, at 500 °C and higher its conductivity is lower. At 600 °C the sample is less conductive by a factor of two.

In order to evaluate the temperature dependence of the conductivities of the samples discussed here, the quasi-equilibrium values of the conductivity at the respective temperatures were extracted. Quasi-equilibrium means the constant conductivity at the end of each heating step. These can be found in table 4.1 together with the activation energy E_A and the conductivity at infinite and room temperature σ_∞ and σ_{RT}. The latter were extracted by using an Arrhenius-plot assuming a temperature dependency of the conductivity σ like shown in equation 4.1

$$\sigma(T) = \frac{\sigma_\infty}{T} \times exp^{\frac{-E_A}{k_B \times T}} \tag{4.1}$$

where $k_B = 8.617 \times 10^{-5}\,\mathrm{eV\,K^{-1}}$ is the Boltzmann constant.

Please note that only the conductivities from heating towards 600 °C have been extracted as they showed a much clearer Arrhenius behavior than after being held at 600 °C.

Table 4.1: Extracted conductivities of epitaxial samples and the activation energy calculated by equation 4.1.

sample	σ					E_A
	400 °C	500 °C	600 °C	$T = \infty$	RT	eV
	$10^{-4}\,\mathrm{S\,cm^{-1}}$			$10^{6}\,\mathrm{S\,cm^{-1}}$	$10^{-11}\,\mathrm{S\,cm^{-1}}$	
((0001))	1.2	7.8	58	4.55	1.51	1.04
$((11\bar{2}0))$	1.1	8.9	62	8.91	0.59	1.08
$((1\bar{1}02))$	1.1	8.5	58	6.62	0.84	1.07
$((10\bar{1}0))$	1.5	6.5	33	0.19	134	0.84

The activation energies of the four epitaxial samples further reveal that there seems to be a difference in the electrical properties only for the $(10\bar{1}0)$orientation. The three other samples show similar conductivities and have activation energies in the same range, as it would be expected. The values are just slightly above 1 eV. Such a value was found previously for undoped hematite and has been explained to be in correspondence to half

the optical band gap.[63, 77] The fourth sample in $(10\bar{1}0)$-orientation, however, shows a slightly lower activation energy of just 0.84 eV.

Differences do also appear in the extracted conductivities at room and infinite temperature. While the former has an important impact on processes which happen at room temperature e.g. water splitting the latter can be regarded to be the maximum conductivity achievable and may be considered as materials quantity for comparison.[13, 15, 18] For these two values the samples in (0001)-, $(11\bar{2}0)$-, and $(1\bar{1}02)$-orientation show quite similar results. At room temperature their conductivity can be expected to be of the order of $10 \times 10^{-11}\,\mathrm{S\,cm^{-1}}$. This is about three orders of magnitude higher than expected from literature for pure hematite.[77] The same applies for their conductivity at infinite temperature which is about two to three orders of magnitude lower than found by Morin.[77]

The differences, however, are reasonable if the differences in sample preparation and experimental setup are considered. Morin used ceramic samples which have been sintered at 1100 °C. The samples discussed here are thin films which were deposited at 400 °C. While the sample in his study were never heated above their sintering temperature during measurement, the samples from this study were measured while being at such a high temperature for the first time. It can, therefore, be assumed that several processes like grain growth still occurred in these samples while being absent in Morin's study.

This difference can be expected to have a tremendous impact on the outcome of the experiment. One of the outcomes of Morin work was that grain boundary resistance is significant for hematite. The reason for the higher conductivities of the samples presented here might, therefore, be found in fewer or less resistive grain boundaries.

The sample with $(10\bar{1}0)$-orientation shows again completely different behavior than the three samples discussed above. It's room temperature conductivity is higher by about two orders of magnitude while it's conductivity at infinite temperature is smaller by one order of magnitude. As the four samples of this study can be assumed to only differ in their orientation any reason for the observed difference in the conductivities must be related to the structural properties of the samples. Namely, the surface/interface itself can be regarded to be very influential due to grain boundary effects.

Especially the polarity of oxide surfaces can have a high impact on the stability and/or the interaction with e.g. oxygen from the atmosphere.[198–200] In order to standardize surfaces, Tasker has established three types of different surfaces which differ in the charge Q associated with their layers and the dipole moment μ which may be present.[201] In his nomenclature, Type 1 and 2 do not show a dipole moment on the surface but differ in their layer charge. While type 1 has stoichiometric layers and does not show a charge, type 2 does have charged layers. Type 3, has charged layers and a dipole moment. It is,

therefore, not stable without reconstruction while the former two can be stable and might only show some relaxation.

In order to be able to classify the different surfaces of hematite representations of their unreconstructed bulk truncated structure were constructed[9]. These are shown in Figure 4.16. Each surface is shown from the view direction which is indicated by square brackets. The normal of every surface is pointing upwards. Iron cations are represented in yellow, while oxygen anion are shown as red balls.

Presented are the first and second repetitive units of the surface. The first unit is being classified in terms of the charge within each of its layers Q and the dipole moment μ within the unit. For the charge within a layer only the algebraic sign is important as there is no restriction in the lateral dimensions.

The (0001)-surface shows an alternating stacking of oxygen and iron containing layers. Each oxygen layer contains three oxygen ions for every two iron ions below. Compared to the first iron layer the second is laterally slightly displaced. This displacement is repeated throughout the crystal. Hence, the repetitive unit is only achieved after the sixth layer. As it begins with an oxygen layer but ends with an iron layer, there is a dipole moment associated with this surface. From this, the (0001)-surface of hematite can be classified to be of Tasker type 3.[200, 201] This indicates that it will not be stable but will show reconstruction. In addition, the layered structure will most likely allow for either an oxygen or an iron termination depending on the environment.[200, 201]

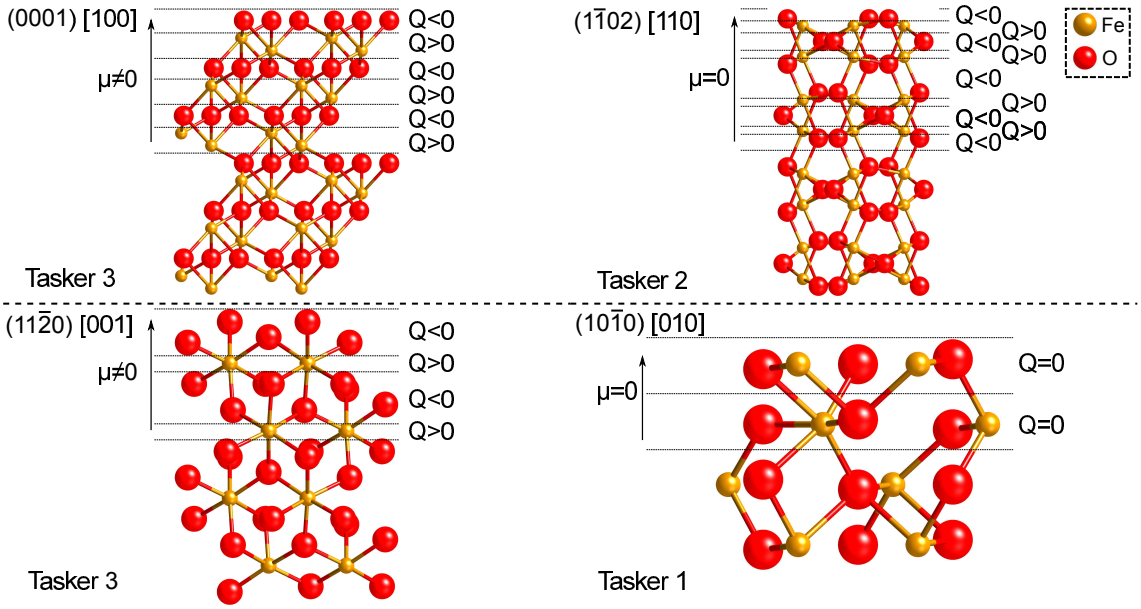

Figure 4.16: Side view on the unreconstructed surfaces of hematite.

[9] Images created with: CrystalMaker®, CrystalMaker Software Ltd, Oxford, England (`http://www.crystalmaker.com`)

The $(11\bar{2}0)$-surface is also of Tasker type 3. Again, oxygen and iron layers are stacked on top of each other. However, the repetitive unit is already reached after the fourth layer. It can be concluded again, that the surface will reconstruct to be stabilized and that in principle different terminations might be possible.

For the $(1\bar{1}02)$-surface the situation is different. Even though it also shows layers of oxygen and iron the stacking sequence is different. After a sequence of four closely packed layers (two oxygen and two iron) an oxygen containing layer with larger dimensions is reached. This layer connects the sequence of closely packed layers to a second sequence which is also closely packed but displaced. Only after this second sequence the repetitive unit is achieved. As there is no dipole moment associated with this surface it can be classified to be of Tasker type 2.[200, 201] Hence, it will most likely be stable and only show some relaxation. [35, 74]

Finally, the $(10\bar{1}0)$-surface is the only stoichiometric surface of the four which are discussed here. It shows layers in which always two iron are bound to three oxygen, sharing one of which. This results in no charge associated with this layer. As there is some displacement from layer to layer the repetitive unit is rather large. Please note, that it is not represented in Figure 4.16. That is, however, not necessary as the layer sequence itself does not change and no dipole moment is created. The surface can, therefore, be classified to be of Tasker type 1.[200, 201] It can be expected to be stable with only some relaxation.

The similar conductivities of the three surfaces suggest that the relaxation of the (0001)- and $(11\bar{2}0)$-surface might result in a situation which resembles the $(1\bar{1}02)$-surface. Hence, their conductivity show quite the same values. This assumption is reasonable as this specific surface is prevalent on nano-hematite due to its stability. [35, 74]

The stoichiometric character of the $(10\bar{1}0)$-surface, however, seems to result in different electronic properties. Unfortunately, it was not possible to further investigate the four different surfaces by means of PES as there were no conductive substrates available of all orientations except (0001). It can, therefore, only be assumed that a difference in the surface composition might result in different electronic properties e.g. work function which then influence the electrical properties by e.g. difference in oxygen exchange/ defect structure.[198, 200]

One aspect of the different orientations that should be discussed is the coordination of iron at the surface. In the bulk iron is sixfold coordinated in a slightly distorted oxygen octahedron.[34] At the surface the coordination of iron depends on the orientation and atmosphere.

Wasserman et al. performed calculations of the (0001)- and $(1\bar{1}02)$-surfaces in different atmospheres.[202] They found that the iron ions on the (0001)-surface are sixfold coordinated if no other species are present. From Figure 4.16 it is evident that this is the case for an oxygen-terminated surface. Less coordinated iron seems to be unstable and is being passivated or chelated away.[184, 202] This is in disagreement with results from Ketteler et al. who experimentally found that a single iron layer can exist on the (0001)-surface.[191] This, however, is also only discussed for certain conditions whereas in e.g. oxygen-rich atmospheres an oxygen termination prevails.

For water-containing atmospheres the sixfold coordination of the (0001)-surface is not present anymore as well.[202] Instead, indications for a fourfold coordination were found. Other species like hydrogen or hydroxides can influence the surface coordination of iron ions as well.

For unreconstructed surfaces without any adsorbates most oxygen-terminated hematite surfaces seem to show a sixfold coordination of iron. In addition to the (0001)-surface that was shown for the $(10\bar{1}1)$-surface and is evident from Figure 4.16 for the $(10\bar{1}0)$- and $(11\bar{2}0)$-surfaces.[203] An exception is the $(1\bar{1}02)$-surface which has fivefold coordinated iron ions at the surface.[202]

For less coordinated iron it could be expected that valence band measurement by XPS and UPS show additional states in the band gap due to the dangling iron (and oxygen) bonds. Within this work this could not be observed. For the epitaxial films only measurements on the (0001)-surface were possible. Polycrystalline samples seem to show similar surface properties which indicates that a stabilization of the sixfold coordination seem to appear for these samples as well.

Unfortunately, however, there is no certainty whether this coordination prevails when being brought into contact with an electrolyte. Dedicated calculations and experiments are necessary to find the present surface structure in a real application. For any logically based approach on the coordination and resulting properties in a certain application, however, the issue seems to be too complex.

4.4 Surface potentials of hematite

The surface potentials of a material are important parameters in order to evaluate the positions of the band edges and Fermi level relative to the vacuum potential. If no other data is available the ionization potentials of different materials can be used a a first approximation to make an educated guess of relative band edge position which e.g. determine charge transfer barriers.[12]

Values for the work function extracted using the procedure described in 3.3.2 are presented in Figure 4.17. Figure a) shows the work function versus Fermi level position from the samples which were presented in Chapter 4.1, to show the oxygen dependency (O), as discussed in Chapter 4.2, to evaluate the influence of the temperature (T). In addition, partly epitaxial samples (epi) as described in Chapter 4.3 are presented. Please note, that for the latter the temperature range of deposition was from 200 °C to 600 °C. Epitaxial growth, however, does only occur above 300 °C. Lines of constant ionization potentials are added. The difference from line to line is 0.4 eV. The lines which refer to an ionization potential of 6.2 eV and 6.6 eV are labeled, respectively. Figures b) and c) show the temperature and oxygen dependency of the work function of the respective sample.

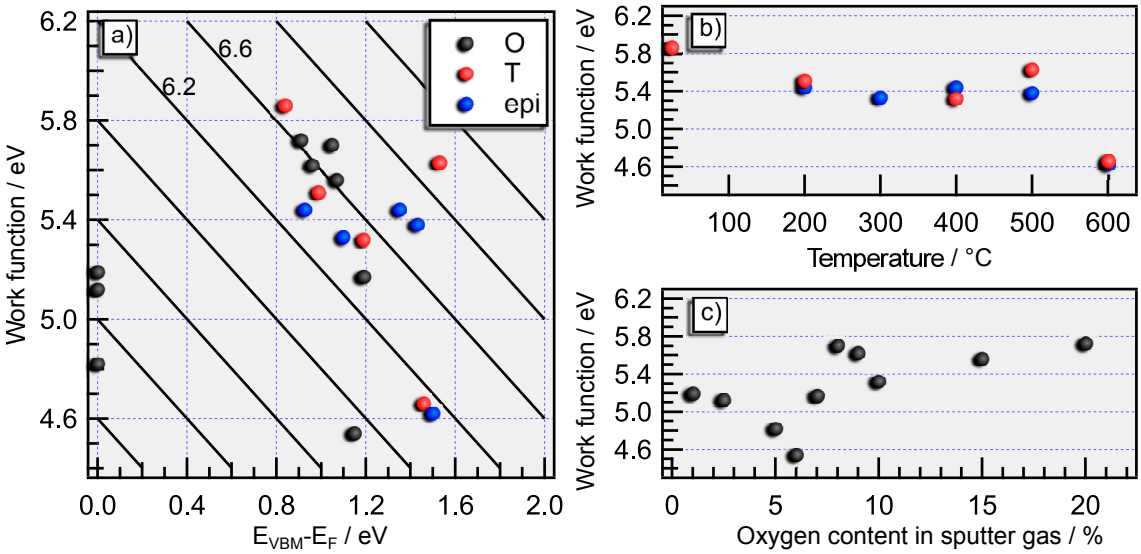

Figure 4.17: Surface potentials of iron oxide thin films determined by UPS. a) Work function versus Fermi level position. The straight lines indicate constant ionization potential which can be read from the point of zero Fermi level. b) Work function in dependence of temperature and c) Work function in dependence of oxygen content in the sputter gas.

Figure 4.17a) reveals that most samples show a work function of about 5.2 eV to 5.8 eV while the Fermi level is between 0.8 eV to 1.5 eV. The ionization potentials of the films are between 6.2 eV and 7.0 eV with a mean value of 6.6 eV. This is considerably lower than the ionization potentials for hematite films which can be found in literature. Here, a value of 7.2 eV is widely accepted. [6, 22] The impact of this finding will be further discussed in the framework of polaron formation in part 8 of this work. It will be shown that the determination of the ionization potential from electrochemical methods leads to band edges lower than the values from UHV experiments.

In Figure 4.17a) six points are not within the described range. The first two have a Fermi level position of about 1.5 eV and work function of just about 4.6 eV. These can be found in Figure 4.17b) again and both result from samples deposited at 600 °C. It was, however, observed within our studies of depositing hematite that often samples deposited

at 600 °C showed surface inhomogeneities which were even visible by eye. Such inhomogeneities at the surface make a determination of the work function by UPS unreliable. The value of 4.6 eV should, therefore, be disregarded.

Below 600 °C the work functions in Figure 4.17b) are within 5.3 eV and 5.8 eV with the room temperature deposited sample showing the highest work function. This is expected as the Fermi level position of such a sample is much lower than for a sample deposited onto heated substrates[10]. The samples which were deposited between 200 °C and 500 °C show a work function of about 5.5 eV, regardless whether they show epitaxy (blue above 300 °C) or not (red).

The other work functions which are outside the described range are all from samples which were deposited with 6 % oxygen in the sputter gas or less. Their Fermi level is at zero as these samples show a mix of different phases[11]. Following the increasing oxygen content in Figure 4.17c) the work function decreases and shows its lowest value for the sample deposited with 6 % oxygen in the sputter gas.

Afterwards, the work function shows a small trend to increase with increasing oxygen content in the sputter gas. The reason for the lowest work function observed at conditions where hematite is just started to being formed as a single phase is not completely clear. The reason might be found in trace amount of reduced phase (e.g. Fe_3O_4) which could not be detected by Raman or XPS. This argument seems to be reasonable as the ionization potential of this sample is about 5.7 eV which is much lower than for hematite samples.

4.5 Summary

The aim to verify the phase and find deposition parameters for phase pure hematite was achieved. It could be shown that above 6 % oxygen in the sputter gas a pure Fe_2O_3 phase will be formed. If the samples are deposited at room temperature Fe_2O_3 will be amorphous while at temperatures of 300 °C and above, crystalline $\alpha - Fe_2O_3$ sample are achieved. On sapphire substrates these samples will be epitaxial. The same temperatures allow for the crystallization of amorphous samples. However, oxygen has to be present as heating under reducing conditions results in the formation of Fe^{2+}.

The temperature and oxygen content do have an influence on the position of the Fermi level. With increasing temperature the Fermi level position is increased while for higher oxygen contents it shifts downwards. The range of Fermi level positions after deposition is scattered from 0.8 eV to 1.6 eV.

[10] Please compare to Figure 4.4
[11] Please compare to Figure 4.1 and 4.2

The ionization potential of most samples is situated around 6.6 eV and the work function is between 5.2 eV to 5.8 eV.

It was observed that the peak positions of the Fe2p- and O1s-core level correspond to the Fermi level position by shifting parallel to the valence band maximum. Their distant to the valence band maximum can, therefore, be assumed to be a constant of 709.5 eV for the $Fe2p_{3/2}$- and 529.4 eV for the O1s-core level, respectively.

Whether a sample is crystalline or amorphous has an influence on the electronic properties. For crystalline samples a "pre-edge" in the Fe2p-spectrum is observed. At the same time the valence band shows two distinct emission peaks. The following chapter will further explore these two observations.

5 The electronic structure of the valence band of hematite

In the previous chapter the deposition conditions at which phase pure hematite films can be deposited were established. Now, the results from these well defined samples regarding the electronic structure of the valence band of hematite shall be discussed.
The motivation of this work origins in the suggested application of hematite in a water splitting device. In this application light should be absorbed to create an electron-hole pair with a sufficient energy difference. Then, these charge carriers need to be separated and being transferred via the interface to the electrolyte or the electrode. On their way they should not recombine e.g. via trap states from defects in the bulk or the surface. In all these processes, the electronic structure of the material plays a crucial role[1].

Important aspects of this chapter

- ... the "pre-edge" in the Fe2p-core-level spectrum is a result of symmetry
- ... the "two-peak" structure of the valence band results from the same symmetry considerations
- ... the valence band maximum origins from Fe3d e_g-states

[1] Please see Figure 1.1

This Chapter of the thesis is based on the observations of the "pre-edge" which occurs in the Fe2p$_{3/2}$-core level spectra and the connected "two-peak" structure of the valence band which were both described in the previous Chapter. The spectra which are shown in Figure 5.1 are from samples which have been described in the in-situ and ex-situ heating experiments in 4.2. All samples were prepared with 8 % oxygen in the sputter gas on quartz at room temperature and afterwards annealed. It was shown in Figure 4.9 and 4.10 that these samples are amorphous before and crystalline after annealing.

The differences in the DOS of the valence band between annealed and non-annealed samples are also reflected in the difference of the Fe2p$_{3/2}$-core level peak shapes. Gupta and Sen have shown that the removal of an electron from the Fe2p$_{3/2}$ state by e.g. photoexcitation results in a different multiplet splitting depending on the symmetry of the oxygen ligand-field of the Fe^{3+} ion.[129, 130] Multiplet fits of the Fe^{3+} emission of an annealed (top) and non-annealed sample (bottom) are shown in Figure 5.1a). The fits are based on the results of Gupta and Sen and use a similar fitting procedure as has been described before.[125, 132]The resulting envelopes show a very good agreement with the measured emission structure.

It is, however, necessary to introduce a fifth peak to the four multiplet peaks. Such a peak has been used before and was introduced by Grosvenor et al. as “surface peak”.[132] Its higher intensity in the spectrum of the non-annealed sample might indicate that this sample shows a lower symmetry at the surface, e.g., more dangling bonds and a higher amount of less coordinated Fe ions.[204]

The intensity ratio of the four multiplet lines agrees much better to the theoretical predictions by Gupta and Sen for the annealed sample. This is another indication for the presence of hematite as a defined phase for this sample. Similar differences in the Fe2p core level have been shown to originate from the loss of symmetry at the surface of single crystalline hematite by surface-sensitive photoemission.[156, 205, 206] This shows that the reduced symmetry in the non-annealed sample is responsible for the changes in the shape of core-level emission and valence band spectrum.

An introduction of other oxidation states of iron which would also alter the DOS can be ruled out as the satellite structure of the Fe2p emission in Figure 4.11 clearly shows Fe^{3+}. In addition, Fe^{2+} states would be expected to give rise to a photoemission signal at the Fermi energy, which is not observed here[2]. [37, 51, 57, 156, 207, 208]

The development of the DOS upon crystallization can be discussed in more detail with the valence band spectra from XPS and UPS for an RT deposited and a 600 °C annealed sample (Figure 5.1). Please notice that the UP spectra for the two samples were measured

[2] Please refer to Figure 4.2 and Figure 4.7

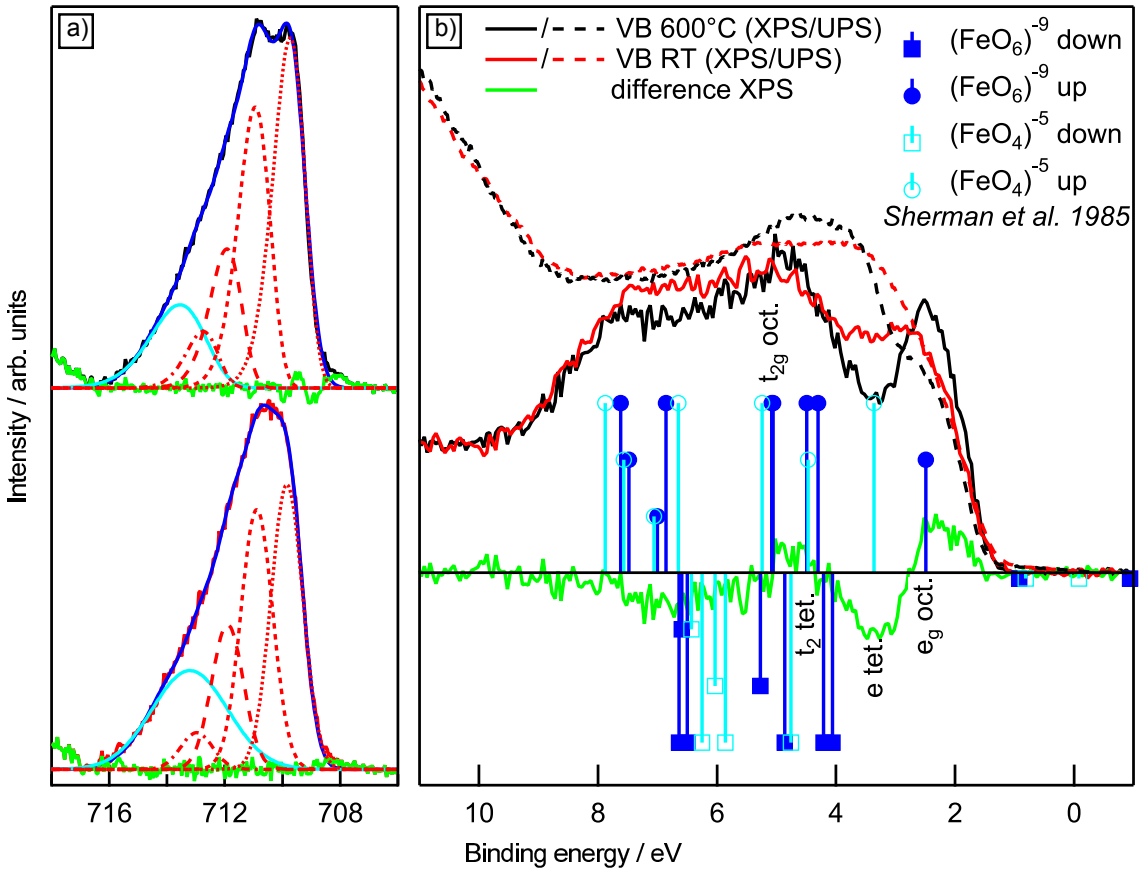

Figure 5.1: Influence of the crystallographic properties on the electronic structure of Fe_2O_3 . a) Multiplet splitting of the $Fe2p_{3/2}$-core level of a crystalline (top,solid black) and amorphous (bottom, solid red) sample and b) valence band measured by XPS (solid line) and UPS (dashed line) of the same samples. The bar graphs in b) represent the theoretically calculated electronic structure of iron-oxygen clusters and were extracted from Ref. [34].

on samples that did not leave the ultra-high vacuum (UHV). In case of the annealed sample, heating was performed at a temperature of 600 °C in 1 Pa oxygen.

The XP spectra of all samples from Figure 5.1 have been discussed in the previous Chapter (Figure 4.11). It is evident that the spectra of the in-situ annealed sample is almost identical with the spectra from the ex-situ annealed samples. The only difference is a missing shoulder to higher binding energies in the O1s-spectrum, indicating the absence of any adsorbents.

It is, therefore, possible to use the in-situ UP spectra in comparison to ex-situ XP spectra in Figure 5.1. All spectra have been shifted to a common valence band maximum position. The difference in the XP valence band spectrum for the sample before and after annealing at 600 °C is shown in green. Positive values of the difference indicate here an increase in intensity for the annealed sample and vice versa negative values a higher intensity for the non-annealed sample. The change from the plateau to a peak at the valence band maximum that has already been observed before indicates a more defined

density of states (DOS) at the valence band maximum of the annealed sample. The non-annealed sample shows a higher intensity in the region between 3 eV to 4 eV and from 5 eV to 8.5 eV. This can be interpreted to originate from a wider distribution of Fe3d states in the amorphous sample.[34, 59, 60] At 5 eV the annealed sample shows a slightly higher intensity which coincides with the presence of the second peak in the valence band.

The origin of these changes in intensity can be discussed on the basis of calculations of the DOS of Fe^{3+}-ions in six- (octahedron, $(FeO_6)^{-9}$) or fourfold (tetrahedron, $(FeO_4)^{-5}$) coordination to oxygen by Sherman.[34] The results from these calculations are included in Figure 5.1 as bar graphs. Indicated are the crystal-field splitted anti-bonding Fe3d states for both, octahedral and tetrahedral coordination. The labeling of other states including the bonding states with Fe3d character was not included for sake of clarity. Please be referred to the work of Sherman for more details on the energetic order of and oxygen/ iron contribution to the respective states.[34]

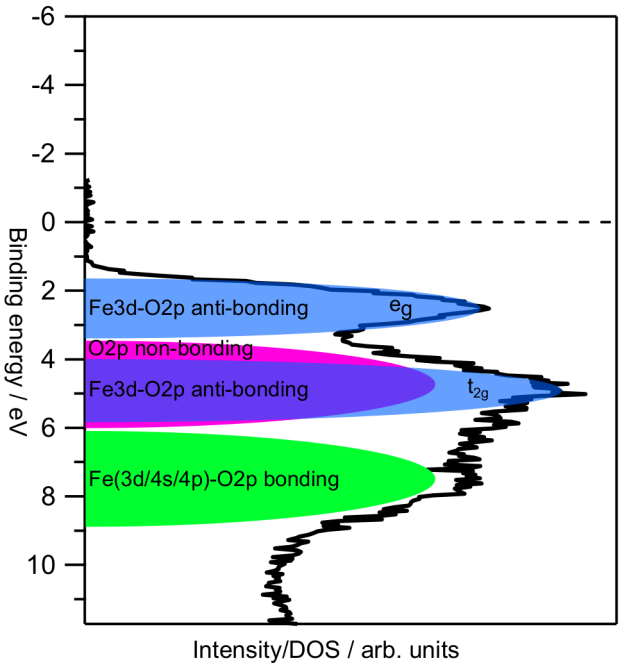

Figure 5.2: Orbital contributions to the valence band of hematite

An artists representation of the positions of the different states can be found in Figure 5.2. The features from a representative measured valence band have been assigned to the states from the calculations.[34] They will be discussed in the following.

The position of the leading peak in the valence band coincides well with the position of the anti-bonding $4e_g$*-states from the calculations of the octahedron. A good agreement is also shown for the second peak in the valence band which is found to be at the corresponding position of the anti-bonding $2t_g$*-states.

The energy difference of 2.6 eV of these states can be interpreted to be the crystal-field splitting (10Dq) of the Fe3d orbitals in the octahedral environment of oxygen. This value is higher than other values of 10Dq which have been extracted from XPS or XAS measurements before.[156, 205]

In the same region from 4.5 eV to 5 eV non-bonding states are expected from the calculations. The bonding orbitals are present below starting at 6 eV and reaching as far as 8 eV. According to the calculations the anti-bonding states are hybrid states from Fe3d

and O2p, the non-bonding states show mainly O2p character, whereas the bonding states are combinations from Fe4s/Fe4p and O2p. At the same binding energy the bonding Fe3d orbitals, hybridized with O2p, can be found as well.

The higher intensity of the non-annealed sample in the plateau region from 3 eV to 4 eV eV could be explained by the existence of the anti-bonding $6\,t_{2g}{}^{*}$-state from a tetrahedral cluster. The corresponding crystal-field splitted anti-bonding $2\,e^{*}$-state lies 1.1 eV below at about 4.5 eV. In the regions of non-bonding and bonding states of the octahedron the tetrahedron also shows states of the same character. Hence, the main difference is the change in the position of the anti-bonding states.

The spectrum of the non-annealed sample, however, does not reflect the DOS of octrahedrons only. In the amorphous phase it can be assumed that the coordination around iron by oxygen is not restricted to the sixfold octahedral coordination. As an example, the DOS from a tetrahedral oxygen coordination around a Fe^{3+} is added in Figure 5.1. It can be observed that the DOS of the tetrahedral coordination shows states at the plateau region between 2 eV and 4.5 eV. It could, therefore, be a possible explanation for the difference in the valence band DOS. Other coordinations, differences in the crystal-field splitting or a distribution of bonding lengths in both polyhedrons are also possible.[156]

Amorphous iron oxide can the regarded to consist of iron and oxygen clusters of different coordination and size. The only constriction is that iron is in a Fe^{3+}-state. However, the far-field symmetry is not present in an amorphous phase. From the observation described above and the comparison to the calculation it can be assumed that the spectral difference between amorphous and crystalline sample are due to the changes in symmetry.

All electronic states presented in Figure 5.1 are hybrids from both oxygen and iron states. The composition, however, is different for every hybrid state. The valence band spectra from XPS have been measured with Al Kα-radiation and do, because of the changes in cross-section, show an increased intensity contribution from the iron d-states. Due to the increased cross-section spectra in UPS, however, oxygen-like states are more intense in the spectra from this technique.[209]

As can be seen from the dashed graphs in Figure 5.1b) the general shapes of XP and UP spectra are similar. However, the leading peak of the XP spectrum is only a shoulder in the UP spectrum which indicates that it is an iron 3d-deduced state. This agrees well to the results of the calculations.

The second peak seems to be present in the UP spectrum as well. However, the DOS in the region of this emission is generally larger and contains a variety of oxygen-like states as well. These conclusions agree well to publications on the origin of the DOS in the va-

lence band of iron oxide from the past by PES and Density Functional Theory (DFT).[40, 42, 43, 56, 59, 60, 210] The valence band spectra presented in literature resemble both shapes of valence bands which we presented here. But a clear correlation to the quality of the samples with respect to the relevant contribution of different coordination, crystallinity, and surface states was missing.

Overall the PES measurements on these defined samples show how sample treatment influences the resulting DOS. It is worth to mention that while most authors only publish the Fe2p-region to proof the presence of Fe^{3+} the peak shape of most presented samples are closer to the non-annealed type. As state-of-the-art hematite photoanodes are mostly nanostructured the surface-to-bulk ratio in these samples is higher than for thin films where the thicknesses are much higher than the information depth of XPS.[13, 18, 73, 211–215]

For materials on the nanoscale the overall effective DOS involved in surface processes might not be the same as for bulk dominated samples. The breaking of symmetry on the surface is more severe as there is a lack of bulk phase. Besides, the higher surface-bulk ratio increases the relative number of dangling bonds. The result would be a DOS which is much better resembled by the amorphous samples from this study.

6 Fermi level manipulation of the bulk

Hematite in the application of water splitting is usually always doped in order to improve the electrical properties of the material. Many foreign atoms have been used as dopants. Among these are n-type dopants like Ti, Si, Zr, Ge, Sn, Mo, Tc, Ru, and Rh, while p-type doping has been achieved by e.g. Mg, Mn, Ni, and Cu. [40, 47, 63, 77, 80, 172, 216–239]

The dopants which are most often used are Ti, Si, and Zr for the case of n-type doping and Mg for p-type doping. All of these are expected to be substitutional dopants that replace an iron cation in the lattice. In order to be active as a dopant it is therefore necessary that their oxidations state is different from +III.

In this part of the work the impact on adding Mg, Si, and Zr into hematite thin films is being explored. The addition of the dopants was achieved by utilizing a co-sputtering setup which is further described in Chapter 3.2.1. The deposition parameters can be found in the table 3.1.

Important aspects of this chapter

- ... the Fermi level is being shifted due to the dopant
- ... Si and Zr are n-type dopants
- ... Mg is a p-type dopant
- ... all dopants introduce disorder
- ... the highest Fermi level position of 1.68 eV vs. E_{VBM} was reached with Zr
- ... the lowest Fermi level position of 0.3 eV vs. E_{VBM} was reached with Mg
- ... Si and Mg might show phase segregation
- ... doping reduces the absorption slightly
- ... only Mg and Zr improve the electrical conductivity
- ... Fe_2O_3 does not show Fermi level pinning between 0.3 eV and 1.68 eV vs. E_{VBM}

6.1 Magnesium doping

To achieve p-type doping in hematite Mg was added during the deposition by means of co-sputtering from a magnesium target. For all depositions the power at the Fe-target and Mg-target (60 W/15 W), the distance of the iron target to the sample (8 cm), the pressure (0.5 Pa), and the oxygen content in the sputter gas (8 %) were being kept constant. Varied was the distance of the magnesium target to the sample (7 cm to 14 cm) and the temperature (RT to 400 °C) [1].

In Chapter 4 it was shown that Fe_2O_3 can be deposited as a crystalline phase for deposition temperatures above 300 °C. In principle the same can be concluded from Raman measurements on Mg-doped samples as well. It was, therefore, decided, not to discuss this particular matter again, but rather focus on the influence of the dopant concentration on the structure in the following [2]. For this purpose the results from XRD and Raman measurements from three different samples a presented in Figure 6.1. The samples were all deposited at 400 °C on quartz and platinized quartz. They differ from 5.3 % to 26.7 % in their Mg-concentration. These concentrations were extracted from XP spectra and describe the magnesium to iron i.e. the cation ratio. It was calculated by using equation 3.1 and will always be referred to as the magnesium content in the following.

The X-ray diffractograms in Figure 6.1 all show only reflections from hematite. Especially, for the sample containing 26.7 % magnesium this result is surprising. Tang et al. have deposited Mg-doped hematite thin films by means of sputter deposition as well and found a small MgO signal in the XRD pattern of a film containing 13.4 % Mg.[232]

The absence of such a signal might originate from the experimental difference of their deposition. While the sample presented here were deposited at 400 °C, Tang et al. deposited their films without further heating but performed at post-annealing in air at 300 °C. The solubility of magnesium in hematite is most likely higher at elevated temperatures. However, once MgO is being formed the post-annealing at 300 °C might actually not be enough to incorporate all Mg into hematite.

In a second publication the same group showed that for films deposited under similar conditions but with the addition of titanium no MgO could be found for magnesium contents as high as 12 % by XRD.[220] XRD, however, will only detect crystalline phases of a certain size and concentration. It cannot be neglected that any impurity phase of magnesium oxide, which might be formed in the deposition of the samples presented here, could be either amorphous or of only little amount and/or size.

[1] Please see table 3.1
[2] Please see Figures A6 and A8

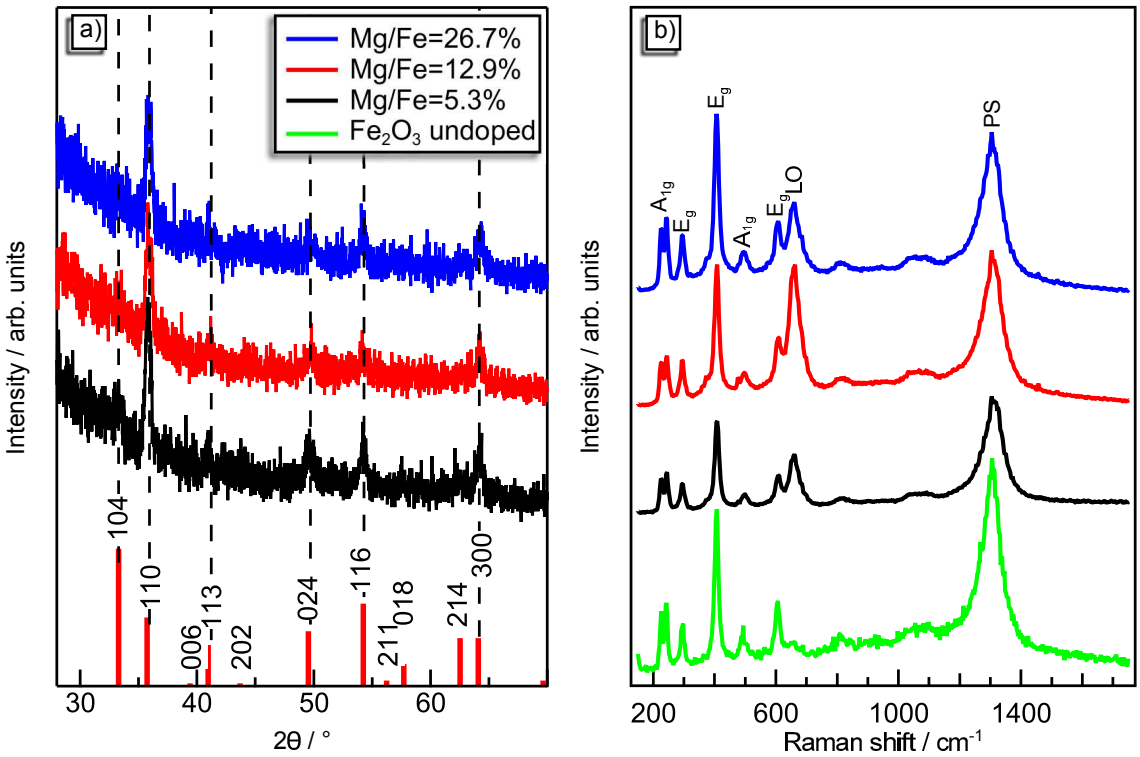

Figure 6.1: Structural characterization of Mg-doped hematite thin films deposited at 400 °C by a) XRD and b) Raman spectroscopy. The films show different doping levels. The XRD reflections in a) were identified with the help of the pdf-card 13-534, which is included as bar graphs. The green graph on the bottom of b) shows the Raman spectrum of an undoped sample that was deposited under the same conditions except for the addition of magnesium.

Compared to the diffraction pattern from powder samples the (110) reflection shows an increased intensity relative to the (104) reflection. This indicates oriented growth of the doped hematite thin films. The intensity of the reflections of the red curve seems to be a little less than for the other two samples. As this sample, however, does neither show the highest nor the lowest magnesium content of the three sample this cannot be attributed to originate from the addition of magnesium. As a consequence it is attributed to a higher disorder within the sample. The diffraction pattern of all samples is rather noisy and can be assumed that all samples presented here exhibit a high degree of disorder.

The assumption of higher disorder is additionally confirmed by the Raman spectra in Figure 6.1. The mode at 660 cm^{-1} (LO) shows the highest intensity for all three samples, reaching the intensity of the E_g line at 412 cm^{-1} for the sample with 12.9 % magnesium. For all samples the intensity of this mode in Figure 6.1b) is much higher compared to the undoped hematite sample (green). This sample was deposited under the same conditions except for the addition of magnesium[3]. Despite this changed intensity there is no other difference and all characteristic Raman modes of hematite could be found.[143, 144]

[3] Please also compare to Figure 4.1 for further spectra of undoped samples

The increased intensity of the mode at 660 cm^{-1} has been reported before.[166, 167, 170–172]. It has been discussed that this mode can be explained by an actually Raman forbidden scattering on longitudinal optical phonons (IR-active) [4]. Due to disorder, however, the mode becomes Raman active.[144, 164, 166–172] A second explanation for the appearance of this mode are traces of magnetite [5]. As there are no traces of magnetite observed in XRD and the XP spectra in Figure 6.2 of all samples only show Fe^{3+} it is concluded that the high intensity of this mode indicates a high disorder within the samples.

Raman measurements alone cannot clarify whether amorphous MgO might be included into the samples as the rocksalt structure of this particular phase is not Raman active at all.[153] The appearance of the high disorder might be associated with the occurrence of such a phase but could also originate from the substitution of the quite heavy Fe^{3+} by very light Mg^{2+}. In the latter case the presence of the LO-mode would evidence the incorporation of the dopant into the hematite lattice at the iron site.

It is also possible, that a combination of both, incorporation and impurity phase formation, occurred. Once the solubility of Mg in Fe_2O_3 has been reached any additional Mg might be part of a MgO phase. Comparing the dopant concentration in this thesis to dopant concentrations in other semiconductors such as Si gives reason to believe in this assumption. For other semiconductors the dopant concentration is usually much lower (range: ppm) while in this thesis concentrations in the range of percent and above have been used. This, however, is common practice for doping of hematite and transition metal oxides in general.[166, 167, 170–172]

The combination of XRD and Raman spectroscopy confirms that the samples grow crystalline at a deposition temperature of 400 °C. The magnesium content does not change this and there is no conclusive evidence for other phases than hematite at this point. Adding magnesium, however, does introduce a high degree of structural disorder. It appears that the degree of disorder does not directly depend on the amount of magnesium that is added.

The electronic structure of Mg-doped hematite has been investigated by means of XPS measurements. The spectra from the same sample, which have been used to examine the structural properties (Figure 6.1) are presented in Figure 6.2. In addition to the spectra from Mg-doped samples the spectra of an undoped sample are included as well. For the sake of a more detailed presentation it was decided to only show the $Fe2p_{3/2}$ core-level.

The spectra of the doped samples are all shifted to lower binding energies with respect to the undoped sample. This indicates that the addition of magnesium successfully in-

[4] Please see Figure 4.9 in 4.2.3 and associated discussion
[5] Please see Figure 4.1 in 4.1

troduces p-type doping. Besides, huge differences in the intensity of the Mg1s core-level shows that the Mg-content of the three doped samples differs quite substantially.

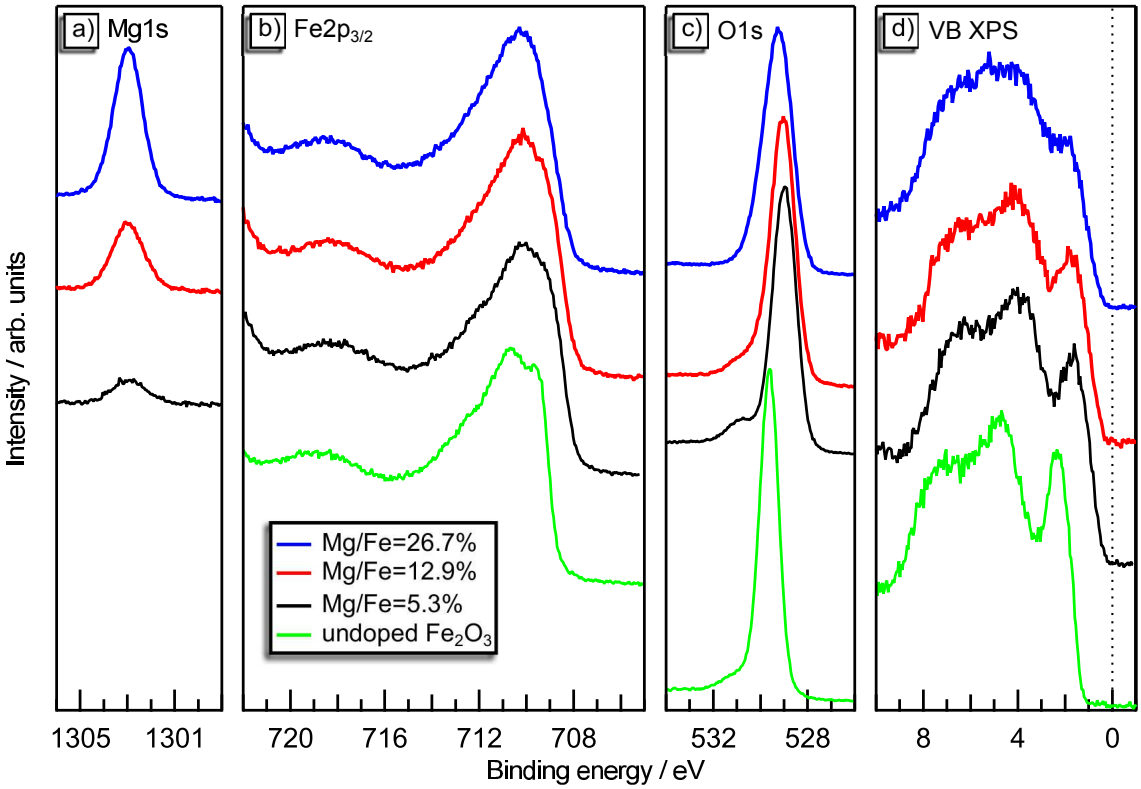

Figure 6.2: XP spectra of Mg-doped hematite thin films.

The Fe2p spectra of all samples are quite similar. Their satellite structure is characteristic for Fe^{3+} in all cases. There are some differences in the spectra of the doped sample with respect for the undoped sample. Namely, the "pre-edge" which is clearly observable for the undoped sample can hardly be recognized in the doped case. In combination with the results from the structural characterization this is taken as further evidence for a high degree of disorder within the samples.[61, 156]

The O1s core-level spectra show some differences as well. With respect to the undoped sample, the sample containing 5.3 % of magnesium exhibits a much more pronounced shoulder to higher binding energies. With increasing magnesium content, however, the shoulder seems to be less intense. At the same time, however, the emission becomes broader.

Finally, the valence band changes upon the addition of magnesium, too. For 5.3 % and 12.9 % Mg in the sample the shape is still quite similar to the undoped case. For both cases it shows the two emission lines representing the crystal field splitted Fe3d states[6].[34, 61]

[6] Please see Chapter 5 for discussion and assignment

With the addition of more magnesium, however, the two seperated emissions are no more observable. Instead, a plateau-like shape is observed. A similar shape has been described in part 5 to originate from the reduced symmetry in an amorphous samples. Here, however, the sample is crystalline as was observed in Figure 6.1a). The disorder, which was observed in the Raman spectra might certainly explain the change in valence band shape. There is, however, the disagreement in the degree of disorder, which was estimated to be the largest for the sample with 12.9 % magnesium. Either, this conclusion is false or another mechanism has to be considered.

In order to further investigate the difference in the electronic structure of the sample, difference spectra have been calculated. These are displayed in Figure 6.3. Here, the spectra of the sample containing 5.3 % of magnesium is used as reference and will be referred to as such in the following. The intensity of it's spectra was scaled by a factor y and the spectra are shifted in energy by a value of x. Then, these spectra were subtracted from the spectra of the other samples.

The spectra from the sample with 5.3 % of magnesium will first be compared to an undoped sample in order to investigate the changes from the addition of magnesium. Then, it will be compared to spectra from samples with higher concentrations of magnesium in order to discuss which influence the further addition of the dopant has. This procedure was chosen as it allows for a better distinction between the changes in hematite due to different amounts of magnesium.

Comparing the Fe2p spectra shows that the only difference between the undoped sample and the reference is in the almost non-existing "pre-edge" of the former. This was already observed from the spectra in Figure 6.2. The higher doped samples, however, show even less intensity here. This indicates that with the increasing dopant concentration the disorder becomes more severe. The possibility of the presence of another oxidation state of iron, namely Fe^{4+}, can neither be completely proven nor omitted here.[240]

The O1s difference spectrum between the reference and the undoped sample reveals two observations. First of all, there is a clear difference in the width of the peak. Upon doping the peak becomes much broader. This can be an indication of the aforementioned disorder but might also just be attributed to the addition of the dopant which changes the chemical environment of oxygen. In addition, there is the high-binding energy shoulder (HBES). Even though the undoped sample has some emission there as well, the reference clearly shows a higher intensity in the region between 531 eV to 533 eV. The origin of this emission is not known, yet.

It is, however, also observed in the O1s spectrum of the sample containing 12.9 % magnesium. Here, no difference in peak width to the reference can be observed. The intensity

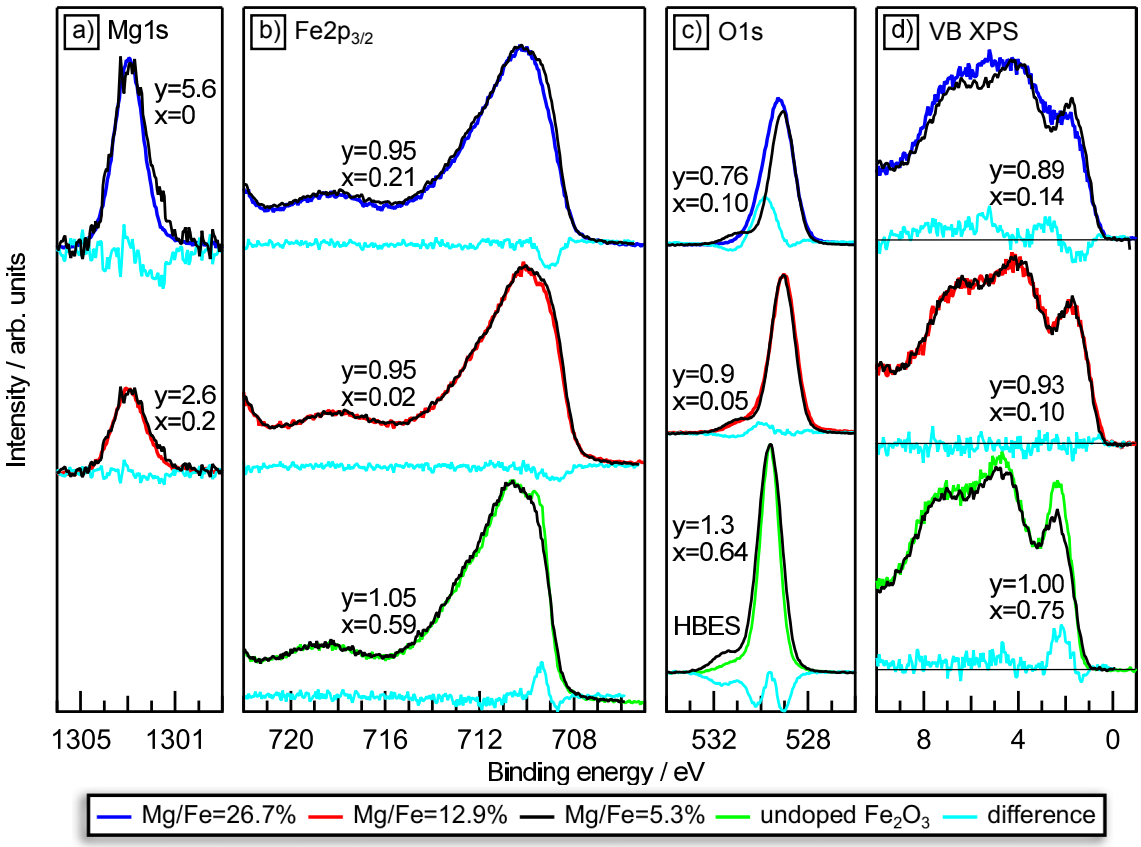

Figure 6.3: Difference spectra of the peaks shown in figure 6.2. For all difference spectra the spectra from the sample with 5.3 % Mg (black) was scaled in intensity and shifted and then subtracted. The scaling factor y and the shift x are given in the figure.

of the HBES is also the same. This could not be observed without the difference spectrum, however, as there seems to be an additional emission between 529 eV to 531 eV. This emission is even more intense in the most heavily doped sample where it explains the difference in the O1s spectrum to the reference. It's position could indicate that it belongs to MgO which was reported to show a O1s binding energy of 530.3 eV.[241, 242] The range of binding energy, however, can be found for the O1s-peak in other oxides as well.[76]

The difference in the valence band spectrum between the undoped sample and the reference is almost solely constricted to the two emission lines in the valence band which originate from the Fe3de$_g$- and Fe3dt$_{2g}$-states, respectively. The doped samples shows less intensity there. The effect is more pronounced for the Fe3de$_g$-state that forms the leading edge and emission peak at about 2 eV. Additionally, the doped sample shows a different slope at the valence band maximum. Due to this the valence band maximum of the reference slightly smears out into the band gap which results in a little higher intensity at the valence band maximum of the reference.

The observed changes in the DOS of the valence band upon the addition of magnesium show a good agreement with theoretical calculations of the DOS of undoped and Mg-doped hematite from Kosa et al.[239] They reported that the substitution of about 9.3 % iron by magnesium slightly changes the DOS. Due to the incorporation of Mg the DOS of the spin-down channel is shifted towards the Fermi energy which might be the explanation for the smearing out at the top of the valence band that was observed here. The lower intensity of the Fe3de_g-states could result from the assumable higher disorder within the doped sample which changes the crystal field splitting.[104] In part 5 it was observed that the change from amorphous to crystalline phase changes the DOS to a large extent. Here, the changes are not as pronounced but at the differences are mostly observed in the crystal-field splitted Fe3d-states it can be concluded that the DOS is affected by the higher disorder.

For a higher content of magnesium of 12.9 % no additional changes in the valence band are observed. This changes if the magnesium content is further increased. Now the two valence bands differ quite a lot. The changes are, however, the same as observed in Figure 5.1[7]. They are, therefore, attributed to a higher degree of disorder due to the higher content of magnesium.

Finally, comparing the Mg1s emission seems to reveal some more differences. Obviously, no difference spectra for the undoped sample could be created. The higher doped samples, show small deviations in the peak shape. The best agreement is achieved if the reference peak is adjusted to the high binding energy side of the sample emission. Then, for both higher doped samples the emission at smaller binding energies is larger for the reference.

This might be attributed to magnesium in a different environment and could be evidence that not all magnesium could be incorporated into the hematite lattice by substituting iron. On one hand this conclusion is being consolidated by the observation that the oxygen emission also shows some signal which might be connected to a different bonding of oxygen. On the other hand, there was no evidence of another phase in the structural characterization. It should also be noted that the signal of the reference had to be up scaled by a factor of 2.6 and 5.6 in order to give a good agreement with the measured emissions, respectively. These factors are rather large and will also affect the noise. Hence, the reliability of signal of the reference is lowered.

[7] Please note that the order of subtraction is different in the two figures. As a consequence the difference is mirrored around the x-axis.

A brief summary of the observations on Figure 6.3 is given by the following:

- Mg-doped films show a slightly changed DOS which can be explained by the combination of doping effects and disorder. For too high doping concentrations the valence band seems to be highly affected by the disorder and possibly also additional phase formation.
- The Fe2p-spectra also seem to be affected by disorder as the "pre-edge" vanishes. This seems to be more severe for higher doping concentrations.
- The O1s-spectrum broadens upon addition of magnesium. With a higher dopant concentration a new signal arises.
- For the Mg1s-emission evidence for another chemical environment around Mg can be observed.

These observation raise some disagreement to the observation from the structural characterization in Figure 6.1. There, the sample with 12.9 % magnesium seemed to have the highest degree of disorder. No other phase than hematite could be observed. For the XPS results, the degree of disorder seems to scale with the amount of magnesium and there is evidence for another phase in the Mg1s- and O1s-spectra.

This disagreement might be related to the different probing depths of the three methods that have been discussed so far. XRD is a bulk method that probes the whole sample. In Raman spectroscopy the wavelength of the laser (and the optical properties of the sample) determines the penetration depth. For the 532 nm laser, which was used the penetration depth is in the range of hundreds of nanometer which is again the whole film.[243] XPS on the other hand only gives information on the very surface (few nanometers). It may, therefore, be assumed that the bulk of the doped samples is different from the surface. Assuming MgO to be formed for high doping concentration is reasonable as it was observed before.[232]

In the samples presented here, however, any second phase would have to be X-ray amorphous as otherwise XRD would have detected it. XPS indicates that the degree of disorder is higher at the surface for higher amounts of magnesium. From this it can be assumed that the MgO-phase is present with a higher concentration on the surface than in the bulk. There is no clear trend of the disorder indicated by the Raman mode intensity with the dopant concentration. All observations combined might indicate a thin (and thereby not detectable by XRD and Raman) layer of MgO on the surface or small MgO clusters in the bulk below the XPS detection limit.

For Mg-concentrations around or below 5.3 % the XP spectra are very similar to the black ones presented in Figure 6.2 for samples that have been deposited at 400 °C. It was,

therefore, decided not to show these spectra here. They can be found in the appendix in figure A5. In addition, there are Raman spectra for the same samples to be found in figure A6. Here, all samples show the characteristic spectrum of crystalline hematite with the disorder indicating mode at 660 cm^{-1} being clearly observable. The conclusions drawn above do, therefore, apply to all samples which have been deposited at 400 °C.

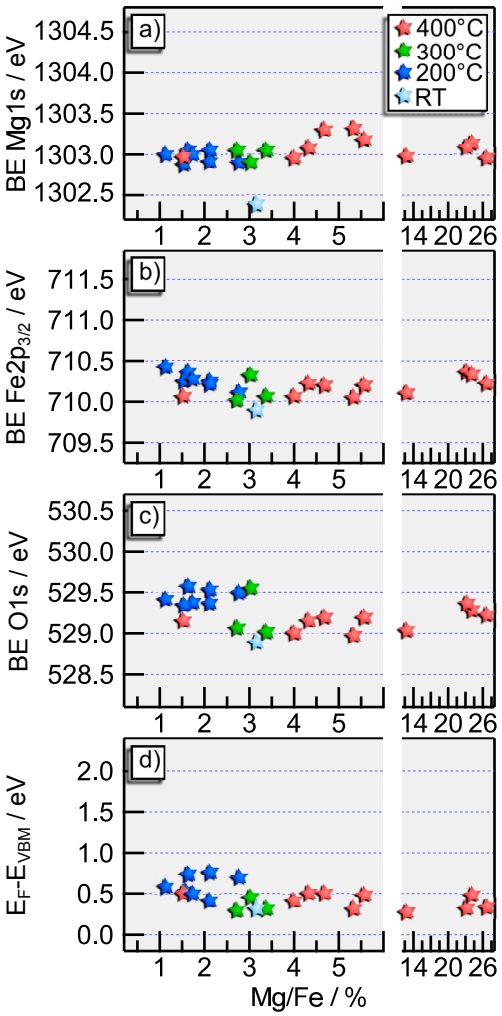

Figure 6.4: Binding energy positions in dependence of Mg-concentration

For a lower deposition temperature of 200 °C the same observations as for undoped samples are possible. They have a plateau-like appearance of the valence band and the Raman spectra indicate an amorphous structure. It was again decided to limit the discussion on these samples. The corresponding XP and Raman spectra can be found in Figures A7 and A8.

The binding energies of the core-levels and the valence band maximum for samples deposited at different temperatures and with different concentrations of Mg are presented in Figure 6.4. All Fermi level positions shown here are in the lower half of the optical band gap between 0.3 eV to 0.8 eV.

The core-level distance to the valence band maximum E_{CL-VB} are in average 528.7 eV, 709.7 eV, and 1302.6 eV for the O1s-, $Fe2p_{3/2}$-, and Mg1s-core-level, respectively. In case of the former two these values are higher than for undoped hematite samples by 0.35 eV and 0.25 eV for the O1s- and $Fe2p_{3/2}$-core-level, respectively. This topic will be further discussed with the results from other dopants in Chapter 6.5.

In Figure 6.4 a parallel behavior of the binding energy is only given to a good degree for the Fe2p- and O1s-core-level of the samples which have been deposited at 400 °C. The position of the Mg1s-core-level shows some deviation. This peak, however, has the lowest signal-to-noise-ratio and, therefore, the highest uncertainty in peak position.

6.2 Silicon doping

The expected n-type dopant silicon was introduced into the hematite thin films by co-sputtering from a silicon target. The depositions were performed at temperatures of 300 °C and 400 °C. While the power at the iron target was kept constant at 60 W, the power at the silicon target was altered between 15 W to 30 W. The same applies for the target to sample distance, where the distance of the iron target was kept at 8 cm for all depositions while the distance of the silicon target was changed between 8 cm to 12 cm. The oxygen content in the Ar/O_2 mix was 8 % during all depositions at a total pressure of 0.5 Pa. All samples were deposited onto quartz/platinized quartz substrates.

The structural properties of the thin films were evaluated with the help of XRD and Raman measurements. These are presented in Figure 6.5 for three samples with a silicon to iron ratio of 4.2 % to 4.9 %. All three samples have been deposited at 400 °C. Even though the dopant concentration does not differ dramatically there are significant changes in the structural properties.

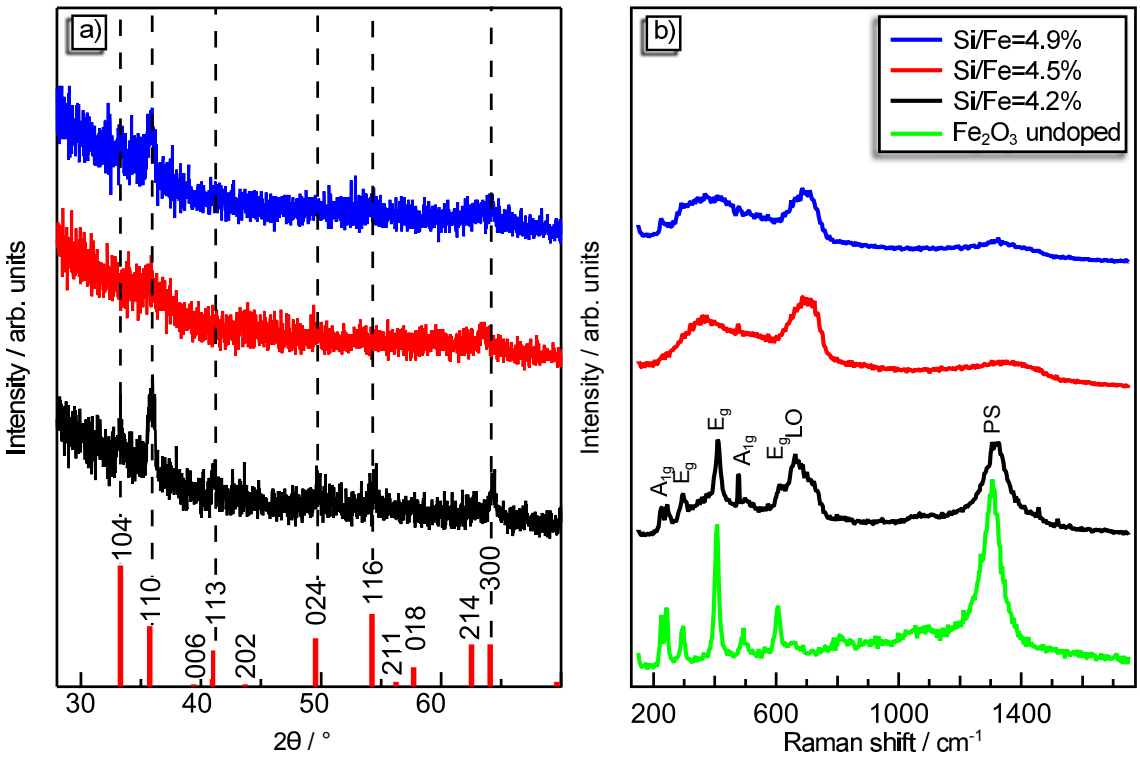

Figure 6.5: Structural characterization of silicon doped hematite deposited at 400 °C by a) XRD and b) Raman spectroscopy. The films show different doping levels. The XRD reflections in a) were identified with the help of the pdf-card 13-534 ($\alpha - Fe_2O_3$) which is included as bar graphs. The green graph on the bottom of b) shows the Raman spectrum of an undoped sample, which was deposited under the same conditions except for the addition of silicon.

For the lowest dopant concentrations the sample exhibits some reflections in the XRD pattern in Figure 6.5a). These are much weaker than compared to undoped or magnesium-doped samples. The highest intensity arises from the (110) reflection which has been observed on, both, undoped and doped hematite before[8].

For higher silicon concentrations the intensity of the reflections becomes even weaker. This is especially the case for the sample that shows a dopant concentration of 4.5 %. Still, some signal can be observed for the position of the (110) reflection indicating that the orientation of the samples is similar despite being less crystalline. Please note that the thicknesses of all three samples are in a similar range between 205 nm to 234 nm.

The sample with 4.5 % silicon concentration was the thinnest. The uncertainty in the determination of the thickness using profilometry is estimated to be at least 10 %. For the two samples with the higher silicon concentrations the uncertainty should be estimated to be even higher. Here, it was not possible to obtain three measurements on each side of the substrate that was covered by the mask[9]. Additionally, the values that could be obtained showed a rather large deviation from the mean value. Assuming a thinner film can explain the less intense signal in the XRD pattern for both cases.

The disorder within all samples, however, is significant. This becomes evident from the Raman spectra in Figure 6.5b). While the sample with 4.2 % silicon shows a weakened but still characteristic Raman spectrum of hematite the two higher doped samples show spectra of amorphous hematite.[61, 144, 163, 244]

In the spectrum of the lowest doped sample the LO mode, which indicates disorder is quite intense already compared to the intensity in the spectrum of the undoped samples. This shows that the sample also exhibits a high disorder as it was observed for Si- and Ti-doped hematite before.[172, 225, 227, 245] It is, therefore, most likely that its presence indeed originates from the incorporation of the dopant into the hematite lattice at the iron site.

The two samples with the highest silicon contents clearly show a broadened LO mode. Additionally, the sample with the second highest dopant concentration shows a small signal from the A_{1g} vibration at about 500 cm^{-1}. For the sample with the highest silicon content a small but clearly observable feature at about 220 cm^{-1} is observed.

This feature can be assigned to arise from the A_{1g} mode of hematite. In addition, the spectrum shows small intensity gains at the positions of the characteristic modes for hematite. Their presence shows that the appearance of $\alpha - Fe_2O_3$ related X-ray reflections

[8] Please compare to Figure 4.1, Figure 4.10, and Figure 6.1
[9] Please see Chapter 3.3.5

with higher intensity compared to the sample with 4.5 % silicon is also resembled in the Raman spectrum. As a consequence, the disorder within the sample is most likely less compared to other samples.

The Raman spectra in Figure 6.6 reveal that in general a higher silicon content is accompanied by a higher disorder to a degree that the samples are most likely more or less amorphous. This could be accompanied by the formation of a silicon oxide of an unknown stoichiometry. This assumption is solely based on the similarity to the observations from the Mg-doping in Chapter 6.1 in the structural analysis at this point. It will be discussed later again in combination with results from PES measurements.

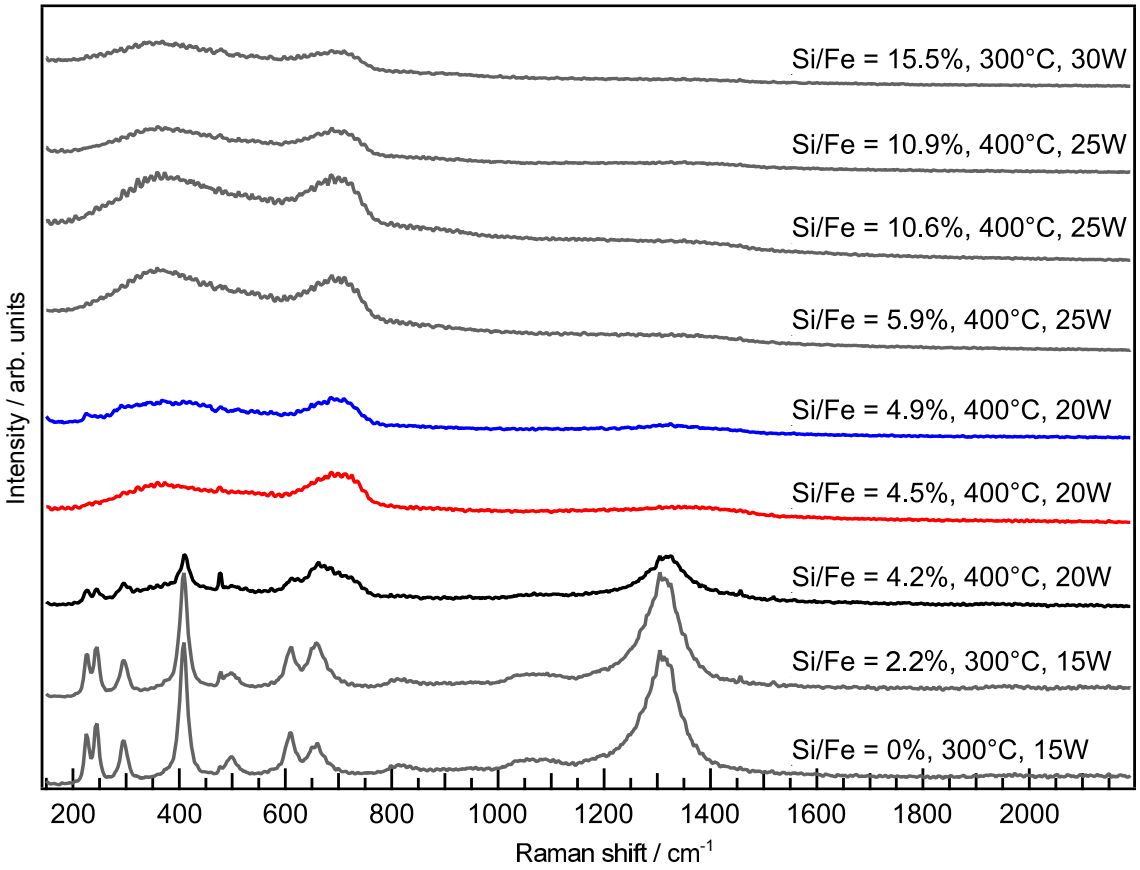

Figure 6.6: Additional Raman spectra for Si-doped Fe_2O_3 . The spectra are ordered with the silicon content from bottom to top. For each sample the silicon content, deposition temperature, and power at the silicon target is indicated.

It is evident that the spectra with high silicon content do not exhibit modes that are characteristic for hematite. Glasscock et al. observed very similar Raman spectra for DC-magnetron sputtered Si-doped Fe_2O_3 with a dopant concentration of 5.0 %.[225]

The less silicon-containing samples show a Raman spectrum which is characteristic for $\alpha-Fe_2O_3$.[223] Whether the tendency to form amorphous films described here are due to the high RF-power or the high silicon content is not completely clear. Observation and

discussion on Zr-doped hematite on Figure 6.10, however, suggest that the high sputter power and not the dopant concentration is responsible for the loss of structural integrity.

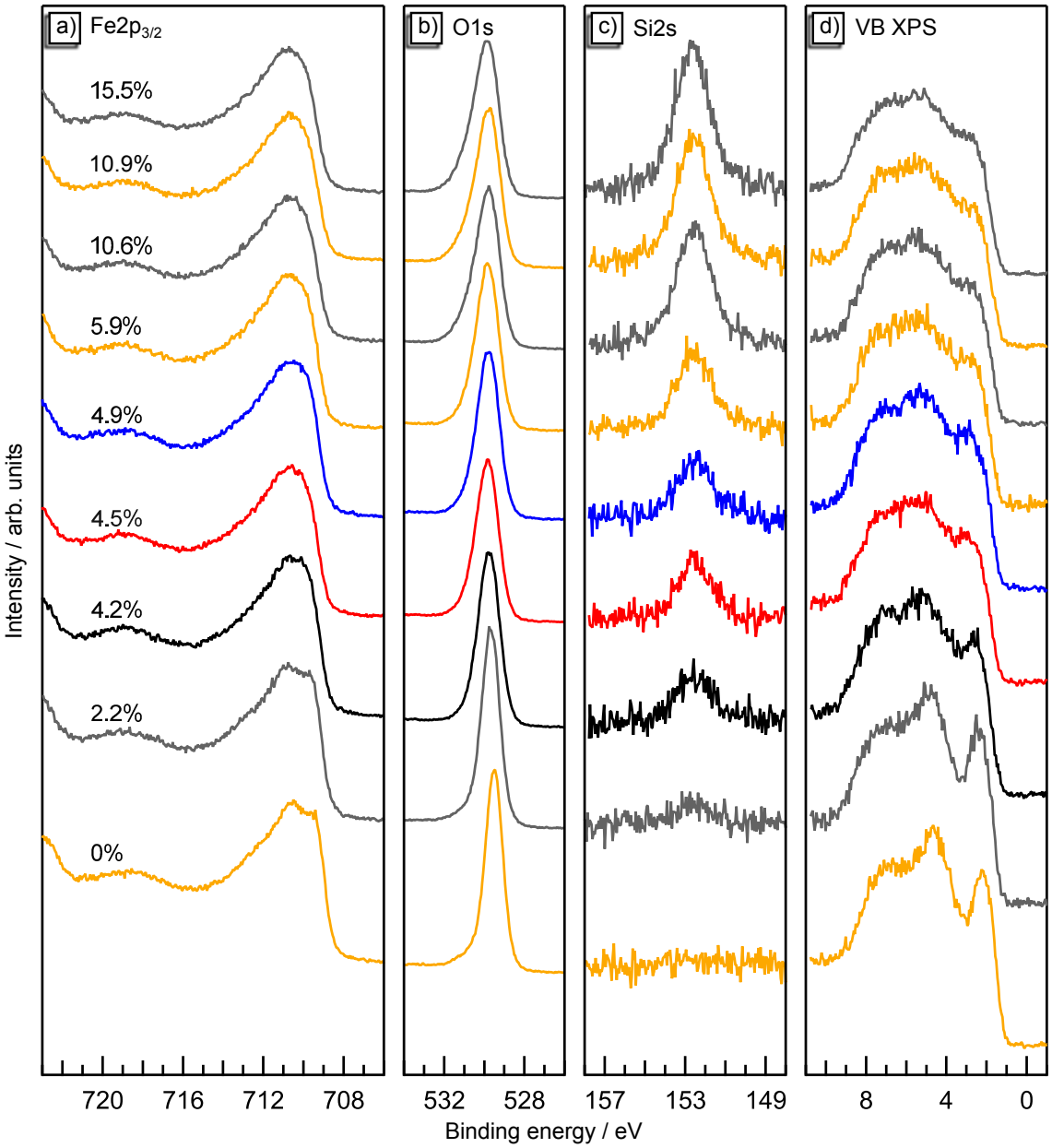

Figure 6.7: XP spectra of Si-doped hematite thin films.

For the sample labeled with Si/Fe=0 % no silicon is observable in the XP spectra of Figure 6.7. The disorder indicating LO-mode at 660 cm^{-1} is, however, increased if compared to an undoped sample. This can be regarded as evidence for the incorporation of silicon into the hematite lattice. The amount of silicon, however, is most likely less than 1 % which is a good agreement with the detection limit of XPS.[246]

It has to be noted that the ordering of the spectra in Figure 6.6 and Figure 6.7 not only resembles the amount of silicon but also the power which was applied to the silicon

target. A higher power at the target manifests itself in a higher kinetic energy (velocity, momentum) of the sputtered species. The increased energy of the sputtered species can result in a higher rate of defect formation.[112, 247] It cannot be completely excluded that besides the silicon content also the energy of the silicon species in the sputter process influence the order within the thin films.

As it was observed before, the increasing disorder within the samples affects the shape of XP spectra. These are presented in Figure 6.7. The changes are as expected evident from the "pre-edge" of the $Fe2p_{3/2}$ and the clear emission maxima in the valence band which disappear with the increasing disorder. As these observations have been discussed in more detail in Chapter 4.2.3 and Chapter 5 no further discussion is needed here.

Table 6.1: Binding energy of silicon in different phases from literature. The values are given as reported in the cited references. For some a range was given in the original studies.

Phase	Valency	Coordination	BE Si2p	BE Si2s	Ref.
Si	Si^0	4Si	99.3*	150.55	[248]
			99.5	-	[249]
Si_2O	Si^{1+}	3Si,1O	$Si^0 + 0.8$	-	[250]
SiO	Si^{2+}	xSi,(4-x)O	103.5	-	[251]
			$Si^0 + (1.7 - 2.2)$	-	[252]
Si_2O_3	Si^{3+}	1Si,3O	$Si^0 + (2.9 - 3.4)$	-	[250, 252]
SiO_2	Si^{4+}	4O	104.1	155.1	[253]
			103.5	-	[249]
			103.0	-	[251]
			$Si^0 + (4.1 - 5.4)$	-	[250, 252]
Fe_2O_3	Si^{4+}	6O	100.5	-	[254]
			102.4***	153.5*	[53]
			102**	154**	[223]
			102.1***	-	[255]
			102****	-	[214]
			101.5	152.6 ± 0.2	This work

* Binding energy graphically extracted

** Spectrum very noisy

*** Spectrum not shown

**** Two Si-species (Si^0 and Si^{4+}) observable.

The position of the Si2s core-levels is about 152.6 ± 0.2eV for all samples (see also Figure 6.8). The binding energy of silicon is often used to verify its oxidation state. As can be seen from table 6.1 this value is significant smaller than reported binding energies of tetravalent silicon in quartz.[253]

The usefulness of this comparison, however, is questionable as the bonding environment around silicon is different in quartz and hematite, respectively. In the former silicon is four-fold coordinated in an oxygen tetrahedron while in the latter it is six-fold coordinated in an oxygen octahedron, if substitution of iron by silicon is assumed. The difference in environment will certainly influence the binding energy of silicon.

It was shown that a change from four-fold to six-fold coordination with oxygen lowers the binding energy by about 1.5 eV.[256] In addition, changes due to the difference of the electronegativity of iron compared to silicon can be expected. For other dopants in hematite these considerations have been briefly discussed before to explain lower binding energies of the dopants compared to a binary oxide with the same cation valency.[228, 257]

It seems, therefore, more useful to compare the binding energy to data for Si-doped hematite. Unfortunately, the number of reports is rare and in general the quality of the spectra is poor. In addition, most authors only measure the Si2p core-level which is superpositioned with the emission from Fe3s. It was found that for low doping concentration the Si2p emission is not usable[10]. Hence it was decided to rely on the measurement of the Si2s core-level in this work.

Comparing the binding energy of this emission to data from literature is, however, also challenging. Only two studies, which report the position of this particular emission in hematite, could be found.[53, 223] Both, however, show rather poor spectra. In addition, the samples exhibit differences compared to the thin films of this thesis which should not be neglected, e.g. a reduction observed in the Fe2p-spectrum. In addition a high-intensity component in the O1s-spectrum can be observed. Thus the literature data suggest high amounts of adsorbates not present on the thin films of this work or not very well defined films.

Despite these inconsistencies the substitution of iron by tetravalent silicon seems to be most reasonable for several reasons. First of all, Raman spectroscopy shows the strong LO-mode at $660\,\mathrm{cm}^{-1}$ already for low silicon concentrations. From this observation an incorporation of silicon into the hematite lattice onto the iron position is suggested.
Secondly, despite the disorder induced effects that were discussed above there are no severe changes in the XP spectra with increasing Si concentration e.g. a second component within the O1s core-level. This shows that the samples have a lot of similarities at high

[10] Please see Figure A9. BE of Si2p in table 6.1 from these samples.

and low doping concentrations. This is true not only for the shape but also for the intensity of the spectra. Despite a huge variation in silicon content there is no severe damping of the iron signal observed which would be expected if a second silicon rich phase e.g. SiO_2 would be present.

Finally and most importantly the position of the Fermi energy for Si-doped samples will be discussed. For most samples in Figure 6.7 it is around 1.3 eV whereas for undoped hematite with similar deposition conditions it is around 1.1 eV. Of all possible valencies for silicon in table 6.1, only tetravalent silicon will probably cause this n-type doping.

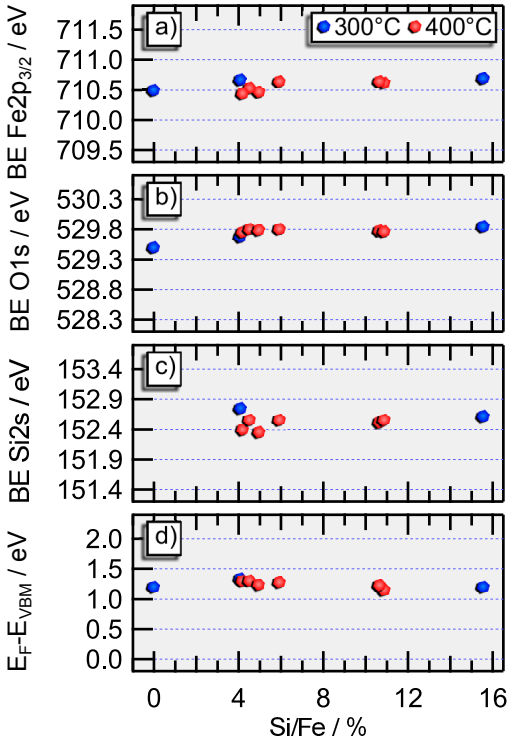

Figure 6.8: The dependency of the Fermi level position on the silicon concentration.

The shift of the Fermi level is, however, not depending on the concentration of silicon. There are at least two possible mechanisms for this behavior. These can also appear at the same time.

First, it should be kept in mind that silicon can only act as a donor if it can transfer an electron into the lattice. As will later be discussed in more detail the transfer happens from the donor to an iron site (also see Chapter 6.7).[40] As a consequence, silicon is in a tetravalent state. It is, however, possible to calculate the charge transition state of Si^{4+}/Si^{3+}. At this position the electron is not transferred to iron anymore. As a consequence, the Fermi level is pinned at this position.

This charge transition point was calculated to be positioned 1.41 eV above the valence band maximum.[40] This energy position is only slightly above the highest Fermi energy that has been achieved by the silicon doping in this thesis. It might be assumed, that this point has already be reached with only a little amount of silicon and the further addition of the dopant does not result in additional electrons anymore.

A second mechanism for the Fermi level behavior in silicon doped sample can be suggested to originate from the amount of silicon and of the bonding properties of silicon towards oxygen. The dopant can only act as such if it is positioned in the hematite lattice. It is, however, also possible that a phase separation occurs and silicon is present in a oxide. This does indeed seem to be likely as the silicon concentrations presented here are

quite large. For other semiconductors the doping levels are in the range of ppm whereas here percents are achieved.[258] In addition, the ionic radii of silicon (0.4 Å) and iron (0.645 Å, high-spin) in a sixfold coordination are quite dissimilar.[259] As a consequence the incorporation of silicon into the hematite lattice on an iron site would result in tensile stresses and be energetically more unfavorable compared to a dopant with a ionic radius that is more similar to the one of iron. At a certain amount of silicon the tensile stresses would be too large. Consequently, defect formation such as phase separation can occur. Following this argumentation, leads to the conclusion that it is most likely that the observed position of the silicon emission originates from Si^{3+} species which either are positioned on the iron site of the hematite lattice or are present in a silicon oxide. Especially, the second mechanism is seen to be very likely to occur. The resulting silicon oxide that can be assumed would then be Si_2O_3. There are, however, some Si^{4+} species present as well which lead to the doping effect. Whether the other authors have achieved a higher amount of Si^{4+} on the iron site remains questionable as such mechanisms are governed by thermodynamic laws and cannot be avoided easily.[40, 258, 260]

The core-level position in Figure 6.8 also show that there is no shift of Fermi level with the increasing silicon content. The distance of the $Fe2p_{3/2}$ and O1s core-level to the valence band maximum, however, is not the same as for undoped samples. This issue will be discussed in detail with the results from differently doped samples in part 6.5.

6.3 Zirconium doping

In order to investigate a second n-type dopant besides silicon and examine whether a different element can shift the Fermi level in hematite to higher positions zirconium was introduced into the sputter process by using a metallic zirconium target. The choice for this particular dopant was done on basis of the electrochemical potentials of the two reactions

$$SiO_2(s) + 4H^+ + 4e^- \rightleftharpoons Si(s) + 2H_2O$$
$$ZrO_2(s) + 4H^+ + 4e^- \rightleftharpoons Zr(s) + 2H_2O$$

with a standard potential of $E^\circ = -0.91\,V$ for the former and $E^\circ = -1.553\,V$ for the latter.[109] From these potentials it was assumed that the charge transition point of zirconium could potentially be positioned higher in energy than the CTP of silicon which would allow for a higher Fermi level position i.e. more charge carriers.

The results which will be discussed in the following were measured on samples which have been deposited at 400 °C onto quartz and platinized quartz. The oxygen content in the sputter process was always 8 % at a pressure of 0.5 Pa. For all depositions the distances of the targets to the samples was kept at 8 cm and 10 cm for the iron and zirconium

target, respectively. The deposition was performed with different RF powers. While this parameter was kept at a constant 60 W for the Fe target, it was varied between 15 W to 45 W for the Zr target.

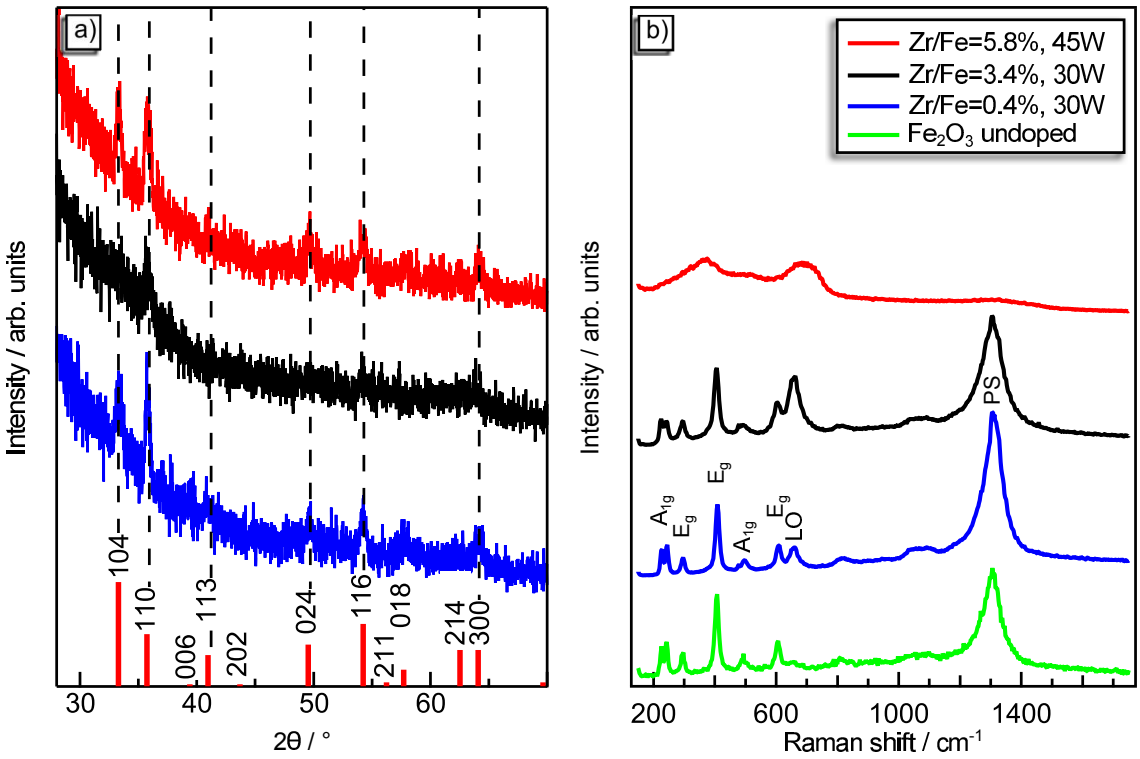

Figure 6.9: Structural characterization of zirconium doped hematite deposited at 400 °C by a) XRD and b) Raman spectroscopy. The XRD reflections in a) were identified with the help of the pdf-card 13-534 ($\alpha - Fe_2O_3$) which is included as bar graphs. The green graph on the bottom of b) shows the Raman spectrum of an undoped sample which was deposited under the same conditions except for the addition of zirconium.

Results from the structural characterization by XRD and Raman spectroscopy of three samples are shown in Figure 6.9. The films show different doping levels depending on the power applied to the zirconium target. Observation of the zirconium concentration and applied power in the legend of Figure 6.9 reveals that the zirconium content follows the power which was applied at the zirconium target. With the tuning of this parameter a variation in the zirconium content between 0.4 % to 5.8 % could be achieved.

The addition of zirconium has a direct impact on the structural properties of the thin films. The XRD pattern of all three films show reflections which can be assigned to originate from the hematite phase, while no traces of any crystal structure of ZrO_2 can be found.[187, 261–263]

What has changed, though, is the orientation of the thin films. For undoped samples a preferred growth in (110) was observed[11]. Once zirconium is added, the (104) reflection

[11] Please see Figure 4.1

increases in intensity which shows that the samples are not as oriented as in the undoped case.[112] This seems to be the case for all three samples in Figure 6.9.

For the sample with the second highest Zr-concentration the intensity of the XRD pattern is slightly lower than for the other two samples. The reason for this observation is not clear. It might be attributed to a slightly lower temperature during the deposition.

The Raman spectra in Figure 6.9 do not show tremendous differences for the first two doped samples. Their spectra are characteristic for the hematite phase with an increased LO. As has been discussed in previous parts of the work this mode can be regarded as evidence for the incorporation of the dopant into the hematite lattice on the iron site.[144, 164, 166–172] The increased intensity of this mode with the Zr-concentration which can be observed for the first two samples has been observed before but was falsely attributed to originate from traces of magnetite[12].[257] No traces of any crystal structure of ZrO_2 can be found in the Raman spectra.[262]

The sample with the highest zirconium concentration shows a different Raman spectrum. The characteristic peaks of hematite cannot be identified anymore and the spectrum resembles that which would be expected for an amorphous hematite film.[61, 144, 163, 244] This sample was deposited using a higher power at the zirconium target. It was observed that for Zr-contents above 4 % associated with an applied power at the zirconium target of 35 W or more the Raman spectrum starts to show these changes. This is being shown in the additional Raman spectra presented in Figure 6.10.

Comparing these spectra to literature suggests that the applied power is responsible for the higher disorder evident in the Raman spectra. Kumarn et al. reported Raman measurements on Zr-doped hematite with Zr-contents up to 10 % for wet-chemically deposited and in air post-annealed thin films. Their spectra show an increasing LO-mode and the characteristic peak of the hematite phase for all Zr-contents.[257] This indicates that the high kinetic energy of the Zr-species when sputtered with a high RF-power leads to an increased defect density resulting in the observed Raman spectrum. Post-annealing in an oxygen containing atmosphere to prevent reduction might be able to reduce the defect density.

Spectra from XPS measurements on representative samples are presented in Figure 6.11. Besides the spectra of the three samples, which have been discussed in Figure 6.9, there are spectra shown in light blue of the sample which showed the highest Fermi level position (1.68 eV) of all doped samples.

[12] The Fe2p spectra from their work clearly only show Fe^{3+}

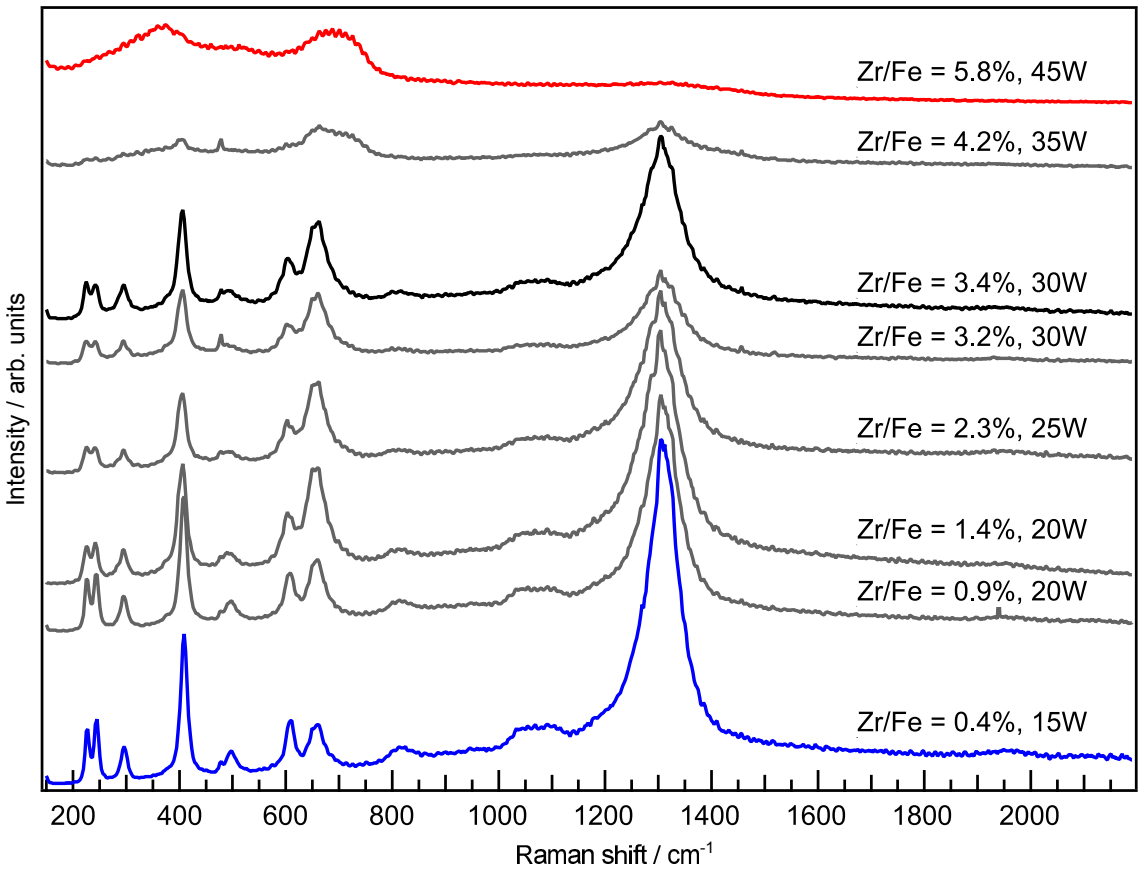

Figure 6.10: Additional Raman spectra for Zr-doped samples which have all been deposited at 400 °C.

No changes in the shape of the emission can be observed for the three first samples. This could be expected as the Raman spectra of the samples containing 0.4 % and 3.4 % zirconium were quite similar. No structural characterization was performed on the sample with 2.9 % zirconium which showed the highest Fermi level as this sample was used for an interface experiment with the deposition of ITO[13].

For the highest Zr-content the sample shows a Fe2p emission structure and valence band shape which could be expected for amorphous Fe_2O_3 .[61, 156] These shapes have been discussed before in part 5 of this work. Hence, a discussion is being omitted here.

It should be noted that the intensity of the Zr3d emissions increases from bottom to top of Figure 6.11. There is, however, no change in the appearance (FWHM and intensity ratio) of thelines. This shows that no change in the environment around Zr is present for these samples.

The binding energies of the core-levels and the position of the Fermi level within the band gap in dependency of the zirconium concentration is being shown in Figure 6.12.

[13] Discussed in part 7.3.3

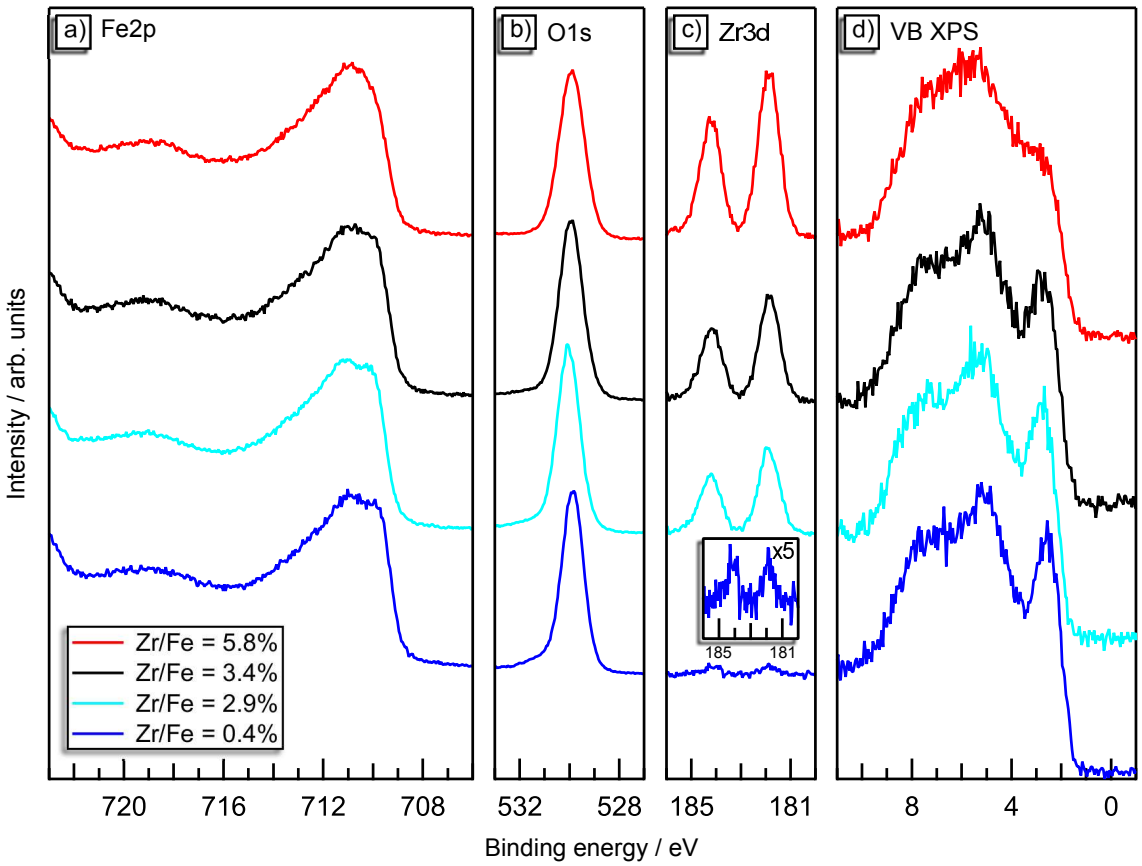

Figure 6.11: XP spectra of Zr-doped hematite. The sample in light blue containing 2.9 % zirconium shows the highest Fermi level of all doped samples.

All samples show a Fermi level position between 1.3 eV to 1.68 eV above the valence band maximum. This is higher than in undoped or Si-doped hematite thin films. There is, however, no obvious dependency on the amount of zirconium. It seems that the addition of this dopant in any amount raises the Fermi level. The highest position was being found for a sample that contained 2.9 % of Zr. Around this amount of zirconium there seems to be a maximum which is not only resembled in the Fermi level position but also in higher binding energies of the iron and oxygen lines. The statistics on this are, however, questionable due to the low number of samples. It should also be noted that the samples with higher doping concentrations also showed more disorder. In case of defect creation this could result in a compensation of the additional zirconium.[232, 264] Post-annealing to lower the possibly created defect density could solve the issue and may allow for higher Fermi level positions.

The binding energy position of the core-levels are increased as well if compared to undoped samples. In average the distance of the core-level to the valence band maximum is 709.3 eV, 528.5 eV, and 180.4 eV for the $Fe2p_{3/2}$ O1s and $Zr3d_{5/2}$ core-levels, respectively. The distances for the iron and oxygen emission are slightly different than for undoped films. This issue will be discussed in Chapter 6.5 in more detail.

For the $Zr3d_{5/2}$ core-level position in hematite only a few references are available. Franking et al. reported a binding energy of 182.6 eV.[245] A slightly lower binding energy of 182 eV was reported by Su et al. with an associated Fermi level position of 1.55 eV above the valence band maximum.[53]

In both cases the authors concluded on a Zr^{4+} oxidation state from these binding energies. A similar conclusion was being drawn for a much lower binding energy of 180.8 eV in another work.[257]
For zirconium dioxide the binding energies of this peak can be found to be in the range around 182 eV.[263, 265]
For the samples discussed here the binding energy of the $Zr3d_{5/2}$ core-levels are around 181.85 eV. This agrees quite well with the position reported from Su et al.[53] In their work, also the distance to the Fermi level position agrees very well with the value derived from the binding energies in Figure 6.12.

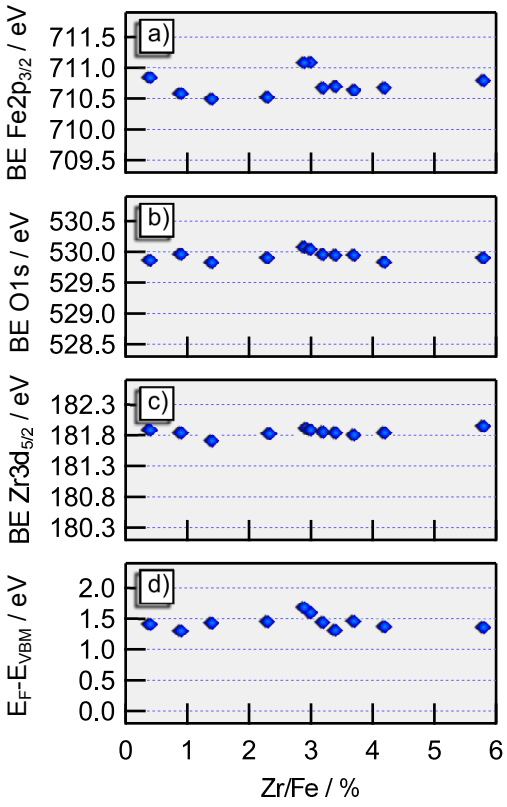

Figure 6.12: The dependency of the Fermi level position on the zirconium concentration.

For silicon as dopant it was argued that the oxidation state was Si^{3+} and that this might be correlated with the charge transition point of silicon in hematite or a phase separation. For zirconium the Zr^{4+} state seem to be present if the results from Su et al. are considered. It might be, however, that their assignment was already a mistake. The large scattering of the binding energies with a similar assignment gives reason to doubt. In 6.7 this issue will be discussed in more detail and it will be tentatively concluded that not all dopant can be in the +4 oxidation state as then a change in the oxidation state of iron would need to be observable. The higher position of the Fermi level within the band gap compared samples confirms the n-type doping that was expected for zirconium. Also confirmed is the assumption that the electrochemical potential that is higher for zirconium than for silicon can be used to predict the effectiveness of a dopant.

6.4 Surface potentials of doped hematite

Changing the position of the Fermi level within the band gap of a conventional semiconductor usually results in a change of the work function whereas it is generally assumed that the ionization potential remains constant. In order to examine whether this is also the case for the doped hematite samples the surface potentials where determined from UPS measurements[14].

The resulting work functions are presented in Figure 6.13a) in dependency of the Fermi level position for undoped and doped hematite thin films. The diagonal lines correspond to constant ionization potentials. In Figure 6.13b) and c) the work function ϕ and Fermi level position $E_F - E_{VBM}$ are displayed in dependency of the relative dopant concentration, respectively.

This parameter is given by the ratio of the dopant concentration to the maximal dopant concentration of the respective dopant. The maximal dopant concentrations for the three dopants were 8.2 %, 15.5 %, and 5.8 % for doping with Mg, Si, and Zr, respectively. In case of the undoped thin films the oxygen content in the sputter gas relative to the maximal oxygen content of 20 % was used to include the data. If not indicated differently all samples in Figure 6.13 were deposited at 400 °C.

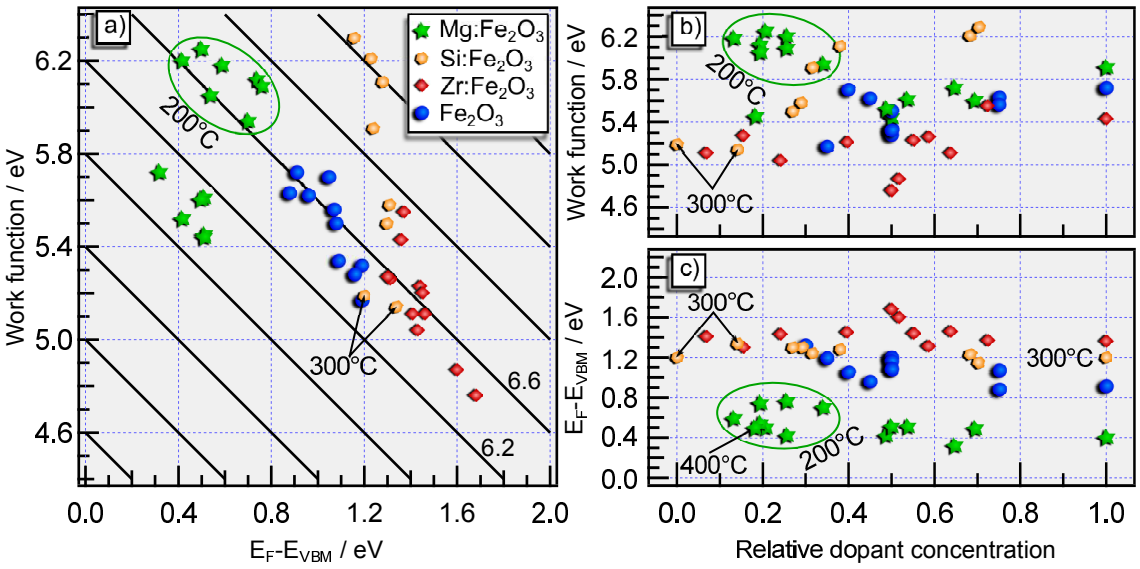

Figure 6.13: Surface potentials of doped and undoped iron oxide thin films determined by UPS. a) Work function versus Fermi level position. The straight lines indicate constant ionization potential which can be read from the point of zero Fermi level. b) and c) Work function and Fermi level position in dependence of relative dopant concentration (further explained in the text). If not indicated differently all samples were deposited at 400 °C.

[14] Procedure explained in 3.3.2

For most samples in Figure 6.13a) the combination of work function and Fermi level position result in an ionization potential around 6.6 eV and a range of 6.2 eV to 7.0 eV. Especially, all undoped and zirconium doped samples fall into this range indicating that for a Fermi level range of 0.8 eV to 1.7 eV the changes in Fermi level position are directly reflected in the work function which results in a constant ionization potential.

The Mg-doped samples show an interesting dependency on the deposition temperature. Samples that have been deposited at 200 °C show an ionization potential of 6.6 eV. The samples that were deposited at 400 °C, as it was the case for all undoped and Zr-doped samples, exhibit, however, a much smaller work function. Due to this the samples are found at ionization potentials between 5.8 eV to 6.2 eV. It should be noted that Mg-doped thin films which have been deposited at 300 °C are positioned between these two groups. For the sake of clarity within this figure, however, their presentation was omitted.

From the Si-doped samples four data points are within ionization potential of 6.2 eV to 7.0 eV as well. There are, however, also four point outside this range. These samples all show a quite similar Fermi level of 1.2 eV whereas the work function increases from 5.9 eV to 6.3 eV. Due to this dissimilar behavior of the two energies the ionization potential of the samples is increased reaching values of up to almost 7.5 eV.

In order to examine the different behavior of the Mg-doped thin films deposited at 400 °C and the Si-doped samples the work function and Fermi level position are displayed in dependency of the relative dopant concentration (definition given above) in Figure 6.13b) and c). For the Si-doped films it is immediately obvious that the observations stated above are due to the different dependency of ϕ and $E_F - E_{VBM}$ on the concentration of the dopant. While the latter does not show any significant changes with an increasing dopant content, the former shows a steady raise.

This raise causes the increase in the ionization potential. Tt has to be clarified, however, that all of the possible reasons given in the following are only of speculative nature. The exact reason for the changes in the ionization potential remains unclear. From the results discussed in the previous chapters it might be reasonable to assume the formation of an oxide film to be responsible. But it would need further, more sophisticated experiments, to prove this assumption.

From the structural characterization it was deduced that a high silicon content is manifested in a higher disorder within the samples. This disorder could be responsible for the change in ionization potential. Possible mechanisms can be either direct e.g. a change in the electronic structure or indirect e.g. changes in the surface composition or surface dipole.[38, 266–268]

Alternatively, strain induced by the high dopant concentration can also change the ionization potential tremendously as was shown by Chen et al. for $\alpha-Fe_2O_3$ films.[39] Another possibility that should not be neglected is the formation of an ultra-thin SiO_x layer on the surface. Such a segregation could be assumed due to the high silicon concentrations and the elevated temperatures during deposition.[269]

It was shown that the work function of metals can be increased by adding an ultra-thin layer of SiO_2 due to a charge-transfer at the interface.[270] This charge transfer alters the surface dipole which results in an increased work function. Obviously the contact in this work is different but a charge transfer at the interface of two semiconducting/insulating oxides is still possible.[114] Interestingly, the same study that suggests an increase in work function by an ultra-thin SiO_2 layer also shows by the addition of an ultra-thin MgO layer the work function can be decreased.[270] The mechanism for the metal-insulator interface in their study does not involve charge transfer but solely considers a compression of the metal electron density.

Assuming the possibility of a similar effect on the work function of hematite it could be deduced that the decrease in the work function by depositing Mg-doped thin films at 400 °C originates from the formation of an ultra-thin MgO_x film on the surface. This would, then, indicate that a deposition temperature of 400 °C is too high in order to deposit thin films with a stable, homogenous composition. It has, however, to be noted as well that the lowest Fermi level are reached at this deposition temperature.

At this point the question arises in how far the formation of ultra-thin oxide films on the hematite samples are reasonable. The structural characterization by XRD and Raman spectroscopy did not show any evidence for the films. The same was the case for the XPS analysis where no conclusive evidence for the formation of a thin oxide layer was found. Hence, the thickness of these oxide films has to be very low in order to allow the XP spectra to remain unchanged (including attenuation).

A thickness in the sub-nanometer regime can be expected as even the highly surface sensitive UP valence band spectra did not show any direct evidence for another phase. One indication, however, that the segregation of SiO_2 is possible is a sample that showed a silicon content above 30 %. Here, the O1s emission clearly showed the formation of a second oxide phase. Until now, the sample was omitted from the discussion due to this apparent second phase. The spectra are, however, shown in Figure A10. The O1s emission shows a clearly observable shoulder which is evidence for a SiO_2 phase at the surface.

6.5 Core-level to valence band maximum distance of doped hematite

In Chapter 4 the differences of the $Fe2p_{3/2}$ and O1s core-levels to the valence band maximum in undoped samples were found to be 709.5 eV and 528.4 eV, respectively. Generally, it can be assumed that these values are a materials constant and do not change when the Fermi level is shifted.[134] As a consequence, it can be assumed that other mechanisms occurred in the samples that prevents the core-level to valence band maximum distance from being constant.

Comparing the binding energies of the two core-levels of undoped and differently doped samples in Figure 6.14 shows that this assumption does not fully apply for hematite. This is indicated by the slope S of the doted lines. In an ideal semiconductor with fully screened photoholes this slope should be $S = 1$.[121] For hematite, however, values of $S = 0.7$ and $S = 0.87$ are being found for the $Fe2p_{3/2}$ and O1s core-levels, respectively. As it will be seen, a full explanation of this observation cannot be given here. Possible contribution should, however, at least be discussed.

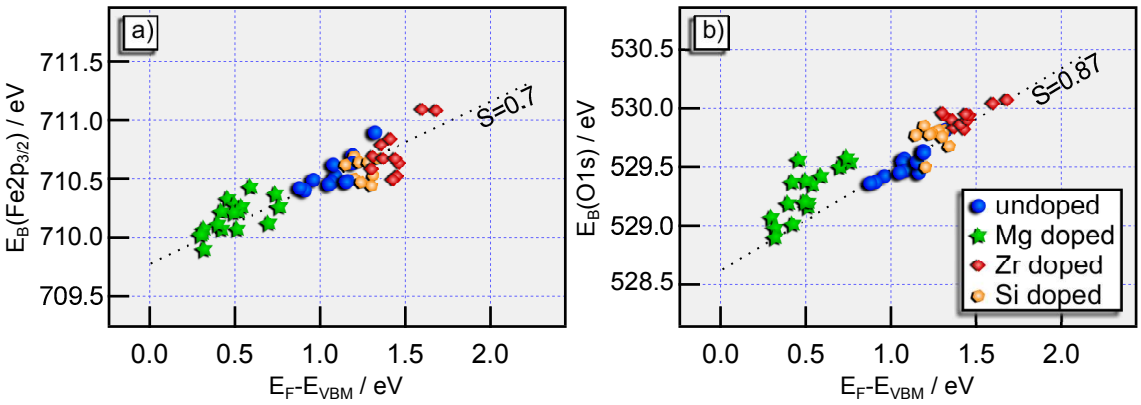

Figure 6.14: Binding energies of the Fe2p (a) and O1s core-level (b) in dependency of the Fermi level position for undoped and differently doped hematite thin films.

The deviation from a slope of $S = 1$ can indicate that no fully screened core holes are present. In other words, the removal of an electron from the system by the photoexciation changes the energy state of the complete system.[121] The introduction of dopants in a high amount (as present in this thesis) will most certainly influence the screening of core holes due to a change in the density of states of the valence band. This change originates from several different contributions.

On the one hand, is the charge carrier concentration affected by the dopants (Fermi level shift, occupation of states). For the strongly localized Fe3d orbitals in hematite this needs obviously to be considered.[92–95, 99–101] Hence, the position of the valence band maximum might be affected due to the self-correlation of the electrons.

On the other hand, will the substitution of iron by a dopant result in a lesser density of (localized) Fe-states. Instead valence states from the dopant are present in the valence band. For high enough amounts of dopant a band formation might occur from which the screening of the core holes might be affected as well.

Another possibility is the screening of the photohole by charges such as e.g. free electrons in the conduction band.[271] This mechanism would have a larger effect on localized photoholes (e.g. Fe2p) than on delocalized (e.g. O1s) ones.[121] Reasoning the different slopes in Figure 6.14a) and b). The charge carriers in hematite that could cause this effect could potentially be the polarons that will be discussed in part 8. In difference to results on In_2O_3 the different slope seems to be present for all Fermi energy positions.[271] This would indicate that the formation of polarons occurs at all Fermi energies. This does not agree with the observations that will be discussed in Chapter 8.

A third reason for the deviation from a slope of $S = 1$ can be found in the spectral shape of core-level and valence band. As has been discussed previously the degree of crystallinity has strong influences on the Fe2p core-level and valence band of hematite.[61, 156] Hence, the core-level to valence band maximum difference might depend on the crystallinity or order within the sample as well. For the doped samples a huge disorder was discussed and agrees with the spectral shapes in XPS and Raman results. This disorder could also be a reason for the different value of the slope. As the O1s shape is not affected this could also explain why the slope in Figure 6.14b) is closer to $S = 1$ than in a).

The dopant might have another influence on the binding energy of a certain core-level. By changing the dielectric properties of the material the coulombic forces for the charges within the material are changed. This can for example be the case when the bonding length and angle is changed due to a different ionic radii of the dopant compared to iron. Compressive and tensile stresses are associated with this.

For doping concentration in the percent range as are present here, this needs to be considered. Iron and oxygen would be affected differently as their bonding and core-level orbitals are different. The O1s for example can be assumed to be less affected by a change in bond distance or angle than the more oriented Fe2p. The same applies to the O2p compared to the more oriented Fe3d states.

A final reason which is also affected by the spectral shape is the uncertainty of the determination of valence band maximum and core-level positions. At the valence band maximum a linear extrapolation to the lower part of the valence band is used to determine a Fermi level position. Especially for the highly disordered samples with a smeared out valence band maximum the uncertainty might easily exceed values of 0.2 eV.[114]

At the same time the $Fe2p_{3/2}$ core-level broadens in absence of the "pre-edge".[61] Hence, the binding energy of the peak is more uncertain as well. As a consequence, the distance to the valence band maximum cannot be determined without a certain error anyway.

A conclusive statement which of the imaginable reason is dominant is not possible here. Dedicated experiments would be necessary to separate the different mechanisms. For this purpose the spectral quality should be carefully considered in order to minimize uncertainties in the determination of the energy positions.

The change in the dielectric properties due to the incorporation of the dopant is tentatively regarded to be the main reason for the deviation. It then follows that even though the distance of the core-level to the valence band maximum shows a deviation it can still be regarded to be constant within a single sample. This allows for the use of such a distance in interface experiments.

6.6 Opto-electronic properties of doped hematite

Being the active material in a photoelectrochemical process the opto-electronic properties of hematite are of great importance. Here, the influence of doping on the light-absorption shall be discussed. In addition, the dependency of the electrical conductivity on the different dopants, temperature, and measurement atmosphere will be addressed.

In Figure 6.15 the optical absorption coefficient of doped films in dependence of the dopant concentration is being shown. The respective dopants are a) magnesium, b) silicon, and c) zirconium. The concentration of the dopant is given in the table. The blue line does always represent the highest concentration whereas the black line shows the lowest amount of dopant in the sample. In all graphs the absorption coefficient of the same undoped sample has been added in green. The transmission and reflection spectra which were used to obtain these graphs can be found in the appendix in Figure A11.

The optical absorption coefficient of the magnesium doped samples in Figure 6.15a) is only being changed slightly when compared to the undoped sample. As is being shown in the inset the absorption already starts to increase at lower photon energies. This change is strongest for the sample with the lowest Mg-concentration.

A stronger absorption at lower photon energies was observed by Kosa et al.[239] Their derivation of the optical band gap of Mg-doped hematite thin films with different doping concentrations by using a Tauc-plot showed a large scattering.[179] A higher band gap of 2.19 eV was reported from UV-Vis reflectance spectroscopy before.[233]

An onset of absorption at lower photon energies can indicate an increased defect concentration or a higher disorder with the sample. The latter has been discussed for all doped samples. Why this behavior is the strongest for the sample with the lowest dopant concentration cannot be explained finally. In Figure 6.3 it was found that the valence band maximum of magnesium doped hematite smears into the band gap. These additional states might be the reason for the lower onset of the absorption. For the higher doped samples it might be the case that the density of optical absorption site has been decreased due to the formation of a second phase as was already reasoned about. This effect would dilute the small changes and make these unobservable.

For the high magnesium concentrations it can be argued that these values were deduced from XPS measurements due to a surface segregation. Then, the bulk concentration of the dopant would be much lower and the optical properties would not be changed as much compared to the undoped sample. A magnesium oxide on the surface on the other hand would not be detected by the optical measurement due to the large band gap of magnesium oxide of 7.3 eV.[272]

In comparison to the other dopant the addition of magnesium to hematite changes the optical spectra the least. Especially, for photon energies above 2.2 eV the spectra of the Mg-doped samples are quite similar to the undoped sample. It should be noted that all three doped samples discussed here showed XRD reflections and a Raman spectrum that are characteristic for hematite as shown in Figure 6.1. The disorder is, therefore, not as large as for the other dopants which naturally explains why the optical properties are not changed as much.

This, however, is different for the Si-doped samples in Figure 6.15b). Here, the deviation of the absorption coefficient above 2.2 eV is rather large and seems to depend on the amount of dopant in the sample. This behavior can directly be explained with the increased disorder which was indicated by the change of the Raman spectrum in Figure 6.5b). The sample with 4.2 % silicon shows a Raman spectrum which indicates a high amount of disorder but is still characteristic for hematite. For higher dopant concentrations, however, the disorder even increases and the spectra do not represent crystalline hematite anymore.

A lowering of the optical absorption of hematite by the incorporation of silicon has been observed by Chemelewski et al. before.[226] An onset of absorption at lower photon energies has been shown as well. The same can be observed for the Si-doped samples in the inset of Figure 6.15b).

Chemelewski et al. also showed, however, that this earlier onset does not improve the photocurrents for lower photon energies. It can, therefore, be assumed that the earlier

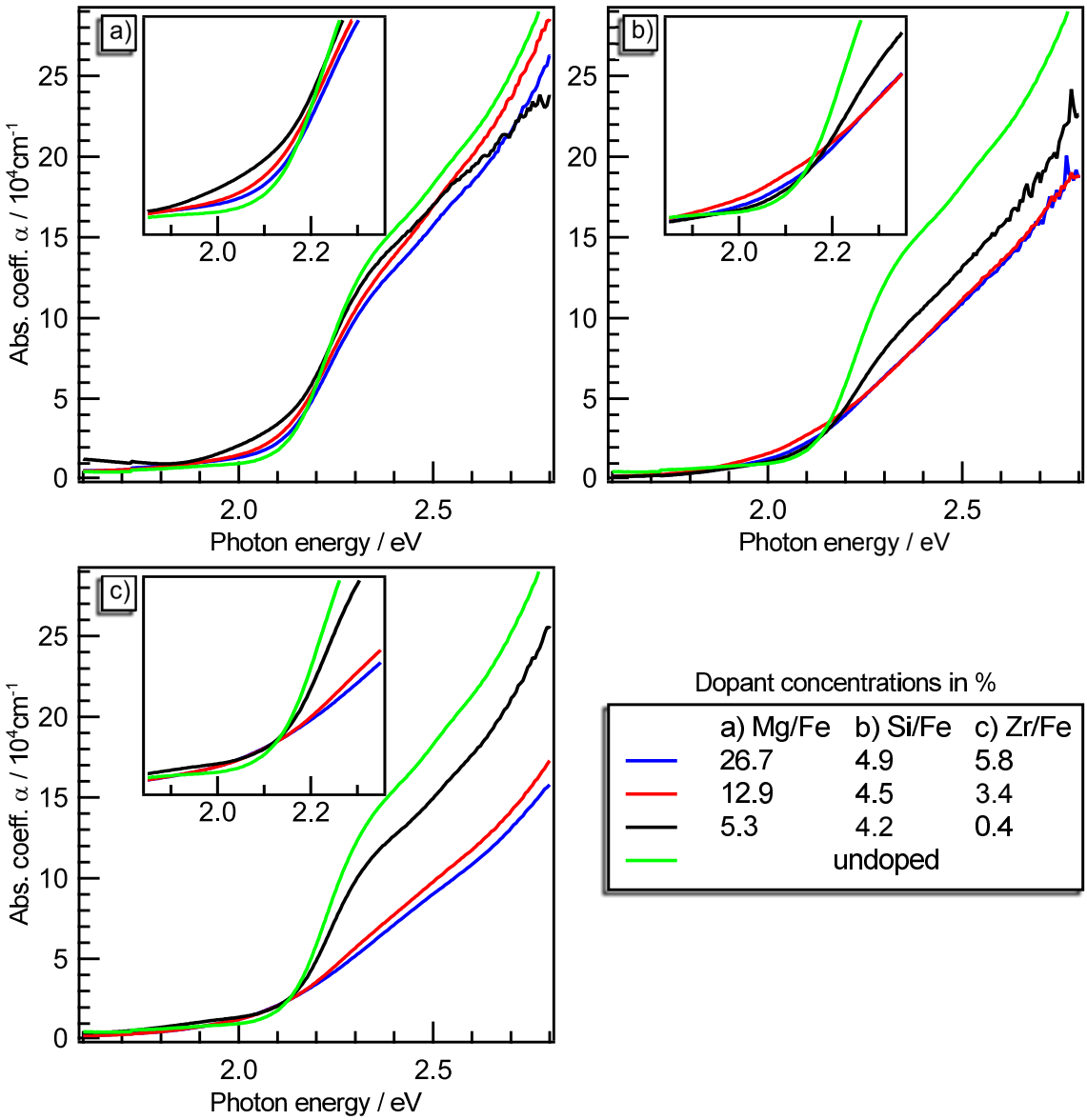

Figure 6.15: Optical properties of hematite thin films doped with a) magnesium, b) silicon, and c) zirconium.

onset is due to a high disorder. As a consequence, a not-as-defined dispersion of the band edges or defect states which give to band edge tails exist.

A similar conclusion can be found for the doping with zirconium. For the highest dopant concentrations the absorption coefficient in Figure 6.15c) is drastically lowered compared to the undoped sample. Again, this agrees well with the observation of an increasing disorder with increasing dopant concentration from Figure 6.9b). A slightly increased onset of absorption for lower photon energies can be found in the inset as well. It is, however, not as strong as for the other dopant. An earlier absorption due to Zr-doping has been observed for hematite before.[47]

To summarize, the optical properties of hematite are changed by the addition of the dopants. Especially for high dopant concentration the absorption coefficient is decreased at higher photon energies. On the other hand, the absorption seems to start at lower photon energies already for all doped samples. Whether this, however, is beneficial in the water splitting process has not been further investigated.

The electrical properties of hematite thin films of different orientation and doping were tested by measuring the conductivity at elevated temperatures. In difference to the conductivity measurements presented in Figure 4.15 in the following measurement also the atmosphere was changed during the measurement. For each temperature the gas was changed either from an argon-oxygen mix containing 10 % oxygen to pure argon and back or vice versa.

From the change of the conductivity due to the change in oxygen partial pressure conclusions on e.g. the defect chemistry and on the majority charge carrier type might be possible:

For many transition metal oxides the oxygen vacancy formation is the principle defect mechanism.[264, 273–275] For these materials a lowering of the oxygen partial pressure results in the formation of more oxygen vacancies which are compensated by electrons (thereby lowering the number of holes): $2[V_O^{\bullet\bullet}] = n = \frac{n_i^2}{p}$. Hence, for a n-type semiconducting oxide the conductivity tends to increase when the oxygen partial pressure is lowered while the opposite is the case for a p-type semiconducting oxide. For an intrinsic semiconductor where the number of holes and electrons is equal no change is expected.

This can only be regarded to be a first assumption. Detailed knowledge on the defect chemistry of a material is necessary to fully comprehend the dependency of the conductivity on the oxygen partial pressure. This includes also ionic contribution and can only be addressed by means of a sophisticated combination of computational and experimental results. This, however, was not the aim of this work. Here, the conductivity measurements are being used to show differences due to the orientation and the doping. There is a number of studies on the defect chemistry and conductivity of hematite, which are partially also combinations of both.[30, 63, 68–70, 77, 78, 80, 195, 219, 220, 225, 276–279]

The conductivity measurements in Figure 6.16 were measured over the course of several days. As it was only possible to measure two samples at once the time scale of the three figure a)-c) is different. However, the data will not be used to access the kinetics of oxygen exchange. Hence, the time can be regarded to be arbitrary. Please note, that the ranges of conductivity are different in a)-c), as well.

As already mentioned the measurements were performed in either Ar- or Ar/O_2-atmosphere. The different atmospheres are indicated by a different background color. In addition, the temperature is indicated as color bar on top of the respective graph. The figures a)-c) show conductivity measurements on a) epitaxial samples on sapphire in $(10\bar{1}0)$(red) and (0001)(black) orientation, b) n-doped samples on quartz with zirconium (blue) and silicon (green) as dopant, and c) a p-doped sample on quartz with magnesium as dopant (purple). Prior to these measurements all samples had been heated in order to measure conductivity for the pristine samples. For the epitaxial samples in a) the highest temperature was 600 °C, whereas the doped samples in b) and c) had already been at a temperature of 700 °C.

The conductivity variations due to the change in oxygen partial pressure is different for each sample. For the epitaxial samples in a) a dependency on the orientation can be observed. Here, the $(10\bar{1}0)$oriented sample shows a decrease in conductivity when changing from the Ar/O_2-mix to pure argon at 500 °C and 600 °C. At 700 °C the opposite is the case and the conductivity is increased.

For the sample in (0001)orientation the change in conductivity is different. Upon changing to the more reducing conditions of pure argon the conductivity of this sample increases at 600 °C. At 700 °C no change is observed. The reason for this might be a problem with the Pt contacts that tend to be degraded at too high temperatures.

At 500 °C the measurement was unreliable and should be neglected. At this temperature the quality factor given by the ratio of the resistances across the different directions of the sample which are measured with the van-der-Pauw method was not at 100 where it is supposed to be.[146, 147, 280] The changes discussed above indicate that the $(10\bar{1}0)$oriented sample shows a behavior that is rather p-type below 700 °C whereas it is n-type at 700 °C. The (0001)oriented sample shows a change in conductivity at 600 °C that can be attributed to be rather n-type as well.

Why the sample in (0001)orientation cannot be measured at 500 °C can only speculated about. Here, the oxygen partial pressure might be too high and the sample might be in the intrinsic regime with a low conductivity. Heating the sample at such a temperature in argon might raise the Fermi level and increase the conductivity again.[273, 275]

Such a behavior was observed for the two n-doped samples presented in Figure 6.16b). After being heated up to 700 °C in Ar/O_2 the samples could not be measured in the same atmosphere anymore. Only in pure argon a measurement was possible. This is why in contrast to the measurements in a) and c) the atmosphere was changed from pure argon to Ar/O_2 and back for the two n-doped samples.

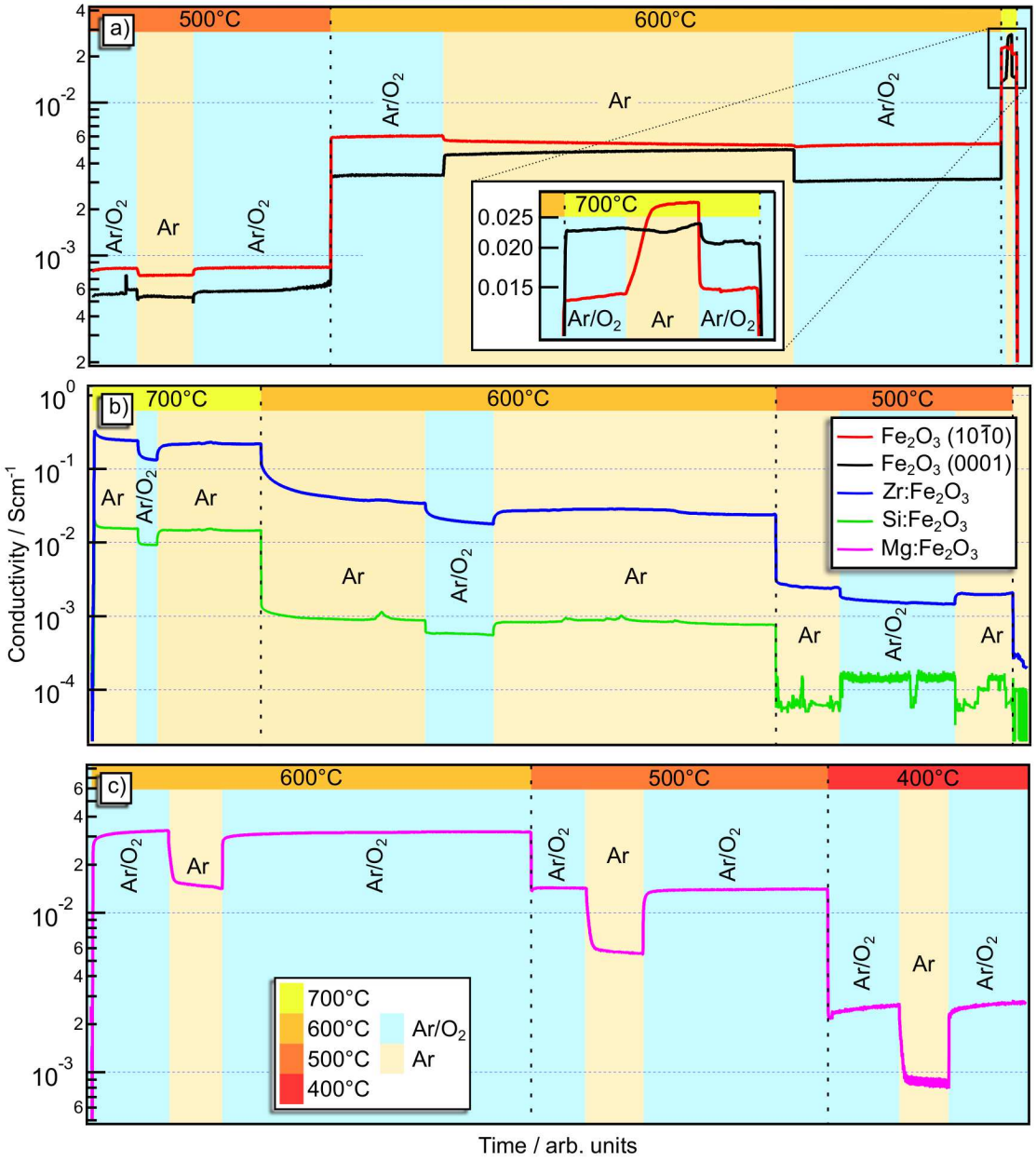

Figure 6.16: Dependency of the conductivity of hematite thin films on dopant, temperature, and measurement atmosphere. The color of the background indicates the different atmosphere while the colored bar on the top of the graphs represent the temperature.

The reaction for both sample is a drop in conductivity once the oxygen partial pressure is increased. This process is almost reversible as the conductivity increases once the gas is changed to pure argon again. The conductivity in pure argon after the introduction of oxygen, however, is smaller than before.

The time until an equilibrium is established with oxygen was very long. Even after days in the same atmosphere there was still a change in conductivity to be observed. Both observations indicate that the processes are not fully reversible. In addition, it can be assumed that it is kinetically easier to remove oxygen than to incorporate it.

The conductivity of the Zr-doped sample is always larger than for the Si-doped one. For the latter a measurement at 500 °C was not possible anymore as the quality factor was again not at 100. For the Zr-doped sample this was the case at 400 °C. The same argument as for the (0001)oriented sample in a) applies. The reason for the different temperatures at which this occurs can be found at the Fermi level positions for the different samples. From Figure 6.13 it can be seen that the Zr-doped sample can be expected to show the highest Fermi level position. Hence, the other two two have less charge carriers, a smaller conductivity, and will sooner reach the intrinsic regime where they cannot be measured. It should be mentioned that the conductivity of the undoped sample is higher than for the Si-doped sample. This might indicate that the Fermi level in the Si-doped sample is lower. The reason for this assumption is unknown. It does agree, however, with the history of that specific sample. It could not be measured in an Ar/O_2 atmosphere at any given temperature.

Finally, the Mg-doped sample shows a behavior that is expected for a p-type doped oxide. Upon lowering the oxygen partial pressure the conductivity is reduced. By reintroducing oxygen into the oven the conductivity reaches very similar values again. This indicates that the reversibility of the processes is the highest for this p-type sample.

Comparing the conductivities in table 6.2 it can be observed that at 600 °C the highest conductivity is being reached for either the Zr-doped sample in argon or the Mg-doped sample in Ar/O_2. Both sample reach a conductivity of about 0.033 $S\,cm^{-1}$. At 500 °C the Mg-doped sample is even more conductive than the Zr-doped sample. For both the conductivities are always above the one for the undoped samples which indicates that these dopants are a good choice. This, however, cannot be said for the silicon doping. There is no improvement in the conductivity associated with this dopant.

The activation energies that have been extracted from an Arrhenius-type plot based on equation 4.1 are presented in table 6.2 as well. From literature a value of 0.7 eV for hole conduction in single crystals and 1.0 eV for polycrystalline sample with impurities are known.[281] These values are in very good agreement with the activation energy of the Mg-doped and undoped $((10\bar{1}0))$-oriented samples.

The activation energies of the n-doped samples, however, are rather high. A reason for this might be found in grain boundary effect on the mobility of electrons. For hematite there are several reports on their poor electrical conductivity.[157, 186, 225, 279]

Especially for silicon as dopant it was found that it can segregate to the surface and grain boundaries and thereby most likely increases the recombination rate.[255] At the same time it can be expected that a silicon oxide layer on the surface of the photoactive hematite layer decreases the charge transfer into an electrolyte or even electrode.

Table 6.2: Extracted conductivities σ and activation energy E_A of the undoped and differently doped samples that were measured in different atmospheres.

	$(10\bar{1}0)$						
Atmosphere	400 °C	500 °C	600 °C	700 °C	$T = \infty$	RT	E_A
	S cm^{-1}						eV
Ar/O_2			0.0034	0.014	4.6×10^{3}	6.4×10^{-15}	1.06
Ar	-	-	0.0049	0.028	1.1×10^{5}	4.7×10^{-17}	1.27
Ar/O_2			0.0031	0.015	1.1×10^{4}	9.5×10^{-16}	1.14
	(0001)						
Atmosphere	400 °C	500 °C	600 °C	700 °C	$T = \infty$	RT	E_A
	S cm^{-1}						eV
Ar/O_2			0.0061	0.023			
Ar	-	-	0.0053	-	-	-	-
Ar/O_2			0.0054				
	$Zr:Fe_2O_3$						
Atmosphere	400 °C	500 °C	600 °C	700 °C	$T = \infty$	RT	E_A
	S cm^{-1}						eV
Ar		0.0024	0.034	0.24	1.4×10^{7}	1.1×10^{-18}	1.49
Ar/O_2	-	0.0015	0.018	0.13	4.0×10^{6}	2.0×10^{-18}	1.45
Ar		0.002	0.024	0.22	1.6×10^{7}	4.5×10^{-19}	1.52
	$Si:Fe_2O_3$						
Atmosphere	400 °C	500 °C	600 °C	700 °C	$T = \infty$	RT	E_A
	S cm^{-1}						eV
Ar			0.000 88	0.0154	1.1×10^{9}	6.8×10^{-27}	2.1
Ar/O_2	-	-	0.000 55	0.009	3.6×10^{8}	1.5×10^{-26}	2.05
Ar			0.000 76	0.0145	2.2×10^{9}	1.2×10^{-27}	2.16
	$Mg:Fe_2O_3$						
Atmosphere	400 °C	500 °C	600 °C	700 °C	$T = \infty$	RT	E_A
	S cm^{-1}						eV
Ar/O_2	0.0026	0.014	0.033		194.3	2.7×10^{-9}	0.65
Ar	0.000 88	0.0056	0.014	-	196.3	2.3×10^{-10}	0.71
Ar/O_2	0.0027	0.014	0.03		151.2	4.0×10^{-9}	0.63

The change in conductivity due to the change in atmosphere is proof that the electrical properties of hematite depend on the intrinsic defect concentration within the material. In several studies before no such dependency was observed.[63, 79] It might be the case, however, that extrinsic defects predominated in their samples.

Other works on hematite were performed to investigate the material as oxygen sensor on the basis of a change of the electrical properties.[81] This shows that the results ob-

tained here showing conductivity changes with oxygen partial pressure are reasonable, even for doped samples. The conductivity changes are summarized below and related to observed Fermi level shifts.

6.7 On doping mechanisms and effects in hematite

The doping in hematite is widely accepted to be based on the substitution of an iron ion by the dopant.[40] In case of an tetravalent dopant an electron is being transferred into the hematite lattice whereas a duovalent dopant accepts an electron from the lattice. Especially the former case has been investigated to a high degree already.[40, 224] At this point, however, a few more thought shall be added.

In their work on group IV dopants in hematite Zhou et al. found that the substitution of iron by Sn, Si, or Ge occurs by the already mentioned substitutional mechanism.[40] Their study further revealed that the excess electron is most likely being transferred to an iron ion where it creates an electron polaron. In addition, they showed that the replacement of iron by any dopant changes the bond distances. Once an electron is being transferred to a specific iron cation the oxygen anion that connects the dopant to that iron is being pushed towards the dopant and away from the iron ion.

All of the finding from above are in good consistence with experimental results from Cesar et al. who determined charge carrier concentrations of Si-doped hematite.[224] They investigated samples with a doping content of 1.6 % iron ions nominally being replaced and found a charge carrier concentration of $1.7 \times 10^{20}\,\mathrm{cm}^{-1}$. On first glance, this result seems to be in good agreement to a simple theoretical calculation in which 1.6 % of the $4 \times 10^{22}\,\mathrm{cm}^{-1}$ iron ions are being replaced with Si ($6 \times 10^{20}\,\mathrm{cm}^{-1}$) donating one electron each.

Two details, however, are inconsistent with the present work:

First, Cesar et al. argued that the charge carrier concentration they found should result in a Fermi level position which is about 0.1 eV below the conduction band minimum. From Figure 6.13a) it is clearly observable that this is not the case for any doped sample in this work. This statement holds for most cases even if the polaron state at 1.75 eV above the valence band maximum that will be introduced and discussed as effective band edge in Chapter 8 is being considered. Even more so, as such a position is strictly not possible in hematite if the conduction band edge in their proposal is assumed to be the classical (optical) band edge 2.2 eV above the valence band maximum.

Second, the transfer of an electron to an iron ion results in the formation of a polaron which is a Fe^{2+}-ion on a site nominally occupied by Fe^{3+}. The dopant concentration that

were investigated in this work are in the range of 5 % and larger. A change in oxidation state of that many iron ions should be observable by XPS.

The first statement on the Fermi level position is, at least for silicon, inconsistent with the calculated charge transition level at 1.41 eV above the valence band maximum of this dopant.[40] This level effectively pins the Fermi level in Si-doped hematite as has been argued before in Chapter 6.2. Below this position silicon will be in a Si^{4+} state and act as a donor. Once the Fermi level has reached this charge transition level, however, silicon will be found in a Si^{3+} transition and does not act as a dopant anymore. Hence, the number of dopant that have donated an electron to hematite are much less than the number of iron ions that were substituted by silicon.

In the work of Cesar et al. the dopant concentration was four times higher than the charge carrier concentration.[224] In this thesis it was argued before that for silicon and magnesium a phase separation occured as not all of the dopant atoms could be incorporated into the hematite lattice. It can be assumed that this appeared in the study of Cesar et al. as well but remained undetected.

The assumption of phase separation adds to the argumentation above and indicates that only about 0.4 % of the iron ions have been given an electron. This low number of Fe^{2+}-ions would not be detectable by XPS an the second inconsistency could be explained by this as well.

For the Zr-doped sample a similar statement would hold as well. As the assumed charge transition point of zirconium in hematite is higher more electrons could be donated to Fe_2O_3 . There are still no changes in the oxidation state of iron visible which leads to the conclusion that not all zirconium ions can be in the +4 oxidation state as well. A phase separation cannot be omitted with this dopant as well.

To summarize, both inconsistencies can be explained by a much less fraction of the dopant being active and the presence of charge transition points. With this conclusion it is acceptable as well, that no large deviations despite by disorder were observable in the valence band measurements of this work. For higher amounts of Fe^{2+} observable states close to the Fermi level could be expected. This was clearly not the case for any sample.

The speculated phase separation in this thesis occurred presumably for magnesium and silicon as dopant and maybe for zirconium as well. The impact of the former two might be larger compared to the incorporation of zirconium due to several reasons:

First of all, the investigated dopant concentration of zirconium was much smaller than for the other two dopants. Hence, the amount of second phase would be smaller. Investi-

gating samples with higher zirconium contents could result in a higher amount of second phase and worsened properties.

Secondly, the ionic radii of Zr^{4+} (0.72 Å), Si^{4+} (0.4 Å), and Fe^{3+} (0.645 Å,high-spin) are quite dissimilar in a sixfold coordination.[259] From this, it can be expected that the incorporation of silicon into hematite will result in tensile stress whereas the incorporation of zirconium will result in compressive stress. Also, as the ionic radius of zirconium is much closer to iron than silicon the absolute stress should be higher for the same amount of incorporated silicon. Dualvalent magnesium, has the same ionic radius as zirconium (0.72 Å) in a six-fold coordination.[259] From these considerations it can be deduced that the substitution of iron by zirconium and magnesium is easier achieved and silicon is more prone for phase separation in hematite.

Magnesium can be assumed to be quite mobile as it is a rather light atom. This agrees quite well with the conclusions on a higher phase separation at 400 °C compared to sample temperatures of 200 °C for this dopant.

All in all, the doping mechanism in hematite seems to be reasonably well understood. The direct effects of the dopant on the hematite layer which include not only an increased charge carrier concentration but also increased disorder and phase separation are a topic that has to be investigated more detailed for each dopant itself. A modulation of charge carrier mobility for certain dopants which was observed before seems to implicate that not only the charge carrier concentration is modified but also the band structure itself.[53] This statement seems reasonable considering the high dopant concentrations that are used in literature and this thesis. As long as detrimental effects of the dopant onto the opto-electronic properties can be expected the dopant concentration should be kept as low as possible.

6.8 Summary

In this chapter it was shown that the Fermi level positions in hematite can be manipulated by using dopants. It was possible to shift the Fermi level in both directions, upwards and downwards, compared to the undoped thin films.

For the known p-type dopant magnesium it was shown that it shifts the Fermi level towards the valence band maximum. The lowest Fermi level position that could be obtained with this dopant was 0.3 eV. This downward shift was accompanied a p-type behavior in the electrical measurements. The conductivity at a given temperature increases if the conditions become more oxidizing, reflecting a change from p-type conductivity to mere intrinsic behavior.

With silicon and zirconium the Fermi level could be shifted upwards. That was more the case for zirconium which showed the highest value of 1.68 eV. Also, in average the Fermi level positions were higher for Zr-doped samples than for Si-doped ones. Zirconium can, therefore, be considered to be the more effective dopant. This might be attributed to the lower lying charge transition point of silicon were the initial Si^{4+} is being reduced to Si^{3+} and does not act as a donor anymore. For the high dopant concentrations in this work the binding energy positions of silicon gave reason to believe that a phase separation occured and some of the silicon is not incorporated into the hematite lattice anymore. Instead, it is present as a silicon oxide phase.

The assignment of zirconium to be a more effective n-type dopant can also be seen in the electrical measurements where it showed much higher conductivities than the Si-doped sample. Also, its reaction on a change of oxygen partial pressure was more defined to be a n-type behavior with higher conductivities in low oxygen partial pressures.

All dopants showed a certain degree of disorder as was given by the appearance of an initial forbidden mode in the Raman spectra. This disorder affects the spectral shape in the XPS measurement and might be the reason that the distance of the core-level to the valence band maximum is changed compared to undoped hematite. For magnesium and silicon a surface segregation for the highest dopant concentration was concluded.

The disorder also affects the optical properties slightly where an earlier onset of the absorption was observed. In addition, the doped samples show a smaller absorption coefficient compared to undoped samples. This can be attributed to a dilution of the absorbing iron ions and a variation of bonding geometry and strength.

Overall, it was shown that by doping the Fermi level can be shifted from 0.3 eV to 1.68 eV. Fermi level pinning between these two values can, therefore, be ruled out for hematite unless it is introduced by the dopant itself.

7 Fermi level manipulation of the surface

In this part of the work the position of the Fermi level of hematite in contact with different materials and molecules is explored. The experiments that are presented here can be divided into two groups. In the first group hematite thin films were brought into contact with molecules in an oxygen-plasma and by water exposure. In the second group so-called interface experiment to the solid contact materials ITO, RuO_2, and NiO have been deducted. The procedure and basic assumptions of an interface experiment are described in part 2.3.2.
An experiment which can be regarded to belong to both groups was the modification of the surface of hematite by Al_2O_3 from an atomic layer deposition. Here, metal-organic molecules attach to the surface of hematite and then further react with water to form a solid.
Additionally to these experiments where hematite acted as substrate it was also examined how hematite grows onto a $SrTiO_3$ single crystal.

Important aspects of this chapter

- ... an oxygen plasma treatment shifts the Fermi level to about 0.66 eV where it is pinned by states formed by surface adsorbates
- ... H_2O exposure reduces the sample and shifts the Fermi level to 1.75 eV
- ... surface modification by Al_2O_3 reduces the sample and shifts the Fermi level to 1.75 eV
- ... the Fermi level in hematite at the interface to RuO_2 is at about 0.85 eV
- ... the Fermi level in hematite at the interface to NiO is at about 0.4 eV
- ... the Fermi level in hematite at the interface to ITO is pinned at 1.75 eV
- ... a Fermi level depending reduction of iron is observed during the ITO interface formation
- ... hematite acts as seed-layer for ITO grown at room temperature and induces a higher crystallinity and higher conductivity
- ... the valence band of hematite is 1.1 eV above the valence band of $SrTiO_3$

7.1 Surface treatment by oxygen plasma and exposure to water

In the following it shall be explored how hematite reacts once treated with an oxygen plasma or is being exposed to water in vacuum. The oxygen plasma acts as an oxidizing treatment whereas with the water exposure a reduction is observed. The latter is a somewhat surprising observation as water usually cannot be regarded to be a reducing agent. A mechanism to explain the behavior in the experiments presented here will be suggested. Hence, they show how hematite reacts towards the exposure to such conditions.

7.1.1 Oxygen plasma treatment of hematite

To study the effects of highly oxidizing treatments an oxygen plasma was used. The treatment was performed at room temperature for 15 min with a current of 40 mA in the atom mode of the plasma source. In this mode sputter effects due to high energy particle from the plasma are minimized.

The results from two samples shall be discussed here. First, a presumably amorphous sample that has been deposited at room temperature and second, a presumably crystalline sample that was deposited at 400 °C. The crystallinity of the two samples can only be assumed from the XP spectra as no dedicated structural analysis have been performed. The spectra, however, resemble perfectly the spectra from amorphous and crystalline samples that have been discussed in part 4 of this work.

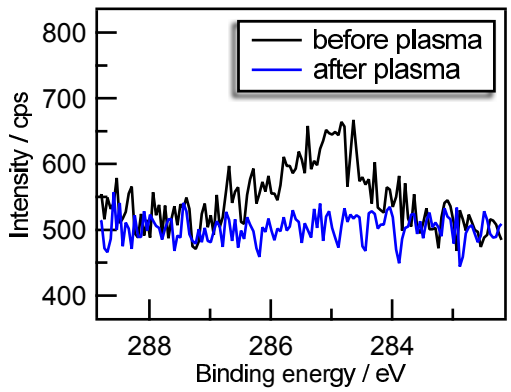

Figure 7.1: C1s-spectra of adventitious carbon before and after the plasma treatment.

Please note, that prior to the oxygen plasma treatment the crystalline sample had already undergone other treatments like water exposure and heating. In immediate advance to the measurement presented here, the sample had been stored under UHV-conditions for five days after it was heated at 400 °C in vacuum before. From this storage some adventitious carbon could be found in the survey spectrum as shown in Figure 7.1. After the plasma treatment no carbon could be found on the surface anymore. This carbon, however, should not affect the effect of the oxygen plasma treatment tremendously and is, therefore, in the discussion of the treatment neglected in the following.

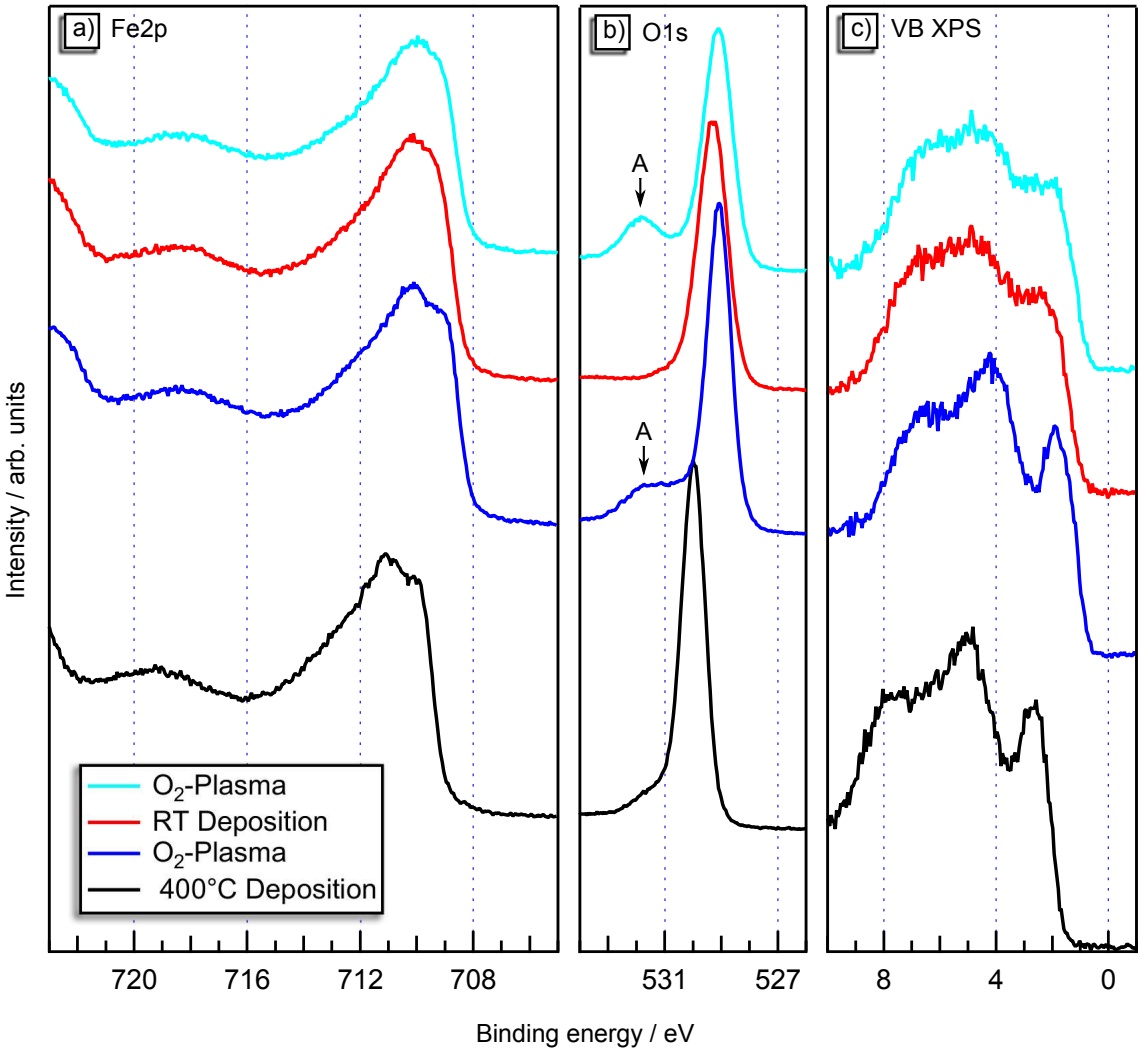

Figure 7.2: XP spectra for an (presumably) amorphous and a (presumably) crystalline sample before and after a treatment in an oxygen plasma.

The XP spectra from the two samples before and after the oxygen plasma treatment are being presented in Figure 7.2. Besides the crystallinity and the resulting spectral changes the sample differ in their Fermi level position before the treatment. While the amorphous sample shows a low Fermi level position of 0.87 eV, the crystalline sample exhibits a Fermi level position of 1.6 eV which is rather high. It could actually result from the prior heating in vacuum which shifts the Fermi level position to higher values.

One minor difference is a small shoulder towards higher binding energies in the O1s-spectrum of the crystalline sample. It is assigned to originate from carbon hydrates or OH^--adsorbates due to the storage in the system.

After the treatment a shift towards lower binding energies is observed in the core-levels of both samples as well as in the valence band. The shift is larger for the crystalline sample which can be explained by the initial higher Fermi level. After the oxygen plasma treatment the Fermi level in the two samples are rather similar. Positions of 0.66 eV and

0.6 eV are deduced for the amorphous and crystalline sample, respectively. Within the precision of XPS these values are the same.

In order to interpret this observation three important aspects need to be considered. First, the treatment is the same for both samples. Second, the Fermi level positions before the treatment are very different. This results in a different amount of charges that have to be transferred in order to shift the Fermi level in the two samples to the similar position by the oxygen plasma treatment. Third, magnesium doped films showed a lower Fermi level position than the one that was achieved here.

From the first two statements it can be deduced that the Fermi level is pinned at around 0.65 eV. Otherwise the different Fermi level positions before the treatment should result in different Fermi level positions after the treatment (assuming similarity of the two treatments). Including the third aspect clearly shows that the pinning cannot originate from within the hematite thin films but that it has to result from the charge neutrality level associated with the surface conditions induced by an adsorbed species.

The presence of this adsorbed species can be proven from the O1s-spectra in Figure 7.2b). Here, an additional signal emerges at higher binding energies for both sample after the treatment which was labeled with A. This signal is positioned about 2.75 eV above the main line in both samples indicating that it is the same species. In literature the presence of a similar signal after a treatment in air or oxygen plasma with slightly smaller difference to the main line has been observed before. Zhu et al. explained the signal by the presence of oxygen vacancies that were created during their air plasma treatment.[282] This assignment is rather unreasonable as oxygen vacancies should first of all not emit any photoelectrons and secondly it is hard to believe that oxygen vacancies are formed under very oxidizing conditions. This possibility is, therefore, omitted.

Another assignment can be found from Hu et al. who explained the signal to originate from OH^- group attached to the surface after an oxygen plasma treatment. They also include the possibility that this signal arises from nonstoichiometric oxygen like O_2^{2-} or O^- but only omit the latter in their discussion[1]. The presence of peroxides, however, is not further discussed.[57]

In the present case the signal can be reasonably explained by adsorbed peroxide (O_2^{2-}) species as for this species a difference to the main line of O1s of about 2-3 eV was shown.[241] In a further step on the crystalline sample it was shown that this species can be removed by a mild heating at 200 °C in vacuum. Afterwards, the Fermi level is also higher again.

[1] O_2^- was not included in their discussion

An additional indication for an adsorption on the surface is the observed shift that had to be used in the difference spectra in Figure A12. For the Fe2p-, O1s and valence band slightly different shifts of $-0.1\,\text{eV}$, $-0.18\,\text{eV}$, and $-0.21\,\text{eV}$ had to be applied. Even though, the difference is marginal it might indicate that there is band bending present on the surface after the plasma treatment. This conclusion is based on the different information depth of the three region with Fe2p being the most surface sensitive and the valence band having the highest information depth. It should be noted, however, that the expected difference are rather small.[116, 137]

Despite the obvious changes in the O1s-spectra there are no further changes that are as obvious. Difference spectra that are shown in the appendix in Figure A12 revealed that the valence bands do not change at all due to the plasma treatment. Small changes were observed in the difference spectra of the Fe2p-spectra. Here, an adjustment of the intensity on the Fe^{3+}-satellite resulted in a slightly larger intensity of the main line after the plasma treatment. This was especially the case for the amorphous sample. Assuming that an adjustment of satellite intensity can be interpreted as a similar amount of signal from Fe^{3+} in the difference spectra, the additional intensity might be explained by the presence of another oxidation state of iron. Namely, Fe^{4+} could be considered.Braun et al. found evidence for the formation of Fe^{4+} for low Fermi level positions in hematite.[240]

The lower Fermi levels of Mg-doped samples, however, seem to be reason enough to disregard this possibility. It could, however, be shown in Figure 6.3 that with higher Mg-contents (associated with lower Fermi level) almost similar changes in the Fe2p-spectra were observed. A tentative assignment of the difference to the formation of Fe^{4+} can, therefore, not completely be omitted. However, further investigation on this topic by more suited techniques, e.g. surface sensitive Mößbauer spectroscopy (achieved in a grazing incidence geometry), are necessary.

7.1.2 Exposure of hematite to water

After having discussed the effect of highly oxidizing conditions on the surface of hematite the exposure to water will be considered. This treatment was performed by exposing the sample to water vapor in the ALD chamber of the DAISY-MAT lab.

The water exposure was performed at room temperature. The water was introduced into the chamber by 15 pulses from the ALD valve of 500 ms each. After each pulse the chamber was allowed to be pumped for one minute. Before the sample was transferred the pressure in the ALD chamber had reached a value below 1×10^{-6} mbar.

As before, two undoped samples with different crystallinity shall be discussed. The assignment of the crystallinity is again based on the shape of the XP spectra (Figure 7.3).

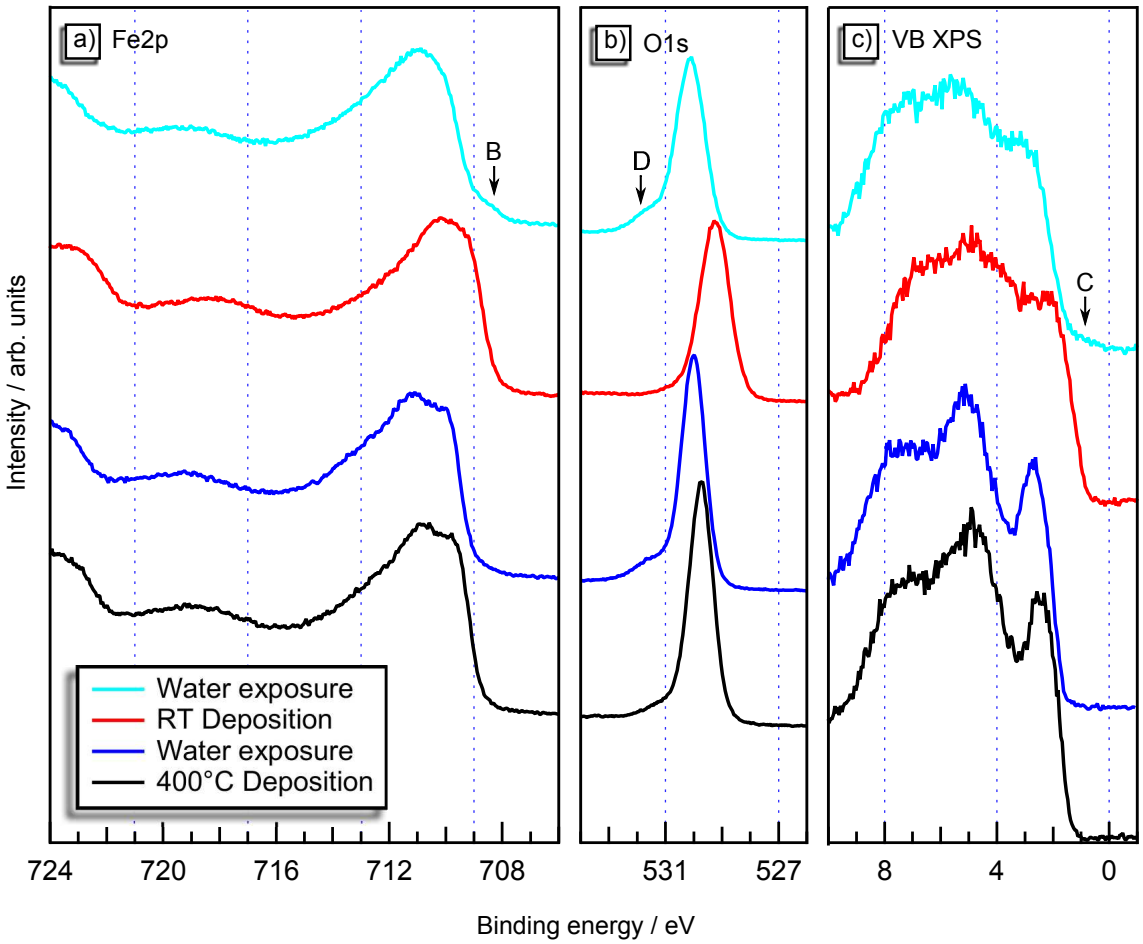

Figure 7.3: XP spectra for an (presumably) amorphous and a (presumably) crystalline sample before and after the exposure to water.

The two sample differ in their initial Fermi level position. While the amorphous sample shows a low Fermi level of 0.82 eV, the crystalline sample has a higher Fermi level of 1.4 eV[2]. Please note that the "as is" state of the crystalline sample originates from being heated in oxygen over night after being reduced by a similar heating in vacuum[3].

The different Fermi level position are also clearly visible in the position of the core-level where the crystalline samples shows higher binding energies for both. After the exposure to water the two samples show a Fermi level position of 1.59 eV in the amorphous and 1.67 eV in the crystalline case, respectively. This change in Fermi level is accompanied by a shift of the core-level towards higher binding energies. Since the change in Fermi level

[2] The crystalline sample is the same which has been used for the oxygen plasma treatment. The water exposure, however, took place before the oxygen plasma treatment. After the water exposure this sample was heated to remove any residual water on the surface.

[3] The spectra of the in-situ heating in vacuum of this particular sample can be found in Figure 4.7. There, the reoxidation is shown as well.

position is more drastic for the amorphous sample the shift towards higher binding energies is also larger here. It should be noted, that after the exposure to water the core-level positions of the crystalline and amorphous sample are rather similar with 711.1 eV and 710.9 eV for the Fe2p$_{3/2}$- and 530.0 eV and 529.75 eV for the O1s-core-level, respectively.

Despite the changes in the peak positions there are three observable features emerging after the water exposure. These are labelled with the letters B, C, and D and shall be discussed with the help of difference spectra in Figure 7.4 for the amorphous sample. The conclusion are assumed to be applicable to the crystalline sample as well. There, however, the changes are not as obvious. Similar difference spectra can be found in Figure A13 for this sample.

The discussion on the changes after water exposure shall be started with feature D from the O1s spectrum. It is positioned about 1.6 eV away from the main line and has been identified as OH^-.[127, 128] The signal from water molecules which might be present after the treatment as well would be found at about 3 eV above the main line.[128] No increased intensity can be observed there which indicates that only dissociated water is bound strongly enough to the surface of hematite in the UHV conditions during the measurement. This is in contrast to measurements on hematite at near ambient pressure while being exposed to water.[128]

Features B and D are clearly connected and can be attributed to the formation of Fe^{2+}.[51, 125, 126] Quite similar spectral changes have been observed in Figure 4.7 and discussed with difference spectra in Figure 4.8 after a sample was reduced for elongated time in vacuum. This shows that the sample has been reduced during the water exposure.

The necessary shifts to create the difference spectra are quite different for the three region. This might indicate a band bending in the sample as the shift increases with decreasing surface sensitivity of the respective region. On the other hand, after the water exposure the Fe2p-core-level was the first region to be measured. It was followed by the O1s-region with the valence band being the last. It is possible, that some water evaporates during the measurement and, thus, the shift decreases.

The presence of signal C in the valence band, however, shows that the Fe^{2+}species are still present. In the discussion on charge transitions of the iron species in hematite in Chapter 8 it will be argued that the charge transition from $Fe^{3+}$to $Fe^{2+}$is depending on the Fermi level position. It occurs for Fermi level positions around 1.75 eV which agrees very well with the Fermi level position derived from the shift in the Fe2p spectrum.

This is taken as evidence for the band bending model. In agreement to this model the valence band region as a higher information depth than the core-levels and extents further into the unchanged region within the sample. As a consequence a lower Fermi level position is shown from the valence band.

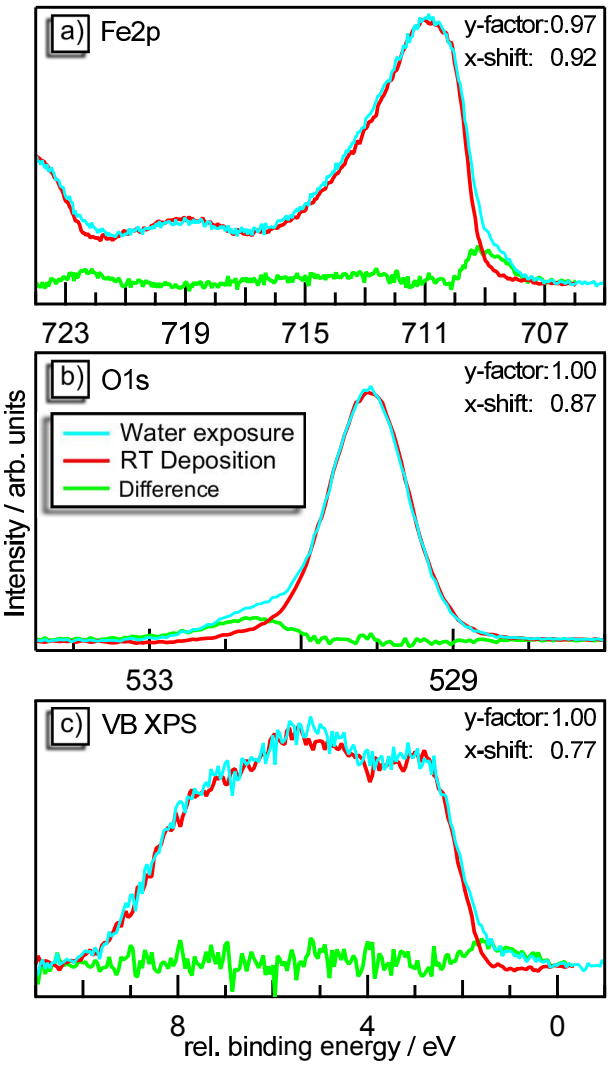

Figure 7.4: Difference spectra for the amorphous sample for the water exposure experiment. The spectra before the treatment has been subtracted from the spectra before the treatment.

The crystalline sample shows the same changes upon water exposure as the amorphous sample but to a lesser degree. This is observed, despite the higher initial Fermi level position in the crystalline sample. Assuming a pure electronic (Fermi level depending) reduction this should not be the case. The samples, however, differ in their crystallinity and, therefore, the bonding.

It can be argued that the bonding is not as strong in the amorphous case and the reduction might be easier to achieve. Also, in the multiplet fits in Figure 5.1 the "surface peak" was enhanced in the amorphous sample which could indicate that more water molecules could be adsorbed on this sample.

Finally, a different defect chemistry in the two samples cannot be excluded and the formation of other defects (that, then, trigger the formation of Fe^{2+}) might occur in the amorphous sample. This topic was not further examined but could be investigated with a more defined water exposure and suitable techniques e.g. low energy electron diffraction (LEED). A change in oxidation state of the iron ion in hematite upon water exposure has not been described in literature, yet.

Using more suitable techniques could also potentially solve the question why the adsorption of OH^- species should introduce a reduction. With negatively charged molecules it would make much more sense if a hole accumulation would occur at the surface of

hematite. The donor effect of OH^- must, therefore, be more complex. A possible mechanism could include the removal of lattice oxygen in order to react with the split-off hydrogen from the dissociated water. This, however, is highly speculative and there is no evidence for this. Dedicated experiment with e.g. oxygen isotopes could give insight into the prevalent mechanism on the surface of hematite.

The proposal of a definite mechanism for the reduction of iron by water absorption is hardly possible. Two possibilities should, however, be discussed at this point. First, it was suggested by Wasserman et al. that the (0001)-surface shows fourfold coordination of iron at the surface to a water containing atmosphere instead of a sixfold coordination in the vacuum.[202] Such a change in bonding environment and number of bonding partner might result in a change of oxidation state. There was, however, no evidence for such a change in oxidation state in the study of Wasserman et al.

Another possible answer to the question why water seems to act as a reducing agent can be found from a study by Jaegermann and Mayer on H_2O absorption on $WSe_2(0001)$.[283] They explained the observed electron transfer from water into WSe_2 with a mechanism that is based on the electronic interaction of the $W5d_{z^2}$ at the top of the valence band with the occupied lone pair O p-states ($1\,b_1$) from water. Due to this interaction electronically occupied states are formed above the Fermi level and a charge transfer into WSe_2 occurs. Such a model has not been proposed for the interaction of water with hematite before but might be able to explain the observed reduction.

7.2 Surface modification by atomic layer deposited alumina

The surface of hematite was modified by depositing Al_2O_3 in an atomic layer deposition procedure onto the sample. The process was performed at 250 °C in the ALD chamber of DAISY-MAT. The deposition involves alternating pulses of Trimethyl Aluminium (TMA) and water. After each pulse the chamber was allowed to be pumped for five minutes. Each sample here was modified by three ALD cycles which means three pulses of TMA and water each plus the additional pumping. It was shown before that the Fermi level in a SnO_2 substrate can potentially being shifted upwards tremendously by an ultra-thin layer of Al_2O_3 which has been deposited from this process.[114] The electron charge transfer necessary for this shift in Fermi level position was explained by a charge transfer from hydrogen defect states in Al_2O_3.

On hematite the modification of the surface by alumina from a similar process was described in order to improve the photoelectrochemical performance. The reason was given by a passivating of surface states. As a consequence the recombination rate was proposed to be decreased.[23]

Besides, a XPS/XAS study of the interaction of hematite with TMA is available where the authors report quite similar findings to the observations that will be discussed in the following.[51] This included the reduction of hematite. Their interpretation, however, was not as far reaching as the one given here.

As the experiments that are reported here are not new, the discussion shall be brief. In Figure 7.5 XP spectra from an amorphous (top two) and a crystalline (bottom two) sample before and after the modification with alumina are displayed. Difference spectra as were used in the previous parts of the work are being omitted here to shorten the discussion. They can, however, be found in Figure A14 with a brief discussion.

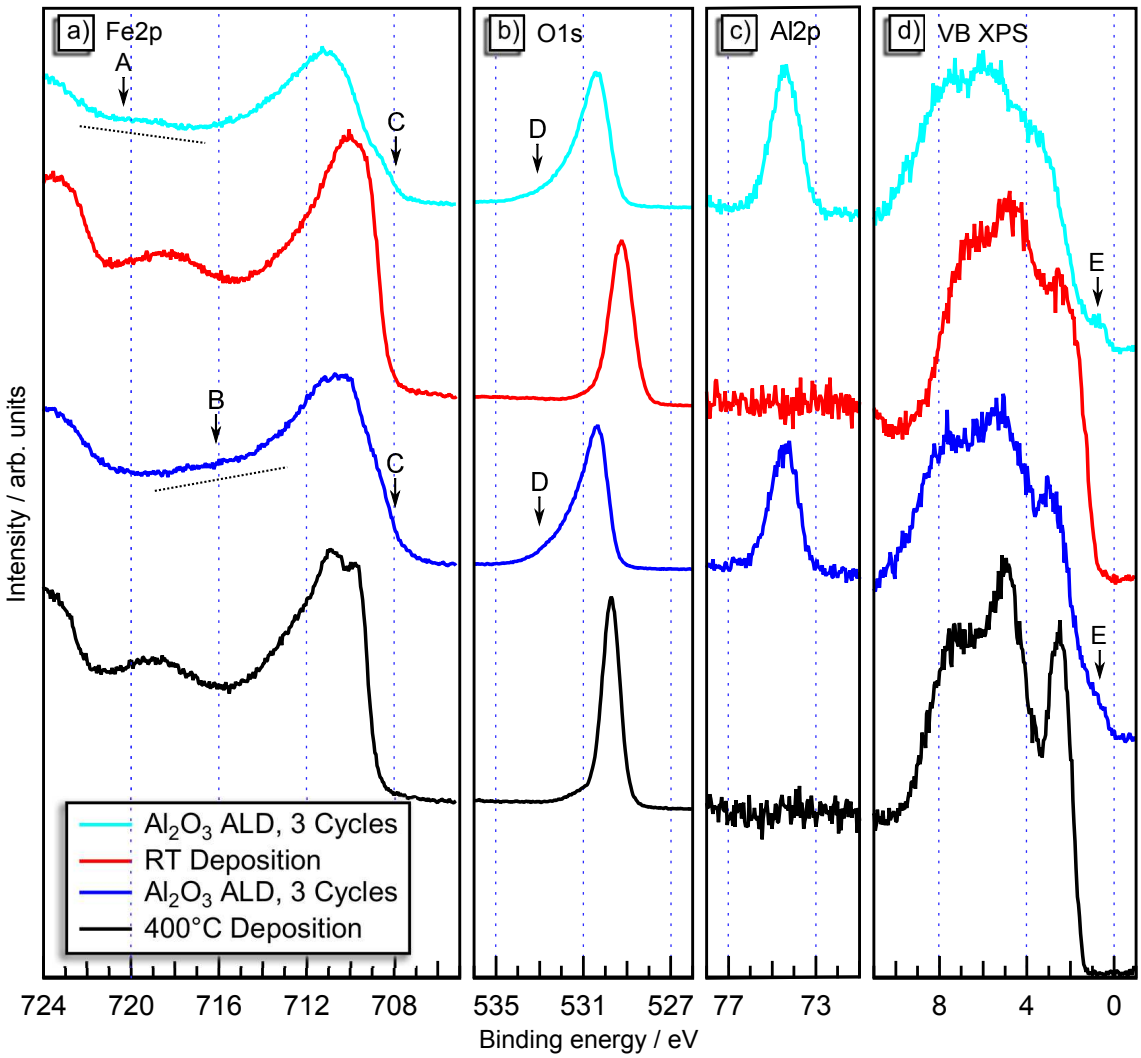

Figure 7.5: Surface modification of an amorphous (top two) and a crystalline (bottom two) sample by atomic layer deposited alumina.

The two samples show a Fermi level of 0.73 eV in the amorphous and 1.36 eV in the crystalline case before the modification, respectively. Afterwards the determination of the exact Fermi level position is challenging. This is due to the strong changes in all spectra. These are labeled as A-E.

Features A and B in the Fe2p spectra are of similar origin and can be clearly explained by the formation of Fe^{2+}.[125, 126] This was described by Tallarida et al. to already occur from a charge transfer from TMA to Fe_2O_3 .[51] The reduction also changes the low binding energy side of the $Fe2p_{3/2}$ emission (label C) and the valence band maximum (label E). These two features were also found in Figure 7.3 and discussed there.

The difference between A and B originates from the amount of Fe^{2+} that was formed. B is much closer to the satellite that could be expected for Fe^{2+}, whereas A can be better explained to be the absence of the Fe^{3+} satellite.[129, 130] This is in agreement with the intensity of feature E and the difference spectra of the two alumina-modified spectra in Figure A14. There, the difference clearly resembles the spectrum from a Fe^{3+} compound which shows that the amorphous sample contains more of this species.[125, 126]

Feature D in the O1s peak can be assigned to originate from the alumina top layer. As water is involved in the process some traces from molecular water or OH^- could be present as well. The difference spectra in Figure A14 of the O1s peak before and after the addition of alumina, however, only show one peak to be responsible for feature D. As OH^- and water can both be regarded to be rather volatile and the sample was heated for the reaction to take place it is most likely that these species have been evaporated.

Finally, the Fermi level position of the samples after the modification can be found with the difference spectra as well. From the shift of the valence band of the unmodified samples it is deduced that both samples have a Fermi level position of 1.75 eV after the modification. This is in very good agreement with the discussion on the charge transition of iron within hematite that can be found in chapter 8 and the findings from the water exposure. It also sheds light on the question why the amorphous sample contains more Fe^{3+} than the crystalline sample.

For the latter, less charge carriers need to be transferred in order to raise the Fermi level from 1.36 eV to 1.75 eV than it is the case in the former where the difference is from 0.73 eV to 1.75 eV. With Fermi level pinning present no additional electrons are allowed in a region of the sample where the Fermi level is already at 1.75 eV.

In the situation described here, any electron originates from the interface formation with alumina. Hence, once the Fermi level in the close vicinity of the interface is raised to 1.75 eV the electrons have to move deeper into the sample. For the crystalline sample this

results in a higher fraction of the measurement volume of XPS being reduced than for the amorphous sample. The interpretation is schematically depicted in Figure 7.6.

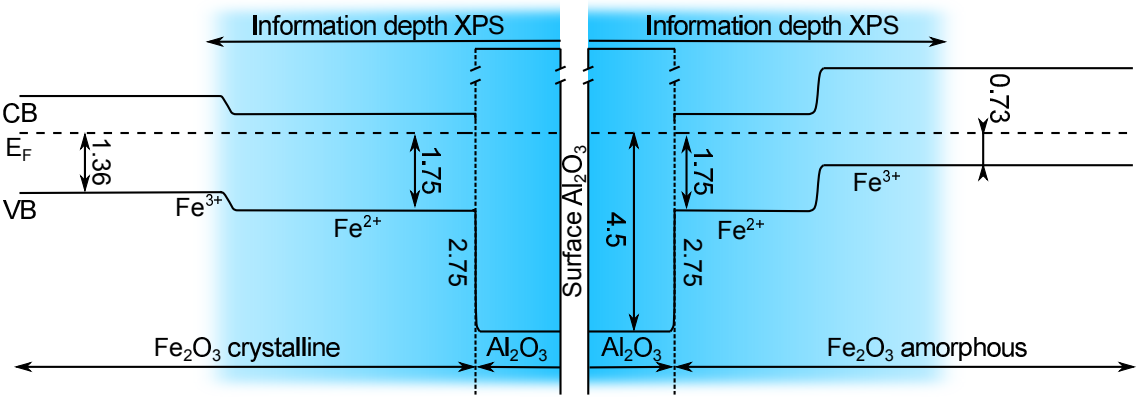

Figure 7.6: Schematic illustration of the possible band alignment at the interface between crystalline and amorphous hematite and alumina. The Fermi level position in alumina is taken from Refs.[108] and [114]. A potential drop in the alumina layer is neglected in this illustration. All annotated energies are in eV.

7.3 Interface experiments

Interface experiments are a way to study the contact formation between two materials. For this purpose a thin film of a contact material is being deposited in a step-wise process onto the material that is to be studied[4]. XPS measurement between the depositions allow for the determination of the Fermi level position after each deposition step. For the studies presented here, the aim was to find extreme Fermi level positions in order to gain knowledge on Fermi level pinning mechanisms that might be prevalent in hematite. A more detailed description of interface experiments can be found in Chapter 2.3.2.

7.3.1 Interface to RuO_2

The interface behavior of hematite towards RuO_2 was studied on two hematite films in two independent experiments. Once, a nominally undoped Fe_2O_3 thin film deposited at 400 °C was used and then, a similar experiment was carried out on a Zr-doped Fe_2O_3 thin film that was deposited at the same temperature. Both films were deposited onto platinized quartz. Detailed deposition conditions for the two films can be found in table 3.3.

[4] The contact material is being referred to as "film", whereas the material below (hematite in most cases) is being referred to as "substrate" in the following

RuO_2 was deposited at room temperature with the conditions found in Table 3.4. These parameters are standard conditions.[55, 284–286] As a consequence, the results discussed here can easily be compared to other interface experiments with RuO_2 as contact material.

The acquired spectra of the two experiments only show a shift in core-level position due to the growing film thickness. No spectral changes were observed. For the sake of briefness these spectra are not shown here but can be found in Figure A15. Instead only the Fermi level behavior during the experiment and the resulting band alignment of hematite towards RuO_2 is being shown in Figure 7.7.

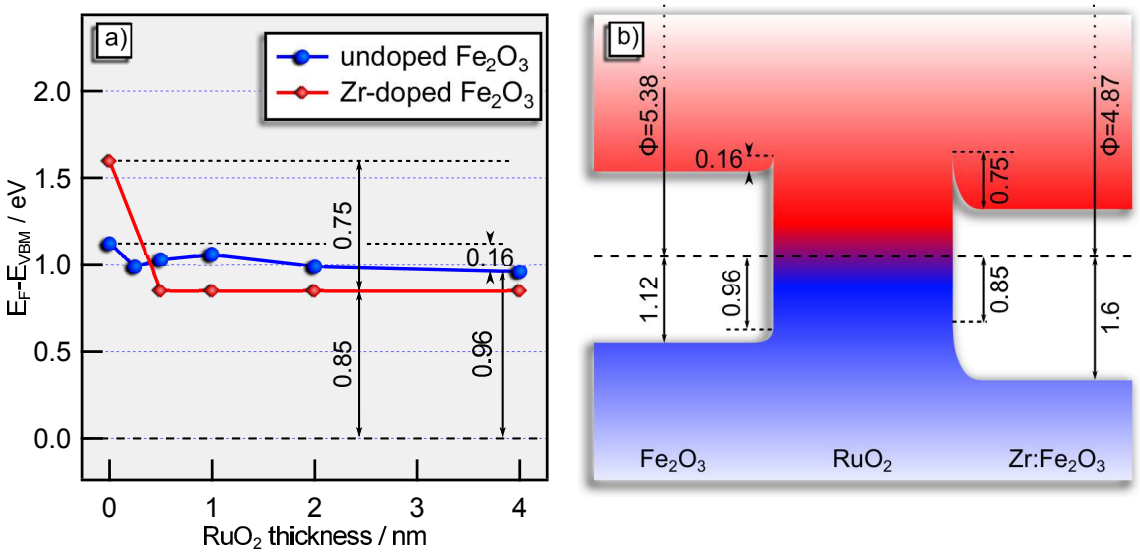

Figure 7.7: Interface behavior of hematite to RuO_2. a) Fermi level dependency in hematite on thickness of RuO_2 film and b) band alignment at the Hematite|RuO_2 interfaces. The film thickness in a) was calculated based on the deposition times with an assumed deposition rate of 3 nm min^{-1}.[110] All annotated energies are given in eV.

The Fermi level behavior in both substrates, i.e. undoped and Zr-doped, has been derived by following the position of the $Fe2p_{3/2}$ core-level during the course of the experiment. The Fermi level of the metallic film is assumed to be at zero for all film thicknesses. It is known that the Ru3d core-level exhibits a change in peak appearance with increasing film thickness. This can be attributed to the complex interaction between oxygen and ruthenium which only forms the complete electronic structure for large enough film thicknesses.[287–289]

Before the first film deposition step the two substrates differ in their Fermi level position. The undoped Fe_2O_3 sample shows a Fermi level position of 1.12 eV which is about midgap of the optical band gap of hematite. Due to the doping with zirconium the other sample has a higher Fermi level of 1.6 eV.

With the deposition of RuO_2 the Fermi level in both samples are being lowered. For the undoped case it reaches a position of about 0.96 eV, whereas in the doped sample it is shifted to 0.85 eV. Within the precision of the determination of the binding energy of the $Fe2p_{3/2}$ core-level these two values are identical. A similar result was found for this interface before.[55] Both are, more or less, independent on the growing film thickness.

This indicates that either during the first deposition step enough charges are being transferred in order to compensate for the difference in work function or that the Fermi level is being pinned at this position. As lower Fermi levels have been found, e.g. by Mg-doping or the oxygen plasma treatment, the second possibility is discarded.

The first possibility only holds, however, if the work function of RuO_2 at the interface is drastically lower than the value of about 6.5 eV which was measured on the thick film in both experiments. This agrees with observations from other interface experiments within this group where the work function of the final film always seems to be too high.[55, 76, 284–286] RuO_2 seems to act as if it had a work function of only 5.5 eV in interface experiments[5].[55, 76, 284–286] Results from differently sputtered RuO_2 thin films indicate that this overestimation might be attributed to the adsorption of oxygen.[290–292]

7.3.2 Interface to NiO

Using NiO as contact material in an interface experiment was tried as nickel oxide has been used as hole selective contact in photovoltaic applications with oxides before and can potentially lower the Fermi level even further than RuO_2.[76, 110] For hematite it was shown that a thin layer of NiO can improve the photoelectrochemical performance by exhibiting the charge separation, lower the recombination, and improve the kinetics through catalytic effects.[293–295]

Li et al. reported a band alignment between the two materials with the valence band maximum of hematite being positioned about 0.2 eV below the valence band maximum of NiO.[293] It was determined from the PES signal of a bare hematite thin film compared to a hematite film partially covered with NiO nanoparticles. The experiment is, therefore, different from the approach which is discussed here but the results will be taken into account in the discussion of the present results.

The experiment was carried out as discussed before. Again, two hematite thin films were used which were both deposited at 400 °C. One was nominally undoped and the other doped with zirconium. The detailed deposition parameters can be found in table 3.3. For the NiO films a room temperature deposition was chosen in both cases. The

[5] Please also see Figure A20 and the associated discussion

oxygen content was 20 % in the sputter gas. More details of the depositions can be found in Table 3.4.

In contrast to the interface experiment with RuO_2 where the $Fe2p_{3/2}$ core-level was used to follow the shift of the Fermi level, for the experiment with NiO the position of the $Fe2p_{1/2}$core-level had to be used. The reason for this different procedure is the superposition of $Fe2p_{3/2}$-emission with the LMM-Auger line from NiO. The core-level and valence band spectra of the two materials can be found in the appendix in Figure A16. Here, only the Fermi level behavior and band alignment shall be discussed which can be found in Figure 7.8.

The thickness of the NiO has been calculated assuming a constant rate of $1.4\,\mathrm{nm\,min^{-1}}$ as has been determined on thicker films before.[110] From the attenuation of the hematite spectra in Figure A16 it can be stated that by using this rate the film thickness is probably under-estimated. This, however, has no influence on the interpretation of the Fermi level behavior during the experiment.

Before the first deposition the Fermi level of the two samples do not differ much. Despite being nominally undoped the sample without zirconium shows a high Fermi level of 1.55 eV. This might be related to the deposition procedure where four samples where deposited at once and then removed from the system. Then, these samples were reintroduced to perform the interface experiment. Possible surface contamination from e.g. carbon hydroxides or water was removed by elongated heating in an oxygen atmosphere.

The heating most likely does have an influence on the Fermi level position but the high Fermi level is rather unexpected. A sample from the same deposition that was used in another experiment and heated in a similar way showed a Fermi level of 1.1 eV.

On the other hand, it cannot be completely disregarded that charging might occur due to poor contact between sample and sample holder. Especially after heating the different thermal expansion can cause such a problem. Also, the ITO sublayer may have a lower conductivity due to the heating in oxygen.

In the present case the binding energy shift due to charging is presumably about 0.5 eV. It could, therefore, not be detected by the regularly performed check during the alignment procedure where the O1s emission was being measured with and without electron flood gun. The Fermi level position from an UPS measurement on this sample was 2.03 eV which is too high and gives another argument for the charging.

A clear determination of the reason for the high Fermi level is not possible but there is a strong tendency to assign it to a charging effect. As a consequence, this value should

be dealt with carefully. The same applies for the band bending and work function in Figure 7.8b)[6]. The values which are affected from charging are labeled by an asterisk.

From the position of the Fermi level in the NiO film it can be concluded that after the second deposition step this film is not charging. This is then also the case for the hematite substrate. As a consequence, the Fermi level position at the interface can be deduced from this experiment.

The Fermi level in the Zr-doped sample is at 1.46 eV before the first deposition. This value is expected for a sample doped with zirconium and a similar value was extracted from the UPS measurement of the valence band. Please note that this sample was not removed from the system prior to the experiment. Also, it was deposited on platinized quartz.

For this sample it was possible to use the position of the $Zr3d_{5/2}$ emission in addition to the $Fe2p_{1/2}$ core-level. As can be observed in Figure 7.8 the Fermi level positions from both core-levels are almost identical for this sample. There is no contribution from NiO in the $Zr3d_{5/2}$ core-level. Hence, by using this peak not only the Fermi level position from the $Fe2p_{1/2}$ emission is confirmed for this sample but the usability of this emission to follow the Fermi level in an interface experiment with NiO is verified.

In Figure 7.8a) the Fermi level positions in the two hematite samples are being shown in large scale. For sake of observability it was decided not to include the Fermi level positions in NiO. These are, instead, presented in the inset. The deposition time and, therefore, the NiO thicknesses for the two experiments were not the same.

In both samples the Fermi level is being lowered after the first deposition of NiO. The nominally undoped sample shows a slightly higher Fermi level position in both, hematite substrate and NiO film. This might still be a charging effect. After the next deposition the Fermi level in the Zr-doped sample has reached it's final position of 0.8 eV above the valence band. Any further deposition does not show an effect on the Fermi level anymore.

The second deposition step in the experiment of the nominally undoped sample was slightly longer and, therefore, lead to a slightly thicker film. The Fermi level position in hematite is now at about 0.53 eV which is below the position in the Zr-doped hematite sample. The Fermi level in the NiO film is now, however, very similar to the Fermi level position in NiO on the Zr-doped sample. This indicates that no charging is present.

[6] The work function was derived by subtracting E_{VBM} from the XPS measurement from the ionization potential from an UPS measurement. This procedure allows for an extraction of a charging independent work function in case of homogeneous, light charging in UPS (but not XPS). In the present case where a charging effect in XPS cannot be neglected, however, it does, unfortunately, not apply.

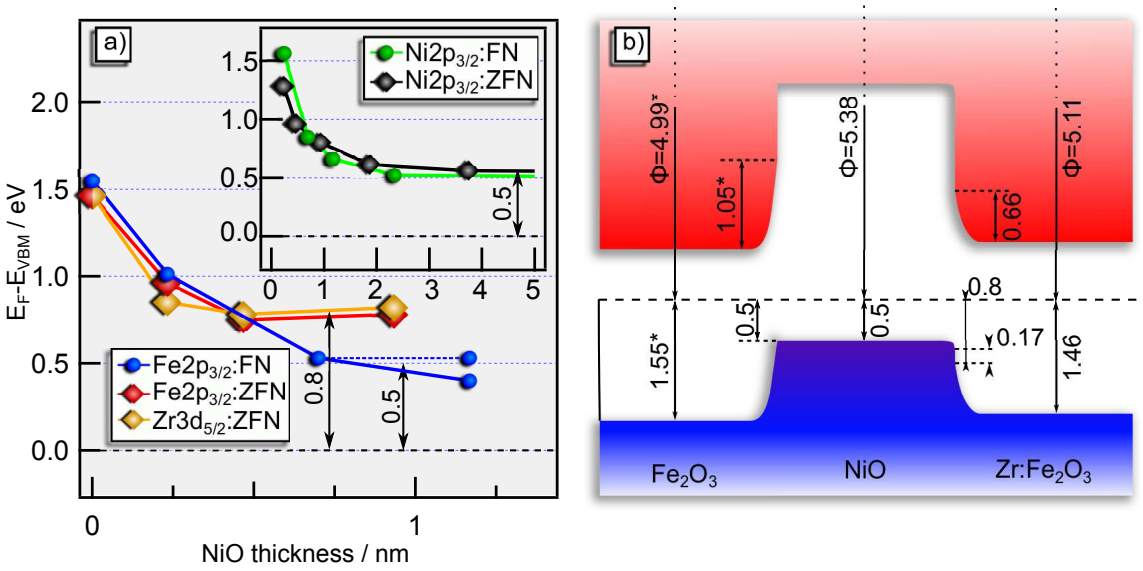

Figure 7.8: Interface behavior of hematite to NiO. a) Fermi level dependency in nominally undoped (FN) and zirconium doped hematite (ZFN) on thickness of the NiO film and b) band alignment at the Hematite|NiO interfaces. The film thickness in a) was calculated based on the deposition times with an assumed deposition rate of 1.4 nm min^{-1}.[110] The inset in a) shows the Fermi level dependency of the NiO films in dependency of the film thickness. All annotated energies are given in eV. Values labeled with an asterisks might suffer from charging effect.

After the next deposition the determination of the peak position becomes less precise due to the low intensity of the iron signal and the broad peak. Initially a value of 0.4 eV was being derived. It is, however, also possible to derive are value of 0.53 eV. In order to show this uncertainty it was decided to include both values in Figure 7.8a). As a final value of the Fermi level position at the interface $E_F - E_{VBM}$=0.5 eV is being assumed.

The band alignment derived from the two different experiments is being drawn in Figure 7.8b). For the undoped hematite no valence band offset is derived. A value for band bending cannot be given as the initial Fermi level position of the bare substrate is questionable.

In the doped case, a different band alignment is derived. Here, a valence band offset ΔE_{VBM} of 0.17 eV could be calculated. A small band bending of 0.13 eV in NiO was assumed. To obtain this value the band bending in hematite of 0.66 eV was subtracted from the difference between first and last Fermi level position in NiO during this experiment of 0.79 eV. The valence band offset agrees very well with the results from Li et al. who determined a value of $\Delta E_{VBM}$of 0.21 eV for Ti-doped n-type hematite and NiO.

The band bending of 0.66 eV in the Zr-doped thin film, however, needs further considerations. From the difference of the work functions of the two materials a maximal band bending of 0.27 eV should be expected. For NiO, however, the work function was

deduced from the surface of the this film. It is most likely not the same at the interface even if band bending is neglected.[110] The reason for this can be found in the complex electronic structure of NiO that is only complete once a certain film thickness has been achieved. This has been calculated by van Veenendal et al. and corresponds to the shape of the Ni2p core-level.[289] From the results shown here, it can be assumed that a higher work function is present for thinner NiO film. This assumption is supported by the reported work function of NiO nano-particles of 6.55 eV from Li et al.[293]

Assuming that the sum of band bending $eV_{BB}^{NiO} + eV_{BB}^{Fe_2O_3}$ is the difference in work function the following applies

$$\phi^{NiO} = \phi^{Fe_2O_3} + eV_{BB}^{NiO} + eV_{BB}^{Fe_2O_3} = 5.11\,\text{eV} + 0.13\,\text{eV} + 0.66\,\text{eV} = 5.9 \tag{7.1}$$

From earlier interface experiments with NiO and RuO_2 it is known that the valence band of NiO is about 0.5 eV below the Fermi edge of RuO_2.[110] Jan Morasch stated in his thesis that this is a strong argument for a work function of RuO_2 of 5.5 eV at the interface. The same argumentation holds for a work function of 6.0 eV at the interface for NiO. This is in very good agreement with the value estimated above.

The different band alignment in the two samples cannot conclusively be explained, yet. The NiO phase should be identical for both experiments. Hence, it should be possible to shift the Fermi level in the Zr-doped samples as far down as in the undoped sample unless there is another mechanism that pins the Fermi level. An intrinsic mechanism within hematite can be omitted because lower Fermi level positions have been achieved in Mg-doped samples. The pinning level might, therefore, be related to the doping with zirconium and the introduced disorder in the sample. The interface experiment of undoped hematite and NiO should be performed again and further evidence for a different final Fermi level position at the interface of hematite to NiO needs to be collected before a model can be proposed to explain these.

7.3.3 Interface to ITO - Effect on Fe_2O_3 and Sn : In_2O_3

In order to examine the possibility of hematite to shift the Fermi level upwards interface experiments towards tin-doped In_2O_3 (ITO) were deduced. During these experiments not only an unexpected behavior of the Fermi level in hematite was observed but also the Fermi level position in the thick ITO film at the end of the experiment was found to be unusually high.[88] Both observations were further investigated and will be discussed in the following.

The first part will deal with the Fermi level behavior in hematite. Then, the changes to ITO due to the underlying hematite layer will be discussed. Finally, the band alignment between hematite and ITO considering all conclusions will be presented.

The Fermi level in hematite

The interface experiments of hematite towards ITO were carried out with ITO films that were deposited at room temperature. For every experiment presented here, the ITO deposition conditions were similar. They can be found in table 3.4. These deposition conditions have been used before for interface experiments.[76, 188, 284, 286]

As substrates different hematite thin films were used. These included depositions at room temperature and 400 °C and differently doped films. The detailed deposition conditions can be found in table 3.3. In the following the experiments on an undoped and Zr-doped hematite film, both deposited at 400 °C, will be discussed. The other substrates showed the same results.

When analyzing the spectra from the interface experiment one challenge had to be faced. Namely, the overlap of the Fe2p region from hematite with the $Sn3p_{3/2}$ emission from the overlying ITO film. While the peak position seemed not to be affected tremendously, the satellite structure was completely changed. In order to be able to interpret the acquired data completely it was, therefore, necessary to implement a procedure to remove the interfering emission from tin. This procedure is graphically displayed in Figure 7.9.

The removal of the tin signal is depicted in panel c) of Figure 7.9. A difference spectra was obtained by subtracting the signal from the Fe2p region (706 eV to 741 eV) from the last measurement on the thick ITO film from the respective spectra that had to be corrected. As an example the spectra after the first deposition step (labeled as II in b) and c)) is shown.

As the film thickness increases with each deposition step the spectral ratio changes from hematite origin to ITO origin. In order to adjust for these changes and the possible shift of the Fermi level the intensity and position of the $Sn3p_{3/2}$ core-level was assumed to scale with the intensity and position of the undisturbed $Sn3d_{5/2}$ peak.

For each $Sn3d_{5/2}$ core-level that was acquired during the experiment the area ratio and relative shift to the $Sn3d_{5/2}$ emission from the thick film was obtained. The former was then used to scale the intensity and the latter to adjust for a change in Fermi level position. The subtracted spectra perfectly resemble spectra from hematite.

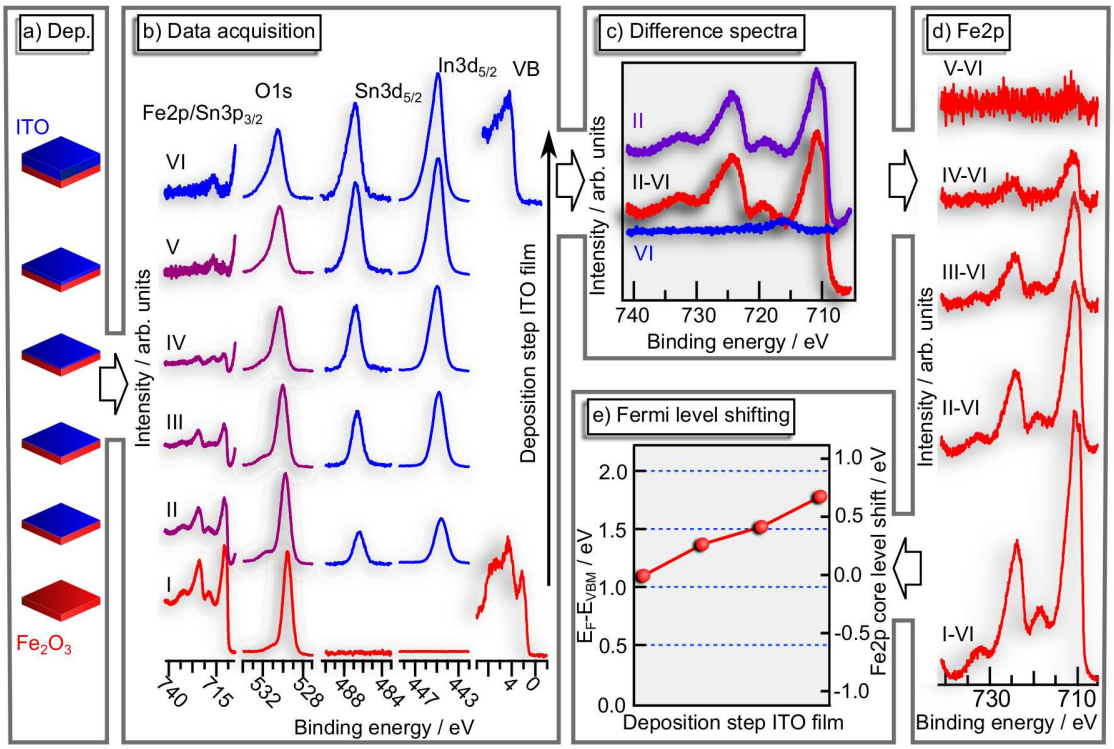

Figure 7.9: Processing steps involved in the analyzation of a hematite|ITO interface. a) Stepwise deposition of ITO film on hematite substrate, b) Stepwise data acquisition (red: only from hematite, blue: only from ITO, purple: superposition of both), c) necessary subtraction of scaled and shifted $Sn3p_{3/2}$ spectra in order to recieve a Fe2p spectra, d) Fe2p spectra, and e) Fermi level position during the experiment from the $Fe2p_{3/2}$ core-level shift.

This is shown in panel d) of Figure 7.9. The position of the $Fe2p_{3/2}$ core-level of these spectra was used to determine the Fermi level position during the experiment. The development of the Fermi level can then be plotted in dependency of the film thickness which is shown in e) as an example.

At this point the story can be told in different ways. Either, as it occurred. which would involve a lengthy discussion and the implementation of different experiments or written with the knowledge which was obtained during and due to the interpretation of the experiments. Obviously, the second approach is chosen. It has to be stated, however, that the observations and first interpretations which will be given in the following and which will lead to the general conclusion in the following chapter were developed over a timelapse of about two years.

The central graph of Figure 7.10 shows the Fermi level positions which were obtained for different doped and undoped thin films as also shown in Figure 6.13. In addition the interface experiment of undoped hematite to NiO is shown as blue line and squares which was discussed in previously around Figure 7.8.

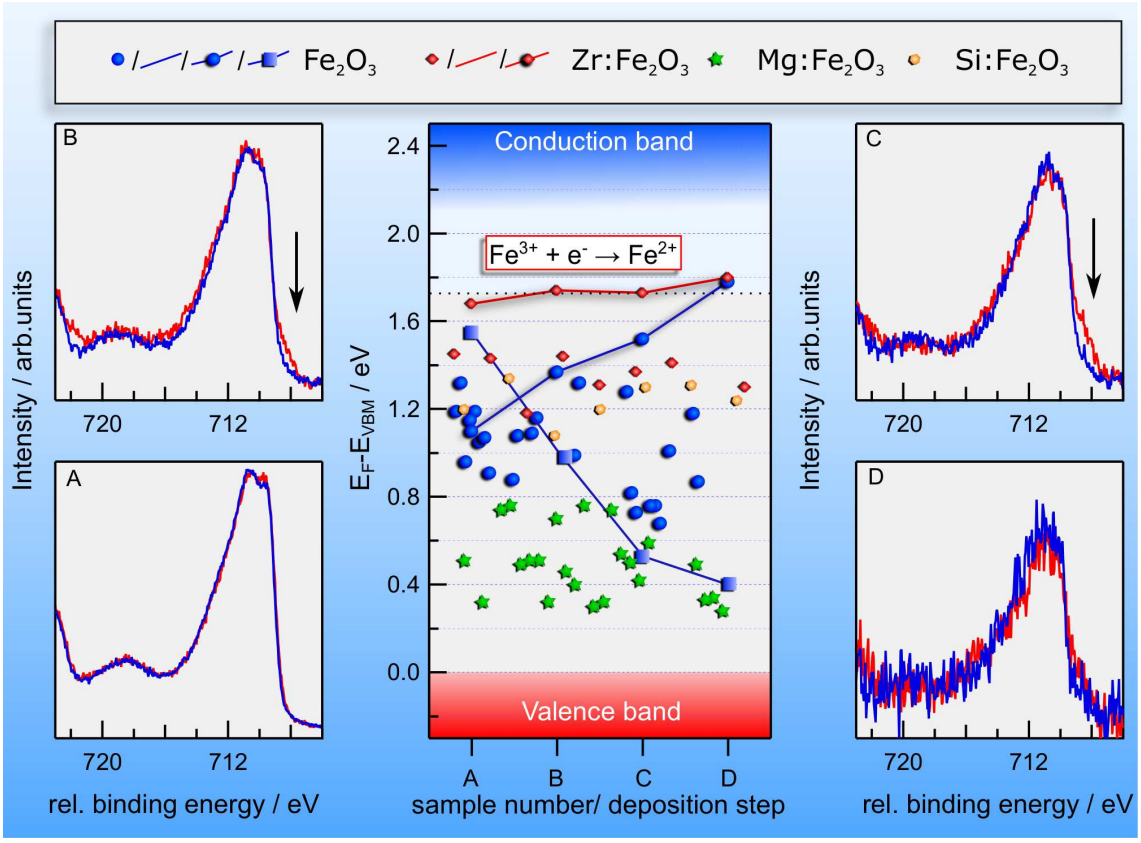

Figure 7.10: Achievable Fermi level positions in hematite. The central graph shows the measured Fermi level positions for nominally undoped (blue circles) and doped thin films with different dopants (red diamonds: Zr, green stars: Mg, and yellow pentagons: Si). In addition the Fermi level position for interface experiments towards ITO on an undoped (blue line and circles) and a Zr-doped (red line and diamonds) thin films and towards NiO on an undoped thin film (blue line and squares) are shown. The comparison of the corresponding Fe2p spectra at the different stages of the experiments are shown on the right and left hand side of the central graph.

Finally, the Fermi level positions during the interface experiments to ITO are displayed for an undoped (blue line and circles) and a Zr-doped (red line and diamonds) hematite thin film. The two substrates were both deposited at 400 °C.

In the undoped sample a Fermi level of 1.1 eV was found whereas the Zr-doped sample showed a much higher Fermi level of 1.68 eV. After the first deposition of ITO the Fermi level for both samples has been raised. This continues unti the third ITO deposition for the undoped sample where a maximum Fermi level position of about 1.8 eV is reached.

The doped sample behaves differently. After the first ITO deposition a Fermi level position of 1.75 eV is reached. With any following deposition no further change in the Fermi level position is observed. As a consequence, both samples show a Fermi level position after the third ITO deposition which, within the margin of error, is the same.

This observation is surprising. ITO shows a work function of about 4.4 eV and should be able to raise the Fermi level much higher in hematite[7]. The non-changing Fermi level position in the doped sample indicates that Fermi level pinning occurs at about 1.75 eV above the valence band.

The reason for the Fermi level pinning can be found in the Fe2p spectra around the central graph of Figure 7.10 which were obtained during the experiments. By comparing the spectra from the two experiment after each deposition step it is possible to find differences. For this purpose the spectra were normalized and set to a common Fermi level.

No difference can be observed for the pure substrates (A). Both, the blue line of the undoped and the red spectrum of the doped sample show a characteristic shape for Fe^{3+} species.[61, 125, 126] This, however, is no more the case after the first ITO deposition (B). While the blue spectrum of the undoped sample did not change, the red spectrum of the doped sample developed shoulders at the low binding energy side of both, the $Fe2p_{3/2}$ and $Fe2p_{1/2}$ emission, of which the former is marked with an arrow. In addition, the intensity of the Fe^{3+} satellite has been attenuated for this sample as well. These observations intensify for the next deposition step (C). Only after the third deposition step (D) the two spectra show a good overlap again, as the blue spectrum has developed a shoulder to its low binding energy side as well. The appearance of the shoulder and the attenuation of the satellite can be explained by a change in the oxidation state of iron from Fe^{3+} to Fe^{2+}.[125, 126, 129, 130, 155] As both can only be observed for Fermi level positions above 1.75 eV and increase in relevance with each ITO deposition step for the doped sample it can be deduced that the reason for Fermi level pinning is the change in oxidation state.

In other words, instead of further raising the Fermi level and preserving the Fe^{3+} oxidation state, part of the Fe^{3+}-ions in hematite are changed to Fe^{2+}. Any additional electron can now be found on an iron site where it is trapped in this oxidation state. The impact of this interpretation and the relation to observations from other experiments will be discussed in detail in chapter 8.

The Fermi level in ITO

In the data from ITO of the interface experiments of hematite to ITO an oddity was noticed. With the deposition conditions, which were used during the experiments, usually a Fermi level position in the thick film of about 2.9 eV is achieved.[61] For the case of ITO on hematite, however, Fermi level positions as high as 3.2 eV were obtained. At the same time the In3d core-levels showed as strong asymmetry on the high binding energy

[7] Based on the Anderson rule a Fermi level position of 2.2 eV can be expected if an ionization potential of 6.6 eV is assumed for hematite

site which is expected for high Fermi level positions in ITO. Additionally, the UP spectra showed a Fermi edge which verified that the high Fermi level was not a charging effect.

It was decided to investigate this topic further. The following section discusses the effect of the hematite layer on the opto-electronical properties of ITO grown at room temperature. It could be shown that hematite acts as seed layer by enhancing the crystallinity of the ITO films. In addition, the metastable rhombohedral phase of In_2O_3 is stabilized.

In order to investigate the role of the Fe_2O_3 layer below on the ITO thin films above ultrathin hematite films with $\leq$10 nm thickness were deposited from a metallic iron target in an Ar-O_2 mix with 8 % oxygen at a pressure of 0.5 Pa in a first step. Amorphous Quartz and c-cut Sapphire (S0001) were used as substrates. If not noted otherwise, the deposition temperature was 400 °C. With these parameters phase pure, crystalline hematite ($\alpha-Fe_2O_3$) thin films are formed.[61] After cooling to room temperature the samples were transferred in ultra-high vacuum (UHV) to a second deposition chamber for the ITO deposition. This was performed using a ceramic ITO target with 10 wt.% SnO_2 doping. The depositions were performed at room temperature in pure Argon atmosphere at a pressure of 0.5 Pa and a power density of 1.23 W cm^{-2}.

In Figure 7.11 the electrical as well as the surface chemical and electronic properties of ITO thin films that were grown with and without Fe_2O_3 seed layer are presented. As shown in b) the conductivities of the ITO films with the seed layer are about one order of magnitude higher compared to those deposited on the bare quartz and sapphire substrates at the same conditions. This improved property originates from a higher carrier concentration as is evident from Figure 7.11a). At the same time carrier mobility is slightly reduced from 40 cm V^{-2} s to 46 cm V^{-2} s to 29 cm V^{-2} s to 40 cm V^{-2} s. The conductivity of ITO films grown on Fe_2O_3 seed layers is rather independent on film thickness as evident from Fig. 7.11(b). The enhanced conductivity is therefore clearly a bulk phenomena and not related to the region next to the Fe_2O_3 interface.

XP spectra, in which the effect has actually been identified originally, confirm the high conductivity. Films grown on Fe_2O_3 seed layers show consistently higher core level and valence band maximum binding energies compared to their counterparts without Fe_2O_3 seed layer. The higher conductivity of the spectra is also evident from the stronger asymmetry of the core level lines towards higher binding energy, which relates to a higher plasmon energy and therefore carrier concentration.[296] Finally, occupied conduction band states are also observed by UPS as a Fermi edge emission shown in Figure 7.11e). The highest intensity of the Fermi edge is observed for the sample on sapphire (0001) with a Fe_2O_3 seed layer. This observation agrees perfectly with the highest charge carriers concentration that was observed in this sample.

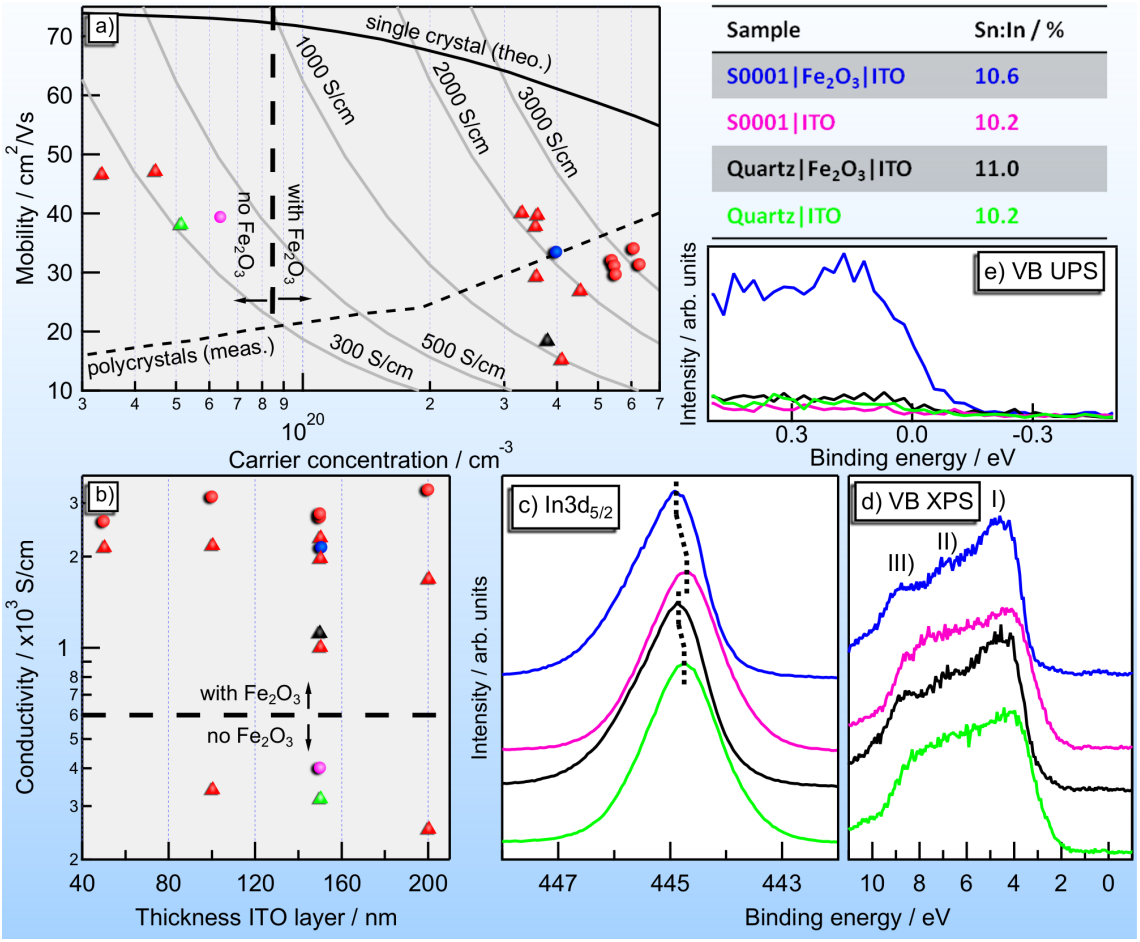

Figure 7.11: Electrical measurements (a, b), In $3d_{5/2}$ core levels (c), XP valence bands (d), and magnified UP Fermi edge spectra (e) of room temperature deposited ITO thin films with and without Fe_2O_3 seed layers. In (a) and (b) films grown on sapphire (0001) are indicated by circles and films grown on quartz by triangles. The colored symbols in (a) and (b) and the spectra in (c)-(e) correspond to the same samples as identified in the table giving the Sn:In ratio determined from XP core level intensities.

In Figure 7.12 optical transmission spectra are being observed. An improved transmission is observed for a seed layer thickness of 2 nm compared to an ITO film grown at room temperature on sapphire without seed layer. Increasing the seed layer thickness to 10 nm reduces the transmission for wavelengths between 370 nm to 630 nm. In this range, the transmission follows the one recorded for a 10 nm thick Fe_2O_3 layer, indicating that the transmission of the ITO layer is still high. By optimizing the Fe_2O_3 /ITO stack the requirements for a transparent electrode can, therefore, be met.

The Sn/In ratio determined from XPS for films with and without Fe_2O_3 seed layer on quartz and sapphire are all within 10 at % to 11 at % as is being indicated in the table included in Fig. 7.11. This corresponds well with the nominal target composition. In contrast, films with high conductivity grown at higher substrate temperatures, often exhibit a significantly enhanced Sn/In ratio.

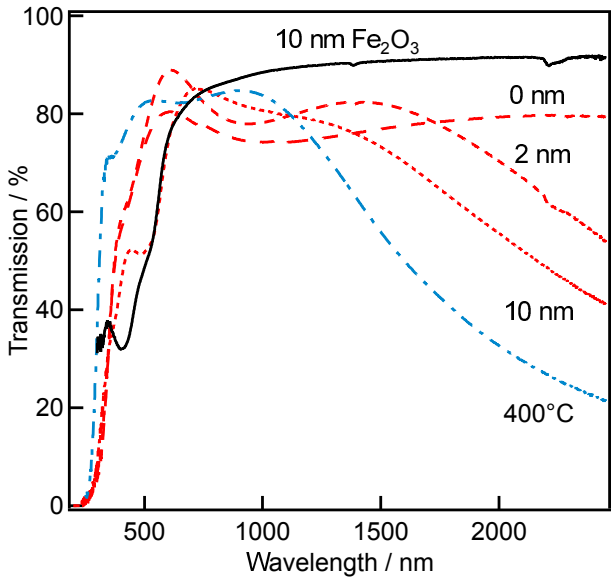

Figure 7.12: Optical transmission spectra of 150 nm thick ITO films grown at room temperature on sapphire with 0 nm, 2 nm and 10 nm thick Fe_2O_3 seed layers. Transmission spectra recorded for a 10 nm thick Fe_2O_3 film on sapphire and of a 150 nm thick ITO film grown at 400 °C on quartz without seed layer are added for comparison.

This indicates a segregation of Sn to the surface in these samples.[297, 298] Such a segregation is evidently not observed when the films are grown at room temperature. This is reasonable given the fact that Sn-donors are mobile only at 300 °C.[280, 297]

The XP valence band spectra of samples grown with and without Fe_2O_3 seed layer exhibit a different shape. In particular, three distinct features are observed for films grown on Fe_2O_3 , which are less pronounced in the spectra of samples without Fe_2O_3 layer. The differences might be related to different crystallinity, orientation or phase composition. In order to reveal the influence of the hematite layer on the structural properties of the ITO, X-ray diffraction experiments have been performed on 150 nm thick films. The corresponding diffraction patterns are shown in Figure 7.13.

The diffraction pattern for the ITO film on quartz without the iron oxide layer does not show any reflections, indicating an amorphous structure. In contrast to this, a number of reflections appear for the film grown on top of the Fe_2O_3 layer. These can be assigned to cubic bixbyite In_2O_3 with (222) being the most intense one. There are, however, also some reflections, which do not belong to this phase. These additional signals can be assigned to the rhombohedral In_2O_3 phase.

In contrast to the ITO film deposited on quartz, the sample on S(0001) without Fe_2O_3 layer shows some reflections. Besides a very small reflection from the Sapphire substrate, only signals from the bixbyite In_2O_3 phase are observed. Again, (222) from this phase is the most intense reflection. The addition of a Fe_2O_3 layer changes the diffraction pattern

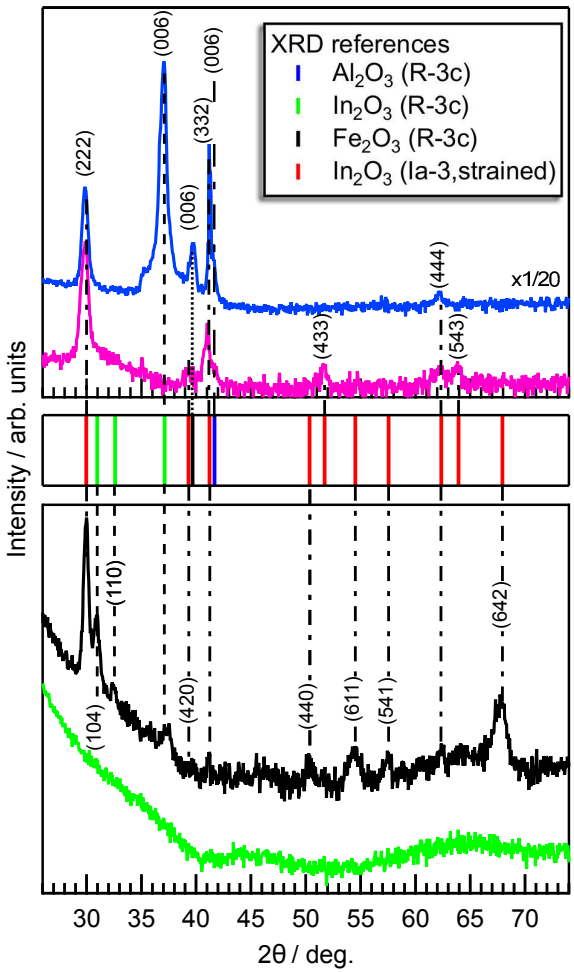

Figure 7.13: XRD pattern from $\theta - 2\theta$-measurements on samples with a ITO thickness of 150 nm. From bottom to top the samples are the following: quartz/ITO (green), quartz/Fe_2O_3/ITO (black), S0001/ITO (magenta), and S0001/Fe_2O_3/ITO (blue). All Fe_2O_3 layers had a thickness of 10 nm. All reflections have been identified and labeled with the help of pdf-card reference data (pdf card numbers rh-Al_2O_3: 11-661, rh-Fe_2O_3 : 84-311, rh-In_2O_3: 73-1809, and cu-In_2O_3: 6-416 (strained)).

considerably. The intensity of all reflections is increased by a factor of 20. Most intense is now the (006) reflection of the rhombohedral ITO phase. In addition, the rhombohedral (006) reflections of Fe_2O_3 and Al_2O_3 can be identified. This indicates epitaxial growth of rhombohedral In_2O_3 and Fe_2O_3 on sapphire (0001), which all share the same space group ($R\bar{3}c$).[299, 300] Among the reflections of the ITO bixbyite phase, the (332) is the most intense one.

The diffraction angles of rhombohedral In_2O_3 match those of the powder reference (pdf-card 73-1809). In contrast, the reflections from the cubic phase are shifted to smaller angles, which corresponds to an expansion of the lattice parameter by about 2 %. This is observed for all samples showing reflections from bixbyite In_2O_3.

The insertion of an ultrathin crystalline Fe_2O_3 film significantly enhances the crystallinity of room temperature deposited ITO films. However, while the cubic bixbyite structure is commonly observed when films are grown at elevated temperature, the Fe_2O_3 seed layer favors the growth of rhombohedral ITO, which is a metastable modification.[301] The different shape of the valence band spectra can be explained with the presence of rhombohedral ITO.[302]

Only few studies report the electric properties of rhombohedral ITO thin films. Solution processed nanoparticles that were fired at 600 °C and aged at 500 °C show a mixture of cubic and rhombohedral phases with a slightly smaller resistance but higher sensitivity towards gaseous ethanol compared to purely cubic films.[303–305] A transition from cubic to rhombohedral structure with film thickness has been reported by Malik and coworkers.[306]. They could show that the mobility of thicker rhombohedral films ($37\,cm\,V^{-2}\,s$) was higher than for thinner cubic films ($19\,cm\,V^{-2}\,s$). The charge carrier concentration was slightly lower for the rhombohedral films ($7.7 \times 10^{20}\,cm^{-3}$) compared to the cubic ones ($9 \times 10^{20}\,cm^{-3}$). Dunlop and coworkers have reported partially rhombohedral thin films at temperatures of 415 °C to 500 °C, showing a carrier mobility of $27\,cm\,V^{-2}\,s$ and a carrier concentration of $5.7 \times 10^{20}\,cm^{-3}$.[307] Both values are higher compared to purely cubic reference samples, which was attributed to lower internal strain. The highest conductivities reported for at least partially rhombohedral ITO are, therefore, in the range of $2400\,S\,cm^{-1}$ to $4500\,S\,cm^{-1}$. These values are comparable to those reported here. However, the previous values have all been obtained with processing temperatures well above 400 °C, while the conductivity achieved in the present work was achieved with room temperature deposited ITO without further annealing.

Based on the studies reported here, different mechanisms might contribute to the enhanced conductivity induced by the Fe_2O_3 seed layer:

(i) the enhanced crystallinity

(ii) the absence of dopant segregation

(iii) the presence of the rhombohedral phase

The literature survey above given above provides no evidence for fundamentally superior electrical properties of the rhombohedral compared to the cubic bixbyite In_2O_3 phase. It was, therefore, concluded that the rhombohedral structure is not responsible for the higher conductivity.

Carrier mobilities in amorphous TCOs are comparable to those of their crystalline counterparts.[308] This is caused by the low concentration of tail states, which is a consequence of the s-orbital character of the conduction band states.[89, 309, 310] On the first glance, it is, therefore, not surprising that the carrier mobility is not much different for films grown with and without Fe_2O_3 seed layer. However, crystallization induces grain

boundaries, which act as carrier traps and scattering centers.[311] The carrier mobilities of the films presented here are noticeably lower than those of single crystalline material (see solid line in Figure 7.11(a) and Ref. [312]). Grain boundary scattering is, therefore, active. There is evidence that the segregation of the Sn dopants to grain boundaries reduces carrier mobility.[280, 298] But the segregation requires elevated temperatures to activate Sn diffusion. No Sn segregation is, therefore, expected for films deposited at room temperature, which agrees with the absence of surface segregation of Sn. In any case, the main improvement in electrical conductivity induced by the Fe_2O_3 layer is the higher carrier concentration. Carrier mobility and the absence of segregation should, therefore, also play a minor role in the improvement of the conductivity.

Films deposited at room temperature are normally amorphous. In such films, the free carriers are not induced by heterovalent dopants, such as Sn, but by the off-stoichiometry (oxygen deficiency) of the samples.[89, 313] Crystallization will activate the donors.

It is, therefore, straightforward to assign the origin of the higher carrier concentration of films grown on Fe_2O_3 seed layer to the enhanced crystallinity. Given the significantly higher diffraction intensities, the enhanced crystallinity of films grown on sapphire/Fe_2O_3 , compared to those grown on quartz/Fe_2O_3 , also explains the higher carrier concentration of the former.

Other seed layers may exits, which favor crystallization at room temperature in the bixbyite phase. These might result in similar improvement. There are indeed literature reports on ITO films prepared at room temperature, which exhibit similar conductivity than the films prepared here with Fe_2O_3 seed layer (see Refs. [314, 315] and references therein). The crystalline state of these films is not reported, however. The deposition conditions that were used here were optimized for deposition at elevated temperatures. It would, therefore, be compelling to see whether there is room for additional improvement by a seed layer in a room temperature optimized deposition[8].

In summary, it was shown that the use of a Fe_2O_3 seed layer can enhance the electrical conductivity of ITO thin films deposited at room temperature by about one order of magnitude reaching yet a maximum conductivity of $3300\,S\,cm^{-1}$. The hematite structure of the Fe_2O_3 seed layer induces a local epitaxial growth and thereby enhances the crystallinity of the In_2O_3 layer. The effect is most pronounced on c-cut sapphire substrates but also observed on amorphous quartz substrates. The Fe_2O_3 layer results in a preferred formation of the metastable rhombohedral In_2O_3 phase, which is not considered to affect the electrical properties. However, crystallization at low temperature offers the advantage of suppressing dopant diffusion and, therefore, segregation. This can result in higher carrier

[8] At the time this thesis was written conductivities as high as $4000\,S\,cm^{-1}$ were achieved by using a reduced ITO target. This shows that improvement is still possible

mobilities compared to films crystallized at higher temperatures. The use of seed layers, therefore, offers an approach to reach high conductivity low temperature processed TCO films. The possibility to stabilize the rhombohedral R$\bar{3}$c phase of In_2O_3 by the Fe_2O_3 seed layer also provides a simple route for the preparation of such films.

A further improvement would be the possibility to deposit a crystalline seed layer at even lower temperatures. Post-annealing at only slightly elevated temperatures of room temperature deposited film might induce crystallinity in the seed layer. The same applies for very small deposition rates at only slightly elevated temperatures. The advantage of lower deposition temperatures could be found in the possibility to use flexible polymer substrates for flexible electronics.

Band alignment between hematite and ITO

In Figure 7.14a) the Fermi level positions in hematite and ITO for the interface experiments on undoped and Zr-doped Fe_2O_3 that were discussed in Chapter 7.3.3 are shown. From the experiment the band alignment between hematite and ITO could be extracted. This is shown in Figure 7.14b).

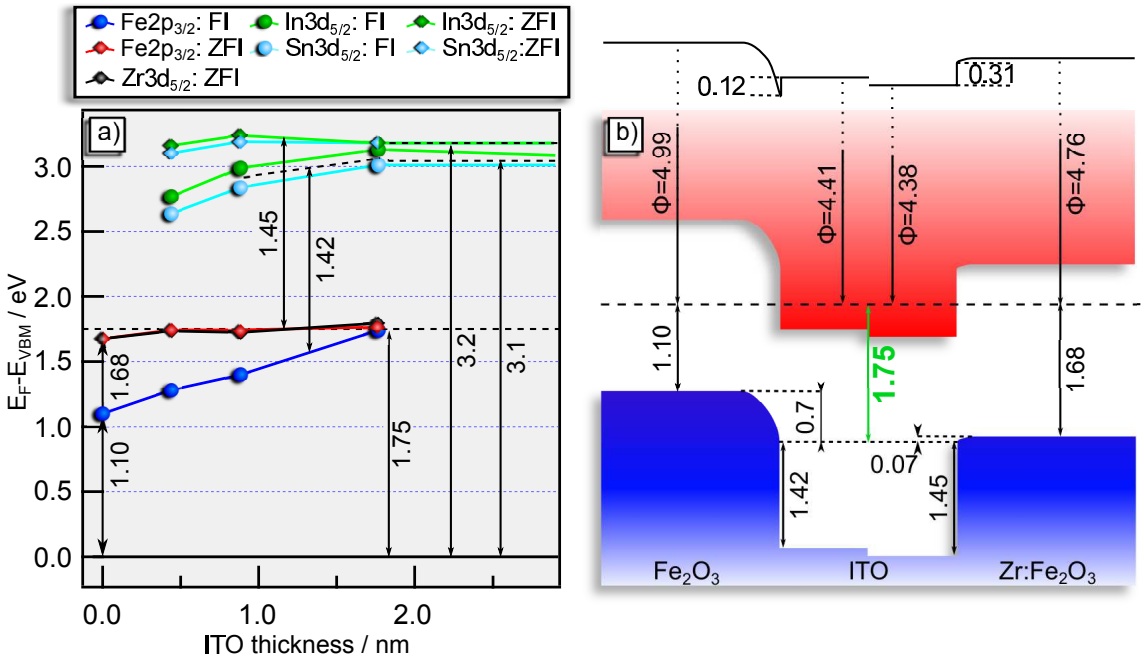

Figure 7.14: Interface behavior of hematite to ITO. a) Fermi level dependency in nominally undoped (FI) and zirconium doped hematite (ZFI) and the respective ITO films on thickness of the ITO film and b) band alignment at the Hematite|ITO interfaces. The film thickness in a) was calculated based on the deposition times with an assumed deposition rate of 5.3 nm min^{-1}. All annotated energies are given in eV.

The evolution of the Fermi energy position in hematite during the course of the experiment has already been discussed. Here, the discussion will, therefore, be restricted to the band alignment.

For both interface experiments a very similar valence band offset can be extracted. Independent on the initial Fermi level in hematite its valence band is positioned about 1.45 eV above the valence band of ITO. This value is in very good agreement with the band alignment of the two materials from transistivity consideration based on an hematite|RuO_2 interface.[55, 138] There, a value of 1.5 eV was proposed.

Other results from literature on the band alignment of the two materials seem to disagree with the results from PES studies presented here. There, the valence band of In_2O_3, which should have the same position as the one of ITO, is reported to be above the valence band of hematite.[6, 316] The difference is, that these band positions were derived from a consideration of theoretically derived surface potentials. These are a first approximation at best and the disagreement shows that detailed studies on the band alignment between two materials are necessary. The results presented here should be regarded to be much more reliable than the theoretically achieved results.

7.3.4 Interface to STO

In this part an interface experiment of hematite towards Nb:$SrTiO_3$ (STO) is described. The aim of this experiment was the determination of the valence band offset between hematite and STO. With the knowledge of this value the position of the band edges of hematite with respect to the vacuum level can be estimated with a higher certainty.[138, 148]

In addition, STO is also often doped with iron instead of niobium. For Fe as dopant the positions of the charge transition levels are still uncertain and it was hoped that the interface experiment could shed light onto this question as well.[317] The discussion on the position of the charge transition levels in STO, however, is beyond the scope of this work and will be disregarded here.

Hematite was grown onto a STO substrate. For this purpose a STO single crystal was heated in 0.5 Pa oxygen at 400 °C for 90 min in order to remove carbon containing surface contamination. Then, an interface experiment with the usual procedure was performed. Hematite was deposited onto STO at 400 °C with 8 % oxygen in the plasma. The accumulated deposition times were 0 s, 5 s, 15 s, 30 s, 60 s, 120 s and 1000 s. The measured spectra can be found in Figure A19

From the core-levels the shift in Fermi level position could be deduced. In STO the initial Fermi level after heating is at 3.0 eV. By depositing hematite it is shifted within two deposition steps to a value of 2.6 eV. Here it remains constant.

In hematite the final Fermi level position is found to be at 1.5 eV. Prior to that there is only a small shift which can be disregarded. The Fermi level behavior in STO and hematite is shown in Figure 7.15a). From these values it can be deduced that the valence band of hematite is positioned 1.1 eV above the valence band of STO. This is presented in Figure 7.15b).

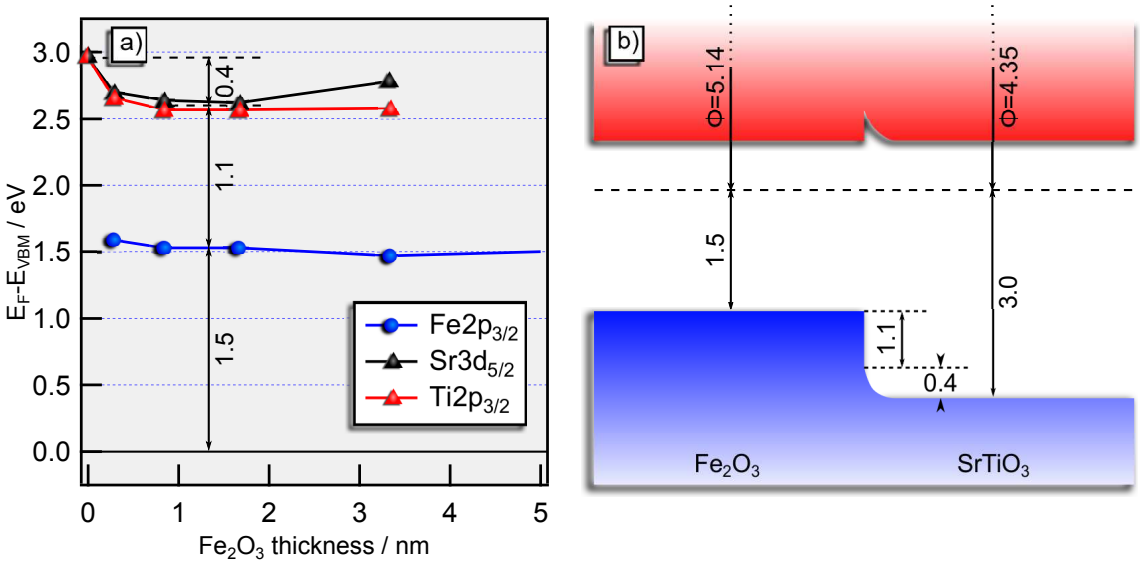

Figure 7.15: Interface behavior of hematite to $SrTiO_3$. a) Fermi level dependency in $SrTiO_3$ on thickness of the Fe_2O_3 film and b) band alignment at the $SrTiO_3$|Hematite interfaces. The film thickness in a) was calculated based on the deposition times with an assumed deposition rate of 3.3 nm min^{-1}. All annotated energies are given in eV.

A higher value of 1.5 eV was deduced from transitivity considerations.[138, 148] The same studies showed a good agreement to the band alignment of hematite and ITO from this work. It should be noted, however, that the validity of the transitivity rule is based on the equality of the contact material. The ITO that was used to deduce the band edge positions of STO was deposited at 400 °C.[111] On hematite, the ITO films has been deposited at room temperature. This makes these two ITO thin films hardly comparable.

The difference in the electronic properties of the contact material can explain the disagreement in the band alignment from transitivity and the direct measurement shown here. In addition, it has been observed is a disagreement in valence band offset between STO and ITO depending which material is grown on which[9].

[9] To be correct, the experiments were carried out with $(Ba,Sr)TiO_3$ thin films.[111]

Growing STO on ITO gives a valence band offset of 0.4 eV instead of 0 eV if the experiment is carried out the other way around. The latter position was used to deduce the value of 1.5 eV as the valence band offset between hematite and STO. The results presented here, however, show a much better agreement with the former result.

For STO it was shown that the Fermi level in STO at the interface to RuO_2 is at about 1.9 eV.[318] For hematite a value of 0.85 eV was obtained.[55] Using transitivity considerations would result in an estimated valence band offset of ≈1.05 eV for STO|Fe_2O_3 This is in very good agreement with the value of 1.1 eV found here.

The most important aspect, however, is the fact that electrochemical methods place the valence band of hematite only 0.56 eV above the valence band of STO. [6, 22] The discrepancy of this value with the finding presented here, indicates that the positioning of the band edges with respect to the vacuum level or redox potential of water for hematite is not correct. This issue will be further discussed in chapter 8.

7.4 Summary

In this chapter it could be shown that the Fermi level within hematite can be manipulated both, upwards and downwards, by contact formation.

With water, ALD-alumina, and ITO it was shifted upwards. In all three experiments a final Fermi level position of 1.75 eV was observed. In addition, the Fe2p core-level spectrum showed the formation of Fe^{2+}.

By an oxygen plasma treatment or contact formation to RuO_2 and NiO a downshift of the Fermi level could be achieved. The lowest Fermi level position was found at the interface to NiO for an undoped hematite sample. A similar experiment with a Zr-doped Fe_2O_3 substrate showed a higher Fermi level which might indicate a Fermi level pinning related to the Zr-doping. For further insight dedicated experiments are necessary.

Spectral changes due to the oxygen plasma treatment might indicate the formation of Fe^{4+}. The Fermi level, however, is not pinned as it is the case for the Fe^{2+} formation but can be shifted lower by the NiO interface or Mg-doping. This makes the assignment of the spectral changes to a change in the oxidation state questionable.

For ITO it was shown that this material benefits from the presence of a hematite seed layer below. The room temperature deposited ITO thin films showed a higher Fermi level and a higher conductivity due to a higher charge carrier concentration. The mechanisms to explain this is the crystallization of the films due to a good match to the structure of hematite with a stabilization of the meta-stable rhombohedral phase of In_2O_3. By this

process the doping with Sn is activated but the known Sn-segregation is prohibited due to the low deposition temperature.

Finally, the valence band offset of hematite to the different contact materials could be found. In the following only absolute values will be given. For the two contact materials RuO_2 and NiO the valence band maximum of hematite is positioned below the Fermi edge of RuO_2 and the valence band maximum of NiO, respectively. This is different in contact to ITO and STO where the valence band maximum of hematite is positioned above the valence band maximum of the respective contact material.

For RuO_2 a value of 0.85 eV was confirmed. The valence band offset to NiO was found to depend on the experiment and was either 0 eV or 0.17 eV. With the interface experiment to ITO a value of 1.45 eV could be deduced. This value agrees very well with a prediction from the transistivity rule.

Finally, the valence band offset to $SrTiO_3$ could be determined to be 1.1 eV. This value is in good agreement with the interface to RuO_2 of both materials and depends on the assumed valence band offset of STO to ITO also with the transistivity rule.

All of these direct experiments, however, show a disagreement with literature if electrochemistry or theoretical predictions are involved. This shows that direct measurements are necessary to gain knowledge on the band alignment of materials.

8 Polarons in hematite and their implication for the band gap

This chapter aims to give a single fundamental reason to all experiments of this work where a reduction of iron has been observed. It includes the results from interface experiments and derives a new picture of the electronic structure of hematite.

Important aspects of this chapter

- ... the Fermi level pinning at 1.75 eV occurs due to a Fe^{2+}/Fe^{3+} charge transition
- ... this charge transition can be assigned to small polaron formation
- ... the *polaron state* acts as effective band edge for the positioning of charge carriers
- ... this *polaron gap* reduces the applicable band gap and therefore the photovoltage to be expected
- ... due to the *polaron state* the band edge positions of hematite are situated at higher energy positions than can be found in literature

Within this thesis hematite was modified by different kind of treatments. After certain treatments a reduction of iron could be observed. Selected Fe2p spectra from these treatments are shown in Figure 8.1. Red and black spectra represent the sample before and after the corresponding treatment, respectively. The green spectra show the difference of the former two.

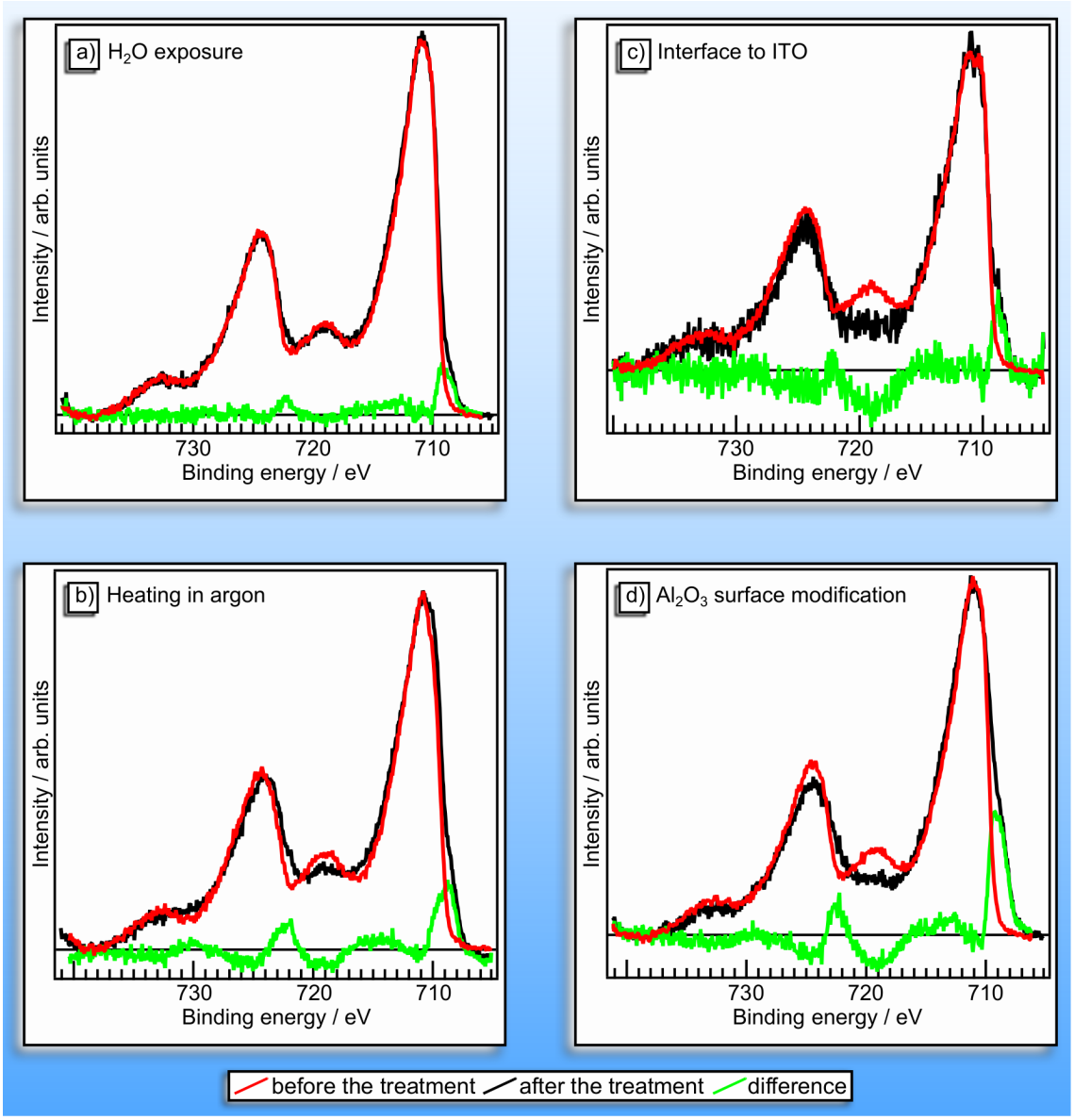

Figure 8.1: Fe2p spectra from experiments where a reduction of iron was observed.

The treatments after which the changes in oxidation state were observed are a) the exposure to water, b) the heating at 400 °C in argon, c) the surface modification during an interface experiment towards ITO, and d) the surface modification by atomic layer deposited alumina.[1]

[1] Please see for water exposure: 7.1.2, heating in vacuum: 4.2.2, interface towards ITO: 7.3.3, and surface modification by alumina: 7.2

For all treatments the difference in spectral feature before and after the corresponding treatment are alike. This is a clear indication for similar reasons of the changes. There is no doubt that the spectral changes correspond to the formation of Fe^{2+}.[51, 74, 124–126, 132, 152, 319] The degree of reduction, however, is depending on the treatment.

With the exposure to water only a mild reduction can be observed. The satellite structure corresponding to Fe^{3+} is almost completely unchanged. Only the shoulders towards low binding energies of the main lines indicated the reduction of iron.

The heating in argon and surface modification by ITO leads to a stronger degree of reduction. After both treatments, the Fe^{3+}-satellite is almost entirely suppressed and strong shoulders developed towards low binding energies. In the spectra shown in Figure 8.1 those changes are even stronger for the surface modification of ITO. It should be noted, however, that the degree of reduction for both treatments can be expected to depend on the heating time or on the ITO deposition time.

Finally, the strongest reduction can be observed after the atomic layer deposition of alumina. Again, no Fe^{3+}-satellite can be observed. In addition, the relative intensity of the shoulders is higher than for all the other treatments.

The differences in Figure 8.1 are partially negative. This can be explained by a non-optimal background subtraction. In order to obtain difference spectra it is necessary to subtract the background. With the formation of another oxidation state, however, the electron energy loss function that must be created with the background function is changed. Hence, the background function should change as well.[31, 152, 198] For practical purposes, however, this effect was neglected which results in a partially negative difference in Figure 8.1.

Of the four treatments discussed here, the heating in argon is a special case. While for the other three treatments the cause of reduction is still present (water, ITO, or alumina) during the measurement, the heating treatment had been performed prior to the measurement and the sample was already cooled down. In addition, the temperature of 400 °C during the heating treatment was much higher than for the other three treatments that were either performed at room temperature (water exposure and interface towards ITO) or just below 150 °C (alumina deposition[2]), respectively. These differences manifest themselves in a different Fermi level position. For the other three treatments a Fermi level position of 1.75 eV could be determined. In case of the heating treatment to low temperatures, however, the sample showed a Fermi level position of 1.5 eV.

[2] Please see 3.2.2

From the ITO interface it is known that the formation of Fe^{2+} occurs at a Fermi level position of 1.75 eV. The presence of Fe^{2+} in the heated sample despite a lower Fermi level position is, therefore, an indication for non-reversible processes e.g. a phase change during heating.

The agreement in the Fermi level position for the other three treatments, however, clearly shows that the Fermi level in hematite cannot move to a higher position than the value of 1.75 eV above the valence band maximum due to pinning. The reason for the pinning is the charge transition from Fe^{3+} to Fe^{2+}. Hence, at this position within the band gap the charge transition point of the reaction $Fe^{3+} + e^- \rightarrow Fe^{2+}$ can be defined.

The existence of charge transition points within the optical band gap of a semiconductor and their ability to pin the Fermi level is nothing new. Until now, however, this concept has been applied only to intrinsic (e.g. interstitials, oxygen vacancies) and extrinsic (dopants) defects.[40, 108, 260, 320] In these cases the pinning of the Fermi level can be partially avoided by minimizing the amount of defects by e.g. an optimization of the sample preparation or the usage of another dopant.

For hematite, however, the situation is different. Here, the cation of the compound shows a change in oxidation state. This has several consequences:

First of all, considering Fe^{2+} to be a defect in hematite the maximal possible concentration of this defect equals the number of cations. This is larger than any defect concentration which is normally associated with any conventional defect or dopant.[277, 321–323]

Secondly, it is nearly impossible to avoid this mechanism of Fermi level pinning. It is obviously not possible to change the deposition conditions in order to have less iron while keeping hematite as a material. To a certain extent iron can be substituted by other elements. This, however, will change the phase if a large-enough amount of substitution is reached.[324, 325]

The trapping of an electron on an iron site in hematite has been thoroughly discussed before. The localized electron on an iron site is considered to be a polaron. Due to the additional charge compared to the initial state the oxygen ligands are being displaced. The elongation of the bond in hematite due to small-polaron formation is about 4 %.[21] Since decades, it is widely accepted that the prevalent electron transport mechanism in Fe_2O_3 is small-polaron hopping.[195, 196, 326–328]

The polaron itself is not only the electron on the iron site but a quasi-particle which includes the disturbance of the bonding environment due to the presence of the electron.[329, 330] If the displacement is confined to one unit cell the quasi-particle

is regarded to be a small-polaron.[331–333] Associated with this are a low mobility ($\leq 0.1\,\mathrm{cm^2\,V^{-1}\,s}$) and, therefore, usually a low conductivity.[71, 80, 195] A schematic representation of the displacement of the oxygen ligands around a Fe^{2+} cation can be found in Figure 8.2.

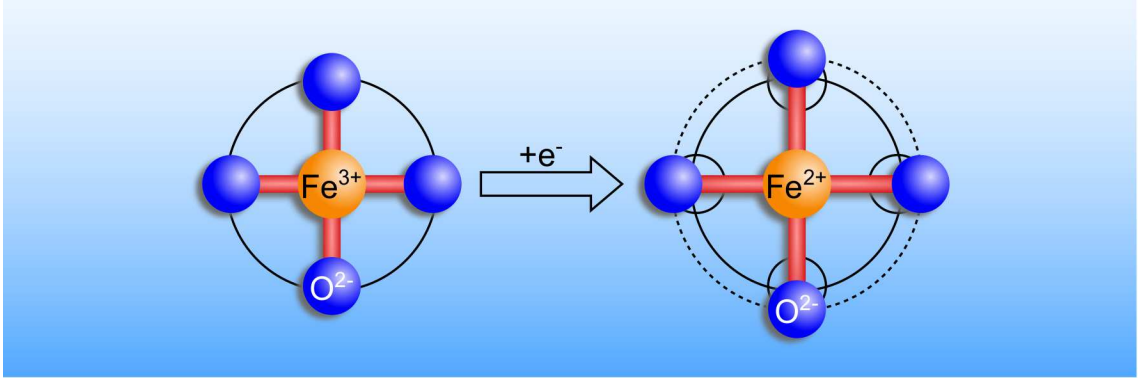

Figure 8.2: Schematic planar representation of an electron polaron in hematite.

Recent experimental studies on the kinetics of small-polaron formation by transient absorption spectroscopy on hematite revealed the lifetime of the electron trapped as small-polaron is about $\approx 10\,\mathrm{ns}$ which larger by orders of magnitude compared to the lifetime of picoseconds of a free electron in the conduction band[3].[21] Using similar time resolved experiments Carneiro et al. showed that the formation of small-polarons occurs within 2 ps and is the major limiting factor for bulk transport and recombination in hematite.[29] With their conclusion they showed that mid-gap or surface states are not as severe as has been claimed before by several authors.[23, 24, 73–75]

Until now, small-polarons have most commonly been suggested to be responsible for limits in the charge-transport properties. The results from this work, however, imply that their impact goes even further. Namely, their formation seems to be responsible for the reduced photovoltages in hematite which are usually far too small for a material with an optical band gap of 2.2 eV.[8, 18, 19, 334]

The generation of a photovoltage within a material depends on its ability to split the quasi-Fermi level upon light absorption.[6–9] This splitting, however, requires the absence of any mechanism that pins the Fermi level. As the formation of polaron prohibits the Fermi level to reach energy positions higher than 1.8 eV (determined in the ITO interface experiment) at least 0.4 eV of the optical band gap are intrinsically lost in the generation of a photovoltage.

The process of reduction before hydrogen production was described in a review paper by J. Schultze before.[335] There, he named PtO and Bi_2O_3 as examples for this process.

[3] Which has been excited from the valence band by light absorption

Hematite should fall into this category as well. The formation of polarons was not discussed in this work. It does, however, show that other materials potentially suffer from similar mechanisms as discussed here.

The position of the charge transition point or polaron level has been directly determined experimentally within this work for the first time. Theoretically, however, it has been calculated with a very good agreement before.[30, 40, 68] Interestingly, the position is independent on the calculation procedures.

Peng et al. calculated the relaxation and stabilization of an electron from the conduction band by transfer into the polaron level. An energy position of about 0.5 eV below the conduction band minimum was found for the polaron state.[30] In this study, the electron has to be excited into the conduction band at first in order to relax into the polaron state.

Lee et al. on the other hand regarded the polaron as an intrinsic defect (additional electron on an iron site) and calculated the charge transition point to be at an equal position to the findings presented in this thesis.[68] Zhou et al. used a similar approach and obtained the same result.[40] In these two studies the charge transition of an iron cation depends on the Fermi level position. No excitation of a charge carrier is needed for the small polaron formation.

The results from the ITO interfaces agree very well with the latter conclusion. There is, however, an additional interpretation based on the experimental results on the kinetic studies, the theoretical considerations and the result on the position of the charge transition point.

Namely, the charge transition point is at the same energy position as the trapped electron can be found. This "**polaron state**" acts as an effective electronic band edge as the Fermi level cannot reach any higher values. In hematite, therefore, the optical and electronic band gap are not the same. For the prediction of device performances based on the band gap it has to be considered to use the smaller "**polaron gap**" instead of the larger optical band gap.

A direct impact of the existence of the polaron state on the characterization of hematite can be found in the band alignment. In literature, the conduction band minimum (corresponding to the optical band gap) can be found to be positioned about 0.4 eV below the hydrogen formation potential.[6, 22, 316, 336] This requires an ionization potential of hematite of 7.2 eV which is larger than the 6.6 eV that have been shown in Figure 6.13.

At this point it has to be discussed where the position of the band edges in literature originate from:

In a first approximation by Butler and Ginley the work function[4] of a material A_xO_y can be derived by the geometric mean of the electronegativities χ of the elements minus half of the band gap E_g as given by equation 8.1.[336]

$$\phi(A_xO_y) = \chi(A_xO_y) - \frac{1}{2}E_g = [\chi^x(A)\chi^y(O)]^{\frac{1}{x+y}} - \frac{1}{2}E_g \tag{8.1}$$

According to their paper this value can then be used to place the material in relation to a reference electrode by the relation given in equation 8.2.

$$\phi = E_0 + V_{fb} + \Delta_{fc} + \Delta_{pH} \tag{8.2}$$

Here, E_0 is a constant relating the reference electrode of the flatband potential V_{fb} measurement to the vacuum level, Δ_{fc} is a correction for doping the semiconductor (assumed to be about 0.1 eV which is obviously way too low as can be seen e.g. in Figure 6.13 and Figure 7.10) and Δ_{pH} is the potential drop across the Helmholtz layer depending on the pH value. It is then assumed that a measurement of the flatband potential can be used to position the band edges in relation to a reference electrode.

A variety of assumptions enter the derivation which shall not be discussed entirely in detail here. However, only the flatband potential is directly measured in this approach while the work function is basically assumed. Hence, this approach should not be taken to find absolute values. Unfortunately, this is the case in literature.

An experimental approach to measure the band edge position is the determination of the flatband potential. It is often assumed for highly doped samples that it directly corresponds to the conduction band edge. In any case, the measurement results in a position of the Fermi level relative to the majority carrier band edge. For an n-type semiconductor the optical band gap is then used to position the valence band maximum.[337, 338]

Here, two assumptions are questionable. It is assumed that no electrons occupy states within the band gap. This is already not the case for samples with a high defect concentration and trap states within the band gap.[264] This issue could be avoided by careful sample preparation. In reality, however, nanocrystalline samples with unknown defect concentrations are being used in order to find band edge positions by determining the flatband potential.[213, 216] In these cases the assumption might often be not fulfilled.

[4] Referred to as electron affinity in Ref. [336]

The second assumption involves the use of the optical band gap to determine the distance of the level which is assumed to be the conduction band [5] to the valence band. This is only the case if first of all the conduction band edge has been found and secondly the optical band gap gives the energetic edges of the two bands. The latter is not always the case for oxides.[339]

It will now be shown that for hematite the polaron level is responsible for deviations of the assumption discussed above and that the position of the band edges from literature are, therefore, not correct.

In literature the valence band maximum of hematite can be found to be positioned 0.56 eV above the valence band maximum of $SrTiO_3$.[6, 22, 316, 336, 340] This value has been derived by theoretical predictions of the band edge positions and measurement of the flatband potential. In Chapter 7.3.4, however, a value of 1.1 eV was measured. As this is a direct measurement of the band alignment of the two materials and agrees very well with the band alignment of hematite towards the other contact materials RuO_2 and ITO, it can be regarded to be more trustworthy.

If now the new band alignment it taken into account the position of the conduction band minimum of hematite is being shifted above the hydrogen formation potential. This does not agree with the electro-chemical flatband potential measurements on hematite.[213, 216, 338]

There is, however, the polaron state to be considered. It is now positioned about 0.3 eV below the hydrogen formation potential. This shows that it indeed acts as an **effective band edge** limitation that has been measured by the electro-chemical methods. Only with the introduction of the polaron state and the interpretation as effective band edge the findings from these measurements come into an agreement with the direct measurement of the band alignment of hematite and the surface potentials that have been measured.

Figure 8.3 shows the real band alignment to $SrTiO_3$, ITO, and RuO_2[6] , the polaron state and the real position of the band edges of hematite with regard to the normal hydrogen electrode. In addition the maximal possible splitting of the quasi-Fermi levels $\Delta\mu* \approx 1.5$ eV as derived by the highest 1.8 eV and lowest 0.3 eV Fermi level positions from this work is shown.

[5] Discussed here for an n-type semiconductor. In case of a p-type semiconductor the same argument holds with the valence band being the assumed level to be found

[6] The Fermi edge of RuO_2 and thereby the maximal DOS is positioned just above the oxygen formation potential. This is a requirement for a good catalyst of this reaction. The combination of the valence band offset of hematite to RuO_2 of this work and the old, lower lying position of the valence band of hematite would disagree with this.

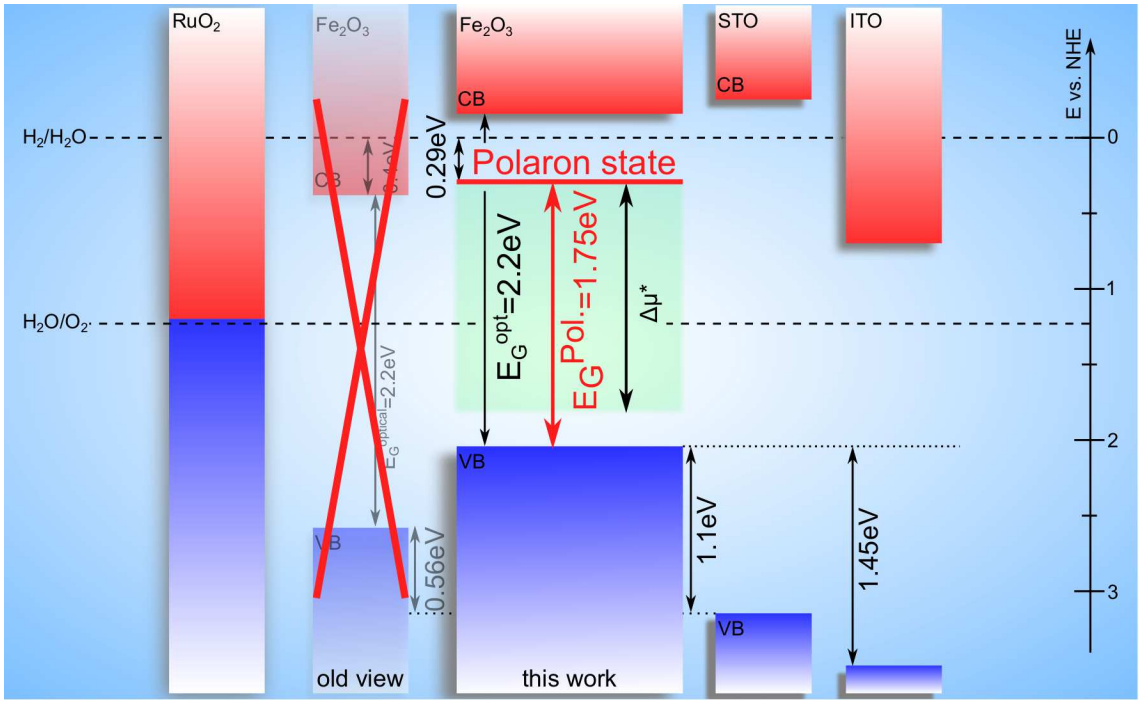

Figure 8.3: Actual band edge positions with respect to the normal hydrogen electrode of hematite including the polaron state that acts as effective band edge of the polaron gap.

This lowest value might be associated with the formation of a hole polaron. This quasi-particle can either involve the formation of Fe^{4+} or O^{-}. The results from this thesis are not clear enough to conclude on the formation of such a hole polaron. In literature the formation of Fe^{4+} was already suggested.[240] On the other hand it was calculated that a hole polaron should be positioned within the valence band.[30, 68] A definite assignment for the origin of the lowest Fermi level position in this thesis is not possible.

9 Summary of results and Outlook

In this work hematite was investigated in very detail in its electronic properties in order to clarify its photovoltages which are observed in hematite-based photoelectrochemical devices. It was assumed that the explanation why hematite devices are lacking behind the expected performance - based on the optical band gap of 2.2 eV - can be found by investigating intrinsic defects in the electronic structure. A special focus was given to the position of the Fermi level within the optical band gap of hematite. This final chapter of the thesis will give a summary on the results which were obtained and end with an outlook for further experiments that could be conducted.

Summary of the results

The oxidation state of iron within the deposited thin film is a good measure for the present iron oxide phase. Hematite being the most stable of all iron oxides should exhibit only the Fe^{3+} oxidation state. The oxidation state, the Fermi level position, as well as the composition, was measured with PES. The structural properties like crystallinity and crystal structure were measured with X-Ray Diffraction and Raman spectroscopy. It was found that the combination of the three techniques allows for a comprehensive conclusion on the phase of the deposited thin films. From this knowledge it was possible to use only two techniques in order to verify the phase in the following film deposition experiments. PE and Raman spectroscopy were used for most samples due to their time efficiency.

The investigation of the electronic structure, as well as the identification of fundamental limitations of the performance, were regarded to rely on well defined samples. As a consequence the first tasks of the study and this thesis was the identification of suitable deposition conditions for phase pure hematite thin films deposited by RF magnetron sputtering. The two main parameters in this part of the study were the oxygen partial pressure during the deposition and the sample temperature. For the latter heating during deposition was considered, as well as post-annealing in different atmospheres.

For a RF-magnetron deposition from a metallic iron target at a power of 60 W in a working pressure of 0.5 Pa it was found that phase pure hematite is being formed at an oxygen partial pressure of 6 % or more. Below this threshold the samples contain foreign phases such as magnetite (Fe_3O_4), wurtzite (FeO), or metallic iron. It was also found that around this threshold the Fermi level in the deposited films is being higher than for thin films deposited with more oxygen. All Fermi level positions, however, were found to be within

0.9 eV to 1.2 eV which is around mid-gap of the optical band gap. As a consequence of this study all films were deposited at oxygen partial pressures of 8 % or 10 % which results in phase pure Fe_2O_3 .

By heating the sample the crystallinity and phase can be manipulated. For depositions on heated substrates it was found that a substrate temperature of 300 °C has to be reached to deposit crystalline thin films. With suitable substrates it is possible to deposit epitaxial hematite thin films at such temperatures. For lower temperatures the sample are amorphous Fe_2O_3 whereas at 300 °C or higher hematite ($\alpha-Fe_2O_3$) is being formed as sole phase. The Fermi level position of Fe_2O_3 thin films deposited onto heated substrates is being increased when the temperature is raised. For amorphous Fe_2O_3 it can be found at about $E_F - E_{VBM}$=0.85 eV, whereas for thin films deposited at 500 °C or more values of $E_F - E_{VBM}$=1.5 eV were observed.

By heating Fe_2O_3 thin films at 400 °C in argon (0.5 Pa) a reduction of iron from Fe^{3+} to Fe^{2+} is achieved. The change in oxidation state of iron was assigned to originate from a phase change of the sample as the Fermi level position was determined to be too low to allow for the electronic reduction of iron that will be discussed later. This change is reversible as heating at the same temperature in oxygen (0.5 Pa) removes any signs of Fe^{2+} in XP spectra.

Post-annealing in oxidative conditions - 0.5 Pa oxygen and air at atmospheric pressure - results in a phase transformation from amorphous Fe_2O_3 to crystalline hematite for temperature of 300 °C and above. No change in the oxidation state of iron was seen. It was, however, observed that the $Fe2p_{3/2}$ and valence band spectra of amorphous and crystalline samples showed some spectral differences.

In the core-level spectra a change in the top-most part of the main emission occurred upon crystallization. The development of a distinct "pre-edge" at the low binding energy side of the top-most part of the Fe2p main line was assigned to originate from the higher symmetry in the crystalline samples.[61] This was described in literature before.[156] It should be mentioned that many studies from literature were performed on poorly defined samples. Due to the better definition of the samples properties in the present study, however, the changes in the core-level were linked to spectral changes in the valence band of Fe_2O_3 upon crystallization for the first time.[61]

As a consequence of the defined environment of iron (given by the oxygen anions) in the crystalline sample the valence band exhibits two distinct features. These could be assigned to originate from the crystal-field splitted anti-bonding Fe3d-states which are hybridized with oxygen. The leading feature which forms the valence band maximum was assigned to the Fe3d e_g-states whereas the Fe3d t_{2g}-states are positioned at binding

energies which are about 2.5 eV larger. Both crystal-field splitted states are occupied by electrons in a high-spin configuration.

It was shown that a co-sputtering process with an additional metallic target of the dopant material is suitable to deposit doped hematite thin films. By varying the sputtering power and/or distance of the dopant target it is possible to change the composition of the resulting thin films. A high sputtering power is associated with a high dopant concentration. Under such conditions, however, the thin films suffer from a large degree of disorder which can be seen in both, PE and Raman Spectroscopy. For too high amount of dopant a phase seperation was suggested which was the most severe for Si-doped hematite.

Despite the disorder the Fermi level can still be manipulated. Using the undoped thin films as comparison it was shown that magnesium is a p-type dopant which lowers the Fermi level position into the bottom half of the optical band gap. Silicon and zirconium are n-type dopants and raise the Fermi level to higher positions than the intrinsic one. Zirconium has shown to be the more effective n-type dopant than silicon with higher Fermi level positions. The highest position was found at $E_F - E_{VBM}$=1.68 eV for a zirconium doped sample, whereas the lowest Fermi level position of $E_F - E_{VBM}$=0.3 eV could be obtained for a magnesium doped thin film.

These two dopants also increased the conductivity of the samples while the silicon doping did not improve the electrical properties. Especially the change in conductivity upon changing the measurement conditions from reductive to oxidative or vice versa was negligible for silicon doped thin films. For the other dopant changes could be observed which can be explained with their n-/p-type conductivity.

The optical properties of the samples were slightly changed as well with low absorption due to a dilution of the absorbing iron cation and some smearing ou of the absorption edge. The latter can be explained by the disorder that is introduced into the system which results in less well defined energies for the optical transitions. Despite these changes, however, the optical band gap of around 2.2 eV could still be found in the doped sample as well.

The surface properties work function and ionization potential were measured on undoped and doped films. The ionization potential the films was found to be about 6.6 eV which is smaller than discussed in literature. The work function corresponds to the doping, if no phase separation is present, and is lowered if the Fermi level position is raised and vice versa. Values of 4.7 eV up to 6.3 eV could be found in the thin films.

Besides the bulk Fermi level variation by doping the Fermi level of hematite was also manipulated on the surface of the thin films. For this purpose the sample were treated by different methods. Shifts in both directions, upwards and downwards, were observed.

A downwards shift of the Fermi level was observed for samples treated in an oxygen plasma. A final Fermi level position of $E_F - E_{VBM}$=0.66 eV was observed. It was concluded that the Fermi level is being pinned at this energy due to surface adsorbents which are introduced by the oxygen plasma treatment. Peroxide groups were identified to be the most reasonable adsorbate in this regard.

With an interface experiment to RuO_2 a Fermi level position at the interface of $E_F - E_{VBM}$=0.85 eV, which had already been published earlier, could be confirmed.[55] An even lower Fermi level position was reached in an interface experiment to NiO. In this particular experiment a Fermi level as low as $E_F - E_{VBM}$=0.4 eV could be obtained. For both experiments it was concluded that no pinning of the Fermi level within hematite occurs in this energy range, as the Mg-doped sample showed even lower Fermi level positions.

The exposure to water at room temperature shifted the Fermi level to a value of $E_F - E_{VBM}$=1.75 eV. The Fe2p emission revealed a change in oxidation state of iron from Fe^{3+} to Fe^{2+} during this experiment. Both, the upwards shift of the Fermi level and the reduction of iron due to the exposure to water were surprising as water is not supposed to act as a "reducting agent". The necessary electron transfer from water to hematite requires states at the Fermi level which water initially does not posses. A hybridization of Fe3d valence band states from hematite with initially occupied states of water, due to which states above the Fermi level are created, was suggested as mechanism. This mechanism was proposed before for similar observations in WSe_2.[283]

A similar Fermi level position of $E_F - E_{VBM}$=1.75 eV was obtained by a surface manipulation with alumina from an ALD process. In this experiment a reduction of iron could be observed as well. The degree of reduction was larger than for the samples which had been exposed to water.

In addition, the degree of reduction seems to depend on the Fermi level position of the hematite sample before the surface manipulation by alumina. It was proposed that the depth until which the reduction of iron takes places is larger for higher initial Fermi level positions. This model is based on the conclusion that the Fermi level cannot be shifted above $E_F - E_{VBM}$=1.75 eV due to the charge transition of iron from Fe^{3+} to Fe^{2+}.

This conclusion was verified by interface experiments to ITO. By using two different hematite substrates with very different initial Fermi level positions it could be observed

that the reduction of iron from Fe^{3+} to Fe^{2+} only takes place if the Fermi level reaches a value of $E_F - E_{VBM}$=1.75 eV. This energy was, therefore, assigned to be the charge transition level of the reaction $Fe^{3+} + e^- \rightarrow Fe^{2+}$.

The ITO films, which were deposited onto crystalline hematite during these interface experiment, were found to posses an unusually high Fermi level position for ITO thin films deposited under the given conditions. Conductivity measurements revealed that their conductivity was higher by an order of magnitude compared to ITO thin films without a hematite layer below. The improved conductivity was found to originate from a much higher charge carrier concentration at still comparable mobilities.

In addition, XRD measurements showed that the crystallinity of ITO sample deposited onto epitaxial hematite was greatly improved and the meta-stable rhombohedral phase of In_2O_3 was stabilized. It was concluded that the high crystallinity of room-temperature deposited ITO due to the hematite seed layer activates the doping by Sn. At the same time no phase separation occurs as usually observed for depositions of crystalline ITO samples (performed at 400 °C) which preserves the mobility.[61]

The most interesting result of this thesis, however, remains the charge transition of Fe^{3+} to Fe^{2+} at a Fermi level position of $E_F - E_{VBM}$=1.75 eV. This transition occurs in the process of small-polaron formation which is the prevalent electron transfer mechanism in hematite. In literature it was found that the formation of polarons after excitation of an electron into the conduction band occurs at a much faster rate than the recombination back into the valence band and that the polaron state was calculated to be positioned at the exact energy which was found in this thesis of 1.75 eV above the valence band maximum.[21, 29, 30, 68]

From this literature review and the findings in this study a model was derived which is an actual explanation for the low photovoltages observed in hematite based devices. According to this model the polaron state acts as an effective band edge (electronic pinning level) for the electronic band gap in hematite as no Fermi level positions above this state are accessible. Further evidence for this concept was given by the band alignment of hematite to $SrTiO_3$ from an interface experiment to this material. It could be shown that the direct measurement of the band alignment does not agree with the electrochemical determination and it was argued that this originates from the electrochemical method itself. Instead of the assumed edge of the conduction band the effective band edge - the polaron state - was probed and the valence band position with respect to the hydrogen formation potential was positioned with the optical band gap value.

A severe consequence of the existence of the effective band edge is that the splitting of the quasi-Fermi level in the photoinduced generation of electron-hole pairs is limited.

As a consequence the optical band gap cannot be used in order to theoretically predict the performance of a hematite based device. Instead the energetic difference between polaron state and valence band (or possibly a hole polaron state close the band edge, see later) has to be used.

This concept is applicable for any material in which the formation of polarons occurs with a faster rate than the charge transfer through an interface. Similar consideration are widely accepted for organic semiconductors but have not been considered for the localized electrons in transition metal oxides, yet. The model is also not constricted to electrons alone. For possible hole polarons similar considerations are possible and it is even imaginable that both, electron and hole polaron exist in a single material. In such a case the effective band gap is given by the energetic difference of the two polaron states. For the hematite thin films of this study, however, no conclusive evidence of a hole polaron could be found. The lowest Fermi level position of $E_F - E_{VBM}$=0.3 eV in a Mg-doped film could also originate from the doping limit of magnesium.

With the concept of an effective band gap due to to the formation of polarons in transition metal oxides an explanation for the photovoltages which are too low if only the optical band gaps are considered has been deduced in this thesis. It is, therefore, shown that a material has to be fundamentally well understood in order to be used or improved for complex applications such as light-driven water splitting. The identification of intrinsic limitations in a material (or even a class of materials) is the key to overcome these limitations. This might even include the classification of a material as unsuitable for a desired application as it is the case for hematite.

Outlook

The most important next step is the transfer of the effective band gap concept due to polaron state to other transition metal oxides. This was partially already started with master theses on Sr-doped $LaFeO_3$ (LSF) and (Co-doped) $BiFeO_3$ (BFO).[341, 342] In both, the results from this thesis could be reproduced. In the case of BFO it was even possible to show that charge transition points exist for bismuth and cobalt as well. There is, however, still a need to reconsider experimental results in the light of the findings of this thesis and readdress the conclusions. Special emphasize should be given to materials that are considered for light-driven water splitting (or catalysis) such as $BiVO_3$ and MnO.

After the experimental prove of the existence of effective band gaps due to polaron formation in other materials there is a need to consider the effective band gap for theoretical predictions on the performance of new materials for light-driven water splitting. Based on these predictions new materials which are not limited by polaron formation should be investigated. Additionally, it should be explored whether by intelligent engi-

neering of the electronic structure the formation of polarons can be prohibited or if at least the charge transition point can be moved closer to the band edges of the optical band gap.

Imaginable would be a material where during the excitation with light the electron is being transferred from transition metal d-states into states derived from an element that does not show polaron formation (non d-states). Thus, it might remain a free charge carrier and can be used in an electron transfer reaction.

Bibliography

[1] N. N. C. for Environmental Information. *State of the Climate: Global Climate Report for Annual 2017*. 2018. URL: https://www.ncdc.noaa.gov/sotc/global/201713 (visited on 09/13/2018).

[2] N. Oreskes. "The Scientific Consensus on Climate Change". In: *Science* 306.5702 (2004), pp. 1686–1686.

[3] J. M. Samet et al. "Fine Particulate Air Pollution and Mortality in 20 U.S. Cities, 1987–1994". In: *New England Journal of Medicine* 343.24 (2000), pp. 1742–1749.

[4] Arbeitsgruppe Erneuerbare Energien-Statisik. *Erneuerbare Energien in Zahlen - Nationale und internationale Entwicklung im Jahr 2016*. 2017.

[5] H. Ahmad et al. "Hydrogen from photo-catalytic water splitting process: A review". In: *Renewable and Sustainable Energy Reviews* 43 (2015), pp. 599–610.

[6] J. Li and N. Wu. "Semiconductor-based photocatalysts and photoelectrochemical cells for solar fuel generation: a review". In: *Catal. Sci. Technol.* 5.3 (2015), pp. 1360–1384.

[7] W. Jaegermann et al. "Interface Engineering of Semiconductor Electrodes for Photoelectrochemical Water Splitting: Application of Surface Characterization with Photoelectron Spectroscopy". In: *Photoelectrochemical Solar Fuel Production*. Ed. by S. Giménez and J. Bisquert. Berlin: Springer, 2016. Chap. II-4, pp. 199–280.

[8] K. Sivula and R. van de Krol. "Semiconducting materials for photoelectrochemical energy conversion". In: *Nature Reviews Materials* 1.2 (2016), p. 15010.

[9] Y. Kuang, T. Yamada, and K. Domen. "Surface and Interface Engineering for Photoelectrochemical Water Oxidation". In: *Joule* 1.2 (2017), pp. 290–305.

[10] A. Fujishima and K Honda. "Electrochemical photolysis of water at a semiconductor electrode." In: *Nature* 238.5358 (1972), pp. 37–38.

[11] A. Kudo and Y. Miseki. "Heterogeneous photocatalyst materials for water splitting". In: *Chem. Soc. Rev.* 38.1 (2009), pp. 253–278.

[12] V. Stevanović et al. "Assessing capability of semiconductors to split water using ionization potentials and electron affinities only." In: *Physical chemistry chemical physics : PCCP* 16 (2014), pp. 3706–14.

[13] M. Mishra and D.-M. Chun. "$\alpha - Fe_2O_3$ as a photocatalytic material: A review". In: *Applied Catalysis A: General* 498 (2015), pp. 126–141.

[14] M. J. Katz et al. "Toward solar fuels: Water splitting with sunlight and "rust" ?" In: *Coordination Chemistry Reviews* 256.21-22 (2012), pp. 2521–2529.

[15] S. Shen et al. “Hematite heterostructures for photoelectrochemical water splitting: rational materials design and charge carrier dynamics”. In: *Energy Environ. Sci.* 9.9 (2016), pp. 2744–2775.

[16] L. He et al. “Enhanced visible photocatalytic activity of nanocrystalline $\alpha-Fe_2O_3$ by coupling phosphate-functionalized graphene”. In: *RSC Advances* 3.20 (2013), p. 7438.

[17] H. Dotan et al. “Resonant light trapping in ultrathin films for water splitting”. In: *Nature Materials* 12.2 (2012), pp. 158–164.

[18] G. Segev et al. “High Solar Flux Concentration Water Splitting with Hematite (α-Fe_2O_3) Photoanodes”. In: *Advanced Energy Materials* 6.1 (2016), p. 1500817.

[19] J.-W. Jang et al. “Enabling unassisted solar water splitting by iron oxide and silicon”. In: *Nature Communications* 6.May (2015), p. 7447.

[20] K. Sivula, F. Le Formal, and M. Grätzel. “Solar Water Splitting: Progress Using Hematite ($\alpha-Fe_2O_3$) Photoelectrodes”. In: *ChemSusChem* 4.4 (2011), pp. 432–449.

[21] J. E. Katz et al. “Electron Small Polarons and Their Mobility in Iron (Oxy-hydr)oxide Nanoparticles”. In: *Science* 337.6099 (2012), pp. 1200–1203.

[22] M. Grätzel. “Photoelectrochemical cells”. In: *Nature* 414.6861 (2001), pp. 338–344.

[23] F. Le Formal et al. “Passivating surface states on water splitting hematite photoanodes with alumina overlayers”. In: *Chemical Science* 2.4 (2011), p. 737.

[24] N. Yatom, O. Neufeld, and M. Caspary Toroker. “Toward Settling the Debate on the Role of Fe_2O_3 Surface States for Water Splitting”. In: *The Journal of Physical Chemistry C* 119.44 (2015), pp. 24789–24795.

[25] S. C. Warren et al. “Identifying champion nanostructures for solar water-splitting”. In: *Nature Materials* 12.9 (2013), pp. 842–849.

[26] Y. Lin et al. “Nanonet-Based Hematite Heteronanostructures for Efficient Solar Water Splitting”. In: *Journal of the American Chemical Society* 133.8 (2011), pp. 2398–2401.

[27] J. H. Kim et al. “Hetero-type dual photoanodes for unbiased solar water splitting with extended light harvesting”. In: *Nature Communications* 7 (2016), p. 13380.

[28] J. Li et al. “Plasmon-induced photonic and energy-transfer enhancement of solar water splitting by a hematite nanorod array”. In: *Nature Communications* 4 (2013), pp. 1–8.

[29] L. M. Carneiro et al. “Excitation-wavelength-dependent small polaron trapping of photoexcited carriers in α-Fe_2O_3”. In: *Nature Materials* 16.8 (2017), pp. 819–825.

[30] H. Peng and S. Lany. “Semiconducting transition-metal oxides based on d^5 cations: Theory for MnO and Fe_2O_3”. In: *Physical Review B* 85.20 (2012), 201202(R).

[31] J. Vura-Weis et al. “Femtosecond M2,3-Edge Spectroscopy of Transition-Metal Oxides: Photoinduced Oxidation State Change in α-Fe_2O_3”. In: *The Journal of Physical Chemistry Letters* 4.21 (2013), pp. 3667–3671.

[32] R. M. Cornell and U. Schwertmann. *The Iron Oxides: Structure, Properties, Reactions, Occurences and Uses*. 2nd ed. Weinheim: WILEY-VCH Verlag GmbH & Co, 2003.

[33] R. Zboril, M. Mashlan, and D. Petridis. “Iron(III) Oxides from Thermal ProcessesSynthesis, Structural and Magnetic Properties, Mössbauer Spectroscopy Characterization, and Applications”. In: *Chemistry of Materials* 14.3 (2002), pp. 969–982.

[34] D. M. Sherman. “The electronic structures of Fe^{3+} coordination sites in iron oxides: Applications to spectra, bonding, and magnetism”. In: *Physics and Chemistry of Minerals* 12.3 (1985), pp. 161–175.

[35] G. S. Parkinson. “Iron oxide surfaces”. In: *Surface Science Reports* 71.1 (2016), pp. 272–365.

[36] J. Tossell, D. J. Vaughan, and K. H. Johnson. “Electronic Structure of Ferric Iron Octahedrally Coordinated to Oxygen”. In: *Nature Physical Science* 244.133 (1973), pp. 42–45.

[37] J. Tossell, J. J. Vaughan, and K. H. Johnson. “The Electronic Structure of Rutile, Wustite, and Hematite from Molecular Orbital Calculations”. In: *American Mineralogist* 59 (1974), pp. 319–334.

[38] X. Li et al. “Effect of Cr-doping on the electronic structure and work function of $\alpha - Fe_2O_3$ thin films.” In: *Physical chemistry chemical physics : PCCP* 19.38 (2017), pp. 26248–26254.

[39] L. Chen et al. “Strain Effect on Electronic Structure and Work Function in $\alpha - Fe_2O_3$ Films”. In: *Materials* 10.12 (2017), p. 273.

[40] Z. Zhou et al. “Understanding Hematite Doping with Group IV Elements: A DFT+U Study”. In: *Journal of Physical Chemistry C* 119.47 (2015), pp. 26303–26310.

[41] Y. Zhang et al. “Doping-Promoted Solar Water Oxidation on Hematite Photoanodes”. In: *Molecules* 21.7 (2016), p. 868.

[42] Z. D. Pozun and G. Henkelman. “Hybrid density functional theory band structure engineering in hematite”. In: *Journal of Chemical Physics* 134.22 (2011), pp. 1–9.

[43] R. Rivera et al. “Density functional theory study of Al-doped hematite”. In: *Physica Scripta* 85.1 (2012), p. 015602.

[44] S. Yin and D. Ellis. “H2O adsorption and dissociation on defective hematite (0001) surfaces: A DFT study”. In: *Surface Science* 602.12 (2008), pp. 2047–2054.

[45] T. Pabisiak and A. Kiejna. “Fe adsorption on hematite ($\alpha-Fe_2O_3$) (0001) and magnetite (Fe_3O_4) (111) surfaces”. In: *The Journal of Chemical Physics* 141.13 (2014), p. 134707.

[46] S. M. Souvi et al. “A DFT study of the hematite surface state in the presence of H_2, H_2O and O_2”. In: *Surface Science* 610 (2013), pp. 7–15.

[47] H. Pan et al. “4d transition-metal doped hematite for enhancing photoelectrochemical activity: theoretical prediction and experimental confirmation”. In: *RSC Adv.* 5.25 (2015), pp. 19353–19361.

[48] G. Rollmann et al. “First-principles calculation of the structure and magnetic phases of hematite”. In: *Physical Review B* 69.16 (2004), p. 165107.

[49] M. Catti, G. Valerio, and R. Dovesi. “Theoretical study of electronic, magnetic, and structural properties of $\alpha-Fe_2O_3$ (hematite)”. In: *Physical Review B* 51.12 (1995), pp. 7441–7450.

[50] G. Dräger, W. Czolbe, and J. A. Leiro. “High-energy-spectroscopy studies of a charge-transfer insulator: X-Ray spectra of $\alpha-Fe_2O_3$”. In: *Physical Review B* 45.15 (1992), pp. 8283–8287.

[51] M. Tallarida et al. “Modification of Hematite Electronic Properties with Trimethyl Aluminum to Enhance the Efficiency of Photoelectrodes”. In: *The Journal of Physical Chemistry Letters* 5 (2014), pp. 3582–3587.

[52] W. Temesghen and P. Sherwood. “Analytical utility of valence band X-ray photoelectron spectroscopy of iron and its oxides, with spectral interpretation by cluster and band structure calculations”. In: *Analytical and Bioanalytical Chemistry* 373.7 (2002), pp. 601–608.

[53] J. Su et al. “On the role of metal atom doping in hematite for improved photoelectrochemical properties: a comparison study”. In: *RSC Adv.* 6.104 (2016), pp. 101745–101751.

[54] L. Minati et al. “Application of factor analysis to XPS valence band of superparamagnetic iron oxide nanoparticles”. In: *Applied Surface Science* 257.24 (2011), pp. 10863–10868.

[55] S. Li et al. “Influence of orbital contributions to the valence band alignment of Bi_2O_3, Fe_2O_3, $BiFeO_3$, and $Bi_{0.5}Na_{0.5}TiO_3$”. In: *Physical Review B* 88.4 (2013), p. 045428.

[56] C.-Y. Kim et al. “Site-specific valence-band photoemission study of $\alpha-Fe_2O_3$ ”. In: *Physical Review B* 66 (2002), p. 085115.

[57] Y. Hu et al. “Molecular Origin and Electrochemical Influence of Capacitive Surface States on Iron Oxide Photoanodes”. In: *The Journal of Physical Chemistry C* 120.6 (2016), pp. 3250–3258.

[58] T Fujii et al. “In situ XPS analysis of various iron oxide films grown by NO_2-assisted molecular-beam epitaxy”. In: *Physical Review B* 59.4 (1999), pp. 3195–3202.

[59] A. Fujimori et al. “Photoemission satellites and electronic structure of Fe_2O_3”. In: *Physical Review B* 34.10 (1986), pp. 7318–7328.

[60] R. J. Lad and V. E. Henrich. “Photoemission study of the valence-band electronic structure in Fe_xO, Fe_3O_4, and $\alpha-Fe_2O_3$ single crystals”. In: *Physical Review B* 39.18 (1989), pp. 13478–13485.

[61] C. Lohaus et al. “Systematic Investigation of the Electronic Structure of Hematite Thin Films”. In: *Advanced Materials Interfaces* 4.20 (2017), p. 1700542.

[62] F. Ciccacci et al. “Electron States in Fe_2O_3 by ultraviolet inverse-photoemission spectroscopy”. In: *Physical Review B* 44.19 (1991), pp. 10444–10448.

[63] J Engel and H. L. Tuller. “The electrical conductivity of thin film donor doped hematite: from insulator to semiconductor by defect modulation.” In: *Physical chemistry chemical physics : PCCP* 16.23 (2014), pp. 11374–80.

[64] J. A. Glasscock et al. “Structural, optical and electrical properties of undoped polycrystalline hematite thin films produced using filtered arc deposition”. In: *Thin Solid Films* 516.8 (2008), pp. 1716–1724.

[65] L. A. Marusak, R Messier, and W. B. White. “Optical Absorption spectrum of hematite, $\alpha-Fe_2O_3$ Near IR to UV”. In: *J. Phys. Chem. Solids* 41 (1980), pp. 981–984.

[66] R. Misho and W. Murad. “Band gap measurements in thin films of hematite Fe_2O_3, pyrite FeS_2 and troilite FeS prepared by chemical spray pyrolysis”. In: *Solar Energy Materials and Solar Cells* 27 (1992), pp. 335–345.

[67] P. Liao and E. A. Carter. “Optical Excitations in Hematite ($\alpha-Fe_2O_3$) via Embedded Cluster Models: A CASPT2 Study”. In: *The Journal of Physical Chemistry C* 115.42 (2011), pp. 20795–20805.

[68] J. Lee and S. Han. “Thermodynamics of native point defects in α-Fe_2O_3: an ab initio study.” In: *Physical chemistry chemical physics : PCCP* 15.43 (2013), pp. 18906–14.

[69] O. Warschkow et al. “Defects and Charge Transport near the Hematite (0001) Surface: An Atomistic Study of Oxygen Vacancies”. In: *Journal of the American Ceramic Society* 85.1 (2004), pp. 213–220.

[70] K. Atkinson et al. “Accommodation of impurities in $\alpha-Al_2O_3$, $\alpha-Cr_2O_3$ and $\alpha-Fe_2O_3$”. In: *Journal of the European Ceramic Society* 23.16 (2003), pp. 3059–3070.

[71] C. Gleitzer, J Nowotny, and M Rekas. “Surface and bulk electrical properties of the hematite phase Fe_2O_3”. In: *Applied Physics A Solids and Surfaces* 53.4 (1991), pp. 310–316.

[72] N. Iordanova, M. Dupuis, and K. M. Rosso. “Charge transport in metal oxides: a theoretical study of hematite $\alpha-Fe_2O_3$.” In: *The Journal of Chemical Physics* 122.14 (2005), p. 144305.

[73] B. Iandolo and A. Hellman. “The role of surface states in the oxygen evolution reaction on hematite”. In: *Angewandte Chemie - International Edition* 53.49 (2014), pp. 13404–13408.

[74] F. Kraushofer et al. “Atomic-Scale Structure of the Hematite $\alpha-Fe_2O_3$ $((1\bar{1}02))$ “R-Cut” Surface”. In: *The Journal of Physical Chemistry C* 122.3 (2018), pp. 1657–1669.

[75] S. M. Souvi et al. “A DFT study of the hematite surface state in the presence of H_2, H_2O and O_2”. In: *Surface Science* 610 (2013), pp. 7–15.

[76] C. Lohaus et al. “Investigations on RF-magnetron sputtered Co_3O_4 thin films regarding the solar energy conversion properties”. In: *Journal of Physics D: Applied Physics* 49.15 (2016), p. 155306.

[77] F. J. Morin. “Electrical Properties of $\alpha-Fe_2O_3$ and $\alpha-Fe_2O_3$ Containing Titanium”. In: *Physical Review* 83.5 (1951), pp. 1005–1010.

[78] S. Mohanty and J. Ghose. “Studies on some $\alpha-Fe_2O_3$ photoelectrodes”. In: *Journal of Physics and Chemistry of Solids* 53.1 (1992), pp. 81–91.

[79] R. Dieckmann. “Point defects and transport in haematite $(Fe_2O_{3-\epsilon})$”. In: *Philosophical Magazine A* 68.4 (1993), pp. 725–745.

[80] P. Liao and E. A. Carter. “Hole transport in pure and doped hematite”. In: *Journal of Applied Physics* 112.1 (2012), p. 013701.

[81] F. Rettig and R. Moos. “α-Iron oxide: An intrinsically semiconducting oxide material for direct thermoelectric oxygen sensors”. In: *Sensors and Actuators B: Chemical* 145.2 (2010), pp. 685–690.

[82] Y. H. Chen and K. J. Tu. “Thickness dependent on photocatalytic activity of hematite thin films”. In: *International Journal of Photoenergy* 2012 (2012).

[83] J.-M. Tulliani and P. Bonville. “Influence of the dopants on the electrical resistance of hematite-based humidity sensors”. In: *Ceramics International* 31.4 (2005), pp. 507–514.

[84] M. Fondell. “Synthesis and Characterisation of Ultra Thin Film Oxides for Energy Applications”. PhD Thesis. Uppsala University, 2014.

[85] S. Sze. *Physics of Semiconductor Devices*. 2nd. John Wiley & Sons, 1981.

[86] H. L. Tuller and S. R. Bishop. “Point Defects in Oxides: Tailoring Materials Through Defect Engineering”. In: *Annual Review of Materials Research* 41.1 (2011), pp. 369–398.

[87] A. Klein et al. “Transparent Conducting Oxides for Photovoltaics: Manipulation of Fermi Level, Work Function and Energy Band Alignment”. In: *Materials* 3.11 (2010), pp. 4892–4914.

[88] C. Lohaus et al. “Enhancing electrical conductivity of room temperature deposited Sn-doped In_2O_3 thin films by hematite seed layers”. In: *Applied Physics Letters* 112.15 (2018), p. 152105.

[89] J. E. Medvedeva, D. B. Buchholz, and R. P. H. Chang. “Recent advances in understanding the structure and properties of amorphous oxide semiconductors”. In: *Adv. Electron. Mater.* 3 (2017), p. 1700082.

[90] W. Schottky. “Halbleitertheorie der Sperrschicht”. In: *Die Naturwissenschaften* 26.52 (1938), p. 843.

[91] R. L. Anderson. “Experiments on Ge-GaAs Heterojunctions”. In: *Solid-State Electronics* 5 (1962), pp. 341–351.

[92] J Hubbard. “Electron correlations in narrow energy bands”. In: *Proceedings of the Royal Society of London. Series A, Mathematical and Physical* 276.1365 (1963), pp. 238–257.

[93] J Hubbard. “Electron correlations in narrow energy bands. II. The degenerate band case”. In: *Proceedings of the Royal Society of London. Series A, Mathematical and Physical* 277.1369 (1964), pp. 237–259.

[94] J Hubbard. “Electron correlations in narrow energy bands. III. An improved solution”. In: *Proceedings of the Royal Society of ...* 281.1386 (1964), pp. 401–419.

[95] J Hubbard. “Electron correlations in narrow energy bands. IV. The atomic representation”. In: *Proceedings of the Royal Society of ...* 285.1403 (1965), pp. 542–560.

[96] G. A. Sawatzky and J. W. Allen. “Magnitude and Origin of the Band Gap in NiO”. In: *Physical Review Letters* 53.24 (1984), pp. 2339–2342.

[97] S. Hüfner et al. “Photoemission and inverse photoemission spectroscopy of NiO”. In: *Solid State Communications* 52.9 (1984), pp. 793–796.

[98] S. Hüfner et al. “On the interpretation of valence band photoemission spectra of NiO”. In: *Solid State Communications* 59.1 (1984), pp. 83–86.

[99] S. Hüfner. “Electronic structure of NiO and related 3d-transition-metal compounds”. In: *Advances in Physics* 43.2 (1994), pp. 183–356.

[100] J. Zaanen, G. A. Sawatzky, and J. Allen. “Band gaps and electronic structure of transition-metal compounds”. In: *Physical Review Letters* 55.4 (1985), pp. 418–421.

[101] J. Zaanen, G. A. Sawatzky, and J. Allen. “The electronic structure and band gaps in transition metal compounds”. In: *Journal of Magnetism and Magnetic Materials* 54-57 (1986), pp. 607–611.

[102] P. Cox. *Transition Metal Oxides An introduction to their electronic structure and properties*. Oxford: Oxford University Press, 1992.

[103] Y. Tokura. “Orbital Physics in Transition-Metal Oxides”. In: *Science* 288.5465 (2000), pp. 462–468.

[104] A. L. Companion and M. A. Komarynsky. “Crystal field splitting diagrams”. In: *Journal of Chemical Education* 41.5 (1964), p. 257.

[105] V. R. Galakhov et al. “X-ray photoelectron 3s spectra of transition metal oxides”. In: (1999), pp. 1–17.

[106] J. Zaanen and G. A. Sawatzky. “Systematics in Band Gaps and Optical Metal Compounds Spectra of 3D Transition Metal Compounds”. In: *Journal of Solid State Chemistry* 88 (1990), pp. 8–27.

[107] S. Hüfner. *Photoelectron Spectroscopy: Principles and Applications*. 3rd ed. Berlin: Springer, 2003.

[108] A. Fuchs. “Der CdTe-Frontkontakt: Charakterisierung und Modifizierung von Puffer- und Fensterschichten und deren Grenzflächen”. PhD Thesis. TU Darmstadt, 2015, p. 283.

[109] R. Weast. *CRC Handbook of Chemistry and Physics*. CRC Press, 1985.

[110] J. Morasch. “Deposition, Charakterisierung und Bandanpassung oxidischer Dünnschichtmaterialien zur Lichtabsorption”. PhD Thesis. Technische Universität Darmstadt, 2017.

[111] S. Li et al. “Electrical properties of $(Ba, Sr)TiO_3$ thin films with Pt and ITO electrodes: dielectric and rectifying behaviour”. In: *Journal of Physics: Condensed Matter* 23.33 (2011), p. 334202.

[112] J. A. Thornton. “Influence of apparatus geometry and deposition conditions on the structure and topography of thick sputtered coatings”. In: *Journal of Vacuum Science and Technology* 11.4 (1974), p. 666.

[113] M. Frischbier. “Die elektrischen Eigenschaften von Indiumoxid-Dünnschichten: *in-situ* Hall-Effekt-Messungen zur Aufklärung des Einflusses von Punktdefekten und Korngrenzen”. PhD Thesis. TU Darmstadt, 2015.

[114] M. Weidner. “Fermi Level Determination in Tin Oxide by Photoelectron Spectroscopy: Relation to Optoelectronic Properties; Band Bending at Surfaces and Interfaces; Modulation Doping”. PhD thesis. TU Darmstadt, 2016, p. 361.

[115] C. Steinert. “Preparation and Characterization of RF-magnetron Sputtered Epitaxial Hematite Thin Films”. Master Thesis. TU Darmstadt, 2017.

[116] F. Reinert and S. Hüfner. “Photoemission spectroscopy—from early days to recent applications”. In: *New Journal of Physics* 7 (2005), p. 97.

[117] A. Klein et al. “Photoelectron Spectroscopy in Materials Science and Physical Chemistry: Analysis of Composition, Chemical Bonding, and Electronic Structure of Surfaces and Interfaces”. In: *Methods in Physical Chemistry*. Weinheim, Germany: Wiley-VCH Verlag GmbH & Co. KGaA, 2012, pp. 477–512.

[118] D. Shirley. “High-resolution X-ray photoemission spectrum of the valence bands of gold”. In: *Physical Review B* 5.12 (1972), p. 4709.

[119] S. Tougaard and C. Jansson. “Background correction in XPS: comparison of validity of different methods”. In: *Surface and interface analysis* 19 (1992), pp. 171–174.

[120] T Koopmans. “Über die Zuordnung von Wellenfunktionen und Eigenwerten zu den Einzelnen Elektronen Eines Atoms”. In: *Physica* 1.1-6 (1934), pp. 104–113.

[121] W. Egelhoff. “Core-level binding-energy shifts at surfaces and in solids”. In: *Surface Science Reports* 6.6-8 (1987), pp. 253–415.

[122] A. Kotani and Y. Toyozawa. “Photoelectron Spectra of Core Electrons in Metals with an Incomplete Shell”. In: *Journal of the Physical Society of Japan* 37.4 (1974), pp. 912–919.

[123] C. N. Berglund and W. E. Spicer. “Photoemission Studies of Copper and Silver: Theory”. In: *Physical Review* 136.4A (1964), A1030–A1044.

[124] S. A. Chambers, Y. J. Kim, and Y. Gao. “Fe2p Core-Level Spectra for Pure, Epitaxial $\alpha-Fe_2O_3(0001)$, $\gamma-Fe_2O_3(001)$, and Fe_3O_4 (001)”. In: *Surface Science Spectra* 5.3 (1998), pp. 219–228.

[125] N. S. McIntyre and D. G. Zetaruk. “X-ray photoelectron spectroscopic studies of iron oxides”. In: *Analytical Chemistry* 49.11 (1977), pp. 1521–1529.

[126] M. C. Biesinger et al. “Resolving surface chemical states in XPS analysis of first row transition metals, oxides and hydroxides: Cr, Mn, Fe, Co and Ni”. In: *Applied Surface Science* 257.7 (2011), pp. 2717–2730.

[127] P. Liu et al. “Reaction of water vapor with $\alpha-Al_2O_3(0001)$ and $\alpha-Fe_2O_3$ (0001) surfaces: synchrotron X-ray photoemission studies and thermodynamic calculations”. In: *Surface Science* 417.1 (1998), pp. 53–65.

[128] S. Yamamoto et al. “Water Adsorption on $\alpha-Fe_2O_3$ (0001) at near Ambient Conditions”. In: *The Journal of Physical Chemistry C* 114.5 (2010), pp. 2256–2266.

[129] R. P. Gupta and S. K. Sen. “Calculation of multiplet structure of core p -vacancy levels”. In: *Physical Review B* 10 (1974), pp. 71–77.

[130] R. P. Gupta and S. K. Sen. “Calculation of multiplet structure of core p-vacancy levels. II”. In: *Physical Review B* 12.1 (1975), pp. 15–19.

[131] C. S. Fadley et al. “Multiplet Splitting of Core-Electron Binding Energies in Transition-Metal Ions”. In: *Physical Review Letters* 23.24 (1969), pp. 1397–1401.

[132] A. P. Grosvenor et al. “Investigation of multiplet splitting of Fe2p XPS spectra and bonding in iron compounds”. In: *Surface and Interface Analysis* 36.12 (2004), pp. 1564–1574.

[133] P. S. Bagus et al. “Atomic Many-Body Effects for the *p*-Shell Photoelectron Spectra of Transition Metals”. In: *Physical Review Letters* 84.10 (2000), pp. 2259–2262.

[134] E. Kraut et al. “Precise determination of the valence-band edge in x-ray photoemission spectra: Application to measurement of semiconductor interface potentials”. In: *Physical Review Letters* 44.24 (1980), pp. 1620–1623.

[135] J. Waldrop et al. “Measurement of semiconductor heterojunction band discontinuities by Xray photoemission spectroscopy”. In: *Journal of Vacuum Science & Technology A: Vacuum, Surfaces, and Films* 3.3 (1985), pp. 835–841.

[136] A. Klein. “Energy band alignment at interfaces of semiconducting oxides: A review of experimental determination using photoelectron spectroscopy and comparison with theoretical predictions by the electron affinity rule, charge neutrality levels, and the common anion”. In: *Thin Solid Films* 520.10 (2012), pp. 3721–3728.

[137] A. Klein et al. “Photoelectron Spectroscopy in Materials Science and Physical Chemistry : Analysis of Composition, Chemical Bonding and Electronic Structure of Surfaces and Interfaces”. In: *Bunsen-Magazin* (2008), pp. 124–139.

[138] S. Li et al. “Intrinsic energy bandalignment of functional oxide”. In: *physica status solidi RRL* 8.6 (2014), pp. 571–576.

[139] E. Smith and G. Dent. *Modern Raman Spectroscopy - A Practical Approach*. John Wiley & Sons, 2005.

[140] J. R. Ferraro, K. Nakamoto, and C. W. Brown. *Introductory Raman Spectroscopy*. Elsevier, 2003.

[141] I. Chamritski and G. Burns. “Infrared- and Raman-Active Phonons of Magnetite, Maghemite, and Hematite: A Computer Simulation and Spectroscopic Study”. In: *J. Phys. Chem. B* 109 (2005), pp. 4965–4968.

[142] J. Yang et al. “Synthesis and Characterization of Cobalt Hydroxide, Cobalt Oxyhydroxide, and Cobalt Oxide Nanodiscs”. In: *The Journal of Physical Chemistry C* 114.1 (2010), pp. 111–119.

[143] D. L. A. de Faria, S. Silva, and M. de Oliveira. “Raman microspectroscopy of some iron oxides and oxyhydroxides”. In: *Journal of Raman Spectroscopy* 28.February (1997), pp. 873–878.

[144] A. M. Jubb and H. C. Allen. “Vibrational spectroscopic characterization of hematite, maghemite, and magnetite thin films produced by vapor deposition”. In: *ACS Applied Materials and Interfaces* 2.10 (2010), pp. 2804–2812.

[145] L. Spieß et al. *Moderne Röntgenbeugung*. Wiesbaden: Vieweg+Teubner, 2009.

[146] A. Wachau. “Sauerstoffaustausch polykristalliner kathodenzerstäubter Indiumoxid-Dünnschichten”. PhD Thesis. TU Darmstadt, 2015.

[147] L. J. van der Pauw. “A method of measuring specific resistivity and Hall effect of discs of arbitrary shape”. In: 13 (1958), pp. 1–9.

[148] A. Klein. “Interface Properties of Dielectric Oxides”. In: *Journal of the American Ceramic Society* 99.2 (2016), pp. 369–387.

[149] A. Klein. “Transparent Conducting Oxides: Electronic Structure-Property Relationship from Photoelectron Spectroscopy with in situ Sample Preparation”. In: *Journal of the American Ceramic Society* 96 (2013), p. 331.

[150] R. Anton et al. “Design and performance of a versatile, cost-effective microwave electron cyclotron resonance plasma source for surface and thin film processing”. In: *Review of Scientific Instruments* 71.2 (2000), pp. 1177–1180.

[151] T. J. M. Bayer. “Atomic Layer Deposition von Al_2O_3-Schichten auf Indiumzinnoxid: Aufbau einer Depositionseinrichtung und Untersuchung von Grenzflächeneigenschaften”. Dipl.-Ing. TU Darmstadt, 2009.

[152] M. Aronniemi, J. Sainio, and J. Lahtinen. “Chemical state quantification of iron and chromium oxides using XPS: the effect of the background subtraction method”. In: *Surface Science* 578.1-3 (2005), pp. 108–123.

[153] S. Merkel et al. “Raman Spectroscopy of Iron to 152 Gigapascals: Implications for Earth’s Inner Core”. In: *Science* 288.5471 (2000), pp. 1626–1629.

[154] T. Ohtsuka, K. Kubo, and N. Sato. “Raman Spectroscopy of Thin Corrosion Films on Iron At 100 °C to 150 °C in Air.” In: *Corrosion* 42.8 (1986), pp. 476–481.

[155] T. Yamashita and P. Hayes. “Analysis of XPS spectra of Fe^{2+} and Fe^{3+} ions in oxide materials”. In: *Applied Surface Science* 254.8 (2008), pp. 2441–2449.

[156] T. Droubay and S. A. Chambers. “Surface-sensitive Fe2p photoemission spectra for $\alpha-Fe_2O_3(0001)$: The influence of symmetry and crystal-field strength”. In: *Physical Review B* 64.20 (2001), p. 205414.

[157] M. P. Dare-Edwards et al. “Electrochemistry and photoelectrochemistry of iron(III) oxide”. In: *Journal of the Chemical Society, Faraday Transactions 1* 79.9 (1983), p. 2027.

[158] T. Fujii et al. “In situ XPS Spectra of Nonstoichiometric $Fe_{3-\delta}O_4(100)$ Films”. In: *Surface Science Spectra* 6.4 (1999), p. 337.

[159] J. F. Anderson, M. Kuhn, and U. Diebold. “Epitaxially Grown Fe_3O_4 Thin Films: An XPS Study”. In: *Surface Science Spectra* 4.3 (1996), p. 266.

[160] K. Asami, K. Hashimoto, and S. Shimodaira. “X-ray photoelectron spectrum of Fe2+ state in iron oxides”. In: *Corrosion Science* 16.1 (1976), pp. 35–45.

[161] K. Wandelt. “Photoemission Studies of Adsorbed Oxygen and Oxide Layers”. In: *Surface Science Reports* 2 (1982), pp. 1–121.

[162] N. D. Phu et al. “Crystallization process and magnetic properties of amorphous iron oxide nanoparticles”. In: *J. Phys. D: Appl. Phys.* 44.44 (2011), pp. 345002–345002.

[163] Y. El Mendili et al. “Insights into the Mechanism Related to the Phase Transition from $\gamma-Fe_2O_3$ to $\alpha-Fe_2O_3$ Nanoparticles Induced by Thermal Treatment and Laser Irradiation”. In: *The Journal of Physical Chemistry C* 116.44 (2012), pp. 23785–23792.

[164] K. McCarty. “Inelastic light scattering in $\alpha-Fe_2O_3$: Phonon vs magnon scattering”. In: *Solid State Communications* 68.8 (1988), pp. 799–802.

[165] M. J. Massey et al. “Effects of pressure and isotopic substitution on the Raman spectrum of $\alpha-Fe_2O_3$: Identification of two-magnon scattering”. In: *Physical Review B* 41.11 (1990), pp. 7822–7827.

[166] C. J. Sartoretti et al. “Photoelectrochemical oxidation of water at transparent ferric oxide film electrodes”. In: *Chemical Physics Letters* 376.1-2 (2003), pp. 194–200.

[167] D. Bersani, P. P. Lottici, and A. Montenero. “Micro-Raman investigation of iron oxide films and powders produced by sol-gel syntheses”. In: *Journal of Raman Spectroscopy* 30.5 (1999), pp. 355–360.

[168] I. V. Chernyshova, M. F. Hochella Jr, and A. S. Madden. “Size-dependent structural transformations of hematite nanoparticles. 1. Phase transition”. In: *Physical Chemistry Chemical Physics* 9.14 (2007), p. 1736.

[169] L. B. Lopez, J. D. Pasteris, and P. Biswas. “Sensitivity of micro-raman spectrum to crystallite size of electrospray-deposited and post-annealed films of iron-oxide nanoparticle suspensions”. In: *Applied Spectroscopy* 63.6 (2009), pp. 627–635.

[170] Y. Y. Xu et al. “Synthesis and characterization of single-crystalline $\alpha-Fe_2O_3$ nanoleaves”. In: *Physica E: Low-Dimensional Systems and Nanostructures* 41.5 (2009), pp. 806–811.

[171] C. J. Sartoretti et al. “Photoelectrochemical oxidation of water at transparent ferric oxide film electrodes”. In: *Journal of Physical Chemistry B* 109.28 (2005), pp. 13685–13692.

[172] I. Cesar et al. “Influence of Feature Size, Film Thickness, and Silicon Doping on the Performance of Nanostructured Hematite Photoanodes for Solar Water Splitting”. In: *Journal of Physical Chemistry C* 113.2 (2009), pp. 772–782.

[173] W. Wang et al. “Fe t2g band dispersion and spin polarization in thin films of Fe_3O_4(001)/MgO(001): Half-metallicity of magnetite revisited”. In: *Physical Review B* 87.8 (2013), p. 085118.

[174] C. Jiménez et al. “Raman Study of CeO_2 Texture as a Buffer Layer in the CeO_2/$La_2Zr_2O_7$/Ni Architecture for Coated Conductors”. In: *Applied Spectroscopy* 63.4 (2009), pp. 401–406.

[175] A. L. Patterson. “The Scherrer Formula for X-Ray Particle Size Determination”. In: *Physical Review* 56.10 (1939), pp. 978–982.

[176] M. E. A. Warwick et al. “XPS analysis of Fe_2O_3-TiO_2-Au nanocomposites prepared by a plasma-assisted route”. In: *Surface Science Spectra* 23.1 (2016), pp. 61–69.

[177] A. E. Bocquet, T Mizokawa, and T Saitoh. “Electronic structure of 3d-transition-metal compounds by analysis of the 2p core-level photoemission spectra”. In: *Physical Review B* 46.7 (1992), pp. 3771–3784.

[178] G. C. Allen et al. “X-Ray photoelectron spectroscopy of iron–oxygen systems”. In: *J. Chem. Soc., Dalton Trans.* 14 (1974), pp. 1525–1530.

[179] J. Tauc, R. Grigorovici, and A. Vancu. “Optical properties and electronic structure of amorphous germanium”. In: *physica status solidi (b)* 15.2 (1966), pp. 627–637.

[180] R Swanepoel. “Determination of the thickness and optical constants of amorphous silicon”. In: *Journal of Physics E: Scientific Instruments* 16.12 (2000), pp. 1214–1222.

[181] R. G. J. Strens and B. J. Wood. “Diffuse reflectance spectra and optical properties of some iron and titanium oxides and oxyhydroxides”. In: *Mineralogical Magazine* 43 (1979), pp. 347–354.

[182] X. Zhou et al. “Facet-Mediated Photodegradation of Organic Dye over Hematite Architectures by Visible Light”. In: *Angewandte Chemie International Edition* 51.1 (2012), pp. 178–182.

[183] X. Zhang et al. “Improvement of hematite as photocatalyst by doping with tantalum”. In: *Journal of Physical Chemistry C* 118.30 (2014), pp. 16842–16850.

[184] H. Guo and A. S. Barnard. “Surface Structure and Environment-Dependent Hydroxylation of the Nonpolar Hematite (100) from Density Functional Theory Modeling”. In: *The Journal of Physical Chemistry C* 116.29 (2012), pp. 15854–15854.

[185] Y. Gao and S. A. Chambers. “Heteroepitaxial growth of $\alpha-Fe_2O_3$, $\gamma-Fe_2O_3$ and Fe_3O_4 thin films by oxygen-plasma-assisted molecular beam epitaxy”. In: *Journal of Crystal Growth* 174.1 (1997), pp. 446–454.

[186] M. Rioult et al. “Single Crystalline Hematite Films for Solar Water Splitting: Ti-Doping and Thickness Effects”. In: *The Journal of Physical Chemistry C* 118.6 (2014), pp. 3007–3014.

[187] D. A. Grave et al. “Heteroepitaxial hematite photoanodes as a model system for solar water splitting”. In: *J. Mater. Chem. A* 4.8 (2016), pp. 3052–3060.

[188] S. Li, G. W. Qin, and L. Zuo. “Epitaxial Growth of $\alpha-Fe_2O_3$ Thin Films on c-Plane Sapphire Substrate by Hydrothermal Method”. In: *Materials Science Forum* 702-703 (2011), pp. 999–1002.

[189] R. F. C. Farrow et al. “Epitaxial growth of Pt on basal-plane sapphire: a seed film for artificially layered magnetic metal structures”. In: *Journal of Crystal Growth* 133.1-2 (1993), pp. 47–58.

[190] R. Vargas et al. “Epitaxial growth of iridium and platinum films on sapphire by metalorganic chemical vapor deposition”. In: *Appl. Phys. Lett.* 65.9 (1994), p. 1094.

[191] G. Ketteler et al. “Bulk and surface phases of iron oxides in an oxygen and water atmosphere at low pressure”. In: *Physical Chemistry Chemical Physics* 3.6 (2001), pp. 1114–1122.

[192] X. G. Wang et al. “The hematite ($\alpha-Fe_2O_3$) (0001) surface: evidence for domains of distinct chemistry”. In: *Physical Review Letters* 81.0001 (1998), pp. 1038–1041.

[193] S. K. Shaikhutdinov et al. “Structure and reactivity of iron oxide surfaces”. In: *Faraday Discussions* 114 (1999), pp. 363–380.

[194] W. Weiss and W. Ranke. “Surface chemistry and catalysis on well-defined epitaxial iron-oxide layers”. In: *Progress in Surface Science* 70.1-3 (2002), pp. 1–151.

[195] F. J. Morin. “Electrical properties of α-Fe_2O_3”. In: *Physical Review* 93.6 (1954), pp. 1195–1199.

[196] S Mochizuki. “Electrical Conductivity of $\alpha-Fe_2O_3$ ”. In: *Physica Status Solidi (a)* 41 (1977), pp. 591–594.

[197] R. Gardner, F. Sweett, and D. Tanner. “The electrical properties of alpha ferric oxide—II.” In: *Journal of Physics and Chemistry of Solids* 24.10 (1963), pp. 1183–1196.

[198] S. H. Cheung et al. “Effects of unreconstructed and reconstructed polar surface terminations on growth, structure, and magnetic properties of hematite films”. In: *Physical Review B* 85 (2012), p. 045405.

[199] J. Goniakowski, F. Finocchi, and C. Noguera. “Polarity of oxide surfaces and nanostructures”. In: *Reports on Progress in Physics* 71 (2008), p. 016501.

[200] C. Noguera. “Polar oxide surfaces”. In: *Journal of Physics: Condensed Matter* 12 (2000), R367–R410.

[201] P. W. Tasker. “The stability of ionic crystal surfaces”. In: *Journal of Physics C: Solid State Physics* 12.22 (1979), pp. 4977–4984.

[202] E. Wasserman et al. “Ewald methods for polarizable surfaces with application to hydroxylation and hydrogen bonding on the (012) and (001) surfaces of $\alpha-Fe_2O_3$”. In: *Surface Science* 385.2-3 (1997), pp. 217–239.

[203] G. A. Waychunas, C. S. Kim, and J. F. Banfield. “Nanoparticulate Iron Oxide Minerals in Soils and Sediments: Unique Properties and Contaminant Scavenging Mechanisms”. In: *Journal of Nanoparticle Research* 7.4-5 (2005), pp. 409–433.

[204] L. Machala, R. Zboril, and A. Gedanken. “Amorphous Iron(III) Oxide - A Review”. In: *The Journal of Physical Chemistry B* 111.16 (2007), pp. 4003–4018.

[205] P. Miedema and F. M. F. De Groot. “The iron L edges: Fe 2p X-ray absorption and electron energy loss spectroscopy”. In: *Journal of Electron Spectroscopy and Related Phenomena* 187.1 (2013), pp. 32–48.

[206] P. Miedema et al. “Iron 1s X-ray photoemission of Fe_2O_3 ”. In: *Journal of Electron Spectroscopy and Related Phenomena* 203 (2015), pp. 8–13.

[207] D. Vaughan, J. Tossell, and K. Johnson. “The bonding of ferrous iron to sulfur and oxygen in tetrahedral coordination: A comparative study using SCF Xα scattered wave molecular orbital calculations”. In: *Geochimica et Cosmochimica Acta* 38.7 (1974), pp. 993–1005.

[208] D. S. Toledano, E. R. Dufresne, and V. E. Henrich. “Photoexcited Fe_2O_3 surfaces: Properties and chemisorption”. In: *Journal of Vacuum Science & Technology A: Vacuum, Surfaces, and Films* 16.3 (1998), p. 1050.

[209] J. Yeh and I Lindau. “Atomic subshell photoionization cross sections and asymmetry parameters: $1 \leq Z \leq 103$”. In: *Atomic data and nuclear data tables* 32 (1985), pp. 1–155.

[210] A. T. Kozakov et al. “Electronic structure of bismuth ferrite and hematite single crystals: X-ray photoelectron study and calculation”. In: *Physics of the Solid State* 53.1 (2011), pp. 41–47.

[211] J. Y. Kim et al. “A Stable and Efficient Hematite Photoanode in a Neutral Electrolyte for Solar Water Splitting: Towards Stability Engineering”. In: *Advanced Energy Materials* 4.13 (2014), p. 1400476.

[212] S. Somekawa et al. “Wet-type Fe_2O_3 solar cells based on Fe_2O_3 films prepared by laser ablation: Drastic temperature effect”. In: *Electrochemistry Communications* 11.11 (2009), pp. 2150–2152.

[213] A. Hankin, J. C. Alexander, and G. H. Kelsall. “Constraints to the flat band potential of hematite photo-electrodes”. In: *Physical Chemistry Chemical Physics* 16.30 (2014), p. 16176.

[214] M. Rahman et al. “The influence of Ti- and Si-doping on the structure, morphology and photo-response properties of α-Fe2O3 for efficient water-splitting: Insights from experiment and first-principles calculations”. In: *Chemical Physics Letters* 592 (2014), pp. 242–246.

[215] A. Mirzaei, B. Hashemi, and K. Janghorban. “$\alpha - Fe_2O_3$ based nanomaterials as gas sensors”. In: *Journal of Materials Science: Materials in Electronics* 27.4 (2016), pp. 3109–3144.

[216] G. Horowitz. “Capacitance-voltage measurements and flat-band potential determination on Zr-doped $\alpha-Fe_2O_3$ single-crystal electrodes”. In: *Journal of Electroanalytical Chemistry* 159.2 (1983), pp. 421–436.

[217] S. Shen et al. “Physical and photoelectrochemical properties of Zr-doped hematite nanorod arrays”. In: *Nanoscale* 5.20 (2013), p. 9867.

[218] E. A. Carter and Peilin Liaw. “New concepts and modeling strategies to design and evaluate photo-electro-catalysts based on transition metal oxides”. In: *Chem Soc Rev* 42 (2013), pp. 2401–2422.

[219] J Peng and C. C. Chai. “A study of the sensing characteristics of Fe_2O_3 gas-sensing thin film”. In: *Sensors and Actuators* 13-14 (1993), pp. 591–593.

[220] H. Tang et al. “Titanium and magnesium Co-alloyed hematite thin films for photoelectrochemical water splitting”. In: *Journal of Applied Physics* 111.7 (2012), p. 073502.

[221] A. Kay, I. Cesar, and M. Grätzel. “New Benchmark for Water Photooxidation by Nanostructured $\alpha-Fe_2O_3$ Films”. In: *Journal of the American Chemical Society* 128.49 (2006), pp. 15714–15721.

[222] I. Cesar et al. “Translucent Thin Film Fe_2O_3 Photoanodes for Efficient Water Splitting by Sunlight: Nanostructure-Directing Effect of Si-Doping”. In: *Journal of the American Chemical Society* 128.14 (2006), pp. 4582–4583.

[223] S. Saremi-Yarahmadi et al. “Nanostructured $\alpha-Fe_2O_3$ Electrodes for Solar Driven Water Splitting: Effect of Doping Agents on Preparation and Performance”. In: *The Journal of Physical Chemistry C* 113.12 (2009), pp. 4768–4778.

[224] I. Cesar et al. “Influence of Feature Size, Film Thickness, and Silicon Doping on the Performance of Nanostructured Hematite Photoanodes for Solar Water Splitting”. In: *The Journal of Physical Chemistry C* 113.2 (2009), pp. 772–782.

[225] J. a. Glasscock et al. “Enhancement of Photoelectrochemical Hydrogen Production from Hematite Thin Films by the Introduction of Ti and Si”. In: *The Journal of Physical Chemistry C* 111.44 (2007), pp. 16477–16488.

[226] W. D. Chemelewski, N. T. Hahn, and C. B. Mullins. “Effect of Si Doping and Porosity on Hematite’s ($\alpha-Fe_2O_3$) Photoelectrochemical Water Oxidation Performance”. In: *The Journal of Physical Chemistry C* 116.8 (2012), pp. 5255–5261.

[227] J. Liu et al. “Silicon-doped hematite nanosheets with superlattice structure”. In: *Chemical Communications* 47.28 (2011), p. 8040.

[228] J. Liu et al. “Ge-doped hematite nanosheets with tunable doping level, structure and improved photoelectrochemical performance”. In: *Nano Energy* 2.3 (2013), pp. 328–336.

[229] J. Liu et al. “Highly oriented Ge-doped hematite nanosheet arrays for photoelectrochemical water oxidation”. In: *Nano Energy* 9 (2014), pp. 282–290.

[230] T.-Y. Yang et al. “A new hematite photoanode doping strategy for solar water splitting: oxygen vacancy generation”. In: *Physical Chemistry Chemical Physics* 15.6 (2013), p. 2117.

[231] C. Leygraf, M. Hendewerk, and G. Somorjai. “The preparation and selected properties of Mg-doped p-type iron oxide as a photocathode for the photoelectrolysis of water using visible light”. In: *Journal of Solid State Chemistry* 48.3 (1983), pp. 357–367.

[232] H. Tang et al. “Synthesis and Characterization of Magnesium-Alloyed Hematite Thin Films”. In: *Journal of Electronic Materials* 41.11 (2012), pp. 3100–3106.

[233] W. B. Ingler Jr and S. U. Khan. “Photoresponse of spray pyrolytically synthesized magnesium-doped iron (III) oxide (p-Fe_2O_3) thin films under solar simulated light illumination”. In: *Thin Solid Films* 461.2 (2004), pp. 301–308.

[234] M. Mohapatra et al. “Structural and magnetic properties of Mg-doped nano-$\alpha-Fe_2O_3$ particles synthesized by surfactant mediation-precipitation technique”. In: *Physica Status Solidi (B) Basic Research* 250.1 (2013), pp. 65–72.

[235] Y.-W. Tai et al. “Preparation and characterization of p-type Fe_2O_3 pellets from Mg doping in pure oxygen atmosphere at high temperatures”. In: *Journal of the Taiwan Institute of Chemical Engineers* 42.4 (2011), pp. 669–673.

[236] Y. Lin et al. “Growth of p-Type Hematite by Atomic Layer Deposition and Its Utilization for Improved Solar Water Splitting”. In: *Journal of the American Chemical Society* 134.12 (2012), pp. 5508–5511.

[237] M. Gaudon et al. “Influence of Sn^{4+} and Sn^{4+}/Mg^{2+} doping on structural features and visible absorption properties of $\alpha-Fe_2O_3$ hematite”. In: *Journal of Solid State Chemistry* 183.9 (2010), pp. 2101–2109.

[238] Z. D. Pozun and G. Henkelman. “Hybrid density functional theory band structure engineering in hematite”. In: *The Journal of Chemical Physics* 134.22 (2011), p. 224706.

[239] M. Kosa et al. “A combined computational and experimental investigation of Mg doped $\alpha-Fe_2O_3$”. In: *Phys. Chem. Chem. Phys.* 18.2 (2016), pp. 781–791.

[240] A. Braun et al. “Iron Resonant Photoemission Spectroscopy on Anodized Hematite Points to Electron Hole Doping during Anodization”. In: *ChemPhysChem* 13.12 (2012), pp. 2937–2944.

[241] J. S. Corneille, J.-W. He, and D. W. Goodman. “XPS characterization of ultra-thin MgO films on a Mo (100) surface”. In: *Surf. Sci.* 306.93 (1994), pp. 269–278.

[242] P Casey et al. “Growth and characterisation of thin MgO layers on Si(100) surfaces”. In: *Journal of Physics: Conference Series* 100 (2008), p. 042046.

[243] J. Song et al. “Penetration depth at various Raman excitation wavelengths and stress model for Raman spectrum in biaxially-strained Si”. In: *Science China: Physics, Mechanics and Astronomy* 56.11 (2013), pp. 2065–2070.

[244] I. Jõgi et al. “Phase Formation Behavior in Ultrathin Iron Oxide”. In: *Langmuir* 31.45 (2015), pp. 12372–12381.

[245] R. Franking et al. “Facile post-growth doping of nanostructured hematite photoanodes for enhanced photoelectrochemical water oxidation”. In: *Energy Environ. Sci.* 6.2 (2013), pp. 500–512.

[246] A. G. Shard. “Detection limits in XPS for more than 6000 binary systems using Al and Mg Kα X-rays”. In: *Surface and Interface Analysis* 46.3 (2014), pp. 175–185.

[247] D. M. Mattox. *Handbook of Physical Vapor Deposition (PVD) Processing*. 2nd. Elsevier Inc., 2010.

[248] A. R. Chourasia. “Core Level XPS Spectra of Elemental Silicon Using Zirconium Radiation”. In: *Surface Science Spectra* 5 (1998), pp. 45–55.

[249] D. S. Jensen et al. “Silicon (100)/SiO_2 by XPS”. In: *Surface Science Spectra* 20.1 (2013), pp. 36–42.

[250] P. J. Grunthaner. “Oxygen impurity effects at metal/silicide interfaces: Formation of silicon oxide and suboxides in the Ni/Si system”. In: *Journal of Vacuum Science and Technology* 19.3 (1981), p. 641.

[251] R. Nordberg et al. “Binding energy of the "2p" electrons of silicon in various compounds”. In: *Inorganic Chemistry* 9.11 (1970), pp. 2469–2474.

[252] F. J. Grunthaner et al. “Local atomic and electronic structure of oxide/GaAs and SiO 2 /Si interfaces using highresolution XPS”. In: *Journal of Vacuum Science and Technology* 16.5 (1979), pp. 1443–1453.

[253] A. R. Chourasia. “Core Level XPS Spectra of Silicon Dioxide Using Zirconium and Magnesium Radiations”. In: *Surface Science Spectra* 13 (2006), pp. 48–57.

[254] C. Y. Lee et al. “Si-doped hem nanotubular/nanoporous layers for enhanced photoelectrochemical water splitting”. In: *Electrochemistry Communications* 34 (2013), pp. 308–311.

[255] F. L. Souza et al. “Nanostructured hematite thin films produced by spin-coating deposition solution: Application in water splitting”. In: *Solar Energy Materials and Solar Cells* 93.3 (2009), pp. 362–368.

[256] D. A. Zatsepin et al. “Octahedral conversion of $\alpha-SiO_2$ host matrix by pulsed ion implantation”. In: *Physica Status Solidi (B)* 252.10 (2015), pp. 2185–2190.

[257] P. Kumarn et al. “Nano Porous Hematite for Solar Hydrogen Production”. In: *Journal of the Electrochemical Society* 159.8 (2012), H685–H691.

[258] M Alonso, M Moreno, and J. L. Sacedo. “Si and Be intralayers at GaAs / AlAs heterojunctions : Doping effects”. In: 58.20 (1998).

[259] R. D. Shannon. “Revised effective ionic radii and systematic studies of interatomic distances in halides and chalcogenides”. In: *Acta Crystallographica Section A* 32.5 (1976), pp. 751–767.

[260] K. Mizushima et al. “Impurity levels of iron-group ions in TiO_2(II)”. In: *Journal of Physics and Chemistry of Solids* 40.12 (1979), pp. 1129–1140.

[261] G Schimanke. “In situ XRD study of the phase transition of nanocrystalline maghemite ($\gamma-Fe_2O_3$) to hematite ($\alpha-Fe_2O_3$)”. In: *Solid State Ionics* 136-137.1-2 (2000), pp. 1235–1240.

[262] S. N. Basahel et al. “Influence of crystal structure of nanosized ZrO_2 on photocatalytic degradation of methyl orange”. In: *Nanoscale Research Letters* 10.1 (2015), p. 73.

[263] G. Yu, B. Tay, and Z. Zhao. “Structure and properties of zirconium oxide thin films prepared by filtered cathodic vacuum arc”. In: *Applied Physics A* 81 (2005), pp. 405–411.

[264] E. G. Seebauer and M. C. Kratzer. “Charged point defects in semiconductors”. In: *Materials Science and Engineering: R: Reports* 55.3-6 (2006), pp. 57–149.

[265] F. Iacona, R. Kelly, and G. Marletta. “X-ray photoelectron spectroscopy study of bombardment-induced compositional changes in ZrO_2, SiO_2, and $ZrSiO_4$”. In: *Journal of Vacuum Science & Technology A: Vacuum, Surfaces, and Films* 17.5 (1999), pp. 2771–2778.

[266] M. T. Greiner et al. “Transition metal oxide work functions: The influence of cation oxidation state and oxygen vacancies”. In: *Advanced Functional Materials* 22.21 (2012), pp. 4557–4568.

[267] H. Tong et al. “Work function contrast and energy band modulation between amorphous and crystalline $Ge_2Sb_2Te_5$ films”. In: *Applied Physics Letters* 107.8 (2015), p. 082101.

[268] K. Jacobi, G. Zwicker, and A. Gutmann. “Work function, electron affinity and band bending of zinc oxide surfaces”. In: *Surface Science* 141.1 (1984), pp. 109–125.

[269] R. G. Schafranek. “Kathodenzerstäubte $(Ba,Sr)TiO_3$-Dünnschichten für steuerbare Mikrowellenkomponenten - Material-, Bauteil- und Grenzflächeneigenschaften”. PhD thesis. TU Darmstadt, 2009.

[270] L. Giordano, F. Cinquini, and G. Pacchioni. “Tuning the surface metal work function by deposition of ultrathin oxide films: Density functional calculations”. In: *Physical Review B* 73.4 (2006), p. 045414.

[271] Y. Gassenbauer. “Untersuchung der elektronischen und chemischen Oberflächeneigenschaften von Zinn-dotiertem Indium-Oxid im Hinblick auf die Funktion in organischen Leuchtdioden”. PhD Thesis. TU Darmstadt, 2007.

[272] L. Yan et al. “Magnesium oxide as a candidate high-κ gate dielectric”. In: *Applied Physics Letters* 88.14 (2006), p. 142901.

[273] P. Moseley. “Materials selection for semiconductor gas sensors”. In: *Sensors and Actuators B: Chemical* 6.1-3 (1992), pp. 149–156.

[274] R Ramamoorthy, P. K. Dutta, and S. a. Akbar. “Oxygen sensors : Materials , methods , designs”. In: *J. Mater. Sci.* 38 (2003), pp. 4271–4282.

[275] K. Singh, J. Nowotny, and V. Thangadurai. “Amphoteric oxide semiconductors for energy conversion devices: a tutorial review”. In: *Chem. Soc. Rev.* 42.5 (2013), pp. 1961–1972.

[276] C. R. A. Catlow et al. “Atomistic Simulation of Defect Structures and Ion Transport in $\alpha-Fe_2O_3$ and $\alpha-Cr_2O_3$”. In: *Journal of the American Ceramic Society* 71.1 (1988), pp. 42–49.

[277] O. Warschkow et al. “Defects and Charge Transport near the Hematite (0001) Surface: An Atomistic Study of Oxygen Vacancies”. In: *Journal of the American Ceramic Society* 85.1 (2004), pp. 213–220.

[278] H. Tang et al. “Synthesis and Characterization of Magnesium-Alloyed Hematite Thin Films”. In: *Journal of Electronic Materials* 41.11 (2012), pp. 3100–3106.

[279] J. de Wit, A. Broersma, and M. Stroband. “Surface instability and nonstoichiometry of $\alpha-Fe_2O_3$”. In: *Journal of Solid State Chemistry* 37.2 (1981), pp. 242–247.

[280] M. V. Hohmann, A. Wachau, and A. Klein. “In situ Hall effect and conductivity measurements of ITO thin films”. In: *Solid State Ionics* 262 (2014), pp. 636–639.

[281] J. B. Goodenough. “Metallic oxides”. In: *Progress in Solid State Chemistry* 5.C (1971), pp. 145–399.

[282] C. Zhu et al. “Plasma-Induced Oxygen Vacancies in Ultrathin Hematite Nanoflakes Promoting Photoelectrochemical Water Oxidation”. In: *ACS Applied Materials and Interfaces* 7.40 (2015), pp. 22355–22363.

[283] W. Jaegermann and T. Mayer. “Surface science studies of elementary processes in photoelectrochemistry: adsorption of electrolyte components on layered transition metal dichalogenides”. In: *Solar Energy Materials and Solar Cells* 83.4 (2004), pp. 371–394.

[284] J. Morasch et al. “Reactively magnetron sputtered Bi_2O_3 thin films: Analysis of structure, optoelectronic, interface, and photovoltaic properties”. In: *Physica Status Solidi (a)* 211.1 (2014), pp. 93–100.

[285] F. Chen et al. “Barrier heights, polarization switching, and electrical fatigue in $Pb(Zr,Ti)O_3$ ceramics with different electrodes”. In: *Journal of Applied Physics* 108.10 (2010), pp. 1–7.

[286] V. Pfeifer et al. “Energy Band Alignment between Anatase and Rutile TiO_2”. In: *The Journal of Physical Chemistry Letters* 4.23 (2013), pp. 4182–4187.

[287] Y. Kaga et al. “Ru and RuO_2 Thin Films by XPS”. In: *Surface Science Spectra* 6.1 (1999), pp. 68–74.

[288] Y. Kim, Y. Gao, and S. Chambers. “Core-level X-ray photoelectron spectra and X-ray photoelectron diffraction of RuO_2(110) grown by molecular beam epitaxy on TiO_2(110)”. In: *Applied Surface Science* 120.3-4 (1997), pp. 250–260.

[289] M. A. van Veenendaal and G. A. Sawatzky. “Nonlocal Screening Effects in 2p X-Ray Photoemission Spectroscopy Core-Level Line Shapes of Transition Metal Compounds”. In: *Physical Review Letters* 70.16 (1993), pp. 2499–2502.

[290] R. Hertwig. “Deposition and Characterisation of Reactive Sputtered RuO_2 Thin Films”. Bachelor Thesis. Technische Universität Darmstadt, 2015.

[291] A. Hartmann et al. “Ruthenium oxide and strontium ruthenate electrodes for ferroelectric thin-films capacitors”. In: *Applied Physics A: Materials Science & Processing* 70.2 (2000), pp. 239–242.

[292] H. Over et al. “Atomic-Scale Structure and Catalytic Reactivity of the RuO_2(110) Surface”. In: *Science* 287.5457 (2000), pp. 1474–1476.

[293] J. Li et al. “Photoelectrochemical performance enhanced by a nickel oxide hematite p-n junction photoanode”. In: *Chemical Communications* 48.66 (2012), p. 8213.

[294] F. Malara et al. “Controlling the Surface Energetics and Kinetics of Hematite Photoanodes Through Few Atomic Layers of NiO_x”. In: *ACS Catalysis* 6.6 (2016), pp. 3619–3628.

[295] Y. W. Phuan et al. “In situ Ni-doping during cathodic electrodeposition of hematite for excellent photoelectrochemical performance of nanostructured nickel oxide-hematite p-n junction photoanode”. In: *Applied Surface Science* 392 (2017), pp. 144–152.

[296] C. Körber et al. “A study of the electronic structure of In_2O_3 and Sn-doped In_2O_3 by hard x-ray photoemission spectroscopy”. In: *Phys. Rev. B* 81 (2010), p. 165207.

[297] Y. Gassenbauer et al. “Surface states, surface potentials and segregation at surfaces of tin-doped In_2O_3”. In: *Phys. Rev. B* 73 (2006), p. 245312.

[298] M. V. Frischbier et al. “Influence of dopant species and concentration on grain boundary scattering in degenerately doped In_2O_3 thin films”. In: *Thin Solid Films* 614 (2016), pp. 62–68.

[299] T. De Boer et al. “Band gap and electronic structure of cubic, rhombohedral, and orthorhombic In_2O_3 polymorphs: Experiment and theory”. In: *Phys. Rev. B* 93.15 (2016), p. 155205.

[300] Y. Kim, Y. Gao, and S. Chambers. “Selective growth and characterization of pure, epitaxial α-Fe_2O_3(0001) and Fe_3O_4(001) films by plasma-assisted molecular beam epitaxy”. In: *Surf. Sci.* 371.2-3 (1997), pp. 358–370.

[301] A. Gurlo, P. Kroll, and R. Riedel. “Metastability of Corundum-Type In_2O_3”. In: *Chemistry* 14.11 (2008), pp. 3306–3310.

[302] P. D. C. King et al. “Band gap, electronic structure, and surface electron accumulation of cubic and rhombohedral In_2O_3”. In: *Phys. Rev. B* 79.20 (2009), p. 205211.

[303] J.-S. Huh et al. “Sensing Characteristics of Cubic and Rhombohedral Nanocrystalline ITO Thick Films”. In: *MRS Proceedings* 704 (2001), W9.35.1.

[304] B.-C. Kim et al. “Effects of crystal structures on gas sensing properties of nanocrystalline ITO thick films”. In: *Sensors and Actuators B* 89.1-2 (2003), pp. 180–186.

[305] K.-H. Seo et al. “Synthesis and Electrical Characterization of the Polymorphic Indium Tin Oxide Nanocrystalline Powders”. In: *J. Am. Ceram. Soc.* 89.11 (2006), pp. 3431–3436.

[306] A. Malik, R. Nunes, and R. Martins. “The Cubic to Hexagonal Phase Transition in Spray Deposited Tin-Doped Indium Oxide Films”. In: *MRS Proceedings* 481 (1997), p. 599.

[307] L. A. Dunlop, A. Kursumovic, and J. L. MacManus-Driscoll. “Highly Conducting, Transparent Rhombic/Cubic Indium Tin Oxide Nanocomposite Thin Films”. In: *Crystal Growth & Design* 10.4 (2010), pp. 1730–1735.

[308] K. Nomura et al. “Room-temperature fabrication of transparent flexible thin-film transistors using amorphous oxide semiconductors”. In: *Nature* 432.7016 (2004), pp. 488–492.

[309] K. Nomura et al. “Local coordination structure and electronic structure of the large electron mobility amorphous oxide semiconductor In-Ga-Zn-O: Experiment and ab initio calculations”. In: *Phys. Rev. B* 75 (2007), p. 035212.

[310] T. Kamiya and H. Hosono. “Material characteristics and applications of transparent amorphous oxide semiconductors”. In: *NPG Asia Mater* 2 (2010), pp. 15–22.

[311] J. Y. W. Seto. “The electrical properties of polycrystalline silicon films”. In: *J. Appl. Phys.* 46.12 (1975), pp. 5247–5254.

[312] N. Preissler et al. “Electrical transport, electrothermal transport, and effective electron mass in single-crystalline In_2O_3 films”. In: *Phys. Rev. B* 88 (2013), p. 085305.

[313] R. Khanal et al. “Composition-dependent structural and transport properties of amorphous transparent conducting oxides”. In: *Phys. Rev. B* 91.20 (2015), p. 205203.

[314] R. B. H. Tahar et al. “Tin doped indium oxide thin films: Electrical properties”. In: *J. Appl. Phys.* 83.5 (1998), pp. 2631–2645.

[315] Y. Wu et al. “Resistivity and oxygen content of indium tin oxide films deposited at room temperature by pulsed-laser ablation”. In: *J. Appl. Phys.* 86.2 (1999), p. 991.

[316] Y Xu and M. A. A. Schoonen. “The Absolute Energy Positions of Conduction and Valence Bands of Selected Semiconducting Minerals”. In: *American Mineralogist* 85 (2000), pp. 543–556.

[317] T. J. M. Bayer et al. “Determination of electrical properties of degraded mixed ionic conductors: Impedance studies with applied dc voltage”. In: *Journal of Applied Physics* 122.24 (2017), p. 244101.

[318] R. Giesecke. “Influence of oxygen vacancies on barrier heights at $SrTiO_3$ / electrode interfaces”. Master. TU Darmstadt, 2016.

[319] S. Roosendaal et al. “The oxidation state of Fe(100) after initial oxidation in O_2”. In: *Surface Science* 442.3 (1999), pp. 329–337.

[320] T. J. Bayer et al. “Atomic Layer Deposition of Al_2O_3 onto Sn-Doped In_2O_3 : Absence of Self-Limited Adsorption during Initial Growth by Oxygen Diffusion from the Substrate and Band Offset Modification by Fermi Level Pinning in Al_2O_3”. In: *Chemistry of Materials* 24.23 (2012), pp. 4503–4510.

[321] A. Zakutayev et al. “Defect Tolerant Semiconductors for Solar Energy Conversion”. In: *The Journal of Physical Chemistry Letters* 5.7 (2014), pp. 1117–1125.

[322] T. R. Paudel et al. “Doping Rules and Doping Prototypes in A_2BO_4 Spinel Oxides”. In: *Advanced Functional Materials* 21.23 (2011), pp. 4493–4501.

[323] P. F. Ndione et al. “Control of the Electrical Properties in Spinel Oxides by Manipulating the Cation Disorder”. In: *Advanced Functional Materials* 24.5 (2014), pp. 610–618.

[324] A. Muan. “On the Stability of the Phase Fe_2O_3.Al_2O_3”. In: *American Journal of Science* 256 (1958), pp. 413–422.

[325] E. Thimsen et al. “Predicting the Band Structure of Mixed Transition Metal Oxides: Theory and Experiment”. In: *The Journal of Physical Chemistry C* 113.5 (2009), pp. 2014–2021.

[326] A. J. E. Rettie et al. “Unravelling Small-Polaron Transport in Metal Oxide Photoelectrodes”. In: *Journal of Physical Chemistry Letters* 7.3 (2016), pp. 471–479.

[327] T. J. Smart and Y. Ping. “Effect of defects on the small polaron formation and transport properties of hematite from first-principles calculations”. In: *Journal of Physics: Condensed Matter* 29.39 (2017), p. 394006.

[328] K. M. Rosso, D. M. A. Smith, and M. Dupuis. “An ab initio model of electron transport in hematite ($\alpha - Fe_2O_3$) basal planes”. In: *Journal of Chemical Physics* 118.14 (2003), pp. 6455–6466.

[329] G. H. Wannier. “On the Energy Band Structure of Insulators”. In: *Physical Review* 76.3 (1949), pp. 438–439.

[330] A. J. Bosman and H. van Daal. “Small-polaron versus band conduction in some transition-metal oxides”. In: *Advances in Physics* 19.77 (1970), pp. 1–117.

[331] S. Dorris and T. Mason. “Electrical Properties and Cation Valencies in Mn_3O_4”. In: *Journal of the American Ceramic Society* 71.5 (1988), pp. 379–385.

[332] A. Stoneham. “Electronic and defect processes in oxides. The polaron in action”. In: *IEEE Transactions on Dielectrics and Electrical Insulation* 4.5 (1997), pp. 604–613.

[333] S. Biswas et al. “Highly Localized Charge Transfer Excitons in Metal Oxide Semiconductors”. In: *Nano Letters* 18.2 (2018), pp. 1228–1233.

[334] A. Duret and M. Grätzel. “Visible Light-Induced Water Oxidation on Mesoscopic α-Fe_2O_3 Films Made by Ultrasonic Spray Pyrolysis”. In: *J. Phys. Chem. B* 109 (2005), pp. 17184–17191.

[335] J. Schultze and M. Lohrengel. “Stability, reactivity and breakdown of passive films. Problems of recent and future research”. In: *Electrochimica Acta* 45.15-16 (2000), pp. 2499–2513.

[336] M. A. Butler and D. Ginley. “Prediction of Flatband Potentials at Semiconductor-Electrolyte Interfaces from Atomic Electronegativities”. In: *Journal of The Electrochemical Society* 125.2 (1978), p. 228.

[337] R. Beranek. “(Photo)electrochemical Methods for the Determination of the Band Edge Positions of TiO_2-Based Nanomaterials”. In: *Advances in Physical Chemistry* 2011.Iv (2011), pp. 1–20.

[338] A. J. Nozik. “Photoelectrochemistry: Applications to Solar Energy Conversion”. In: *Annual Review of Physical Chemistry* 29.1 (1978), pp. 189–222.

[339] A. Walsh et al. “Nature of the band gap of In_2O_3 revealed by first-principles calculations and X-ray spectroscopy”. In: *Physical Review Letters* 100.16 (2008), pp. 2–5.

[340] X. Chen et al. “Nanomaterials for renewable energy production and storage”. In: *Chemical Society Reviews* 41.23 (2012), p. 7909.

[341] K. N. S. Schuldt. “Electronic characterization of thin film Sr-doped $LaFeO_3$”. Master Thesis. TU Darmstadt, 2018.

[342] N. Bein. “The Fermi Level in Bismuth Ferrite”. Master Thesis. TU Darmstadt, 2018.

Important Symbols & Abbreviations

χ	electron affinity
$\Delta E_{\mathrm{VBM/CBM}}$	valence band/conduction band discontinuity
$\Delta\mu$	quasi-Fermi level splitting
$\Delta_{\mathrm{oct}}/\Delta_{\mathrm{tet}}$	crystal-field splitting in octahedral/tetrahedral coordination
ϕ	work function
$\underline{L}$	hole in the ligand
E_{B}	binding energy
E_{CBM}	conduction band minimum
E_{F}	Fermi energy
E_{G},E_{gap}	band gap
E_{kin}	kinetic energy
E_{SEC}	binding energy of secondary electron cut-off
E_{VBM}	valence band maximum
eV_{bb}	band bending
I_{P}	ionization potential
k_{B}	Boltzmann constant, $8.617 \times 10^{-5}\,\mathrm{eV\,K^{-1}}$
$N_{\mathrm{A}}, N_{\mathrm{D}}$	number of acceptors/donors
n_{i}	intrinsic charge carrier concentration
$N_{\mathrm{V}}, N_{\mathrm{C}}$	effective density of states of valence/conduction band
$\mathrm{V_O^{\bullet\bullet}}$	doubly charged oxygen vacancy
AC/DC	famous rockband, also: alternating, direct current
ALD	atomic layer deposition
DAISY-MAT	DArmstadt Integrated SYstem for MATerial research
DOS	density of states
GIXD	grazing incidence X-ray diffraction
IPES	Inverse photoelectron spectroscopy
PES	photoelectron spectroscopy
PLD	pulsed laser deposition
RT	room temperature
TMO(s)	transition metal oxide(s)
UHV	ultrahigh vacuum, below $10^{-7}\,\mathrm{Pa}$
UPS	ultraviolet photoelectron spectroscopy
XAS	X-ray absorption spectroscopy
XPS	X-ray photoelectron spectrscopy
XRD	X-ray diffraction

Additional Figures and Information

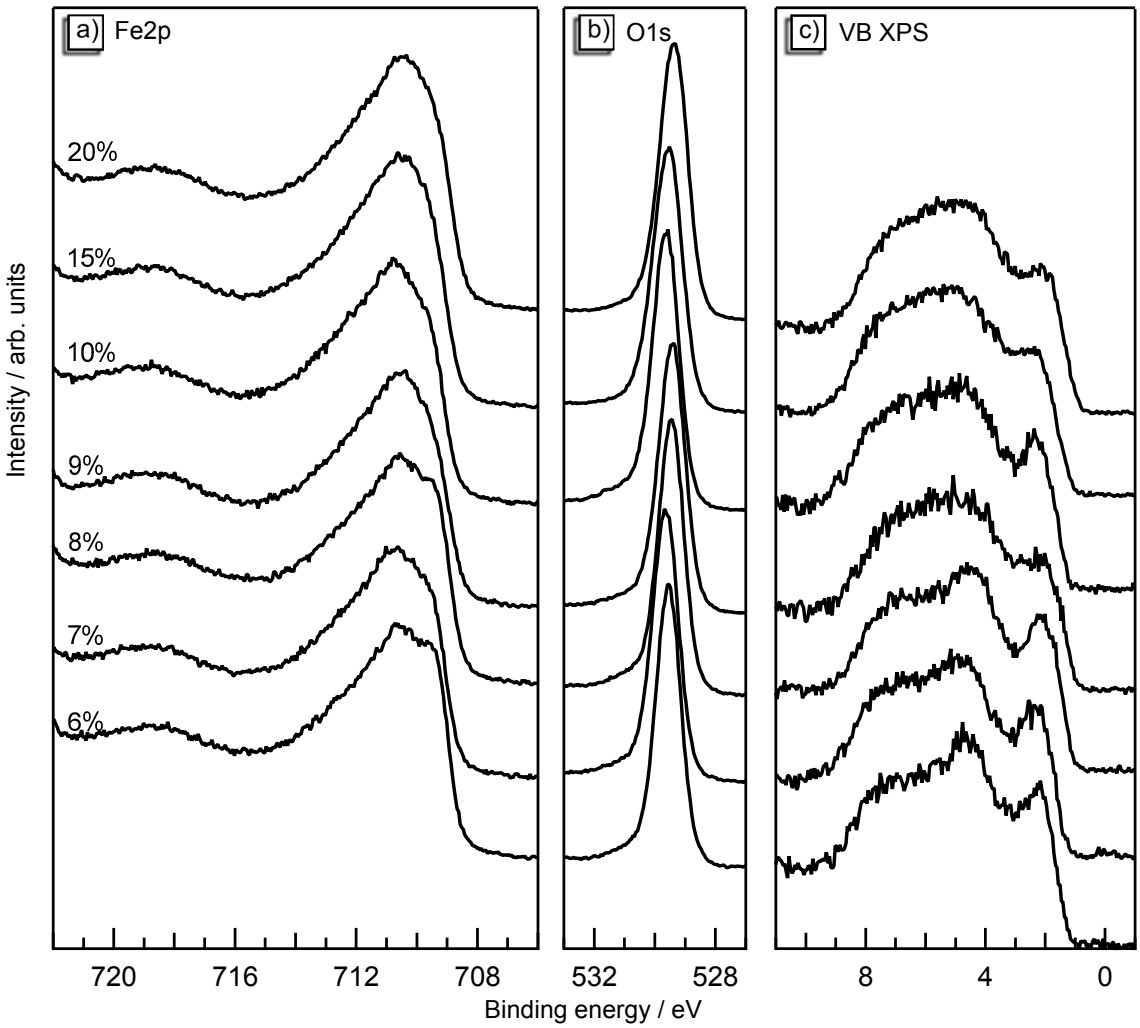

Figure A1: XP spectra of samples deposited with more than 6 % oxygen at 400 °C.

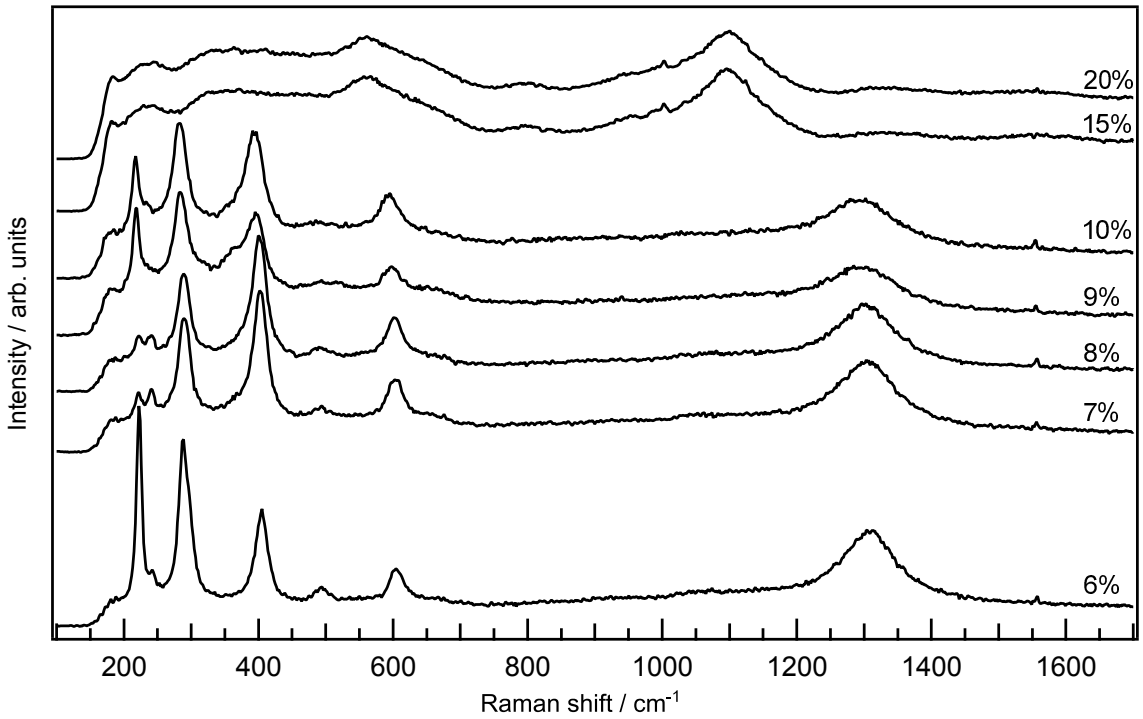

Figure A2: Raman spectra of samples deposited with more than 6 % oxygen in the sputter gas.

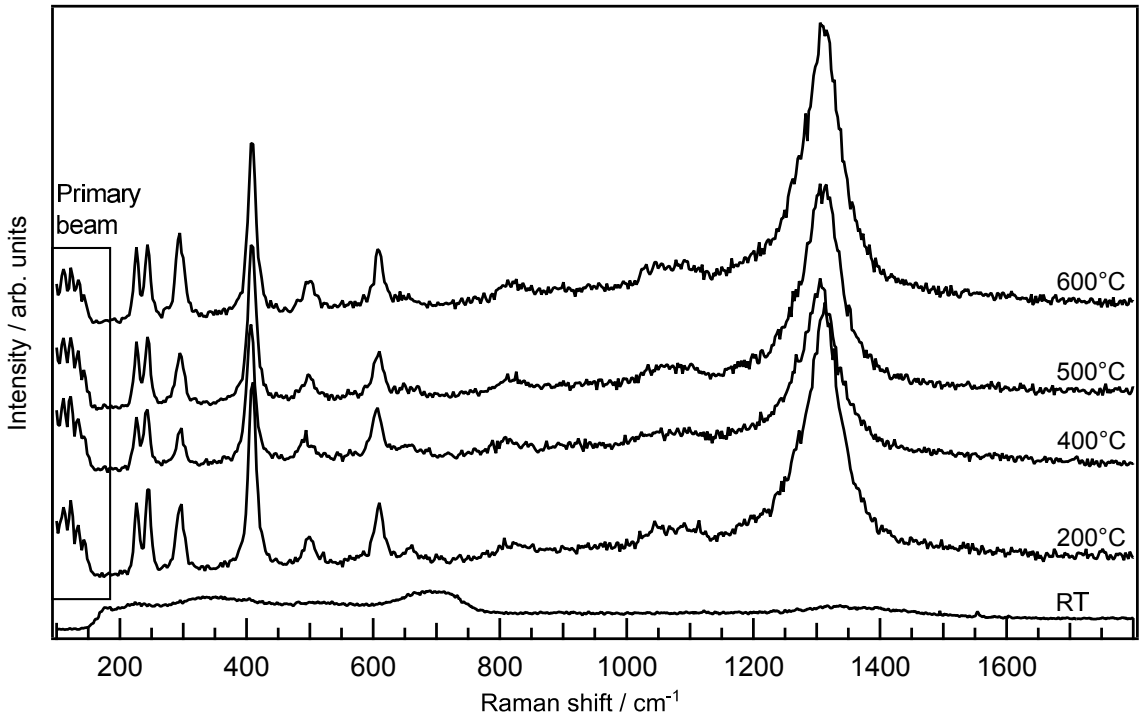

Figure A3: Raman spectra of samples deposited at different temperatures RT up to 600 °C of which the XP spectra are shown in Figure 4.4

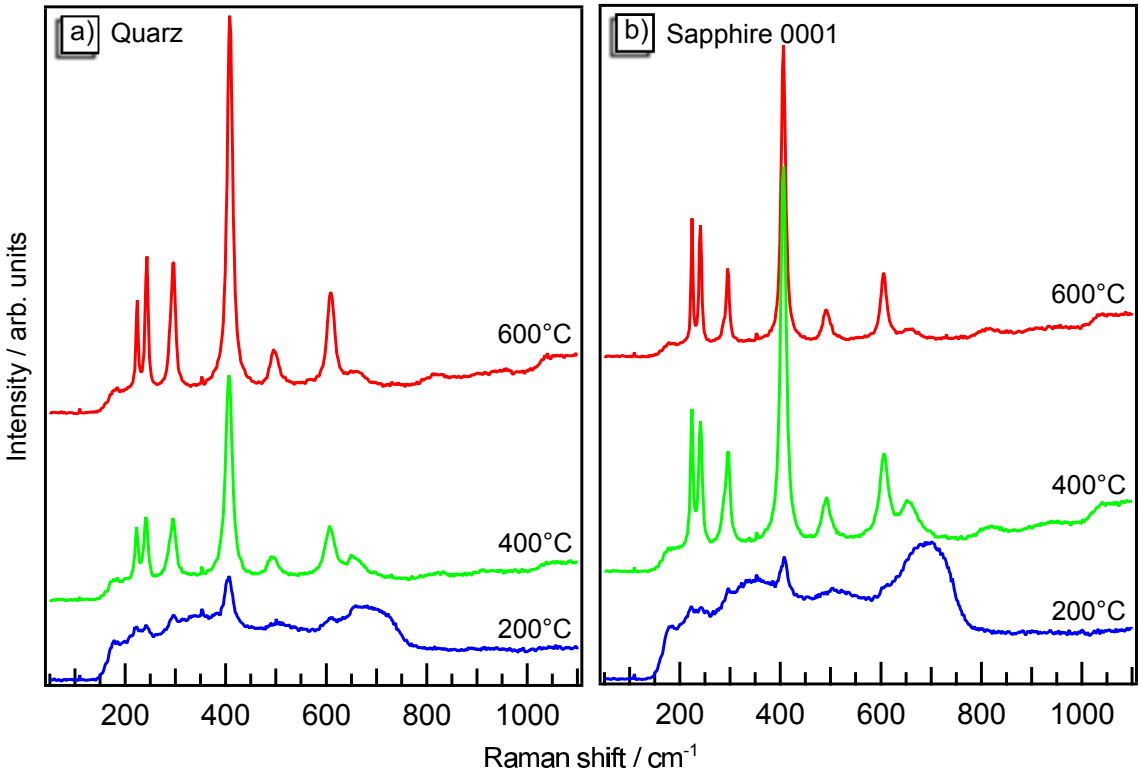

Figure A4: Raman spectra of in-situ heated samples deposited at room temperature on a) quarz and b) sapphire 0001. Same color as in Figure 4.6.

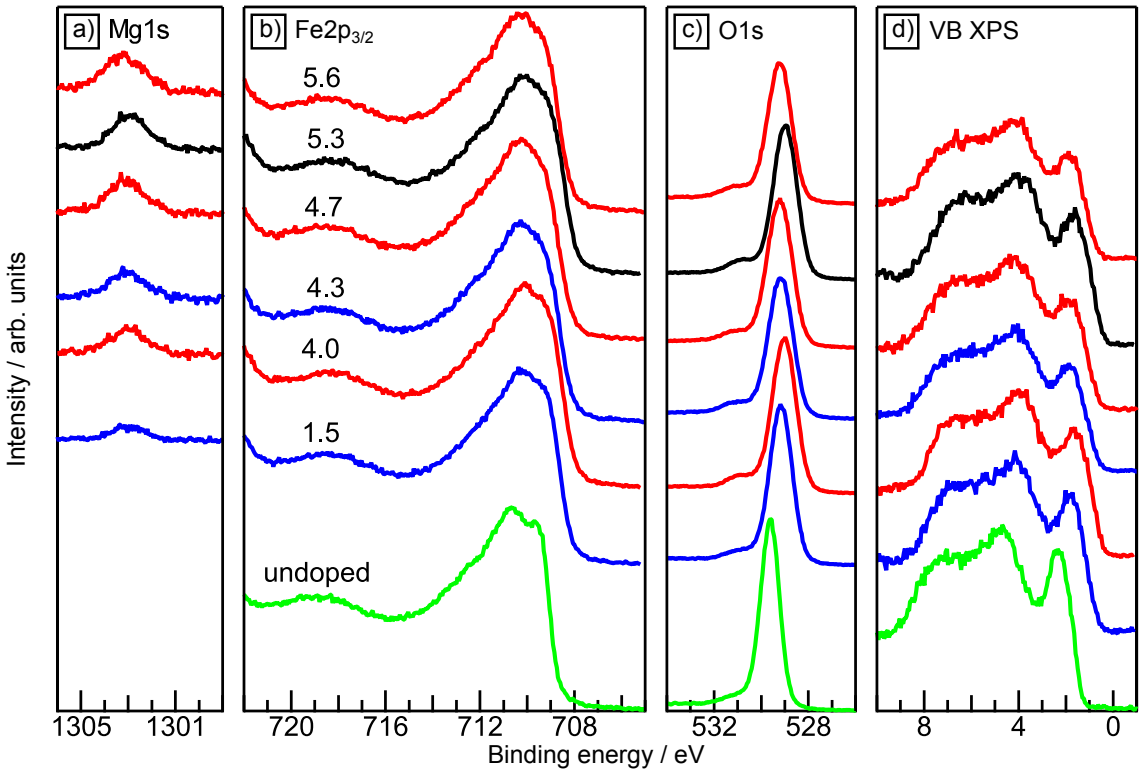

Figure A5: Additional XP spectra for Mg-doped samples deposited at 400 °C. The Mg/Fe ratio in percent is indicated on the $Fe2p_{3/2}$-spectra. The green and black spectra correspond to samples with the same color in Figure 6.2.

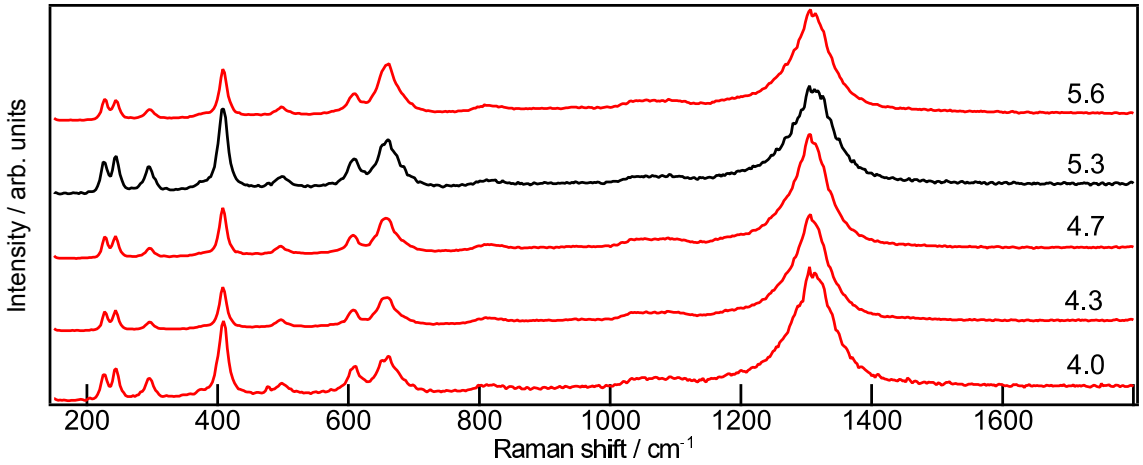

Figure A6: Additional Raman spectra for Mg-doped samples deposited at 400 °C. The Mg/Fe ratio in percent is indicated. The black spectrum corresponds to the sample with the same color in Figure 6.1.

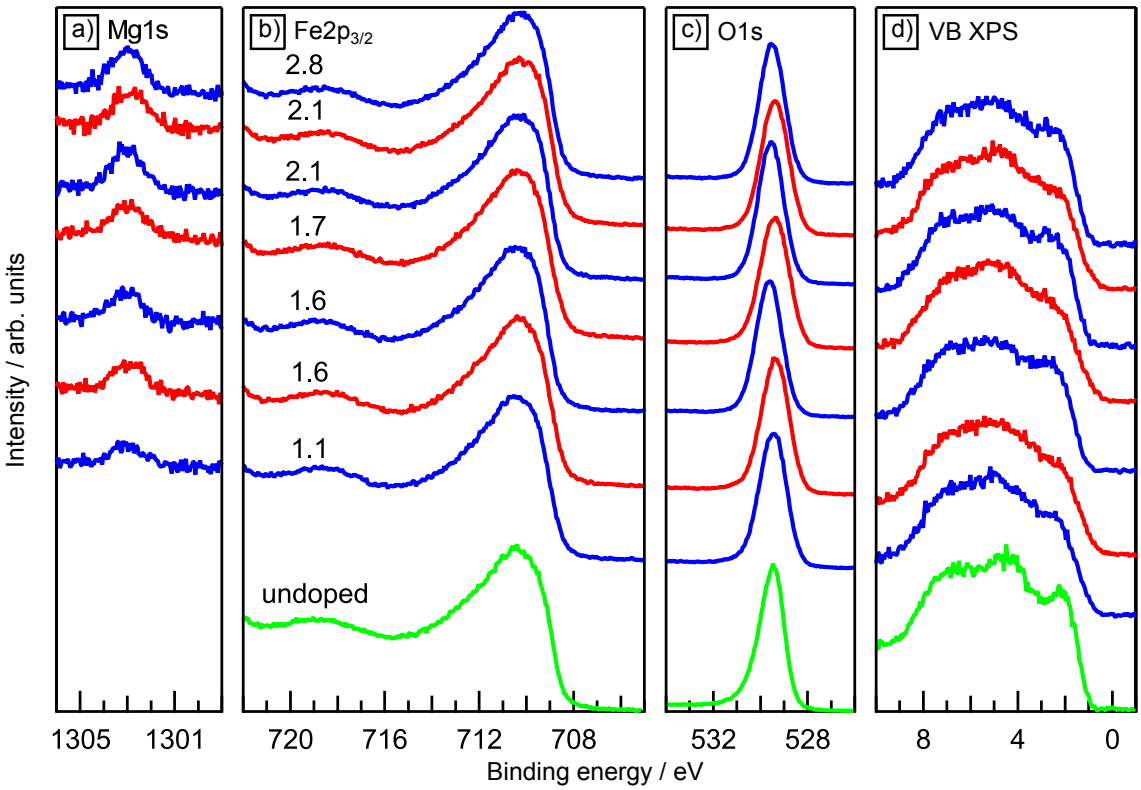

Figure A7: Additional XP spectra for Mg-doped samples deposited at 200 °C. The Mg/Fe ratio in percent is indicated on the $Fe2p_{3/2}$-spectra. The green spectra belong to an undoped sample which has been deposited at the same conditions despite the doping.

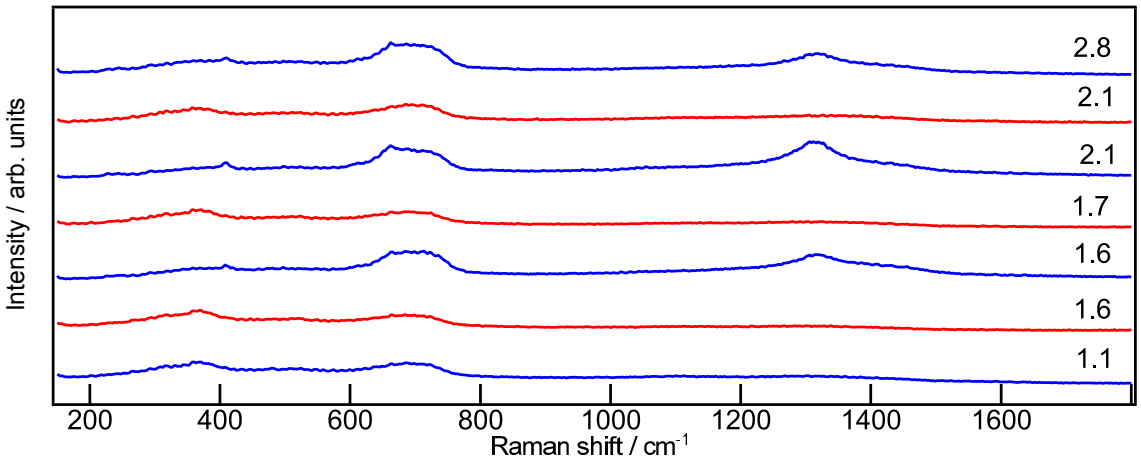

Figure A8: Additional Raman spectra for Mg-doped samples deposited at 200 °C. The Mg/Fe ratio in percent is indicated.

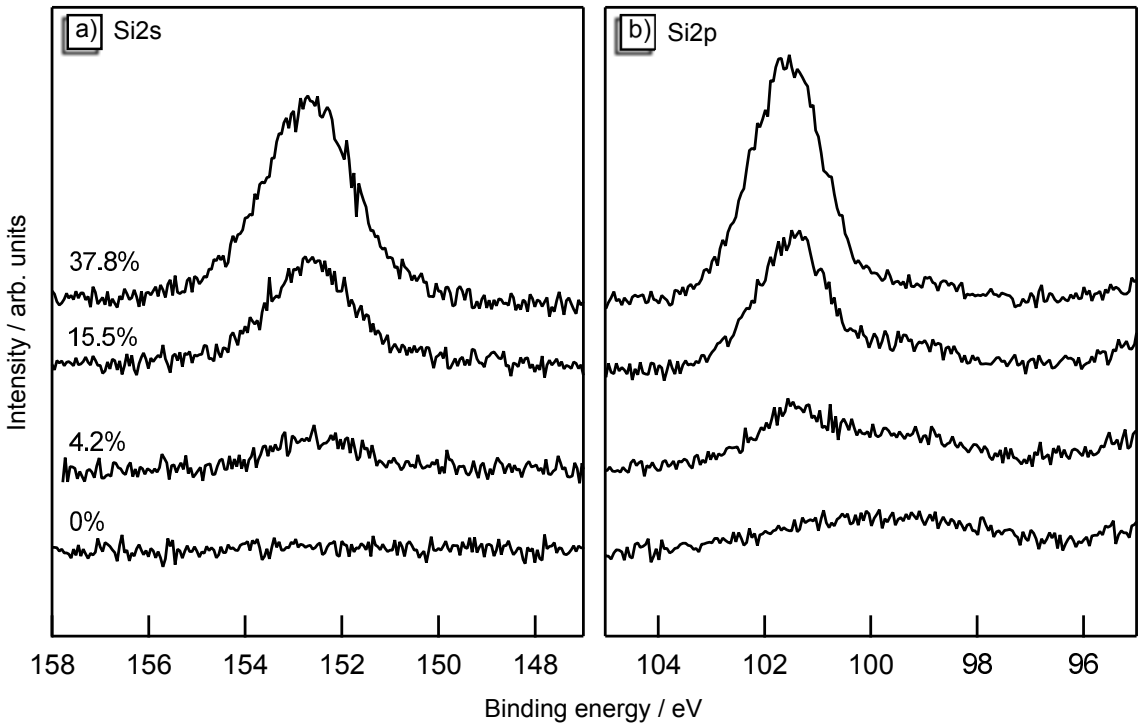

Figure A9: Si core-level spectra of Si doped hematite. In a) the Si2s level shows no overlap with signals from iron or oxygen whereas the Si2p emission in b) clearly shows such an overlap.

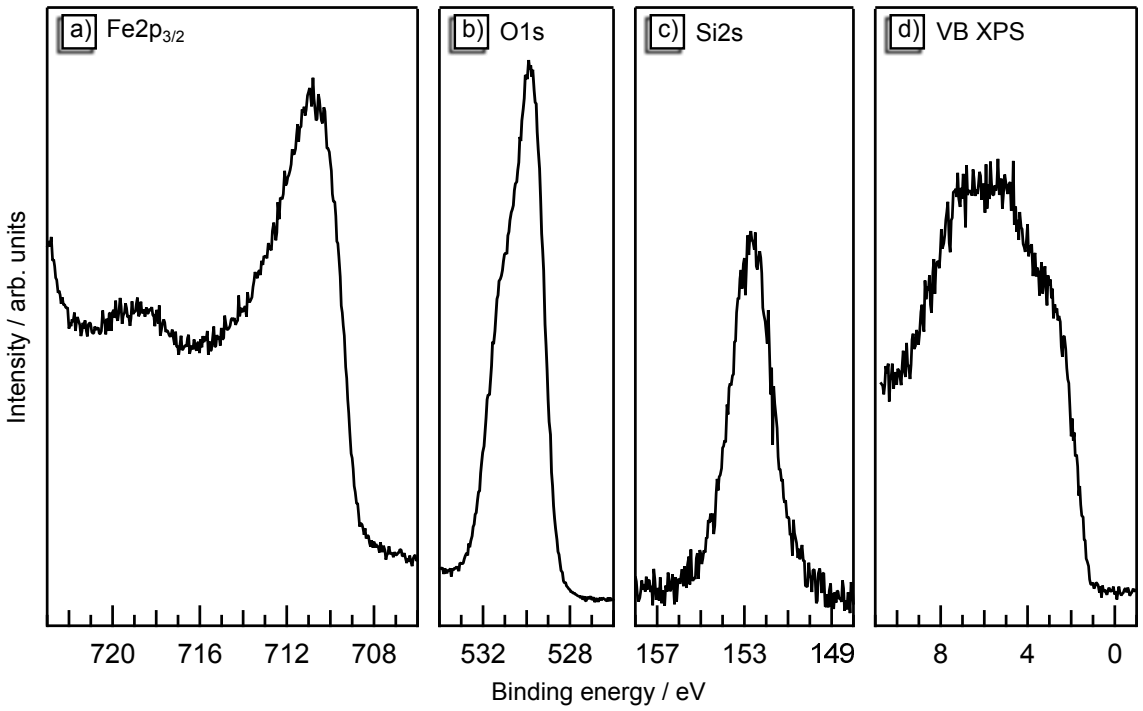

Figure A10: XP spectra of a Si-doped sample with more than 30 % Si. The clearly observable shoulder in the O1s emission can be regarded as evidence for a SiO_2 segregation to the surface.

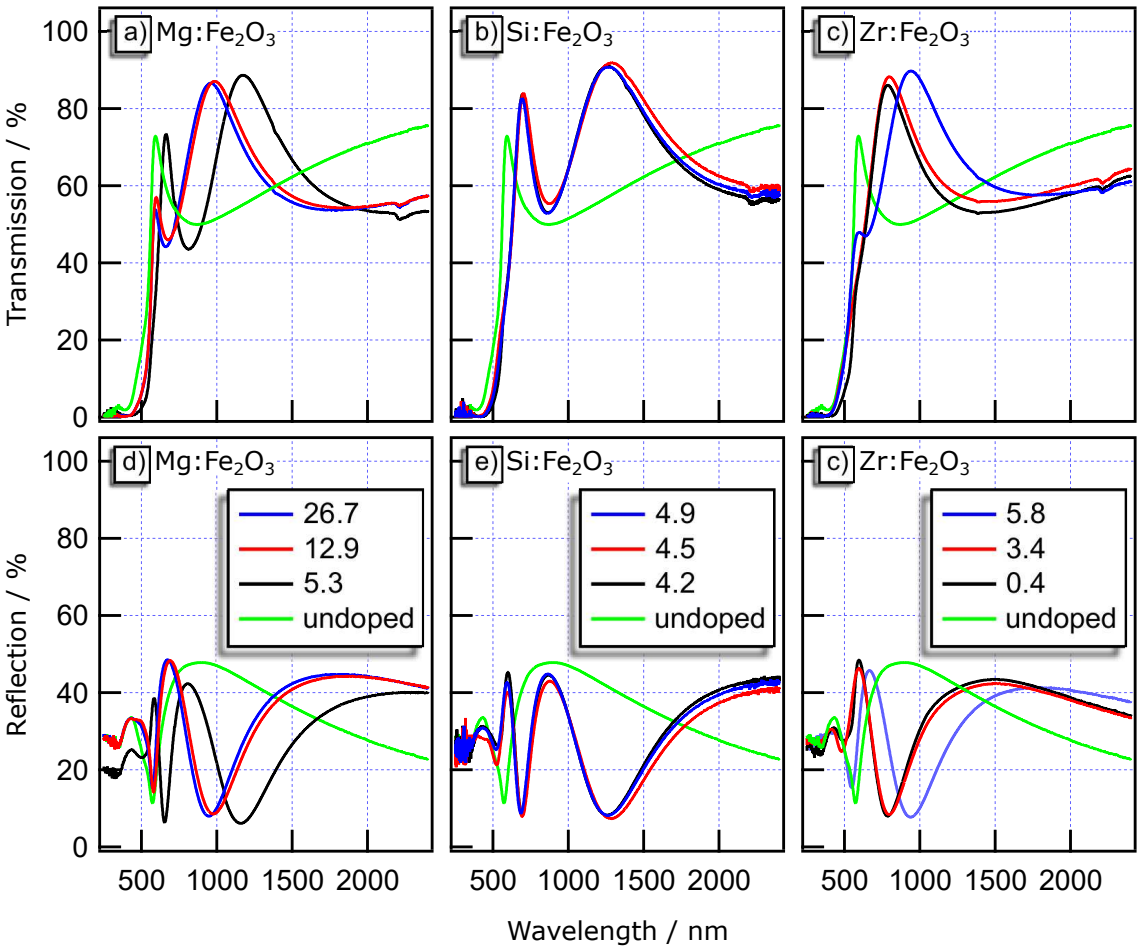

Figure A11: Transmission and reflection measurements of samples presented in Figure 6.15

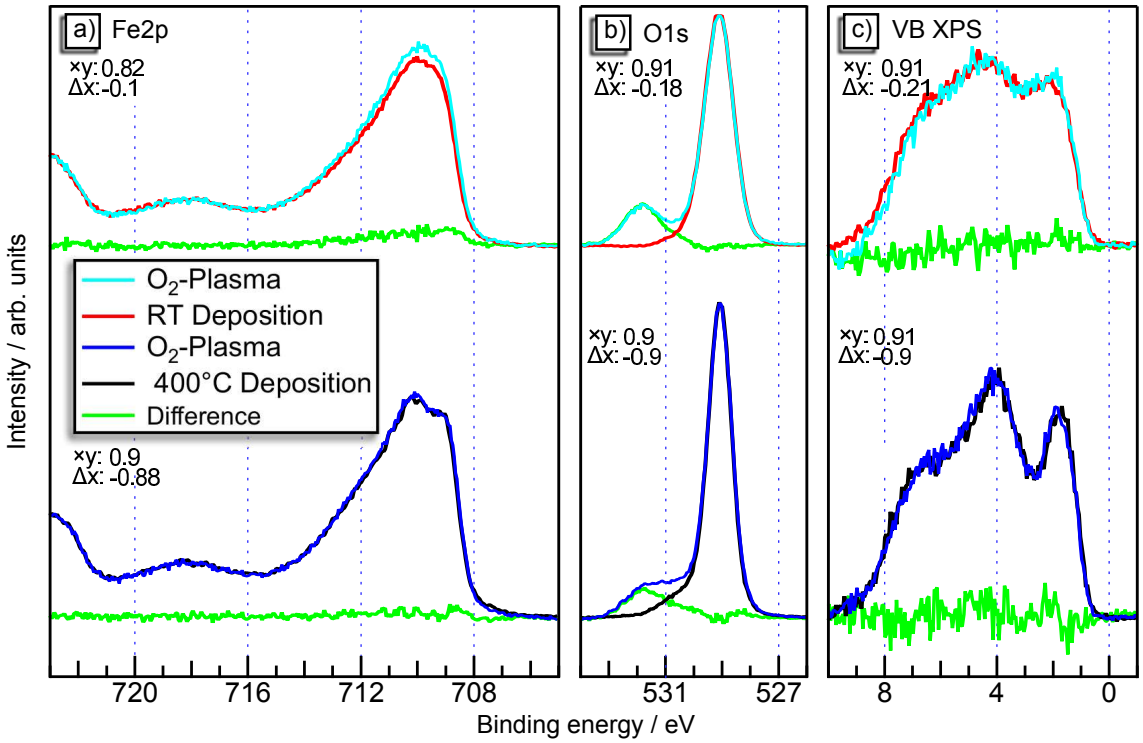

Figure A12: Difference spectra for the oxygen-plasma experiments. Untreated spectra are subtracted from the spectra after treatment.

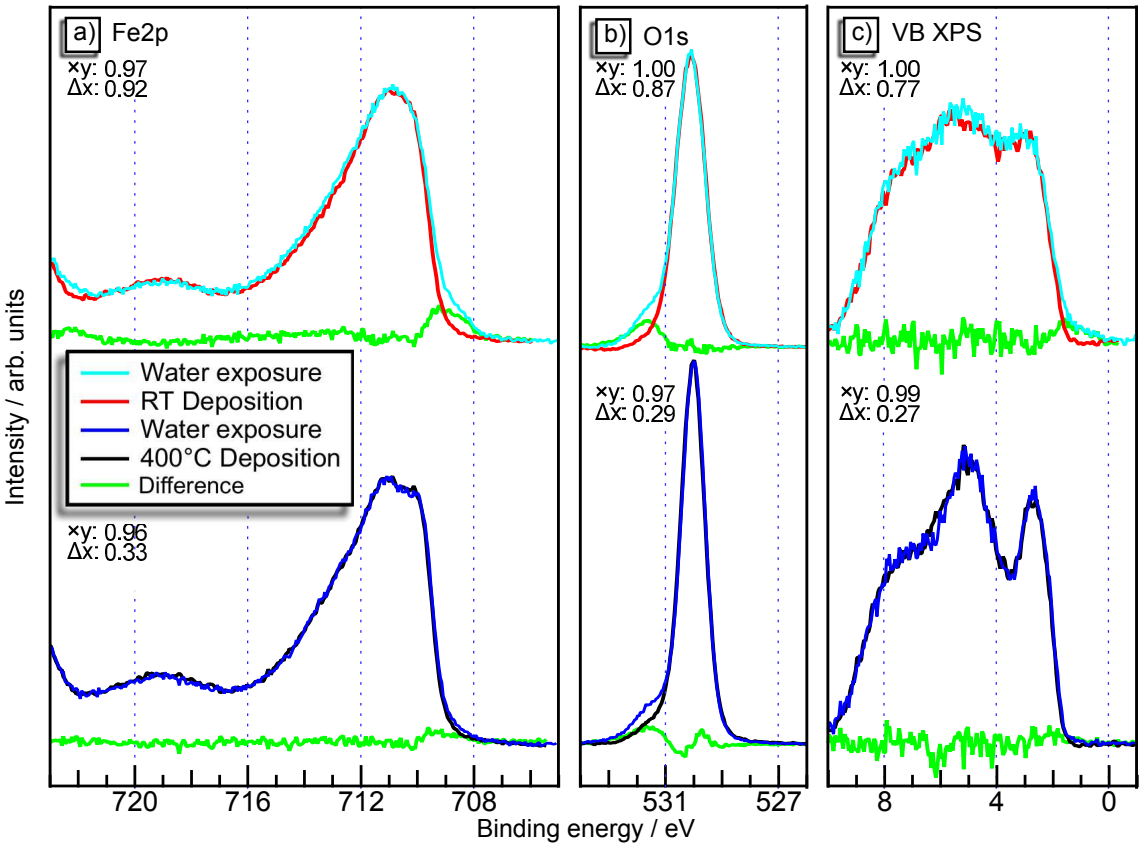

Figure A13: Difference spectra for the water exposure experiments. Untreated spectra are subtracted from the spectra after treatment.

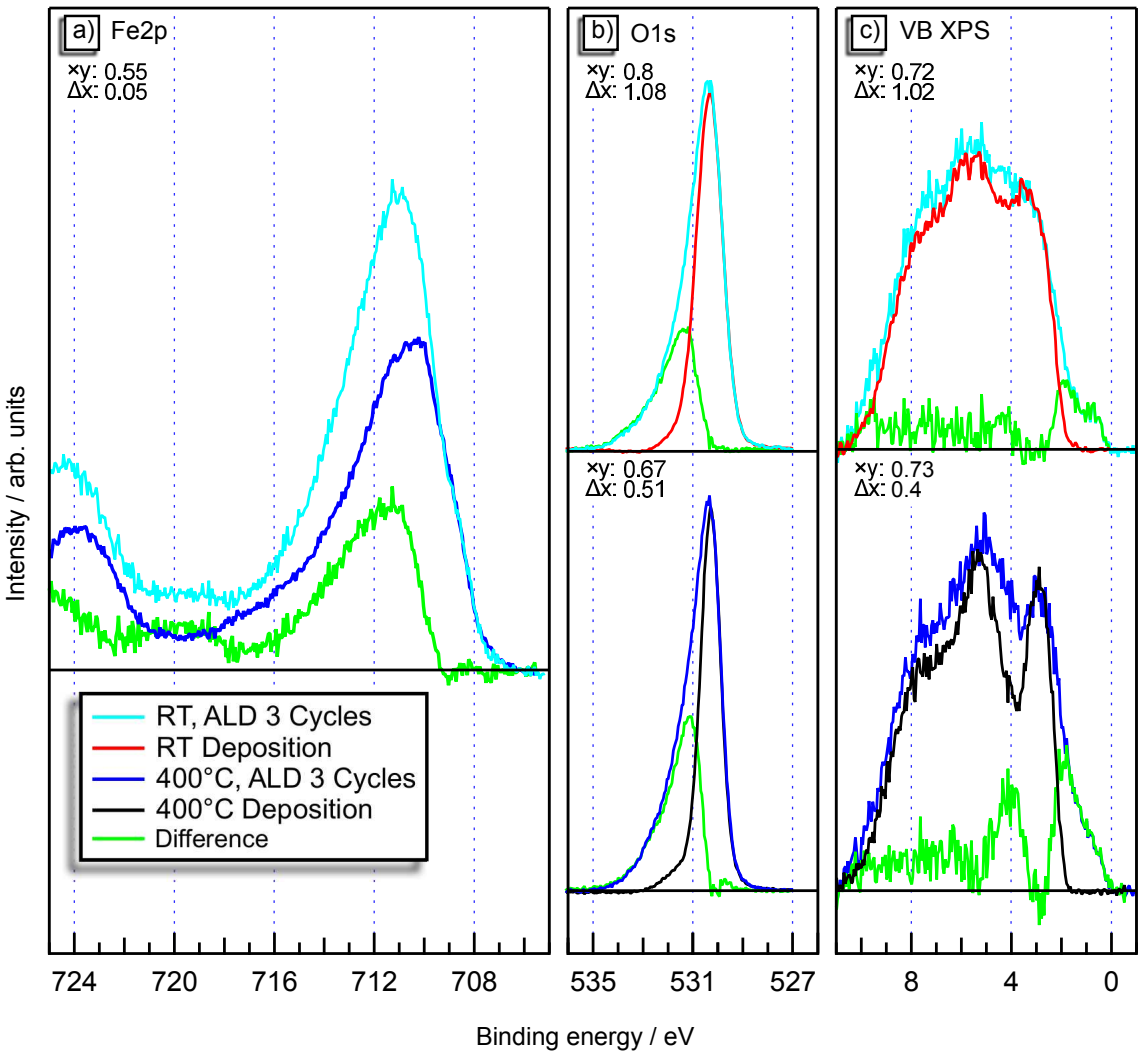

Figure A14: Difference spectra of the surface modification by atomic layer deposited alumina. In b) and c) the spectra from before the modification are subtracted from the spectra measured after the deposition of Al_2O_3. In a) the spectra recorded after the modification of a crystalline hematite sample is subtracted from the spectra after deposition on an amorphous Fe_2O_3 sample.
It can be clearly observed in a) and c) that the addition of alumina involves the formation of Fe^{2+} The difference in the valence band of the crystalline sample shows two signals which can most likely be assigned to orginate from the crystal field splitted Fe3d states. The signals are less intense in the amorphous sample after the deposition of alumina. This agrees nicely to the difference in the Fe2p spectra of the amorphous and crystalline sample after the modification. Here, the difference is clearly the spectrum from Fe^{3+} which shows that the amount of this species is higher in the amorphous sample than in the crystalline sample. The difference in the oxygen spectrum can be explained by the addition of another oxide onto Fe_2O_3 .

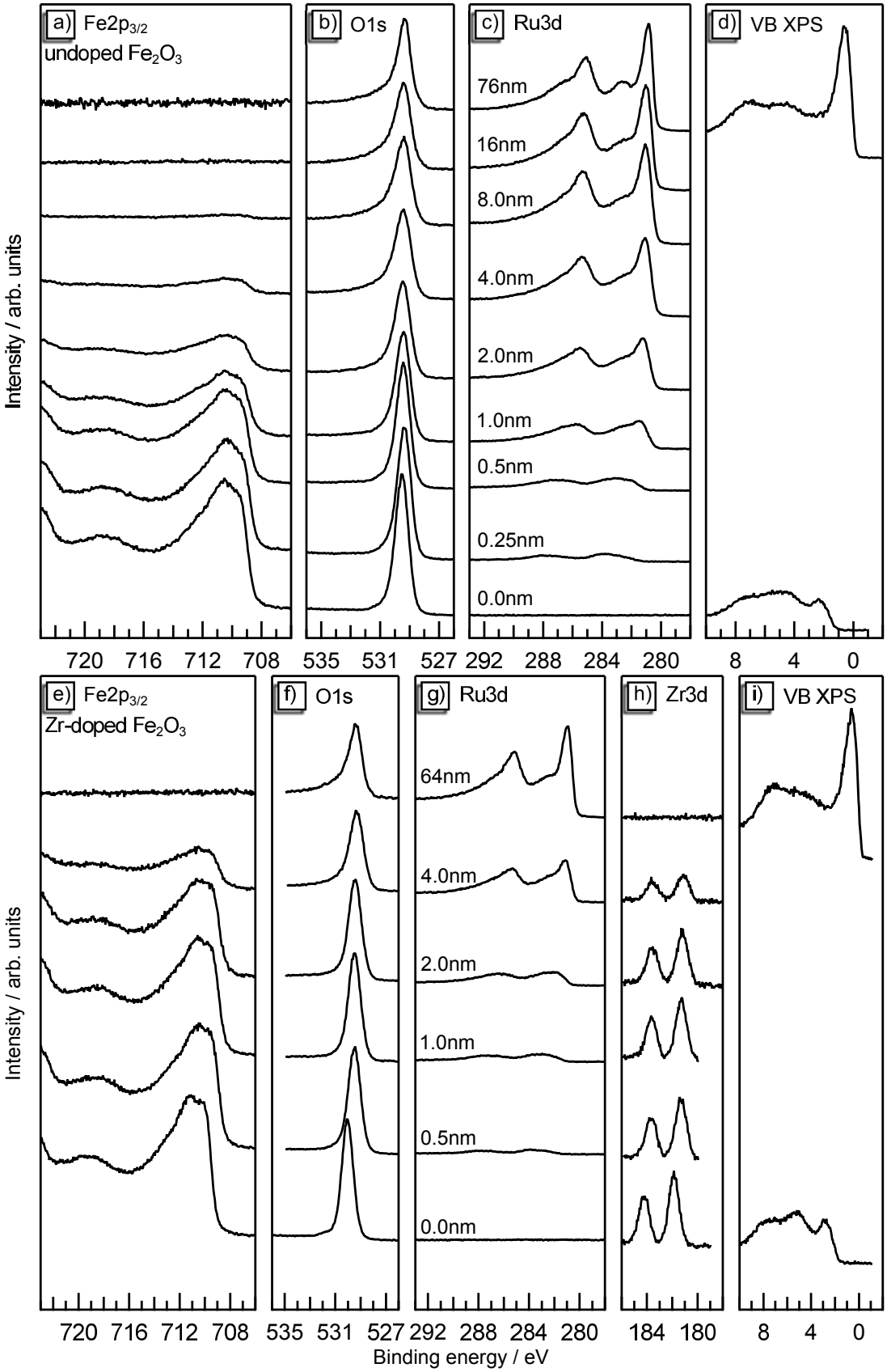

Figure A15: XP spectra for interface experiments of undoped Fe_2O_3 [a)-d)] and Zr-doped Fe_2O_3 [e)-i)] towards RuO_2. The calculated thickness of the RuO_2 film assuming a rate of 3 nm min^{-1} is annotated.

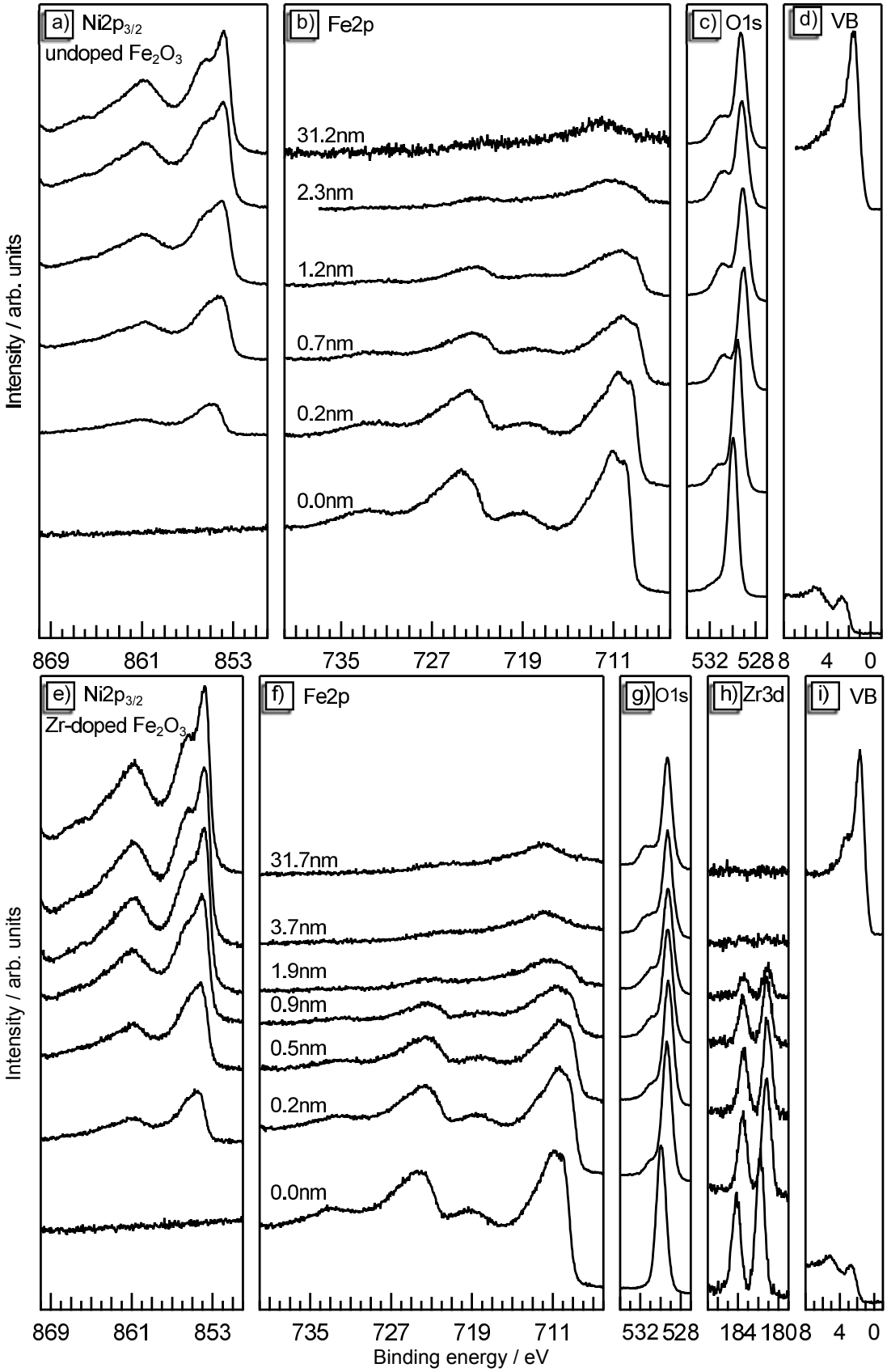

Figure A16: XP spectra for interface experiments of undoped Fe_2O_3 [a)-d)] and Zr-doped Fe_2O_3 [e)-i)] towards NiO. The calculated thickness of the NiO film assuming a rate of 1.4 nm min^{-1} is annotated.

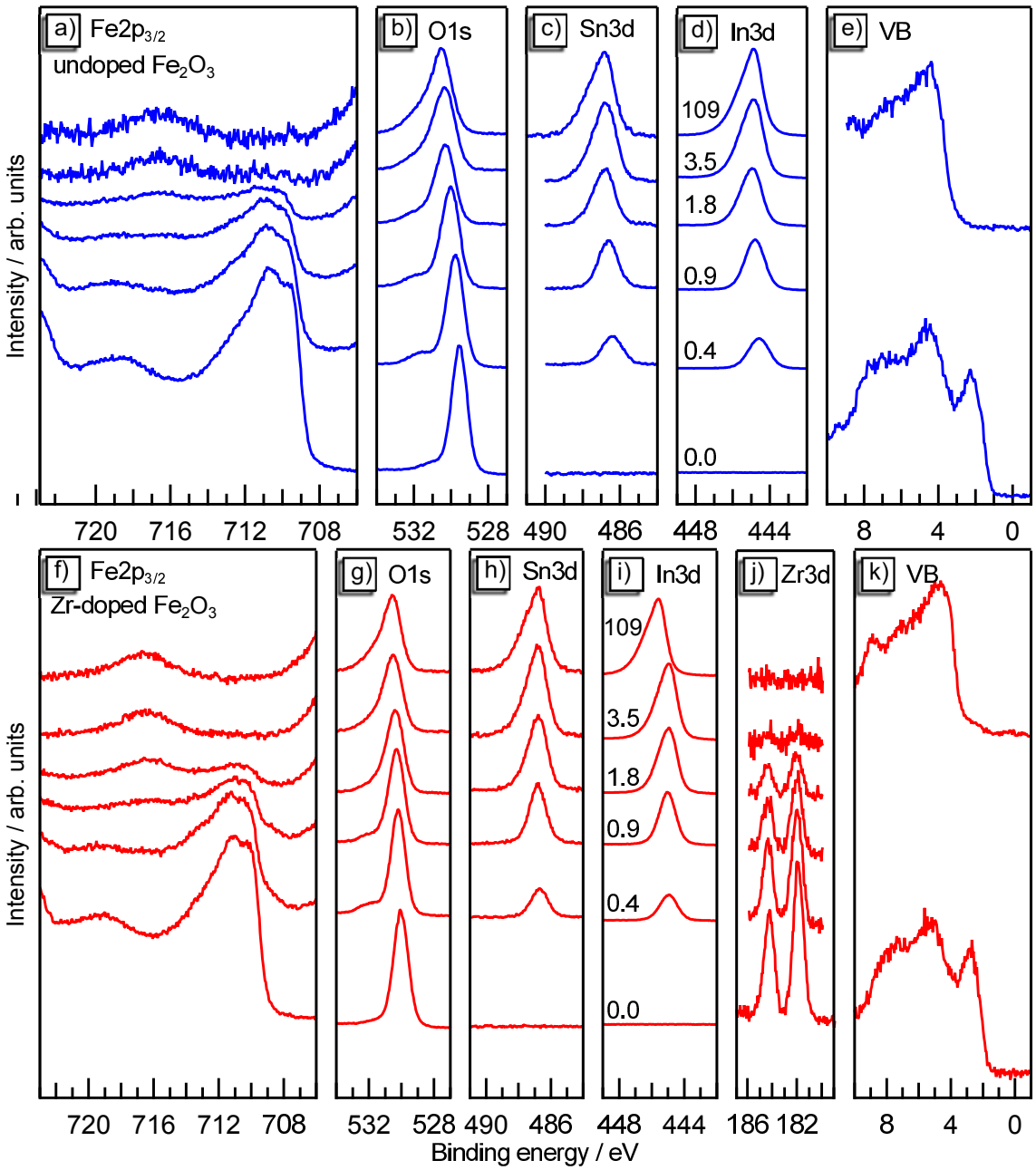

Figure A17: XP spectra for interface experiments of undoped Fe_2O_3 [a)-e)] and Zr-doped Fe_2O_3 [f)-k)] towards ITO. The calculated thickness of the ITO film in nanometer assuming a rate of 5.3 nm min^{-1} is annotated.

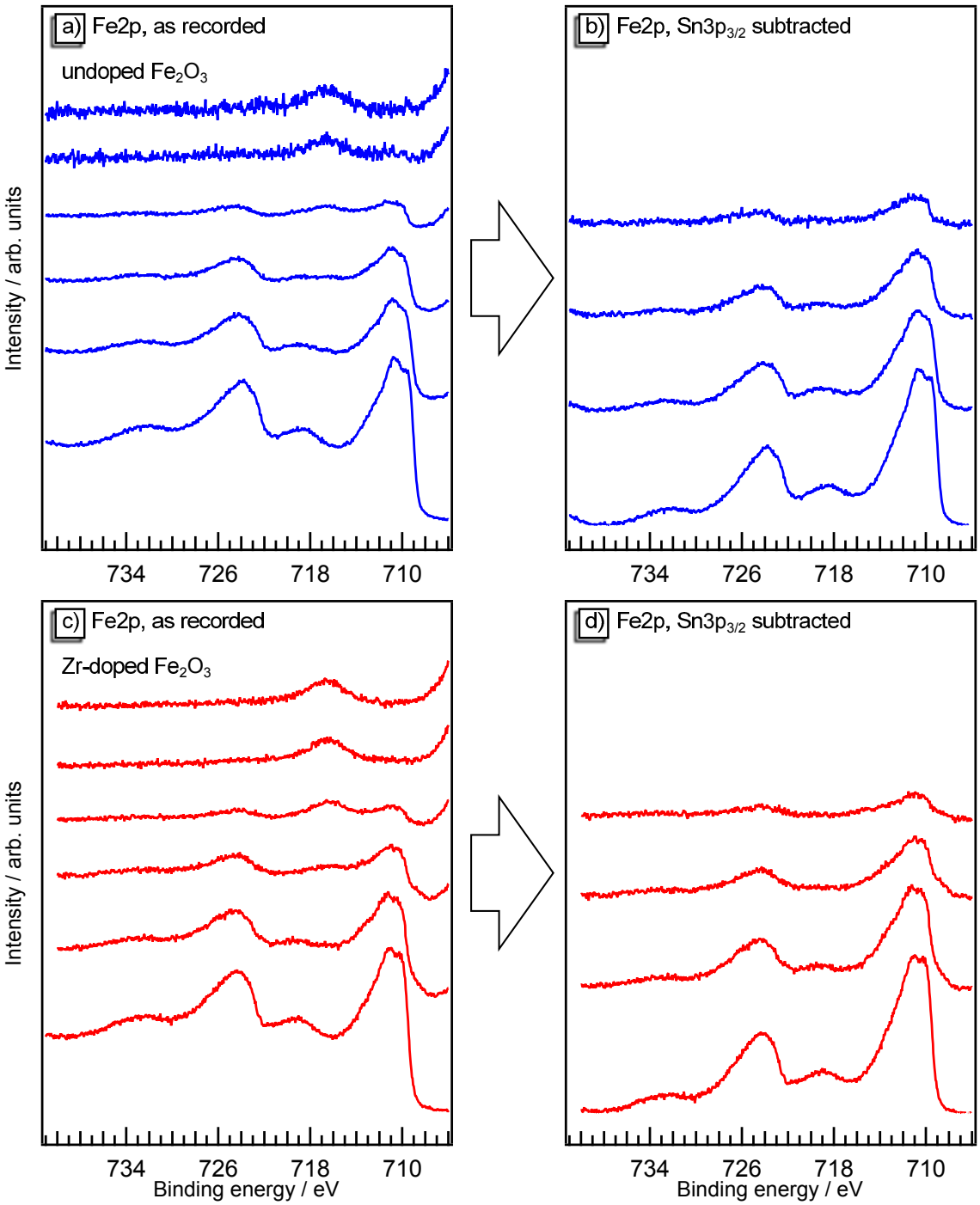

Figure A18: Correction of Fe2p spectra from interface experiments towards ITO by subtracting the y-scaled and x-shifted $Sn3p_{3/2}$ spectrum from the last measurement. a) and b) are spectra from and undoped and c) and d) from a Zr-doped hematite thin film.

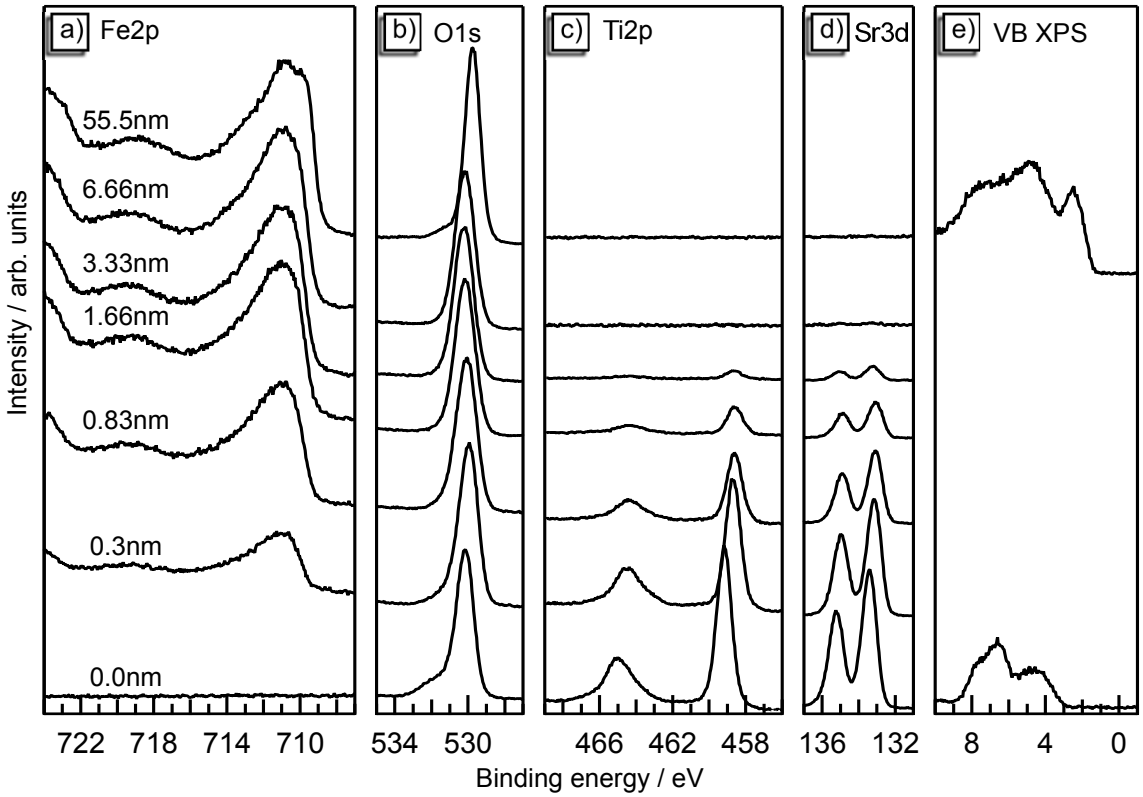

Figure A19: XP spectra for interface experiments of undoped Fe_2O_3 towards $SrTiO_3$. Hematite was grown on STO in this experiment. The calculated thickness of the Fe_2O_3 film assuming a rate of 3.3 nm min^{-1} is annotated.

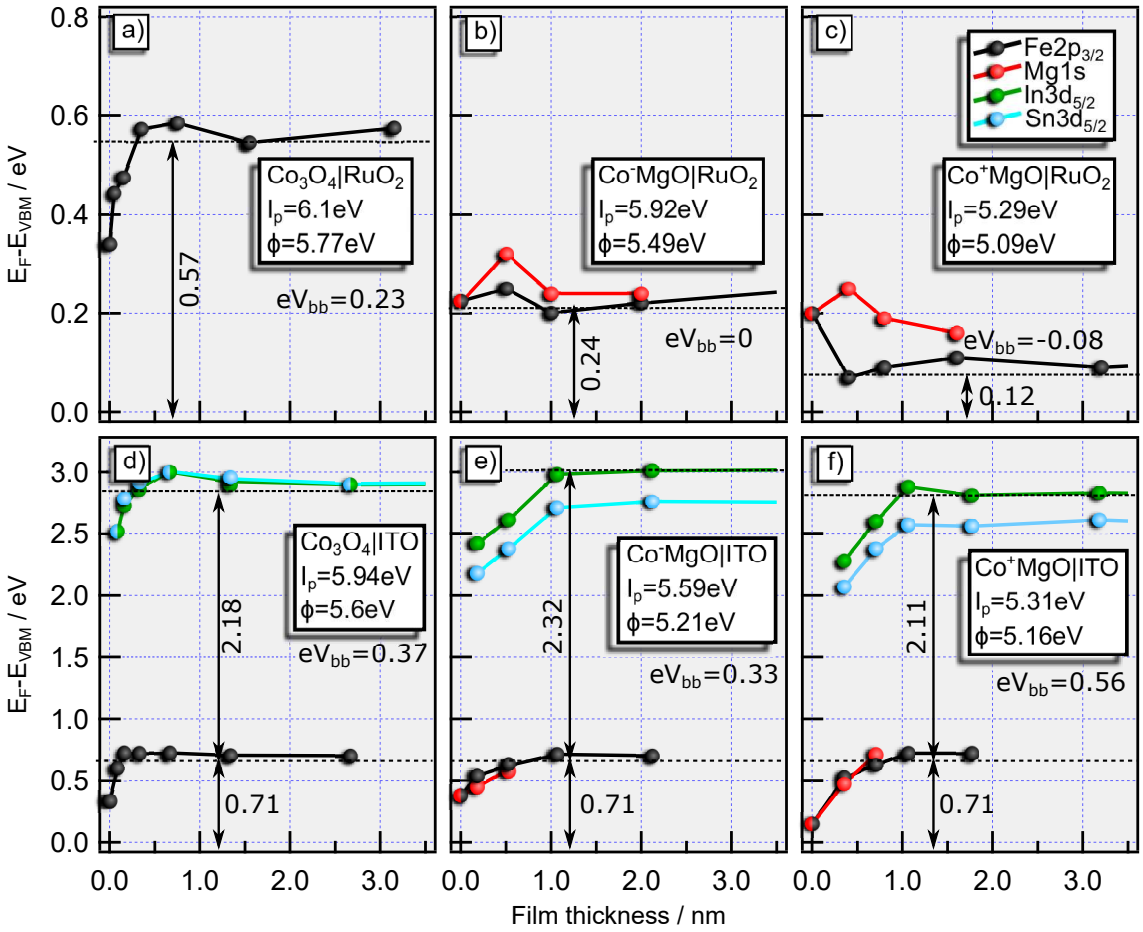

Figure A20: Interface experiments with $(CoMg)_3O_4$ samples towards RuO_2 and ITO. The samples have different compositions with 100 % Co (Co_3O_4), 56 % (Co^-), and 71 % (Co^+) on the cation site. At 66 % Co all cobalt should be Co^{3+}.

In the interface experiments towards RuO_2 in a)-c) the band bending of the three different cobaltoxides is either upwards in a), none existing in b) or downwards in c). The samples differ in their initial work function with a) 5.77 eV, b) 5.49 eV, and 5.09 eV. As the direction of the band bending is depending on the initial work function of the substrate a determination of the work function of RuO_2 is possible. A value of 5.5 eV explains the behavior at these interfaces the best. This is about 1 eV less than what was measured for all experiments on the thick RuO_2 film. In case of the experiment presented in c) a Fermi level pinning in the cobaltoxide can be expected.
The interface experiments towards ITO in d)-e) show similar results as has been observed with hematite. Despite having different initial work functions all three sample show the same Fermi level position at the interface of 0.71 eV. A Fermi level pinning by charge transition of $Co^{3+} + e^- \rightarrow Co^{2+}$ might be the reason for this observation. Due to the duovalent nature of cobalt in these oxides, however, a clear distinction was not possible. Small changes in the satellite intensity might indicate this charge transition but the assignment should clearly be seen as tentatively.

List of Figures

List of Tables

Publications and Conferences

Supervised theses

2018 N. BEIN. The Fermi Level in Bismuth Ferrite. Master-Thesis.**2018**

K.N.S. SCHULDT. Electronic characterization of thin film Sr-doped $LaFeO_3$. Master-Thesis. **2018**

2017 T. JIANG. Investigation of Electrical Resistance of Hematite Films. Advanced Research Lab. **2017**

C. STEINERT. Preparation and Characterization of RF-magnetron Sputtered Epitaxial Hematite Thin Films. Master-Thesis. **2017**

2015 R. HERTWIG. Deposition and Characterisation of Reactive Sputtered RuO_2 Thin Films. Bachelor-Thesis. **2015**

T. COSSUET. Investigation of ZrO_2 thin films deposited by DC magnetron sputtering on Pt. Advanced Research Lab. **2015**

Publications

2018 C. LOHAUS, A. KLEIN, W. JAEGERMANN.
Limitation of Fermi level shifts by polaron defect states in hematite photoelectrodes.
Nature Communications. accepted. **2018**

C. LOHAUS, C. STEINERT, G. DEYU, J. BRÖTZ, W. JAEGERMANN, A. KLEIN.
Enhancing electrical conductivity of room temperature deposited Sn-doped In_2O_3 thin films by hematite seed layers.
Applied Physics Letters, 112, 152105. **2018**

2017 C. LOHAUS, C. STEINERT, J. BRÖTZ, A. KLEIN, W. JAEGERMANN.
Systematic Investigation of the Electronic Structure of Hematite Thin Films.
Advanced Materials Interfaces, 4, 1700542. **2017**

A. KLEIN, C. LOHAUS, P. REISER, L. DIMESSO, X. WANG, T. YANG.
Energy band alignment of antiferroelectric $(Pb, La)(Zr, Sn, Ti)O_3$.
Applied Surface Science 407, 99-104. **2017**

2016 S. SCHÄFER, E.-M. EVA, F. MUENCH, M. ANTONI, C. LOHAUS, J. BRÖTZ, U. KUNZ, I. GÄRTNER, W. ENSINGER.
NiCo nanotubes plated on Pd seeds as a designed magnetically recollectable catalyst with high noble metal utilisation.
RSC Advances, 6, 70033-70039. **2016**

C. LOHAUS, J. MORASCH, J. BRÖTZ, A. KLEIN, W. JAEGERMANN.
Investigations on RF-magnetron sputtered Co_3O_4 thin films regarding the solar energy conversion properties.
Journal of Physics D: Applied Physics, 49, 155306. **2016** (Master-Thesis)

Attended Workshops, Summer Schools, and Conferences

2018 WORKSHOP ON NEW ABSORBERS (Giessen, Germany): Effective bandgaps of metal oxides with localized d^n electron configuration
-Oral Presentation

2017 EUROPEAN MATERIALS SOCIETY SPRING MEETING (Strasbourg, France): Density of states in thin film hematite – How crystallinity influences the electronic properties
-Oral Presentation

2016 21st INTERNATIONAL CONFERENCE ON PHOTOCHEMICAL CONVERSION AND STORAGE OF SOLAR ENERGY (St Petersburg, Russian Federation): Electronic Structure of Transition Metal Oxides
-Oral Presentation

EUROPEAN MATERIALS SOCIETY SPRING MEETING (Lille, France): Valence band density of states in ternary cobalt oxides
-Poster Presentation

2015 EUROPEAN MATERIALS SOCIETY SPRING MEETING (Lille, France): Investigations on RF-magnetron sputtered Co_3O_4 with regard to its usability as a solar energy conversion material
-Oral Presentation

EUROPEAN MATERIALS SOCIETY SPRING MEETING (Lille, France): Low Band Gap Oxides for Light Absorption
-Oral Presentation for J. Morasch

2014 MATERIALS SCIENCE AND ENGINEERING (Darmstadt, Germany): Low Band Gap Oxides for Light Absorption
-Poster Presentation for J.Morasch

INTERNATION SUMMER SCHOOL ON PHOTOVOLTAICS AND NEW CONCEPTS OF QUANTUM SOLAR ENERGY CONVERSION (Hirschegg, Austria)
-Participant

Résumé

Christian Lohaus

born 30.11.1988 in Jugenheim

Professional Experience

09/2014 - 04/2018	**Research Assistant** TU Darmstadt, Surface Science Division Darmstadt, Germany
2010	**Internship** State Materials Testing Institute Darmstadt Darmstadt, Germany

Education

09/2014 - today	**Doctoral Studies** TU Darmstadt, Surface Science Division Darmstadt, Germany Title of Thesis: "The Fermi Level in Hematite"
10/2011 - 04/2014	**Master's degree Materials Science** TU Darmstadt, Darmstadt, Germany Degree: Master of Science (1.02, with honor)
08/2012 - 06/2013	**Stay Abroad** Virginia Tech, Blacksburg, Virginia, USA
10/2008 - 10/2011	**Bachelor's degree Materials Science** TU Darmstadt, Darmstadt, Germany Degree: Bachelor of Science (1.45, very good)
1999 - 2008	**Schuldorf Bergstrasse** Seeheim-Jugenheim, Germany Degree: Abitur (1.0, very good)

Danksagung

Bei Prof. WOLFRAM JAEGERMANN möchte ich mich ganz herzlich für die Möglichkeit der Forschung und Promotion in der Arbeitsgruppe Oberflächenforschung bedanken. Ich bin mir dem Vertrauen und der Freiheit an einem zu Anfang offenen und bis zum Schluss spannenden Themas zu arbeiten und eigene Ideen verfolgen zu können, ohne dabei alleine zu sein, deutlich bewusst.

Kein geringerer Dank gebührt Prof. ANDREAS KLEIN für vier Jahre, in denen ich immer wusste, an wen ich mich wenden kann, um Ideen zu diskutieren und neue Ideen entstehen zu lassen. Deine Begeisterung und Konzepte zu Defekten und dem Fermi-Niveau haben mich angeleitet und die Diskussionen -insbesondere über Umladungspunkt und Polaronen- mir dir sind ein essentieller Teil meiner Arbeit geworden.

Bei Prof. Oliver CLEMENS bedanke ich mich herzlich für die Übernahme des Zweitgutachtens. Prof. RALPH KRUPKE und Prof. WOLFGANG ELSÄßER möchte ich dafür danken, als meine Prüfer zu agieren.

Für die Hilfe bei der Bestimmung der strukturellen Eigenschaften mittels XRD und Raman Spektroskopie möchte ich mich bei Dr. JOACHIM BRÖTZ, DR. FELIX ROTH und MARCUS SCHULZE bedanken.

Den Mitarbeitern der Arbeitsgruppe Oberflächenforschung danke ich für mehrere Jahre mit intensiven wissenschaftliche Diskussionen, regelmäßigen Nusszopf-Meetings, Gruppenseminarwochen in La Clusaz und gemeinsamen Konferenzbesuche. An diese werde ich mich immer mit Freude erinnern.

Dies gilt insbesondere für die Gruppe der HALBLEITENDEN OXIDE. Jede Promotion hat auch Zeiten, in denen es "nicht so läuft" und hier wurde ich von euch immer aufgefangen. Die gemeinsamen Besuche der Kuhle in der Mittagspause werde ich sehr vermissen.

Den Studierenden, die ich betreuen durfte danke ich sehr. Insbesondere die Betreuung der Masterarbeiten von CELINE STEINERT, KATHARINA SCHULDT und NICOLE BEIN waren für mich spannend, lehrreich und prägend.

Für Zerstreuung in der Freizeit, Unterstützung, tiefgründige Gespräche und gemeinsame Urlaube und Klettertrips danke ich RALPH, HANS, CHRISTOPH, SANDRA , SILKE, JUDITH, DEJAN, LASZLO, ANDREAS, LUKAS und LEON und außerdem allen meinen FREUNDEN. Und dem TANJU.

Meiner FAMILIE danke ich für die jahrelange Unterstützung und den Rückhalt, den ich bei euch immer finden werden!

Erklärung zur Dissertation

Hiermit versichere ich, die vorliegende Dissertation ohne Hilfe Dritter nur mit den angegebenen Quellen und Hilfsmitteln angefertigt zu haben. Alle Stellen, die aus Quellen entnommen wurden, sind als solche kenntlich gemacht. Diese Arbeit hat in gleicher oder ähnlicher Form noch keiner Prüfungsbehörde vorgelegen.

Darmstadt, den

_____

(Christian Lohaus)